# *A Computational Chemistry Approach to Cytochrome P450 Metabolism*

*A thesis submitted to the University of Manchester for the degree of Doctor of Philosophy in the Faculty of Science and Engineering*

**2018**


## *Fabián G. Cantú Reinhard**

*Supervisor: Sam P. De Visser*

**School of Chemical Engineering and Analytical Science**

**Word Count: 69'100**

**List of Figures, Tables and Schemes** **Page**

**Abstract**

*Drugs and other xenobiotic compounds exhibit different transformations upon entering the human body, most often starting with an oxidative reaction involving P450 enzymes. Hence, the effectiveness and half-life, and even the toxicity of these drugs is determined in part to their metabolism. Thus, it is imperative to produce better models, either experimental or theoretical, to facilitate the understanding and predict the behaviour of these processes.*

*Herein, I present a computational study using hybrid quantum mechanics/molecular mechanics (QM/MM) and density functional theory (DFT) methodologies to model enzymatic metabolism reactions. The work particularly emphasises on the reactivity patterns of the active species of cytochrome P450, i.e. Compound I or the iron(IV)-oxo heme cation radical species, through the use of biomimetic models and enzymatic structures.*

*I initially started the work with a thorough benchmark study on the reproducibility and limitations of DFT methods and compare a set of calculated free energy of activations against experimental reaction rates for a biomimetic $Fe^{IV}O$ model. In particular, I focus on a range of density functional theory methods, basis sets, empirical dispersion corrections and solvation as well as entropic effects on the free energy of activation. Based on these studies a recommended set of methods and procedures is proposed.*

*Thereafter, a series of projects explore the reactivity of biomimetic models of Compound I against a number of model substrates. Starting with a model of a carbene ligated iron(IV)-oxo system that shows catalytic properties dramatically altered with respect to P450 CpdI. Through DFT characterization and reactivity with a set of common substrates I establish the electronic and catalytic differences. A subsequent set of projects explore the chemistry of a set of iron(IV)-oxo biomimetic models of Compound I with either a pure computational or a mixed computational-experimental approach. Sound characterizations of the catalytic properties and mechanistic descriptions of such systems are presented often with comparisons to P450-Compound I. A gas phase electron deficient metalloporphyrin model, $TPFFP^{+\bullet}$ is explored giving comprehensive evidence and rationalization into the distinctions between the mechanisms of aromatic vs aliphatic hydroxylation with common aromatic substrates. Further experiments and modelling were performed in a follow up project where a stable cationic intermediate is formed in contrast to the more common radical intermediate chemistry as seen in CpdI with the same substrate.*

*Following this investigations, a rather more applied set of projects is presented. First the capabilities of a simplified P450 model are explored for the prediction of toxic metabolic products and sites of metabolism (SOMs) derived from P450-oxidations on a common phthalate derived substrate found frequently on cosmetic products and pharmaceutical formulations, revealing reaches and limitations of this approach. Lastly, a comprehensive DFT and QM/MM approach is employed to investigate the chemistry behind the co-factor independent oxidation of nogalamycin, a naturally occurring antibiotic. Thermochemical cycles, DFT models as well as QM/MM studies highlight possible oxidants in the reaction mechanism and propose relevant factors affecting the chemical reaction.*

**Declaration**

No portion of the work referred to in the thesis has been submitted in support of an application for another degree or qualification of this or any other university or other institute of learning.

**Copyright Statement Declaration**

i. The author of this thesis (including any appendices and/or schedules to this thesis) owns certain copyright or related rights in it (the "Copyright") and s/he has given The University of Manchester certain rights to use such Copyright, including for administrative purposes.

ii. Copies of this thesis, either in full or in extracts and whether in hard or electronic copy, may be made only in accordance with the Copyright, Designs and Patents Act 1988 (as amended) and regulations issued under it or, where appropriate, in accordance with licensing agreements which the University has from time to time. This page must form part of any such copies made.

iii. The ownership of certain Copyright, patents, designs, trademarks and other intellectual property (the "Intellectual Property") and any reproductions of copyright works in the thesis, for example graphs and tables ("Reproductions"), which may be described in this thesis, may not be owned by the author and may be owned by third parties. Such Intellectual Property and Reproductions cannot and must not be made available for use without the prior written permission of the owner(s) of the relevant Intellectual Property and/or Reproductions.

iv. Further information on the conditions under which disclosure, publication and commercialisation of this thesis, the Copyright and any Intellectual Property and/or Reproductions described in it may take place is available in the University IP Policy (see http://documents.manchester.ac.uk/DocuInfo.aspx?DocID=2442 0), in any relevant Thesis restriction declarations deposited in the University Library, The University Library's regulations (see http://www.library.manchester.ac.uk/about/regulations/) and in The University's policy on Presentation of Theses.

## The Author

Before entering this PhD programme, I graduated from a major in Chemical Engineering with a minor in Environmental Engineering, at ITESM (Mexico, Monterrey), followed by a MSc. Degree in Biological and Bioprocess Engineering at the University of Sheffield. After that, I did two years of work experience as a Validations Engineer at Pharmapack, a Pharmaceutical Contract Manufacturing Company located in Mexico.

## List of Abbreviations

- Cpd0 Compound 0
- CpdI Compound I
- CpdII Compound II
- DEHP di(2-ethylhexyl)-phthalate
- DFT Density Functional Theory
- EA Electron Affinity
- ECP Effective Core Potential
- Eq. Equation
- GGA Generalized Gradient Approximation
- GTO Gaussian Type Orbital
- HF Hartree Fock
- HS High Spin
- IE Ionization Energy
- LCAO Linear Combination of Atomic Orbitals
- LDA Local Density Approximation
- LS Low Spin
- LSDA Local Spin Density Approximation
- MM Molecular Mechanics
- N4PY N,N-bis(2-pyridylmethyl)-bis(2pyridyl)methylamine)
- P450 Cytochrome P450
- PCM Polarizable Continuum Model
- PES Potential Energy Surface
- QM Quantum Mechanics
- QM/MM Quantum Mechanics/Molecular Mechanics
- SCF Self Consistent Field
- STO Slater Type Orbital
- TPFPP 5,10,15,20-tetrakis(pentafluorophenyl)-porphyrin
- TS Transition State
- VB Valence Bond
- ZPC Zero Point Correction
- ZPE Zero Point Energy

**List of publications:**

- Cantu-Reinhard, F. G. Sainna, M. Upadhyay, P. Balan, G.A. Kumar, D. Fornarini, S. Crestoni, M.E., DeVisser, S. A Systematic Account on Aromatic Hydroxylation by a Cytochrome P450 Model Compound I: A Low-Pressure Mass Spectrometry and Computational Study. *Chem. Eur. J.* **2016**, 22 (51), 18608–18619.
- Cantu-Reinhard, F.G. Faponle, A.S. DeVisser, S. Substrate Sulfoxidation by an Iron(IV)-Oxo Complex: Benchmarking Computationally Calculated Barrier Heights to Experiment. *J. Phys. Chem. A.* **2016,** 120 (49), 9805 – 9814.
- Cantu-Reinhard, F.G. DeVisser, S. Oxygen atom transfer using an iron(IV)-oxo embedded in a tetracyclic N-heterocyclic carbene system: How does the reactivity compare to Cytochrome P450 Compound I? *Chem. Eur. J.* **2017**, *23, 12, 2935 – 2944.*
- Cantu-Reinhard, F.G. DeVisser, S. Biodegradation of Cosmetics Products: A Computational Study of Cytochrome P450 Metabolism of Phthalates. *Inorganics*. **2017**, 5(4), 77.
- Cantu-Reinhard, F.G. Fornarini, S. Crestoni, M.E., DeVisser, S. Hydrogen Atom vs. Hydride Transfer in Cytochrome P450 Oxidations: A Combined Mass Spectrometry and Computational Study. *Eur. J. Inorg. Chem. **2018**, 1854 – 1865.*
- Brazzolotto, D. Cantu-Reinhard, F.G. Smith-Jones, J. Retegan, M. Amidani, L. Faponle, A. Ray, K. Philouze, C. de Visser, S.P. Gennari, M. Duboc, C. A High-Valent Non-Heme μ-Oxo Manganese(IV) Dimer Generated from a Thiolate-Bound Manganese(II) Complex and Dioxygen. *Angewandte Chemie*. **2017**. 56 (28), 8211-8215
- Cantu-Reinhard, F.G. Barman, P. Mukherjee, G. Kumar, J. Kumar, D. Kumar, D. Sastri, C.V. De Visser, S. Keto–Enol Tautomerization Triggers an Electrophilic Aldehyde Deformylation Reaction by a Nonheme Manganese(III)-Peroxo Complex. *J. Am. Chem. Soc.* **2017***,* 139 (50), 18328–18338.
- Wang, L. Cantu-Reinhard, F.G. Philhouze, C. Demeshko, S. De Visser, S.Meyer, Franc. Gennari, M. Duboc, Carole. Solvent- and halide- induced (inter)conversion between iron(II)-disulfide and iron(III) thiolate complexes. *Chem. Eur. J.* **2018***. https://doi.org/10.1002/chem.201801377*
- Fielding, A.J. Lukinovic, V. Evans, P. Alizadeh-Shekalgourabi, S. Bisby, R. Drew, M.G.B., Male, V. Del Casino, A. Dunn, J. Randle, L. Dempster, N. Nahar, L. Sarker, S. Cantu-Reinhard, F.G. de Visser, S.P. Dascombe, M.J. Ismail, F.M.D. Modulation of Antimalarial Activity at a Putative Bisquinoline Receptor in Vivo Using Fluorinated Bisquinolines. *Chem. Eur. Journal*. **2017**, 28, 6811-6828.

**Acknowledgements**

First of all, I want to thank my wife Monica for her support during these long years. She has given me moral support all the way, while being far away from her family, friends and country.

The current accomplishments are also only possible due to the invaluable and continuous support and guidance of Dr. Sam de Visser, my PhD supervisor. I'm thankful also for the countless inspiring scientific and not-scientific conversations I've had during these years under his supervision.

Also, on this crucial moment for my education, I would like to thank my uncle Manuel, who has given me the most valuable support to finish all previous studies and achievements since I started secondary school.

I would like to thank Dr. Faponle and my other collaborators on the group for enriching comments and support during the development of this PhD.

Special thanks are given to CONACYT (National Counsel for Science and Technology, Mexico) for their sponsorship that is funding this PhD program.

The assistance given by IT services and the use of the Computational Shared Facility (CFS) at the University of Manchester is also acknowledged, and I thank specially Pen Richardson who has solved most of our CSF-related problems.

# Chapter One

# INTRODUCTION

## 1.1 General Overview of P450 enzymes and their role in metabolism

Cytochrome P450 are key drug metabolising, heme-containing enzymes found in the human body that are also found in many other living systems and conform a superfamily of enzymes. These species are commonly found in bacteria, mammals, fungi and plants (Xu, et. al., 2015) and there are now thousands of P450 sequences annotated across hundreds of species (Lauschke, et. al., 2015) where these numbers are still expected to escalate in the following years (Ortiz de Montellano, 2015: Xu et. al., 2015). Perhaps one of the most surprising findings in this matter is that P450 encoding genes are also found in viral species, as found in *Acanthamoeba polyphaga,* opening new areas of discussion adound aspects of P450 related evolution (Lamb et al. 2009). Not only are P450 enzymes present in many different living systems, but for some of these species, they take up a very important fraction of their genetic material. It has been shown that for some species, the genes encoding for P450s take up more than 1% of their total genetic material; still other species have no P450 enzymes at all (Kelly et.al. 2013).

The main role of P450 enzymes in the human body has been regarded as that of detoxifying, with a special protecting role from harmful xenobiotic compounds. Early presence of the enzyme family has been hypothetically traced back to periods of the primitive life forms that were threatened by the changing atmosphere, where the molecular oxygen concentration gradually increased, which was very lethal to many such primitive life forms (Wickramasinghe et.al. 1975). Further support of the earliest presence of P450 genes is found in the fact that all three phylogenetic roots, archaea, bacteria and eukaryotes, make extensive use of these metabolic changers. After its first appearance the enzyme's genes would have been subjected to an always changing environment of chemicals, and thus could diverge, multiply and adapt into a large collection of functions and capacities to sustain the metabolic demands of current life forms, with such diversity that no single residue is conserved across all families today. Many computational and experimental tools have recently provided insight into the evolutionary mechanisms of these enzymes. (Setzu et. al. 2013). Function is often more conserved than structure in proteins overall, and P450 enzymes are no exception. (Illergard et.al. 2009).

Although there is a low sequence identity among most P450's, with similarities as low or less than 20%, it has been revealed by crystal structure studies that the general topography and folding structure is highly conserved across the P450 enzyme superfamily (Feyereisen et. al. 2000). Because of this structural similarity across the family, key elements in the protein can be readily identified upon studying a P450 structure. The following P450 isoenzyme structure (Displayed in Fig. 1.1) is obtained from the Protein Data Bank as (www.rcsb.org), and represents the human CYP2D6 isoenzyme, with Protein Data Bank (pdb) code 4WNU, as visualized with UCSF Chimera (2004). The tertiary structure has been labelled with key segments as seen also in other eukaryotic P450 enzymes (see Johnson et. al. 2013). Segment L is highly conserved across species as it is the helix that binds the heme (depicted in purple) through a thiolate ligand of a cysteinate residue. The thiolate group from a conserved cysteine binds to the heme through an axial coordination site of the iron on the opposite site of the oxygen binding site (Johnson et. al., 2013). On the contrary, the structural elements that affect the substrate specificity are to be expected to vary the most across the superfamily, such a case is the segment B' that may have large variations in its position among various P450's, as this segment is directly involved with substrate binding (Ortiz de Montellano, 2015).

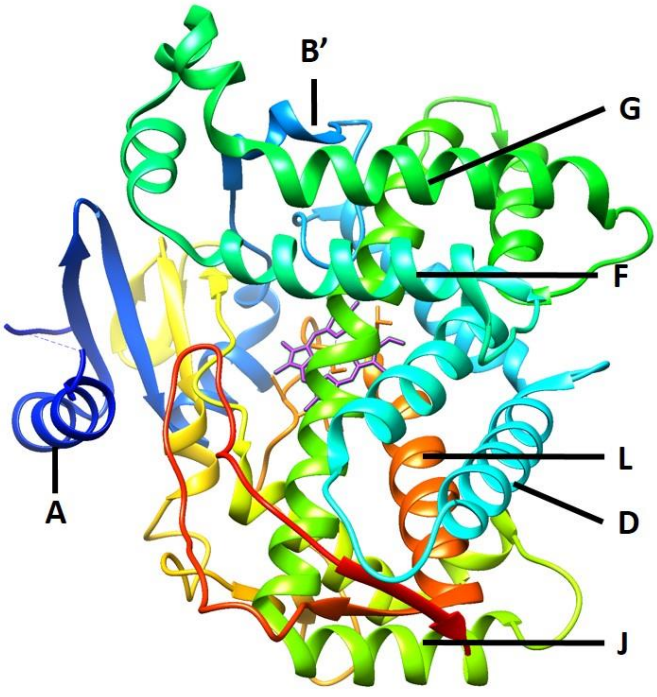


**Figure 1.1**: P450 with Some common Motifs (CYP2D6 PDB 4WNU).

The designation “P450” has its origin in the characteristic spectroscopic peak found at 450nm when these enzymes form a reduced CO complex, as reported by Klingenberg, M. (1958). During the immediate years after discovery, the P450 enzyme family was found to account for a large variety of metabolic oxidation reactions for numerous xenobiotic compounds, and after many decades of research, it has become progressively clear that the P450’s are responsible for a much larger amount of biological functions, such as those related to steroid hormones, fatty acid activation, vitamin biosynthesis, flavonoid oxidations and the metabolism of xenobiotics such as drugs (Mansuy, D. 2007).

The heme is the catalytic heart of the P450 enzymes, where a highly reactive iron(IV)-oxo intermediate termed CpdI (i.e. Compound I) is formed with capacity to oxidize inert carbon-hydrogen bonds of substrates (Rittle, et. al. 2010). It is now a general consensus that CpdI is the main responsible species for the reactions catalysed by the P450s. In hydroxylation reactions, for example, CpdI abstracts a hydrogen atom from the carbon and forms an “Fe(IV)OH” moiety (i.e. Compound II) and a radical substrate which in a *rebound* mechanism converts into the hydroxyl-bound product (McIntosh, et.al. 2014). CpdI is generally considered as the sole active oxidant, but some discussion still exists on whether “Compound 0” (iron(III)-hydroperoxo complex) may also be an active oxidant too (Porro et.al., 2009).

It has been recently suggested that for some non heme iron enzymes, the iron-III hydroperoxo complex (namely Cpd0) is a potential oxidizer of the substrate. In this particular case, a homolytic cleavage of a hydroxyl radical that binds the substrate into hydroxylation where the same pathway is not feasible for the heme CpdI because of a necessary last step involving a strongly endergonic electron transfer to the negatively charged iron heme complex (Faponle, et.al. 2015). In addition, the different reactive patterns observed for the P450 chemistry under varying conditions has led to believe that different oxidative species are involved in some reactions, however it has also been suggested that CpdI is a versatile oxidant that by itself also poses different reactive patterns under different experimental conditions (Nam, W. 2007).

Figure 1.2 depicts the catalytic cycle of P450 enzymes, with key elements identified. The cycle starts from the water bound resting state. The cycle then follows the introduction of the substrate (RH), which changes the EA of the complex and allows an electron transfer from the redox partner to the iron centre ($Fe^{III}$ becomes $Fe^{II}$). Then another stable intermediate is formed with the addition of molecular oxygen that binds to the iron, forming a ferric superoxide. The complex is then reduced to a ferric peroxo complex that will follow a protonation into a ferric hydro-peroxo complex (Compound 0), and a further protonation leads to formation of water via O-O bond cleavage, leading to a short lived radical cation $Fe^{IV}O$ system: CpdI. Commonly, this proceeds to the hydrogen abstraction from the substrate while forming an $Fe^{IV}OH$ system "Compound II", and a subsequent "rebound" step that releases the hydroxylated metabolite (Zhang et.al. 2015; Denisov et.al. 2005; Meunier et.al. 2004; Shaik et.al. 2005).

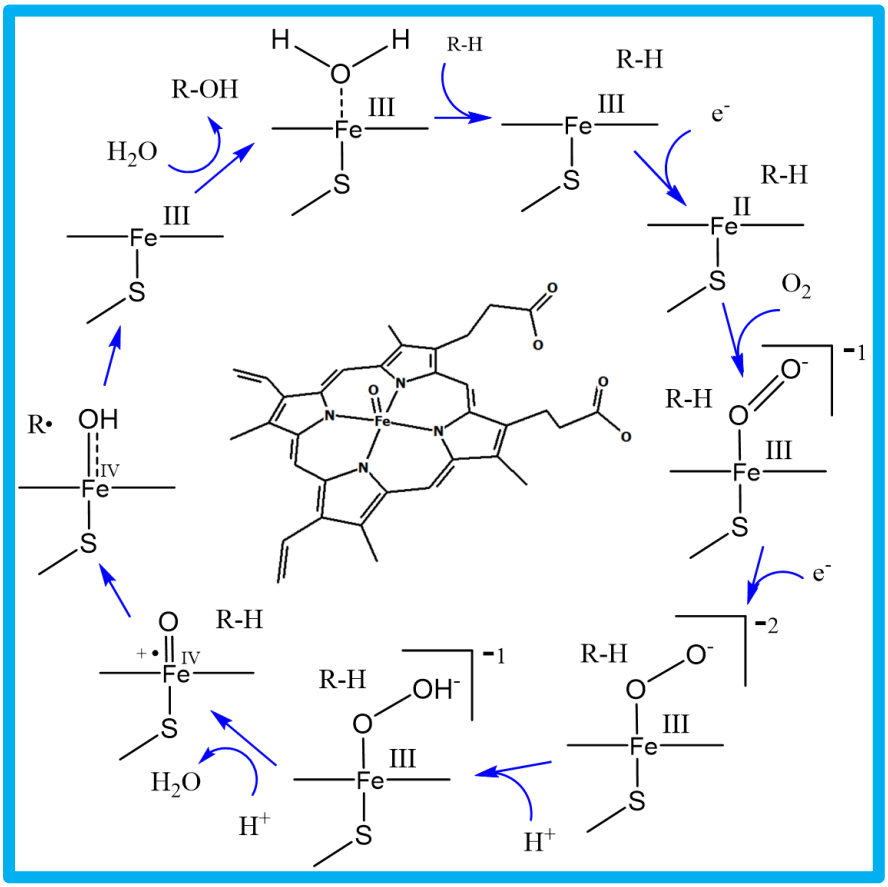


**Figure 1.2:** Catalytic cycle of P450 Enzymes. The porphyrin species is represented by straight lines and "R-H" represents the substrate. Adapted from Zhang et.al. 2015.

P450 enzymes have been shown to be involved in some fundamental internal metabolic reactions like steroids biosynthesis (Kelly et.al. 2013), however, these enzymes have their main role as a detoxifying enzymes and thus have a special interest from the pharmacological perspective. Phase I of metabolic transformations are an initial activation step, usually by incorporation of a polar group to the molecule (e.g. -OH, $-NH_2$, -SH), and Phase II increases the solubility of the compound by transferring a highly soluble group to the "activated" compound, such as a glucuronic acid. Sometimes Phase I or II reactions occur alone, or in reverse mode. P450 enzymes are regarded as key Phase I metabolism enzymes (Katzung et al 2012). Enzymes of the P450 family are the main enzymes responsible of phase I metabolism of pharmaceuticals and other xenobiotic lipophilic substances in humans (Schwab, et. al., 2013) and the genes encoding for human P450s are distributed among autosomal chromosomes to account for 57 known functional genes (Lauschke et. al., 2015). The P450 superfamily accounts for thousands of metabolic substrates. The following charts give an approximation of the relative roles of various P450 enzymes in the human body (data from: Evans et.al. 1999; Ingelman-Sundberg et.al. 2005; Bertz et.al. 1997), considering that a main metabolizing enzyme is responsible for over 50% of metabolite activation, of the reflected data:

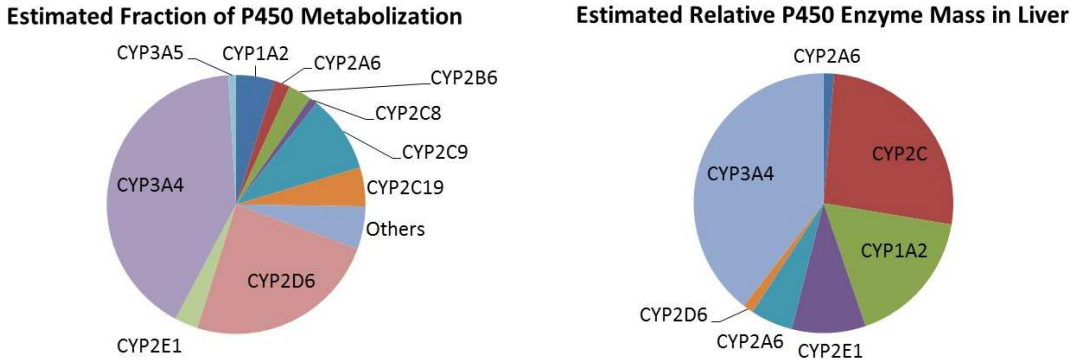


**Figure 1.3**: P450's in Phase I metabolism and their relative contributions. Adapted from (Evans et.al. 1999; Bertz et.al. 1997; Katzung et. al. 2012).

P450 enzymes in the human body have its peak density in the liver where they process the bulk of xenobiotic biotransformations. Isoforms CYP3A4 and CYP2C9 alone account already for half of the liver's Cytochrome P450 enzyme content, whilst CYP3A4 is responsible for almost half of the Phase I transformations (Katzung et al 2012). However, one can find P450s not only in the liver, but virtually in all kinds of tissues. For example, in the skin, the P450s have been suggested as potential therapeutic targets for their role in metabolism of several compounds, including drugs and vitamins, and in particular CYP2S1 expression is shown to be implicated in psoriasis treatment response by affecting therapeutic drug effectiveness, (Ahmad et.al. 2004; Smith et.al. 2003). In the brain, in many of its sub-regions, P450s play an active role in drug transformation and diseases, and have a strong influence on the interactions of psychoactive substances, where for example higher CYP2C9 expression has been correlated with alcohol abuse (Gosh et. al. 2016; Depaz et. al. 2015). Even the heart tissue has been shown to express P450s with effects on fatty acid metabolism and detoxification of environmental agents (Chaudhary et.al. 2009).

Many P450 isoenzymes are unspecific to a particular substrate and hence have strong substrate versatility. This is consistent with their role in detoxification of either xenobiotics or internal by-products. To no surprise they must be able to activate substrates not perceived before in the organism, for example new trial drugs. One effect of this lack of specificity is also that one chemical species can be a substrate to more than one P450 enzyme, or even fit in different orientations in some of them, leading to various pathways of metabolization. If, for instance, we consider the P450 activation of DEHP di(2-ethylhexyl)-phtalate, a phthalate contained in many cosmetic products (Choi et. al. 2012), including some pharmaceutical formulations (Kim et.al. 2005) or even medical devices (Sastri, V. 2014), it is metabolized by a variety of P450 isoenzymes, including CYP3A4, CYP3A5, CYP3A7 and 2C19 among others. However, the product distributions vary strongly with the isoenzyme, and effectively range from various hydroxylation and dealkylation reactions (Choi et. al. 2012).

Despite all of this, P450s may also be very sensitive to small changes in conformation or the structure of the substrate. The well-known proton pump inhibitor, Omeprazole, is one example, where a small switch in the positions of the sulfoxide's oxygen atoms leads to changes in pharmacokinetics strong enough to make a clinical difference. As a consequence, its research led to the discovery of a new patented drug, namely S-Omeprazole (Abelo et. al. 2000).

Extensive research has been done to understand the basic chemistry behind P450 reactions from the computational perspective (Shaik et.al. 2005). Mono-oxidation reactions are frequent chemical transformations done by these kind of phase I metabolic enzymes (Urlacher et.al. 2012), but P450 enzymes have been recognized to catalyse many reaction types, including hydroxylations, epoxidations, allylic re-arrangements, dimer formations, ring couplings, ring formations (Tang et.al. 2017), ring contractions, aromatic de-halogenations (Guengerich, et. al., 2007), fatty acid decarboxylations (Rude et. al., 2011, Faponle et.al. 2016), N-dealkylations, sulfoxidations (Sharma et.al., 2003: Voltz, et.al., 2002), O-dealkylations (Schyman et.al. 2010) among others (see examples in Fig. 1.4). With the means of electronic structure methods one can elucidate the chemical mechanisms of reaction of plausible P450 enzyme mediated biotransformations, and much effort has been placed in the rationalization of the factors leading to the activation barriers, which in turn correlate with rate constants and give thermodynamic insights (Shaik et.al. 2005; Cramer, C. 2004; Cantu-Reinhard et.al.[1] 2016).

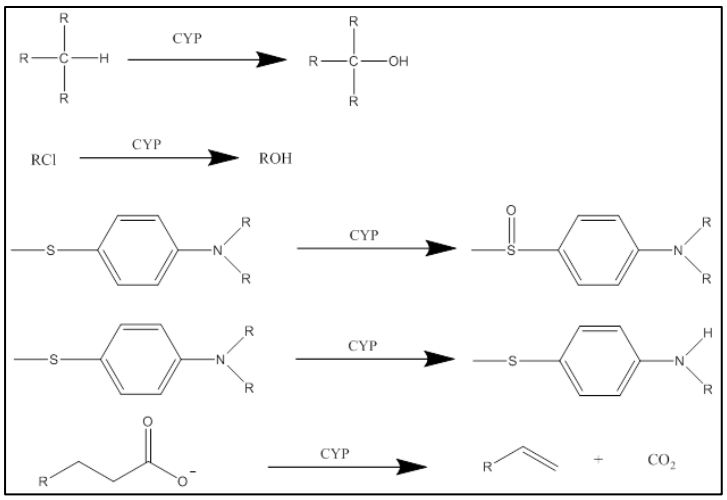


**Figure 1.4:** Some reactions known to be carried out by some P450 isoenzymes.

CpdI is a special reagent that catalyses numerous reactions, and this spectra of possibilities are in part a result to its particular electronic structure: an electron deficient heme radical cation iron(IV)-oxo complex. It also possesses two closely separated spin states: quartet and doublet. These spin states, regarded as high spin and low spin respectively, encompass a two state reactivity pattern of competing reaction mechanisms in heme-containing enzymes (Shaik et.al. 2010[1]; Shaik et.al. 2002).

The electronic configuration of CpdI will expectedly change during its transition across the reaction coordinate as it reacts with any of its versatile plausible reactants, and a great variety of these implicated structures (e.g. transition states, intermediates and products) have been characterized with computational methods but stay elusive experimentally. Common reaction mechanisms have been identified, where for example, aliphatic hydroxylation has a very distinct mechanism from aromatic hydroxylation, or sulfoxidation in heme or non-heme iron(IV)-oxo systems. For instance, aliphatic hydroxylation starts with a hydrogen atom transfer, whilst aromatic hydroxylation starts with a nucleophilic attack of oxygen on carbon (see de Visser, et.al. 2007; Kumar et.al. 2012) whilst sulfoxidation is a concerted reaction.

Aliphatic hydroxylation stands as one of the most common reactions driven by CpdI in P450 enzymes, where the consensus mechanism takes place with an initial step of hydrogen atom transfer from the substrate to the iron(IV)-oxo, forming normally a radical intermediate, proceeded by a "rebound" transfer of the hydroxyl group to form an alcoholic species (Groves, 1985; Ogliaro et.al. 2000; Shaik et.al. 2004). Figure 1.5 depicts a general representation of the substrate hydroxylation process, and is also a representative diagram of mechanistic landscapes in general.

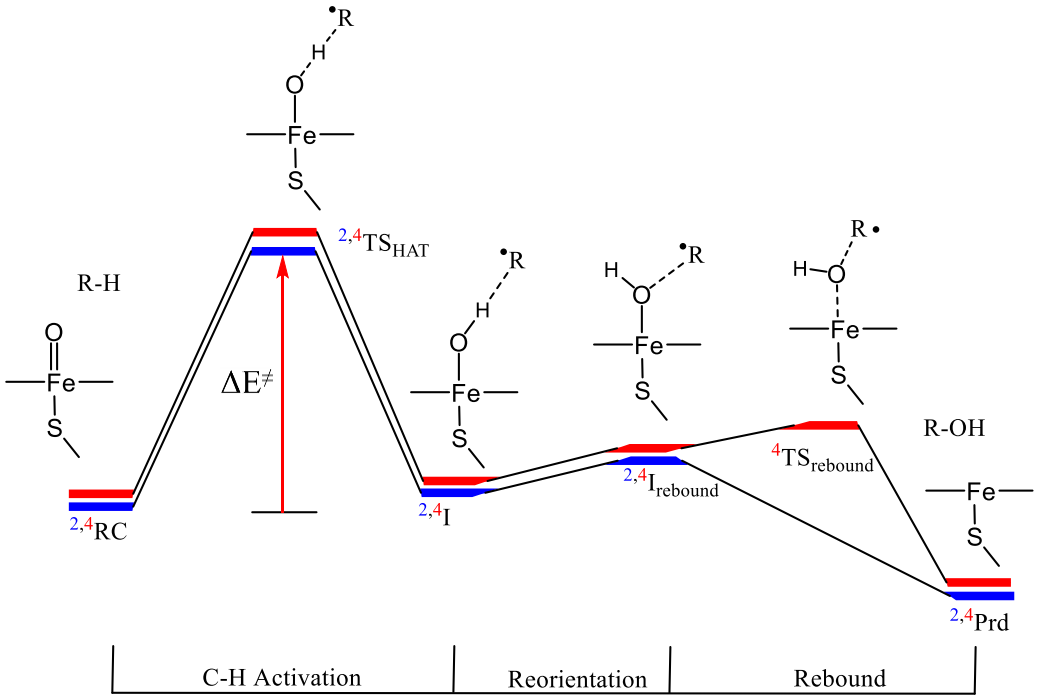


**Figure 1.5:** General scheme of CpdI mediated Aliphatic Hydroxylation. The process starts on the Reactant Complex **$^{2,4}$RC**, followed by a Hydrogen Atom Abstraction Transition State **$^{2,4}$TS$_{HAT}$** that leads to an intermediate **$^{2,4}$I**. Then a OH reorientation leads to **$^{2,4}$I$_{Rebound}$** which can then either go through the rebound transition state **$^{4}$TS$_{rebound}$** or directly proceed to the Hydroxylated product **$^{2,4}$Prd**. Adapted from Shaik et.al. 2005.

A more sophisticated mechanism is that of O-dealkylation, like the demethylation of 5-methoxytryptamine by CYP2D6. Starting similarly to hydroxylation, a hydrogen atom is abstracted from the aliphatic group of the substrate, forming a radical intermediate that is subsequently transformed into an alcohol again also by a hydroxyl rebound mechanism. The resulting hydroxylated ether will internally transfer the hydrogen from the hydroxyl to the ether oxygen, leading to a bond cleavage. However, this last transition process requires a geometrical strain and hence can result in a significantly higher barrier as compared to the initial activation. Nevertheless, in aqueous media the proton can shuttle without any substrate stress through a water chain over a low energy path, dissociating the aliphatic group without any further need of P450 intervention as seen in figure 1.6. Further addition of water molecules in the right position brings the barrier further down (Schyman et.al. 2010).

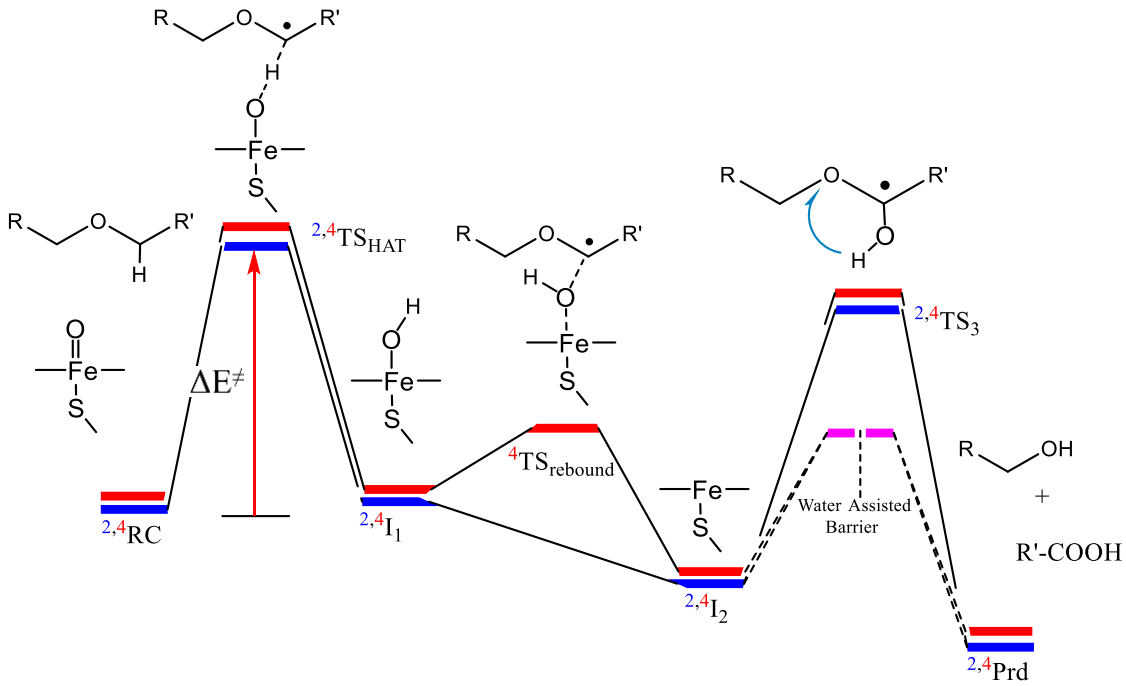


**Figure 1.6:** General scheme of CpdI mediated O-dealkylation. The process starts in a similar fashion to CpdI mediated hydroxylation, on reactant complex $^{2,4}$**RC** which undergoes a C-H activation step through $^{2,4}$**TS$_{HAT}$**, and yielding intermediate $^{2,4}$**I$_1$**. However, after a rebound step, intermediate $^{2,4}$**I$_2$** is formed, which then proceeds via an internal hydrogen atom transfer $^{2,4}$**TS$_3$** towards the alcohol and carboxylic acid products, $^{2,4}$**Prd**. Adapted from Schyman et.al. 2010.

This versatile catalytic spectrum conveys special attention on drug metabolism, drug discovery, pharmacokinetics, bio-activation and toxicology (Lundemo et. al., 2015; Renault et.al. 2014; Lauschke, et. al., 2015) and thus has important implications for the Health Sciences and Industry (e.g. Pharmaceutical, Cosmetic, Polymer). Toxicology is a specially important factor that must be considered when studying P450 chemistry and its relation to drug metabolism and drug design, as different transformations may lead to very toxic secondary metabolites (Guengerich, 2001), or interestingly may even lead to the therapeutically active product via a Pro-Drug mechanism (e.g. Roy and Waxman, 2006). Other important factors that carry special attention include enzyme inhibition and promotion, as well as drug-drug interactions that arise from these complex metabolic relationships (Guengerich, 2001).

The main drivers of research into the metabolism of P450s are associated to drug development, which is a long process starting with the identification of potential drug candidates for a specific therapeutic effect. Subsequently the best candidates of these candidates are filtered out for further drug development studies, as well as pre-clinical and clinical research, prior to approval and commercialization (FDA, 2015). During

drug development, it is preferred, for cost reasons, to identify potential adverse effects on a new drug at an early stage, where the drug candidates selected give a low chance to produce reactive metabolites. Experimental tests *in vitro* are often performed to detect liabilities in the drug candidates to guide the efforts of drug design (Brink et.al. 2017). Specifically, computational tools can be of great assistance in the drug discovery and developmental stages, effectively reducing time and optimizing costs (Muster et.al. 2008).

*In silico* tools used for the studies of drug metabolism have a wide application area, with possibly the greatest interest in virtual ligand library screening for small drug binding affinities in the interest of drug discovery. Complementary to chemical high throughput screening methods, such tools can lead to a dramatic increase in hit-ratio in high throughput screening methods, therefore greatly development reducing costs (Cavasotto, 2016). Many computational tools in the area of drug discovery have been designed upon the concept of "drug-likeness", which relies on filtering potential drug structures based on various intrinsic properties or descriptors. These can be as simple as a threshold molecular weight assumed to be required for proper oral absorption, to more complex analyses based on machine learning techniques of big data sets. With focus on the so called ADMET profile (absorption, distribution, metabolism, excretion and toxicity), the idea is to get a better performance on later drug development stages by filtering out candidates with unlikely good outcomes (Tian et.al. 2015).

Other software of growing interest are based on the large scale approach of QSAR methods (i.e. Quantitative Structure Activity Relationship), which are powerful tools developed to exploit the fact that compounds with structural similarities may have similar properties, and may in fact predict activities of analogue species, employing in some cases 3D molecular models (3D-QSAR) that take into account electrostatics and some steric potentials (Thareka, 2015; Gupta, 1987). Several computational approaches have been developed for drug discovery to specifically explore the substrate-enzyme relationship and the study of metabolism of *drug-like* substances, such as the prediction of toxic and or undesirable metabolites. (De Vivo and Lodola 2012). Software such as Metasite, StarDrop, SMARTCyp, and RS-WebPreditor, are commonly used tools for the rapid prediction of sites of metabolism on a substrate (Ford, et. al. 2015).

Figure 1.7 and Table 1.1 depict a set of results of a Site of Metabolism (SOM) computation performed with the SMARTCyp web interface on P450-2D6 for the drug-substrate Omeprazole. The main expected metabolites (hydroxylation and sulphoxidation) at atoms 20 and 12, are ranked 3th and 16th in the scoring results. Certainly this approach is fast and user friendly, but a significant error can be expected.

**Table 1.1:** SMARTCyp predicted sites of metabolism for Omeprazole:

| Atom | 2D6ranking | 2D6score |
|---|---|---|
| **C.1** | 1 | 59.54 |
| **C.22** | 2 | 59.71 |
| **C.20** | 3 | 64.11 |
| **...** | ... | ... |
| **S.12** | 16 | 1025.07 |

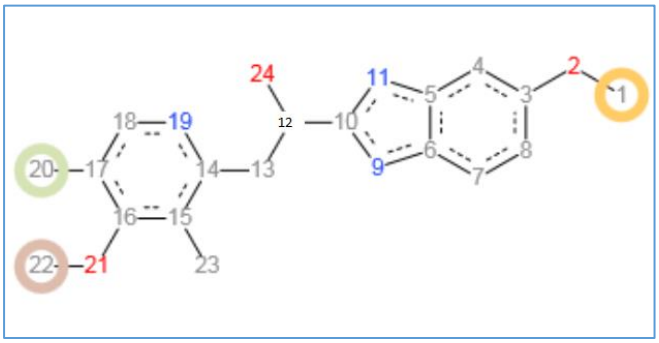


**Figure 1.7:** Top Metabolites predicted by SmartCyp are encircled.

Other approaches such as docking may be used to evaluate the orientation of enzyme bound substrates, while some methods such as MLite combine the latter with Quantum Chemistry derived parameters. These and various other procedures add up to methodologies that may or may not take the protein topology into consideration (Kirchmair et.al. 2012). Nevertheless, the accuracy of these software is not infallible and a significant error on predicting the site of metabolism may be expected yet (Ford et.al. 2015).

Indeed these mentioned implements are mostly scoring or filtering tools, which help in the finding of better drug candidates but may offer little or no insight into the electronic structure of the P450-drug interaction. Hence for a rational understanding of the chemistry of Cytochrome P450 enzymes and their substrate's drug metabolism, electronic structure based methods may sometimes be more beneficial. A computational mechanistic investigation of enzyme chemistry through QM and QM/MM methods based on Transition State Theory (TST) may provide essential and insightful information in terms of drug metabolism studies and even drug discovery (De Vivo and Lodola, 2012; De Vivo, et.al. 2016). During Drug design and drug candidate filtering, a mechanistic understanding is considered of great importance by some authors even if the approach is experimental, especially when one is trying to avoid certain metabolites (Brink et.al. 2017).

One main benefit of TST based on electronic structure methods is thus the revelation of reaction mechanisms otherwise hard or impossible to elucidate by experimental methods, as well as the rationalization of why such a mechanisms may be happening to avoid one metabolite or obtain another (Li et.al. 2015). On the drug discovery side, TST also poses the possibility of inhibition-drugs to be rationally designed as TS analogues that lead to a thermodynamically stable complex with the target enzyme (Schramm, 2005). Another feature of electronic structure methods such as DFT or QM/MM, is that they can provide a better understanding of substrate-target binding affinities and interactions and may be able to explain chiral effects and region-selectivity better than other methods that are not whole - enzyme inclusive (De Vivo and Lodola, 2012). For these reasons, herein most attention will be given to methods relying on Quantum Mechanics (i.e. DFT methods) or QM/MM (Quantum Mechanics/Molecular Mechanics) methodologies for the study of enzymatic reaction mechanisms involved in the metabolism by P450s.

Small DFT models have shown to achieve good agreement with experiments in the computations of biomimetic complexes of CpdI or other iron(IV)-oxo systems, and are often appropriate and not too small for representative systems of enzyme reactions. A small model of P450 CpdI employing a truncated porphyrin, absent propionates and ethyl side chains, where the cysteine is replaced by a thiolate ($-SH^-$) moiety or an ethyl-sulphide group can already be sufficiently accurate with standard modern DFT methods to represent the enzyme chemistry (e.g. de Visser et.al. 2002; Olsen et.al.

2006; Chuanprasit et.al. 2015; Vincent et.al. 2005) although a complete porphyrin may also be employed with similar results (see Jana et.al. 2018). Later herein a project will specifically focus on P450 mediated metabolic predictions of a phthalate additive found in cosmetics and pharmaceutical formulations based on small DFT models (Cantu-Reinhard et.al. 2017) (See Figure 1.8). Thus, if environmental or enzymatic factors are relatively negligible, the small DFT method may be enough and complete for certain questions, biomimetic models or even some regioselective enquiries. However, in some other cases a larger or more comprehensive model may give the required answers.

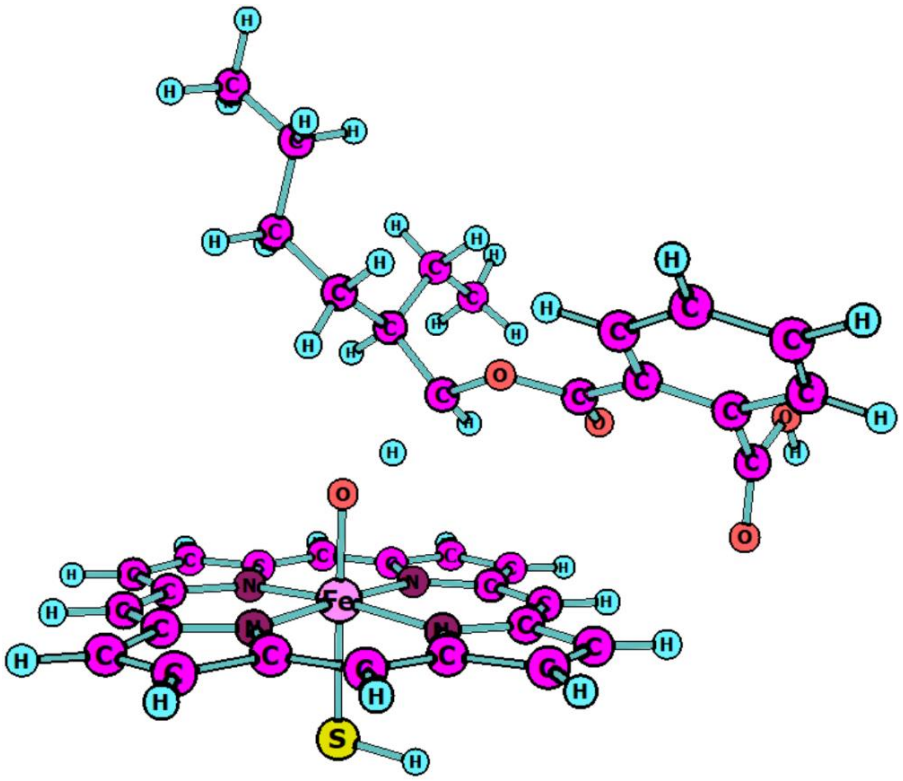

**Figure 1.8:** UB3LYP/6-31G* optimized transition state of a small DFT model of CpdI for the hydrogen atom abstraction from 2-ethylhexyl-phthalate (See Cantu-Reinhard et.al. 2017).

Considerably larger enzymatic DFT models are sometimes employed as well as QM/MM models for a more comprehensive mechanistic metabolic modelling when needed. The larger DFT model, termed as "Cluster model", typically includes several amino acid residues of an enzyme's active site and sometimes several layers of truncated functional groups, which in some cases may have only a steric contribution or may provide further chemical functionality, as well as modify local pKa values or provide hydrogen bonding interactions. The idea is that the system is large enough to

have a realistic representation of the whole-enzyme environment rather than a small DFT model alone. Implicit solvents and dispersion effects are normally included too, and as the number of degrees of freedom increases in terms of conformational space, many starting conformations need to be tested, where the 'lowest-energy transition states' and respective activation energies correlate with the rate of reaction. This is especially true for enantioselective investigations, where the size of the system may be larger to properly describe the problem (Himo, 2017; Siegbahn et.al. 2011). Recent computational modelling from our group on the stereo selective activation of R- and S- 2-methyl butyric acid, was able to reproduce experimental findings through a set of conformations of a relatively small cluster model (a total of 163 atoms) of a P450 isoenzyme (See Fig. 1.9, Pickl et.al. manuscript in preparation).

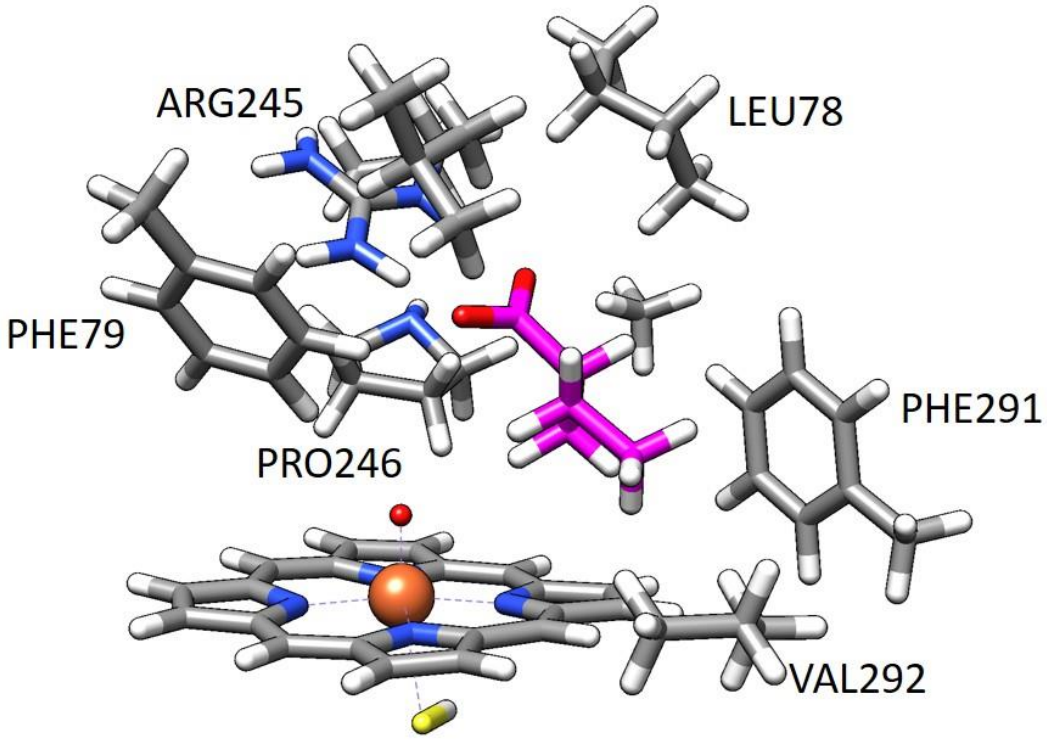


**Figure 1.9:** Cluster model with substrate R-2-methyl butyrate and some of the protein aminoacids included, structure from Pickl et.al. (Manuscript in preparation)

An alternative to small DFT models or to cluster DFT-only models are QM/MM methods which are models that try to encompass most of the enzyme environment in contrast to classic (small) DFT models alone. QM/MM models also consider a larger region of the enzyme than the cluster model although normally with a smaller QM region. These models often include the complete enzyme, however, most of the atoms are part of the protein far away from the active site and hence are located in the "MM" (Molecular Mechanics) region. These MM atoms are treated at a classical level of theory, through the so-called force field potentials that include non-bonding and electrostatic interactions by a force field. As the QM/MM model is normally considered with solvent water molecules explicitly in a cage (box or sphere) surrounded by a solvent potential, it includes the environment as a whole (Quesne et.al. 2015). The QM/MM model has been used extensively in metabolic models with success (Lonsdale et.al. 2014; Ji et.al. 2015). Figure 1.10 presents the substrate bound enzyme of NMO (nogalamycin monooxygenase) with a simplified surrogate of nogalamycin (i.e. dithranol), as part of a QM/MM project investigating the mechanisms behind this natural antibiotic biosynthesis, as later discussed in detail (Cantu-Reinhard, F.G., Dubois, J., de Visser, S.P. manuscript submitted for publication).

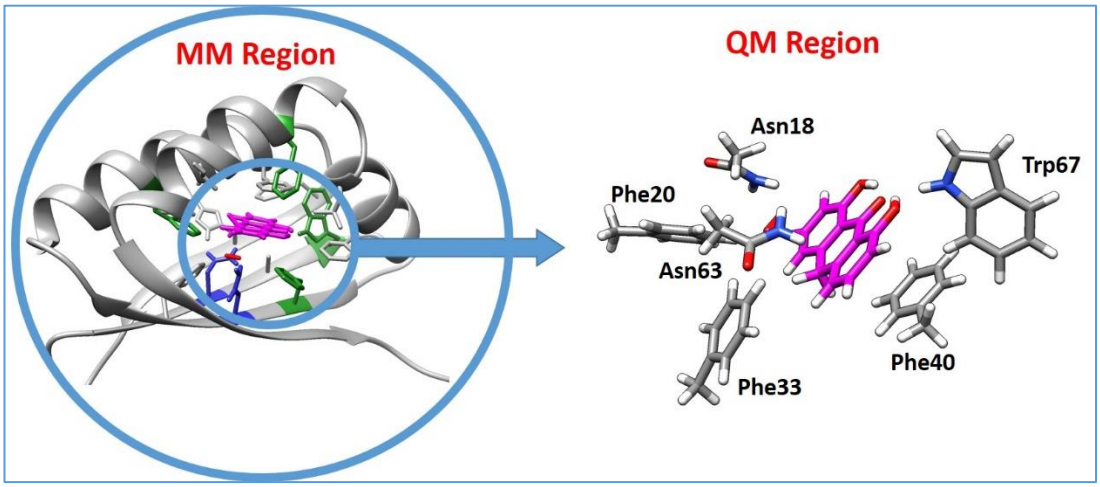


**Figure 1.10:** QM/MM optimized model and its corresponding QM Region. Based on original PDB structure 3KNG, with substrate (Dithranol) in purple. (Cantu-Reinhard, F.G., Dubois, J., de Visser, S.P. manuscript submitted for publication).

Hence, when a small DFT model is not considered sufficient for mechanistic models of metabolism or other electronic structure analysis, a bigger but computationally more demanding DFT cluster or a QM/MM approach may be better suited. Several examples exist of metabolic modelling with the latter methodology, especially those that explore P450 chemistry. For instance, one can enquire what factors determine the product selectivity and/or product distribution of primary metabolites of a P450 isoenzyme on a drug. For example, dextromethorphan (Olah et.al. 2010) was investigated in P450 2D6 and found to be responsible for the oxidation of the substrate. Furthermore, it is shown that a QM computation did not yield the same mechanistic predictions as the more holistic QM/MM methodology, leading to different substrate orientations and bond lengths in the transition state, explaining the lack of aromatic hydroxylation in favour of O-demethylation in metabolism. Likewise, Londsdale et.al. (2013) performed a study on regioselectivity of P450 2C9 activated drugs ibuprofen, diclofenac and warfarin. The main sites of metabolism were accurately predicted as the lowest barrier path for two out of three drug substrates, whilst the not-expected result has been attributed to inadequate binding affinities in the employed model, hence showing also some potential limitations of the QM/MM methodology. In another example of Ji et.al. (2015) a set of DFT and QM/MM models are employed to rationalize the differences on hydroxylation and desaturation pathways in a P450 Drug Metabolism study.

### 1.2 Biomimetic Models of P40 Enzymes

Diverse iron containing enzymes are responsible for a variety of biological chemical reactions through a set of heme and non-heme enzymes, with high valent iron(IV or V)-oxo groups as a common oxidant, directly implied in the metabolization of oxidizable drugs and other foreign compounds in the body. However such catalysts are often hard to study for many reasons including cost, potency and technical problems, among other difficulties. It may thus be convenient to employ biomimetic models to study the oxidative effects expected for drugs and drug candidates such as the main expected metabolites, as well as for the better understanding of the characteristics and mechanisms of reaction of these iron-oxo catalytic species. Hence, a lot of experimental work has been placed into creating smaller and simpler

biomimetic models of heme and non-heme iron-oxo enzymes to study the chemistry of the rather more complex enzymes (Rana et. al., 2015; Bernadou et.al. 2004). Many such systems are metalloporphyrins to mimic the functional properties of cytochrome P450 enzymes, such as meso-tetraphenyl porphyrin (TPP), meso-tetramesitylporphyrin (TMP), meso-tetrakis(pentafluorophenyl)porphyrin (TPFPP) among many others, with the first synthesis of such a species dating to 1979. It has been since shown that the electron-deficient porphyrin ligand system TPFPP, saturated in electron withdrawing fluorine atoms, is the stronger oxidant of organic species as compared to structurally comparable electron-rich ligands (Bernadou et.al. 2004; Nam, W. 2007).

Some years later (2003) the first non-heme $Fe^{IV}O$ species was also characterised experimentally, with some distinct models such as $[Fe^{IV}(O)(N4Py)]^{2+}$, $[Fe^{IV}(O)(R\text{-}TPEN)]^{2+}$ or $[Fe^{IV}(O)(BnTPEN)]^{2+}$ (See Figure 1.11) (McDonald et.al. 2013; Nam, W. 2007). For example, in a recent benchmarking study by Cho and co-workers (2012), several of these biomimetic systems were studied experimentally and computationally.

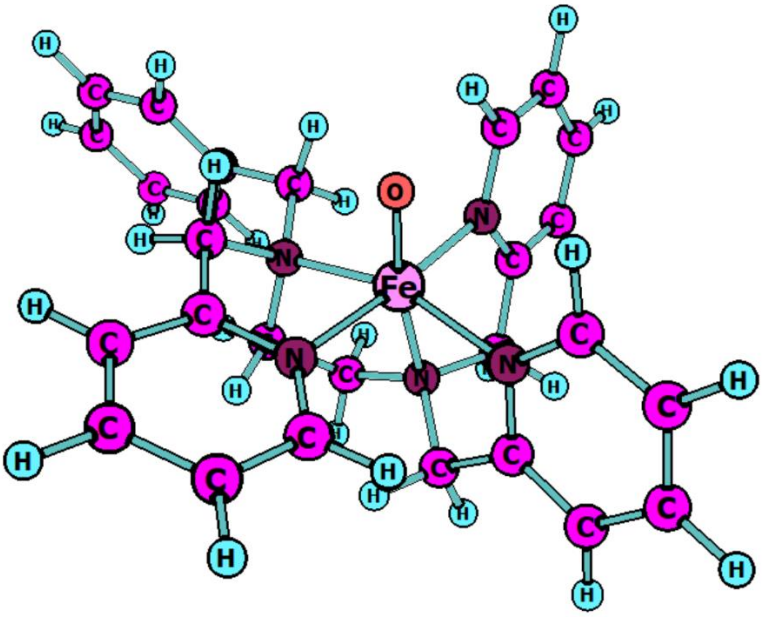


**Figure 1.11:** B3LYP/6-31G* optimized $[Fe^{IV}(O)(BnTPEN)]^{2+}$

The Fenton's reagent ($(H_2O)_5$-Fe(IV)=O) may be considered as the simplest biomimetic model with potential to resemble some of the P450 chemistry. Fenton's reagent is a century old oxidizing catalyst complex involving an iron (II) cation with peroxide ($H_2O_2$) in an aqueous solution (Fenton, H.J.H., 1894; Barbusinski, 2009), with potential to work well in combination with UV light (Photo-Fenton) or without a light source (Thermal-Fenton) at varying pH levels (with different reactivity at varying pH values) and is able to oxidize a large variety of organic compounds (Haag, et. al. 1992).

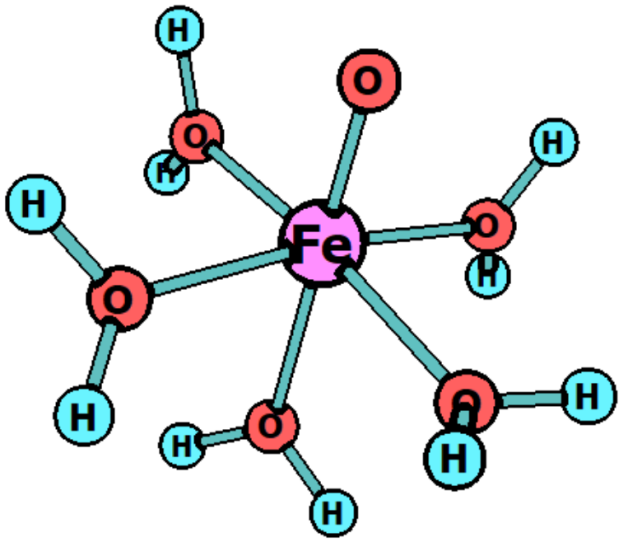


**Figure 1.12:** UB3LYP/6-31G* optimized structure of Fenton's Reagent.

This system is subject to extensive controversy regarding its mechanism of reaction with many directions proposed involving radical or non-radical pathways, where the iron may or may not be the direct oxidant of the organic substrate. Despite these disagreements, the Fenton's reagent is often regarded as working with a similar chemistry to CpdI of iron containing enzymes and thus it is expected to be a good study model for P450s enzymes (Lohmann et.al, 2008; Bach et. al., 2010). However, the lack of consensus over the active oxidant of the reagent suggests that it may not be as simple as it seems, possibly because it is a very un-restrained system where the solvent may have explicit roles and more interactions can occur than the ones expected in penta-ligand or tetra-ligand systems.

N4Py-$Fe^{IV}O$ (N4Py = N,N-bis(2-pyridylmethyl)-bis(2pyridyl)methylamine) is a model that may better (than Fenton's reagent) mimic the behaviour of iron(IV)-oxo enzymatic catalysis, where the iron is contained in a pentadentate ligand of nitrogen atoms, originally characterized as an active iron(III) complex in acetonitrile solution (Lubben, et.al., 1995; Roelfes et.al., 1997) more recent work has explored the iron(IV)-oxo chemistry of this intermediate (see Fig. 1.13) in aqueous solution, which may better represent non-heme enzyme chemistry (Sastri et.al. 2005).

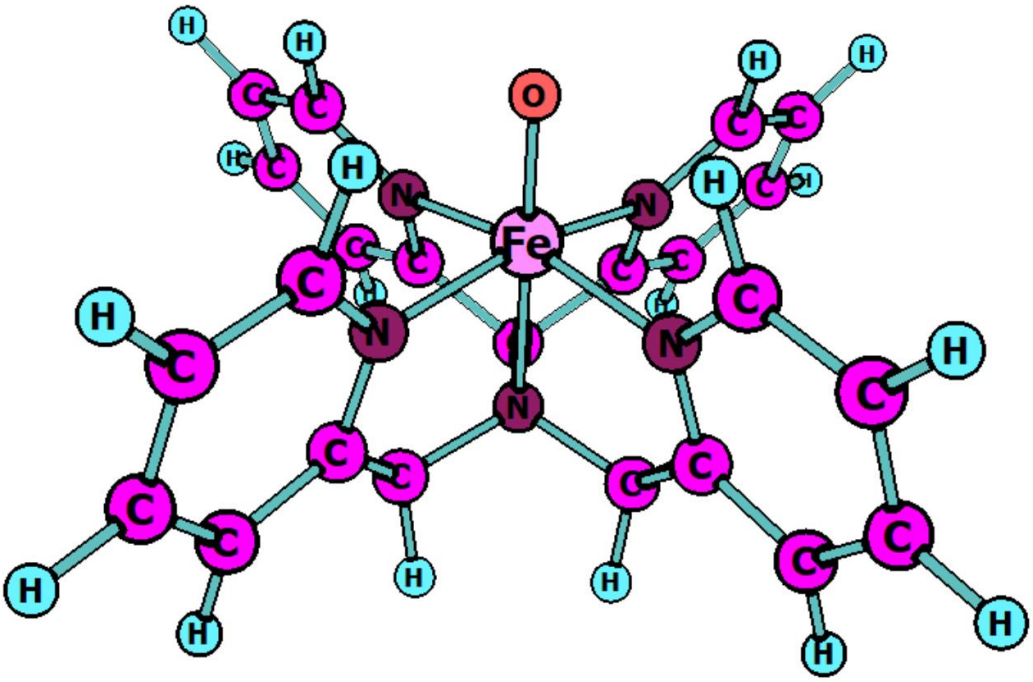


**Figure 1.13** B3LYP/6-31G* optimized structure of $[(N4PY)Fe(IV)=O]^{+2}$

It has been demonstrated that this system is capable of performing diverse oxidation reactions onto various substrates such as alkenes and alkanes. Reaction kinetics with temperature dependence and other thermochemical data have been experimentally obtained on the oxidation of thioanisole with various para-substituents (hydrogen, methylene, chlorine, etc.) giving a stimulating amount of data and making this case and an interesting target for a benchmarking study, as presented herein later (Sastri et.al. 2005, Cantu-Reinhard et.al.[1] 2016).

Also studied by our group is another biomimetic model: NHC-$Fe^{IV}O$, a system that greatly resembles Cpd I structurally, but has some key differentiating aspects as the Iron(IV)Oxo is embedded in a set of four carbene atoms, instead of nitrogen atoms; furthermore, the porphyrin-original carbons are replaced by nitrogen atoms, and a set of extra hydrogen atoms complete the new structure (Fig. 1.14). The saddled new catalyst however has been proven to be a weaker, slower catalyst, whilst undergoing some similar CpdI-like mechanisms. Although lacking a lower coordinating ligand to the iron, when placed in acetonitrile, it will have a good binding affinity towards it with some catalytic properties changing with it (Cantu-Reinhard et.al. 2017).

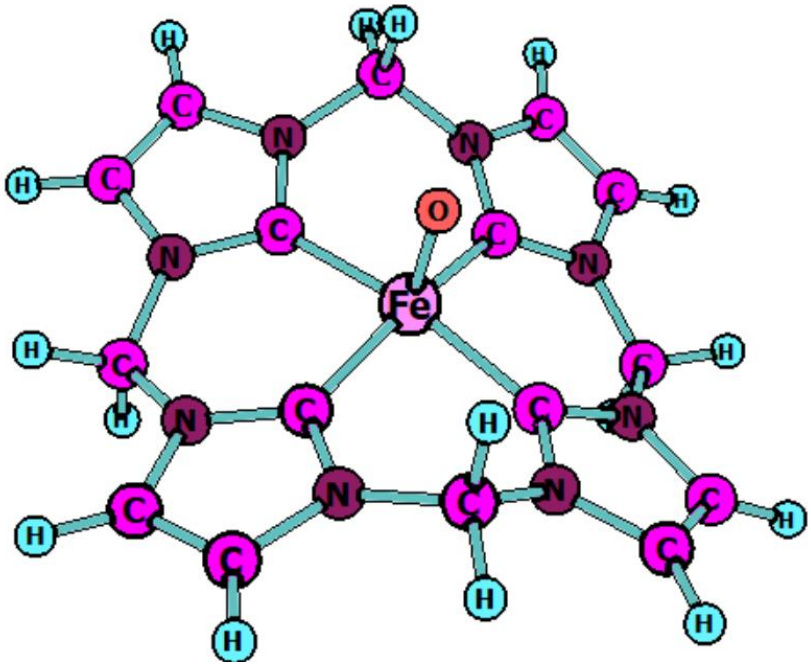


**Figure 1.14:**B3LYP/6-31G* optimized structure of $NHC(Fe^{IV}O)^{2+}$

Metalloporphyrin biomimetic models which resemble P450s-CpdI more strictly have also been studied in collaborations with our group. One such example is $Fe^{IV}(O)(TPFPP^{+\cdot})$ or (5,10,15,20-tetrakis(pentafluorophenyl-$Fe^{IV}O$), a fluorinated tetrapyrrole derivate $Fe^{IV}O$ complex also studied in collaboration with our group (Figure 1.15). This compound resembles CpdI very well, with some key differences as the lack of a sixth, lower ligand on the iron, normally found on CpdI where there is a coordination from either a cysteinate or a histidine amino acid. This may be the main culprit behind an important change in the $a_{2u}$ and $a_{1u}$ orbitals' relative ordering (Cantu-Reinhard et.al.[2] 2016).

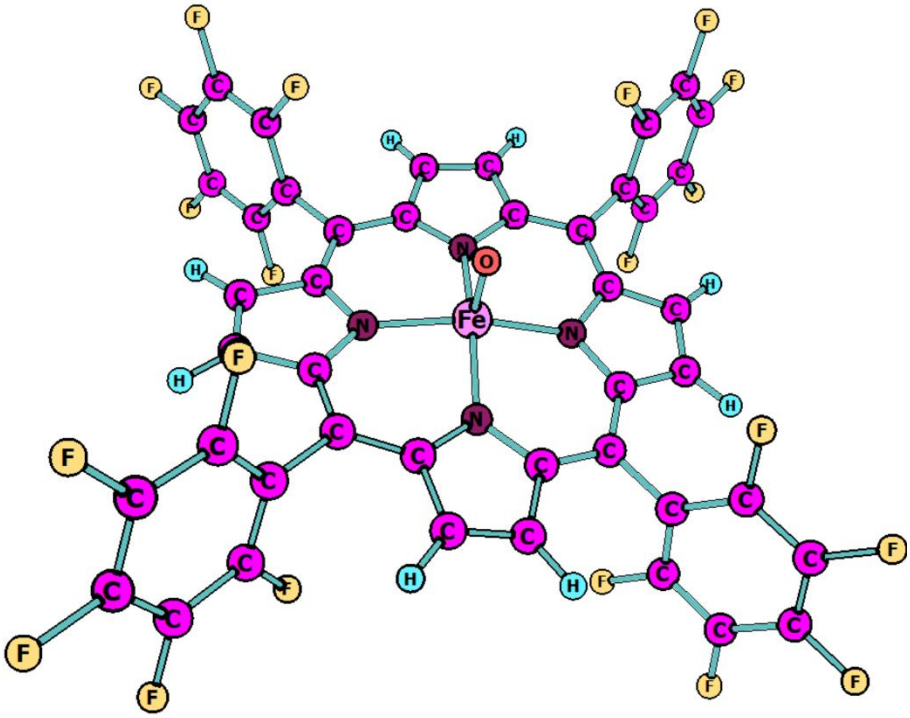

**Figure 1.15:** B3LYP/6-31G* optimized structure of $TPFPP^{\bullet+}(Fe^{IV}O)$.

We have been involved in an extensive experimental and computational study on the characteristics of aliphatic vs aromatic hydroxylation reactions (Cantu-Reinhard et.al. 2016), and in a more recent work, to study key differences on hydrogen atom versus hydride atom activation processes on some common substrates (Cantu-Reinhard et.al. 2018). During this study, another key difference in the properties of this biomimetic model as compared to CpdI was shown, where the EA of the intermediate FeOH of this electron deficient complex is large enough on the biomimetic model to allow an overall hydride transfer, and stabilizing an intermediate cationic complex (Cantu-Reinhard et.al. 2018).

## 1.3 Summary of Research Objectives

Indeed, finding reliable means of predicting and characterizing P450 mediated metabolizations is yet a pressing problematic with imperative implications on human health and industry. While many data-driven approaches have been developed to filter out the most probable drug candidates and to optimize later stages in drug development, these approaches fall short of a detailed description of the enzyme – substrate relationship.

On the other hand, experiments on P450 enzymes are expensive and time consuming, and yet they fail to reveal some crucial intermediates and short lived species relevant for a better description of these enzymes behaviour. And while Fe(IV)-oxo biomimetic models are a simpler alternative to P450s and often present a similar mechanistic behaviour, they may also present the same problematic.

Therefore, DFT and QM/MM methodologies present in many ways an unchallenged capacity to reveal intrinsic and mechanistic properties of biomimetic Fe(IV)-oxo models or P450 enzymatic models, either as pure computational studies or in combined experimental and computational methods. Thus, by understanding and revealing the mechanisms of reaction by which the substrates are activated by P450 enzymes or their biomimetic equivalents, and by unveiling the factors that influence this reactivity, the design and selection of drug candidates can become an ever more rational activity.

Hence, it is the objective of the many projects that comprise this thesis, to further enrich the understanding of the chemistry of P450s and other oxidative enzymes of drug metabolism, in hopes to contribute to the field so that the design of new drug species is benefitted by a broader theoretical understanding of mechanisms of reaction, regio- and enantio-selectivity, sites of activation, toxicology and biosynthesis, while also exploring the potentials and limitations of the computational approaches used to study them.

**Chapter 3, Project 1:** On this project, we studied the kinetics of sulfoxidation by a CpdI biomimetic, N4PY(Fe(IV)=O), on a series of thioanisole substrates. I performed a large amount of calculations on the various substrates under many different theoretical DFT frameworks (basis sets, functionals, dispersion and solvent inclusion) in order to properly benchmark those methods for experimental prediction of kinetic constants. By some methods and with the inclusion of some empirical correction on solvation, it can be shown that a very good agreement with experiment is possible for such models. Dr. Abayomi Faponle guided the initial set-up of some scripts as I learned the methodologies.

**Chapter 4, Project 2:** On this project we characterize and explore the reactivity through a mechanistic study of an Fe(IV)=O N-Heterocyclic carbene complex. The novel system is also a biomimetic of CpdI and opposed to the natural system, is a weaker catalyst. However, similar mechanisms of reaction are observed to that of CpdI, and as this system, unlike CpdI, is stable as a superoxo (Fe(IV)=O) it proves to be a good study model of CpdI chemistry, both experimentally and theoretically.

**Chapter 5, Project 3:** This collaborative project combines experimental data with theoretical calculations on a porphyrin Fe(IV)-oxo model. A detailed mechanistic study is performed by low pressure mass spectrometry on a series of aromatic compounds and the mechanisms of reaction were clarified by theoretical DFT calculations. The experimental results were provided by Dr. Crestoni's group, whilst our group and Dr. Kumar's performed the theoretical calculations. Initial calculations were performed by Dr. Mala Saina with the help of Dr. Kumar, and later on Alex Balan and I took over the calculations to revise and complete them to their full extent.

**Chapter 6, Project 4:** With a similar cooperation on Dr. Crestoni's group, we studied the P450- biomimetic metalloporphyrin TPFPP-$Fe^{IV}O$ in reaction with a set of common substrates to compare and explain the reasons behind the contrasting hydride versus hydrogen atom transfers on substrate activation. The reactions are further rationalized with VB models, and a simplified porphyrin model $Fe^{IV}O$ was compared to the more electron deficient catalyst. Dr. Crestoni's group provided the experimental results and the idea on the project while we performed the computational part.

**Chapter 7, Part 5:** This project explores the capabilities of a simplified DFT P450 enzymatic model to predict a set of common expected metabolites on the metabolism of a phthalate derivate found on pharmaceutical formulations and cosmetic products. Sites of activation (SOM) were identified and discussion is given on the potentials and limitations of this theoretical approach.

**Chapter 8, Project 6:** This project is a combined DFT and QM/MM study on Nogalamycin Mono Oxygenase (NMO), also regarded as SnoaB, an enzyme involved on the biosynthetic path of this natural antibiotic. With a surrogate drug-substrate, dithranol, we explore the mechanism behind the cofactor independent monooxygenation of the substrate by this enzyme, a trait that has relevant implications for the biotechnological industry, especially in drug synthesis, whilst it also presents the potentials of these computational approaches.

# Chapter Two

# METHODS

## 2.1 QM Modelling: Electronic Structure Methods

To quantitatively and qualitatively study reaction mechanisms at an electronic level with an appropriate degree of accuracy, one must attain to the fundamental physics of sub-atomic-particles' systems which are governed by quantum mechanics. Computational numerical methods employed to study many-body electronic systems from first principles are called electronic structure methods (Greeley, et.al, 2002). By definition, "first principles" methods require no adjustable parameters and therefore to employ such tools, a simple description of the system under study is required in order to perform complex calculations: this is to provide information on the respective degrees of freedom. There is a great predictive capacity in these methods, proven by a high accuracy against numerous examples of experimental match (Klepeis, 2006).

Electronic structure methods rely on predicting ground state electronic configurations and nuclear coordinates based on minimal energy states with a set of restrictions on a given system. Most electronic structure methods are built upon the time-independent Schrödinger Equation (2.1) (Greeley, et.al, 2002):

$$\widehat{\boldsymbol{H}}(\boldsymbol{\Psi}) = \boldsymbol{E\Psi} \qquad (2.1)$$

In eq. 2.1, $\widehat{H}$ corresponds to the Hamiltonian operator, $E$ is the total energy of the system, and $\Psi$ is the wave-function. Often, the wave function $\Psi$ is regarded to hold meaning only when squared, as $|\Psi(x)|^2$ represents the probability density distribution of the system (Asharanov et.al, 1993). The Hamiltonian Operator accounts for the total energy of a system, where kinetic and potential contributions are taken into account, including the contributions from all the N-electrons and M-nuclei of charge Z in the system (2.2) (Koch et.al. 2001):

$$H = -\frac{1}{2}\sum_{i=1}^{N}\nabla_i^2 - \frac{1}{2}\sum_{A=1}^{M}\frac{1}{M_A}\nabla_A^2 - \sum_{i=1}^{N}\sum_{A=1}^{M}\frac{Z_A}{r_{iA}} + \sum_{i=1}^{N}\sum_{j>1}^{N}\frac{1}{r_{ij}} + \sum_{A=1}^{M}\sum_{B>1}^{M}\frac{Z_A Z_B}{R_{AB}} \qquad (2.2)$$

Where $\nabla^2$ is the Laplacian operator that in cartesian coordinates is defined by eq. 2.3.

$$\nabla^2 = \frac{\partial^2}{\partial x^2} + \frac{\partial^2}{\partial y^2} + \frac{\partial^2}{\partial z^2} \qquad (2.3)$$

The Schrödinger equation is generally simplified for chemical applications by the Born-Oppenheimer approximation, where nuclei are considered relatively "static" when compared to the electron speed. This assumption leads to the separation of the Schrödinger equation for the nuclear and electronic structures, where the electronic structure can be visualized as a static nuclei surrounded by a cloud of electrons, whose electronic structure is determined by the solution of the Schrödinger equation (Greeley, et.al, 2002).

Analytical solutions for the electronic time independent Schrödinger equation have not been found apart from the simplest systems (e.g. H atom) and therefore numerical approximations are required for practical "real world" chemical systems. The process by which the wave function is systematically approached is the variational principle, where it is stated that for any iteration of the wave function, the energy obtained through the Hamiltonian operator will always be higher (or at best equal) to that of the true wave function (Koch et.al. 2001; Cramer 2004). For a one-electron wave function, the electronic energy is calculated from eq. 2.4.

$$\frac{\int \Phi H \Phi d\boldsymbol{r}}{\int \Phi^2 \, d\boldsymbol{r}} \geq E_0 \qquad (2.4)$$

$\Phi$ is a set of wave functions $\Psi i$, and when squared and normalized becomes equal to 1 (eq. 2.5).

$$\int \Phi^2 \, d\boldsymbol{r} = \mathbf{1} \qquad (2.5)$$

If $\Phi$ is comprised by a set of linear combinations of atomic orbitals, then the previous equation becomes the "secular equation" (eq. 2.6).

$$E = \frac{\int \sum_i (a_i \varphi_i) H (a_j \varphi_j) d\boldsymbol{r}}{\int \sum_i (a_i \varphi_i)(a_j \varphi_j) d\boldsymbol{r}} = \frac{\sum_{ij} a_i a_j H_{ij}}{\sum_{ij} a_i a_j S_{ij}} \qquad (2.6)$$

The terms **H** and **S** correspond to the resonance and overlap one-electron integrals, respectively. Further, a many electron –non interacting- system may be expanded from the "Hartree Product" of the i-electrons (Cramer 2004), where the Hamiltonian of the whole system can be expressed as the product of the one electron Hamiltonians, that results in that the energy of the system is the summation of each one electron Hamiltonians (eq. 2.7) (Greeley, et.al, 2002; Cramer 2004).

$$H\Psi_{HP} = \left(\sum_{i=1}^{N} \varepsilon_i\right)\Psi_{HP} \qquad (2.7)$$

Inter-electronic repulsion may be added to the one electron Hamiltonians via an average potential electronic effect (eq. 2.8).

$$V_i\{j\} = \sum_{j \neq i} \int \frac{\rho_j}{r_{ij}} d\boldsymbol{r} \qquad (2.8)$$

However, electron spin and antisymmetry requires some further considerations. This can be achieved with the aid of the Slater determinant that considers the fermion behaviour of electrons, better known as Pauli exclusion principle. For a two electron system, this can be defined by eq. 2.9, where $\Psi(x_1, x_2)$ is the 2 body wave function, $x_i$ refers to electron i space-spin coordinates, composed of space coordinates $\boldsymbol{r}$ and spin function ω (with either intrinsic spin functions α or β). $\chi = \{r, \omega\}$. $\chi_i$ is the spin-orbital (with inclusion of spin, $\phi(r) \rightarrow \chi(x)$.

$$\Psi(x_1, x_2) \cong \frac{\chi_1(x_1)\chi_2(x_2) - \chi_1(x_2)\chi_2(x_1)}{\sqrt{2}} \qquad (2.9)$$

The difference in energy gained by the use of the Slater determinant is regarded as the exchange energy (Atkins and Friedman, 1997) and can be expanded to an N electron system, with short notation: $\Psi_{SD} = |\chi_1\chi_2\chi_3 \ldots \chi_N\rangle$, substituting the Hartree product for the many electron system (Koch et.al. 2001).

The new inter-electronic potential now becomes equation 2.10, where $J_{ab}$ is the Coulombic repulsion (Coulomb operator), and $K_{ab}$ corresponds to the exchange correction (exchange operator) from the so called "fermi hole" (Koch et.al. 2001).

$$V_{SD} = J_{ab} - K_{ab} \tag{2.10}$$

Hence, the energy can now be represented in a new Hamiltonian as eq. 2.11, further expanded into equations 2.12, 2.13 and 2.14 (Koch et.al. 2001).

$$E_{HF} = \langle \Phi_{SD}|H|\Phi_{SD}\rangle = \sum_{i}^{N}(i|h|i) + \frac{1}{2}\sum_{i}^{N}\sum_{j}^{N}(ii|jj) - (ij|ji) \tag{2.11}$$

$$(i|h|i) = \int \chi_1{}^*(x_1)\left\{-\frac{1}{2}\nabla^2 - \sum_{A}^{M}\frac{Z_A}{r_{iA}}\right\}\chi_1(x_1)dx_1 \tag{2.12}$$

$$(ii|jj) = J_{ij} = \int\int |\chi_i(x_1)|^2 \frac{1}{r_{12}}\left|\chi_j(x_2)\right|^2 dx_1 dx_2 \tag{2.13}$$

$$(ij|ji) = K_{ij} = \int\int \chi_i{}^*(x_1)\chi_j(x_1)\frac{1}{r_{12}}\chi_j{}^*(x_2)\chi_i(x_2)dx_1 dx_2 \tag{2.14}$$

Finally, a method was devised for systematically solving the many-electron wave function and corresponding eigenvalues from a set of Linear Combination of Atomic Orbitals (LCAO) with the mentioned inter-electronic interactions, namely the Hartree-Fock Self Consistent Field (SCF) method. The name arises from the fact that the method requires an input wave function in order to obtain a new improved wave function and corresponding energies, which is done iteratively until a threshold is reached. (Cramer 2004). Thus, the Hartree-Fock Roothan equations were devised in order to optimize the density matrix (Orbital Occupation) based on the new set of one electron operators called the "Fock operators". The Fock operator is defined by eq. 2.15, where $V_i^{HF}$ corresponds to the interaction potential with all the other electrons (i.e. Coulomb and Exchange) (Cramer, 2004).

$$f_i = -\frac{1}{2}\nabla_i^2 - \sum_{k}^{nuclei}\frac{Z_k}{r_{ik}} - V_i^{HF} \tag{2.15}$$

The Fock operator (2.15) then forms part of the Hartree-Fock-Roothaan equations 2.16. Where a basis set is introduced, and hence the new elements $\nu$ and $\mu$ refer to atomic basis functions $\phi_\nu$ and $\phi_\mu$, and the **F** component is defined by eq. 2.17, (Cramer, 2004).

$$\sum_{\nu} \boldsymbol{F}_{\mu\nu} C_{\mu\nu} = \epsilon \sum_{\nu} S_{\mu\nu} C_{\mu\nu} \tag{2.16}$$

$$F_{\mu\nu} = \langle \mu | -\frac{1}{2}\nabla^2 | \nu \rangle - \sum\nolimits_{k}^{nuclei} \frac{Z_k}{r_{ik}} + \sum_{\lambda\sigma} P_{\lambda\sigma} \left[ (\mu\nu|\lambda\sigma - \frac{1}{2}\mu\nu|\nu\sigma \right] \tag{2.17}$$

The first part of eq. 2.17 corresponds to the operator 2.18, where g is the Laplacian operator. The expression $\mu\nu|\lambda\sigma$ now corresponds to the two-electron integral, eq. 2.19, which is equivalent to eq. 2.14, but now within the setting of the LCAOs method, where $\mu$ and $\nu$ correspond to the probability density of one electron in basis functions $\phi_\mu$ and $\phi_\nu$and $\lambda$ and $\sigma$ to other electron in basis functions $\phi_\lambda$ and $\phi_\sigma$.

$$\langle \mu | -\frac{1}{2}\nabla^2 | \nu \rangle = \int \phi_\mu \left( g \phi_\nu \right) d\boldsymbol{r} \tag{2.18}$$

$$V_i^{HF}\{j\} = \mu\nu|\lambda\sigma = \int\int \phi_\mu(1)\phi_\nu(1)\frac{1}{r_{12}}\phi_\lambda(2)\,\phi_\sigma(2) d\boldsymbol{r}(1) d\boldsymbol{r}(2) \tag{2.19}$$

Finally, the term $P_{\lambda\sigma}$ specifies the density matrix, where only occupied MO's will contribute to the energy from the coloumb and exchange interactions. Iterative variation of this density matrix will lead to an "optimum" occupancy of the MOs and the solution to the HF procedure (Cramer, 2004).

## 2.2 Basis sets and the LCAO Method

In the LCAO approach, each one electron orbital is approximated by an artificial orbital function (basis set). This function is commonly described as a Slater Type Orbital (STO) (Slater, J., 1930) or a Gaussian Type Orbital (GTO) (Boys, S., 1950). Each STO or GTO can be completely described by a set of parameters, whereby the complete collection of parameters that fully describe these functions (and the functions hence produced) are regarded as the "basis set". Although STOs are more accurate functions to describe the electron wave functions (GTOs contain no radial nodes), the higher computational cost of using these functions over equal accuracy achievable with a higher number of Gaussian Functions at less computational cost, is the reason of the preference of Gaussian type orbitals in modern calculations (Cramer, 2004). The radial component of an early version of a STO is represented by eq. 2.20 and the radial component of an early version of a GTO represented by eq. 2.21.

$$R(r) = r^{n-1}e^{-\frac{Z-s}{n}*r} \qquad (2.20)$$

$$R(r) = r^{n-1}e^{-\frac{Z-s}{n}*r^2} \qquad (2.21)$$

In these versions, the value of the constant n is assigned based on the principal quantum number, while Z refers to atomic charge, and s refers to the shielding factor of the electron (Slater, J., 1930). Basis sets have been developed for STO or GTO based calculations and rely on the LCAO method, where the molecular wave function is represented by the summation of a linear combination of atomic orbitals. In practice, one would take the mentioned basis sets $\phi_\mu$ with specific pre-exponential and exponential factors depending on the element and atomic orbital. Then only the linear coefficients $C_{\mu i}$ would need to be optimized to describe each molecular orbital $\Psi_i$, as presented in eq. 2.22, where $\phi$ encompasses the atomic orbital basis function, or basis set, and $\Psi_i$ is the i$^{th}$ molecular wave function (Hehre, et.al., 1969; Pople et.al. 1971).

$$\Psi_i = C_{\mu i}\phi_\mu \qquad (2.22)$$

Each STO may be represented by a set if contracted Gaussian functions, but the same logic still applies. These are represented as STO-nG basis sets, such as STO-3G where three primitive Gaussian functions compose each STO. Each atomic orbital is not limited to one basis function and instead, the basis set may differ in size until what is called the infinite basis set, or Hartree Fock Limit, where the maximum accuracy of the Hartree Fock method (one slater determinant) is obtained. This result would however still be an approximation lacking full electron correlation (i.e. electron - electron interactions) (Davidson et. al., 1986; Hehre, et.al., 1969).

For greater accuracy, larger basis sets are used, such as double zeta (two basis functions per atomic orbital) triple zeta (three basis functions per atomic orbital), quadruple zeta, etc. However, most commonly a hybrid approach is used called split valence basis sets. In split valence basis sets only the valence electrons are represented by more than one basis function while the core electrons only have a single orbital each (e.g. STO). A common example is 3-21G, where 3 GTOs compose each of the inner atomic orbitals, while the valence atomic orbitals are composed by a STO (represented by 2 contracted Gaussians) and an additional GTO (Davidson et. al., 1986; Binkly et.al., 1980).

In polarized basis sets, additional "higher energy" functions are added to the set, increasing the mathematical flexibility of systems that cannot be properly described by the normal S and P functions of the original basis set, adding normally a basis function of a higher quantum number than the valence shell, such as a "d" function for first row elements, and possibly allowing a more exact geometrical distribution of electrons. Seemingly, an additional basis function called "diffuse function" may be added to allow localization of electrons that may not be optimized among the remaining density in some higher energy molecular orbitals. (Davidson et. al., 1986; Cramer, 2004).

Additionally, sometimes Effective Core Potentials (ECP) are used as a useful method to reduce the number of basis set functions in the energy calculation by replacing the inner electron orbitals with a representative potential or pseudo-Hamiltonian, which presumably requires lower computational resources without sacrificing relevant accuracy or results for the job (Schwerdtfeger, 2011).

## 2.3 Density Functional Theory

Density Functional Theory (DFT) is an alternative to *ab initio* methods that does not rely on computing the many electron wave function from first principles. Instead, the more tangible electron density is computed considering that the total number of electrons (a needed quantity for the Hamiltonian Operator) corresponds to the space integral of the electron density (Cramer, 2004) (eq. 2.23).

$$N = \int \rho(r) dr \qquad (2.23)$$

Implicit in the electron density matrix is an associated observable, the energy, which the *variational principle*, must be greater or equal to the true ground state energy. For a specific system, the requirement is no longer to obtain the wave function Ψ but instead to obtain the electron density ρ(r) function. The density function is obtained by iterations and hence is also regarded as an SCF (Self Consistent Field) method similar to HF theory, even though it has a different theoretical basis. However, DFT can be seen as analogous to HF theory in many aspects as well as in the practical approaches to its solutions.

The total energy of the system can be expressed by eq. 2.24, which can be further expanded into equations 2.25 and 2.26 (Koch et.al. 2001). Where $T$ refers to the kinetic energy, $V_{ne}$ to the potential for the electron-nucleus interactions, $V_{ee}$ refers to the electron-electron potential, and $E_{xc}$ to exchange-correlation.

$$E_{DFT} = T + V_{ne} + V_{ee} + E_{xc} \qquad (2.24)$$

$$E_{DFT} = T_s + \frac{1}{2}\int\int \frac{\rho(r_1)(r_2)}{r_{12}} dr_1 dr_2 + E_{xc} + \int V_{ne}\rho(r) dr \qquad (2.25)$$

$$E_{DFT} = -\frac{1}{2}\sum_{i}^{N}\langle\varphi_i|\nabla^2|\varphi_i\rangle + \frac{1}{2}\sum_{i}^{N}\sum_{j}^{N}\int\int|\varphi_i(r_i)|^2\frac{1}{r_{12}}\left|\varphi_j(r_2)\right|^2 dr_1 dr_2 + E_{xc} - \sum_{i}^{N}\int\sum_{A}^{M}\frac{Z_A}{r_{1A}}|\varphi_i(r_1)|^2\, dr_1 \qquad (2.26)$$

One can already see the similarity between the HF and DFT equations. By definition, the total energy evaluated by DFT theory is exact but the biggest problem is that the term $E_{xc}$ is not known exactly. Many approximations have been made towards the $E_{xc}$ functional, such as the Slater derivation, which disregards the correlation effects and corrects only for exchange as this is in fact the greatest contributor to error (Cramer, 2004; Koch et.al. 2001). Modern DFT is normally implemented through the Kohn-Sham (KS) approach, which is equivalent to the HF Roothaan approach. The one-electron KS equations are implemented through the operator defined in equation 2.27 that can be written simply as eq. 2.28 (Koch et.al. 2001).

$$\left(-\frac{1}{2}\nabla^2 + \left[\sum_j^N \int \frac{\left|\varphi_j(r_2)\right|^2}{r_{12}} dr_2 + V_{xc} - \sum_M^A \frac{Z_A}{r_{1A}}\right]\right)\varphi_i = \varepsilon_i \varphi_i \qquad (2.27)$$

$$f^{KS}\varphi_i = \varepsilon_i \varphi_i \qquad (2.28)$$

In a similar approach to that of HF theory, this leads to a set of functions encompassing an $\mathbf{F^{KS}}$ matrix in analogy to the **F** Fock matrix. During the solution of the KS equations, a resulting **P** density matrix will contain the charge-density information based on the basis set and the LCAO approach (Koch et.al. 2001).

So what happens with the $E_{xc}$ term? The most common DFT methodologies used today employ the hybrid functional approach, where the $E_x$ of HF theory is also computed and proportionally added to the energetic terms in addition to some DFT-based implementations of $E_{xc}$ normally a version of the GGA (Generalized Gradient Approximation) or LDA (Local Density Approximation) (Koch et.al. 2001).

The most popular functional up to date, B3LYP (Stephens et.al. 1994) was modified from the B3PW91 functional by Becke (1993) and employs expression 2.29 for the energetic contributions to exchange-correlation (Koch et.al. 2001).

$$E_{xc}^{B3LYP} = (1-a)E_x^{LSDA} + aE_x^{HF} + b\Delta E_x^{B88} + (1-c)E_c^{LSDA} + cE_c^{LYP} \qquad (2.29)$$

The LDA approach is defined by equation 2.30.

$$E_{xc}^{LDA} = \int \rho(r)\, \varepsilon_{xc}\big(\rho(r)\big) dr \qquad (2.30)$$

The exchange-correlation energy $\varepsilon_{xc}$ from equation 2.30 can be further separated into equation 2.31, where the exchange part corresponds to the Slater exchange functional as defined in equation 2.32.

$$\varepsilon_{xc}\big(\rho(r)\big) = \varepsilon_x\big(\rho(r)\big) + \varepsilon_c\big(\rho(r)\big) \qquad (2.31)$$

$$\varepsilon_x = -\frac{3}{4}\sqrt[3]{\frac{3\rho(r)}{\pi}} \qquad (2.32)$$

The correlation part has different analytical approximations, such as the Vosko–Wilk–Nusair (Vosko et.al. 1980) or Perdew and Wang (Perdew and Wang, 1992) (correlation functionals commonly employed on DFT functionals. Further inclusion of spin led to the Local Spin Density Approximation (LSDA) (Koch et.al. 2001) defined by equation 2.33.

$$E_{xc}^{LSDA}\big(\rho_\alpha, \rho_\beta\big) = \int \rho(r)\, \varepsilon_{xc}\left(\rho_\alpha(r), \rho_\beta(r)\right) dr \qquad (2.33)$$

Subsequently, the functional was improved by inclusion of the gradient of the charge density $\nabla\rho(r)$ into the gradient expansion approximation, and by some extra constraints, to the GGA (Generalized Gradient approximation) (Koch et.al. 2001).

## 2.4 Geometry Optimizations using DFT

Figure 2.1 represents a three dimensional potential energy surface, where a set of arrows brings together a reactant and a product through the reaction coordinate. Reactants, intermediates and products are local minima, whereas these points are connected through a first order-saddle point, or transition state, which is the lowest possible path connecting these minima. One of the key objectives in DFT modelling, and especially in catalysis based on transition state theory, is the prediction and characterization of these structures through optimization algorithms, generally inbuilt in the software employed (e.g. Gaussian 09). Different algorithms for finding local minima, or geometry optimizations, have been developed, and are either broadly classified into first-order methods or second-order methods, where the first-order ones only an analytical first-order derivative and the second-order versions employ hessians and first-order derivatives to build a quadratic model for optimization (Li, 2006).

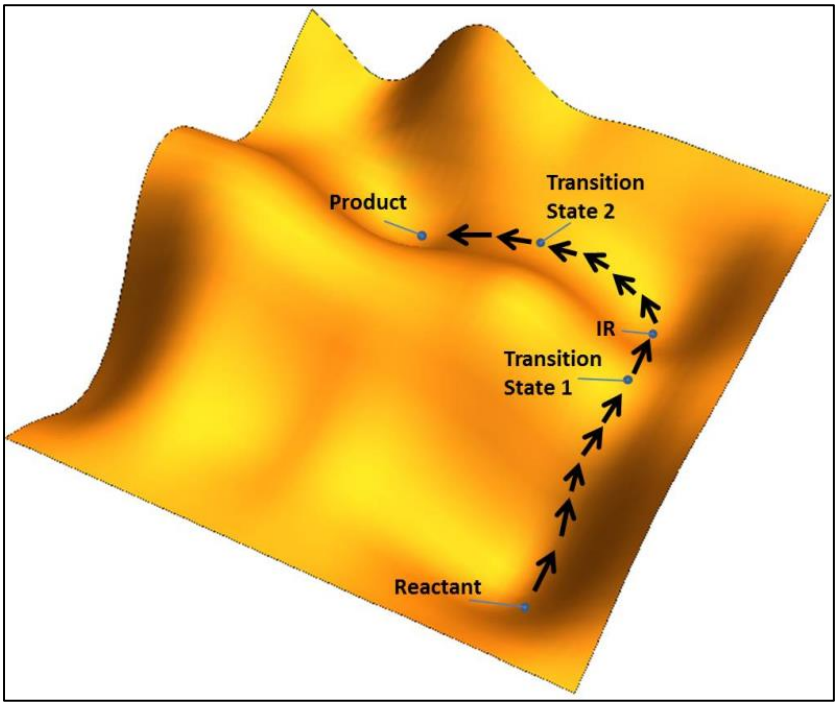


**Figure 2.1:** Potential energy surface representation of the reaction landscape.

## 2.5 Transition State Theory - Reaction Mechanisms from PES

Transition state theory is a chemical kinetics theory that relies on the fact that reactions proceed with highest probability, through the least energetic pathway between reactant and products on the potential energy surface (PES) of the reaction coordinate. The position with the highest energy is called the activated complex or *transition state*, which accordingly determines the minimal potential energy necessary for reaction. (Wright, 2004). Figure 2.2 presents a relaxed (optimized) PES of the reaction coordinate for N4PY + CH3-Thioanisole sulfoxidation products (See chapter 3). The activated complex lies at the top of the energy curve formed by scanning across a reaction coordinate vector.

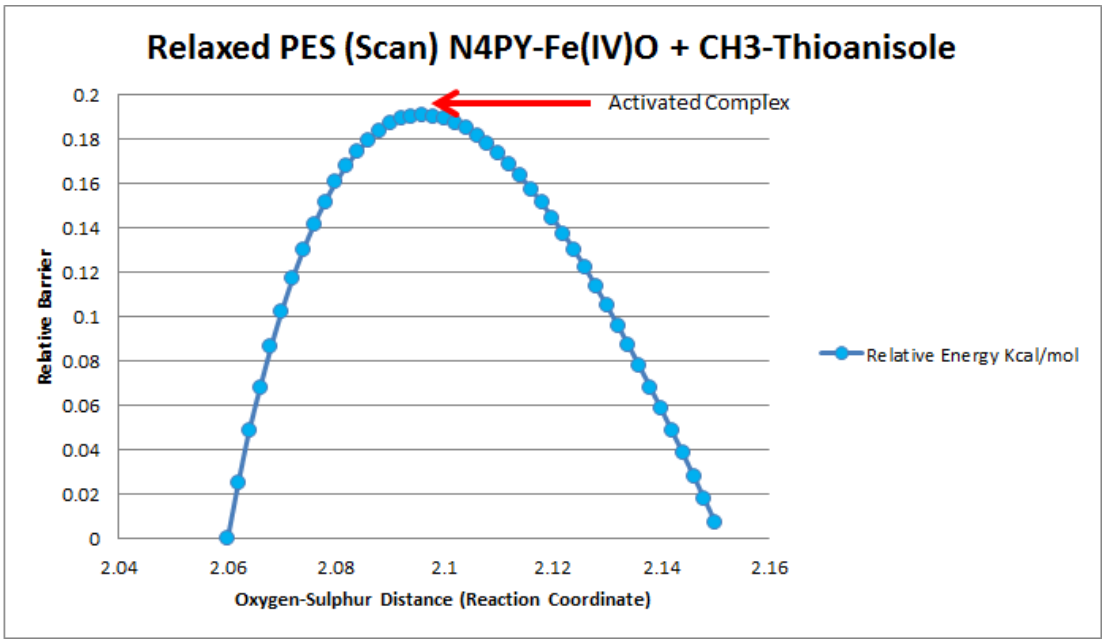


**Figure 2.2** UB3LYP/6-31G* DFT relaxed scan potential energy surface for H-thioanisole sulfoxidation, showing O-S bond distances from 2.06 to 2.15 Ångström. (Cantu-Reinhard, et.al.[1], 2016)

The core concepts of TST relies on statistical thermodynamics. In this field, energy is quantized and can be partitioned according to the different contributors (e.g. electronic, vibrational, rotational, and translational) and the probability of an energy state to occur depends on the energy level, according to a Boltzmann distribution (Dill, 2002). One can define thermodynamic equilibrium based on concentrations and partition functions "Q" as in equation 2.34, where the term $-(\varepsilon oB-\varepsilon oA)$ comes from the dissociation energies from the reactants and products that have been factored out of the partition function Q. This quantity is the zero point vibrational energy difference between the two ground state conformations in the reaction coordinate (Dill, 2002). In TST, one assumes there is an equilibrium between the reactant complex and the transition state, as presented in equation 2.35 (Wright, 2004).

$$K_{eq} = \left(\frac{Q_A}{Q_B}\right) e^{-(\varepsilon_o B-\varepsilon_o A)/RT} \qquad (2.34)$$

$$K_{eq}{}^{\neq *} = \left(\frac{Q^{\neq *}}{Q_B}\right) e^{-(\varepsilon_o B-\varepsilon_o A)/RT} \qquad (2.35)$$

The term $Q^{\neq *}$corresponds to the transition state partition function, and through a series of derivations here avoided, one can define a kinetic constant based on that equilibrium (equation 2.36) (Wright, 2004).

$$k_{kinetic} = \frac{\kappa k_B T}{h} K^{\neq *}{}_{eq} \qquad (2.36)$$

Where * refers to the fact that the partition component of the free translation was rationalized is not present because it cancelled out during the derivation. The terminus κ refers to the transmission coefficient and is normally disregarded for a value of 1 (Wright, 2004).

These equations can be converted to a standard thermodynamic equation, which is readily usable when with the thermodynamic properties of enthalpy, entropy and/or free Gibbs energy between the reactant complex and the transition state (Wright, 2004), currently achievable through QM computational tools (See equations 2.37 and 2.38).

$$k_{kinetic} = \frac{k_B T}{h} e^{\left(\frac{-\Delta G^{\neq}}{RT}\right)} \qquad (2.37)$$

$$k_{kinetic} = \frac{k_B T}{h} e^{\left(\frac{-\Delta H^{\neq}}{RT}\right)} e^{\left(\frac{+\Delta S^{\neq}}{R}\right)} \qquad (2.38)$$

One may notice, however, that the kinetic factor is exponentially related to such quantities, and therefore the error in measuring these physical quantities will propagate also exponentially, and hence the accuracy of these calculations are not trivial when comparing against experimental data, where a difference of 1 or 2 kcal/mol can mean an order of magnitude change in the kinetic factor.

## 2.6 Beyond elementary reaction rates in TST

Transition state theory presents the means to calculate a rate of reaction for elementary reaction kinetic models such as the bi-molecular form like that presented in equation 2.39, where $-r_A$ refers to the rate of change of compound A, and [A] and [B] correspond to the molar concentrations of species A and B respectively.

$$-r_A = k_{kinetic}[A][B] \qquad (2.39)$$

However, often chemical reactions depend on more than one of such elementary reactions, and thus take place on a rate described by higher order rate law of reaction or a rather more complex rate model such as that presented in equation 2.40, studied computationally by Rush et.al. (2014), and Habershon (2016) for the cobalt catalysed hydroformylation of alkenes, and previously experimentally characterized by Bourne (Bourne et.al. 1992).

$$\frac{-d[CO]}{dt} = k \frac{[H_2][CO][Cat]^{0.8}[Alkene]}{(1 + K[CO])} \qquad (2.40)$$

This reaction is not a one step elementary reaction but instead can be modelled as a network of such elementary reactions studied under the DFT and TST context, which for Rush et.al. (2014) led a new model (2.41) based entirely on theory, greatly resembling the older experimental model. Further modelling efforts of Habershon (2016) show a clear match between models and experimental results.

$$\frac{-d[CO]}{dt} = k\frac{\left[p_{H_2}\right]^{0.5}[Co]^{0.5}[Alkene]}{pCO} \qquad (2.41)$$

## 2.7 Solvent Effects on QM models

QM models are very accurate for the gas-phase state of molecules, however for the replication of experiments or modelling of systems in solution, corrections to the energy must be made. Solvation modelling may be done by either implicit or explicit models. Implicit solvation has the advantage of not increasing the degrees of freedom of the system and not needing to measure average effects of an explicit solvent through e.g. Monte Carlo or molecular dynamics. This is especially important in systems that cannot grow too big (in terms of degrees of freedom), such as QM based calculations (Truhlar and Cramer, 1999).

Early implicit solvation models considered only a continuous homogenous medium with the sole purpose of modifying the electric permittivity of the media ε, thus linearly affecting all electrostatic interactions. However, important interactions in the interactive region between solute and solvent where not considered and more complex models were developed to account for other important properties of solvation (Truhlar and Cramer, 1999).

In the basic continuum model, the standard solute's QM Hamiltonian $\widehat{H}^0$ (in vacuum) is modified to include an interaction potential $\widehat{V}_{int}$ into a perturbed Hamiltonian $\widehat{H}$ (see equation 2.42) (Truhlar and Cramer, 1999).

$$\widehat{H} = \widehat{H}^0 + \widehat{V}_{int} \qquad (2.42)$$

This affects the related Schrödinger equation, so that all the relevant effects on the solute by the solvent effects are contained in the resulting eigenvalues and wave functions. The term $\widehat{V_{int}}$ requires a definition itself, and information such as a distribution function of the solvent molecules and a dielectric constant depending on the temperature are required, and an electrostatic field is defined. Overall, this leads to a contribution to the total energy of the system by the solvent-solute interaction (Truhlar and Cramer, 1999).

In most methods, a cavity region is defined in the solvation model where the solute is placed, and special consideration is required for properly describing the shape and size of it. For example, in the original Polarizable Continuum Model (PCM), the cavity is defined by spheres with a radii proportional to their van der Waals radii. With the cavity's geometry defined, through a series of constrains and physical models (mainly the nonhomogeneous Poisson electrostatics equation), the problem relies on predicting the electrostatic potential and its effects on the solute at the QM level to self-consistency for the coupling (Tomasi and Persico, 1994), although it is not in the scope of this work to present such derivations.

Ultimately, methods such as the integral equation formalism model IEF-PCM, which is the standard solvation model in Gaussian, are able to predict solvation effects with great accuracy, and more recently the solvation model based on density (SMD) has been developed as a parameterized IEF-PCM method with the central objective to properly predict free energy of solvation $\Delta G_{solvation}$ for any molecular configuration (Marenich et.al. 2009).

## 2.8 TST in Solution

Enzymatic P450 systems occur naturally in solvent (aqueous solution) and hence it is desirable to adequately model the presence of this solvent in the computational models to replicate and study such systems. Since the publication of Eyring's paper of the famous Eyring equation of TST, discussion already pointed towards an error of the TST from the gas phase to predict values of reactions in solution, partly because there must be a loss in accessible energy levels of the rotational and translational degrees of freedom, hence a decrease in entropy which in turn affects the free energy (Eyring, 1935). Of course, as previously mentioned, solvation is not only important to TST but to molecular modelling in general, but herein we are particularly interested in catalysis.

Implicit solvation models make a great adjustment and diminish the error of the thermochemistry calculations of species in solution by modifying the electronic energies and thus change the activation barriers but still are known for not perfectly predicting the change of entropy of solvation; hence not accurately predicting the absolute entropy of the solvated species. This in turn is a contributor to error when estimating energy barriers of reactions in solvent phase, although it has been shown that in some cases a more accurate method (i.e. including electron correlation) such as coupled cluster have a better role in reducing total error than the error contribution due to from current implicit solvation models. Also, dispersion corrections may greatly improve results, reducing the often overestimated activation barrier. (Harvey, 2009). Nonetheless coupled cluster models are still prohibitive for many small sized systems, as these methods scale at $N^6$ (for CCSD) or $N^8$ rates (for CCSD(T)) (Cramer, C. 2004).

One method to correct the change of entropy has been proposed by Wertz (1980) as adjusting the entropy to compel with the empirical observation described in the next section. Other methods for entropy corrections on TST have been proposed, for instance a different approach that has been employed is to calculate the vibrational frequencies at a much higher pressure, thus leading to a decrease in magnitude of vibrational and translational contributions to entropy (Martin et. al. 1998; Sieffert et. al. 2009).

## 2.9 The Wertz' correction to entropy of solvation

Wertz (1980) found an empiric relation between the entropic losses of a non-electrolyte as it is solvated into a pure solvent. According to these findings, the entropic loss of a molecule going into a solvent is the same fraction as would the solvent lose when going from the gas phase to the liquid (solvent) phase. Further explained by Cooper, et.al. (2002) one could calculate the entropic change of solvation with the following thermodynamic cycle and relations (see figure 2.3):

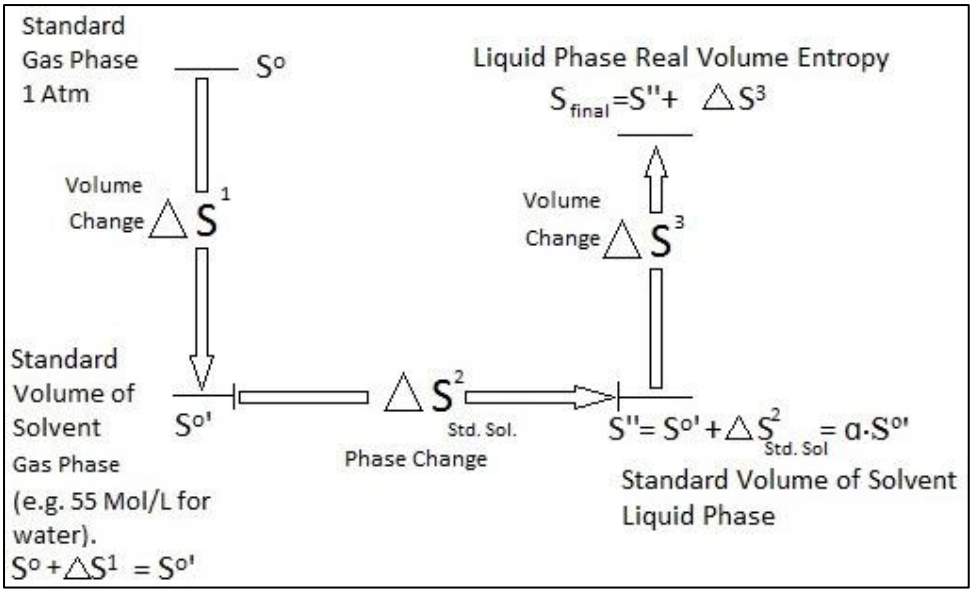


**Figure 2.3:** Thermodynamic cycle for entropic change of solvation.

Where the total change in entropy associated with the solute is given by equation 2.43.

$$\Delta S_{Sol} = \Delta S^{1}_{V1-VL} + \Delta S^{2}_{StdSol} + \Delta S^{3}_{VL-VF} \qquad (2.43)$$

$\Delta S^{1}_{V1-VL}$ is the entropic change associated with isothermal volume change from initial 1atm ideal gas molar volume (i.e. 1/24.405 L/Mol) to the molar volume of the solvent (e.g. for water, 1/55.5 L/Mol), and $\Delta S^{3}_{VL-VF}$ is similarly the entropic change associated the isothermal molar volume change from the solvent molar concentration to the real final solvated molar volume (e.g. 1L/Mol).

The entropic changes associated with volume change in an ideal gas are described in equation 2.44, which comes from the known ideal gas entropy state function (2.45).

$$\Delta S_{Vi-Vf} = Rln\frac{V_f}{V_i} \qquad (2.44)$$

$$\Delta S_{1-2} = \int_{T1}^{T2} \frac{CvdT}{T} + R\int_{V1}^{V2} \frac{dV}{V} \qquad (2.45)$$

Finally and according to the findings of Wertz (1980), the $\Delta S^2_{StdSol}$ can be calculated with the solvent specific factor $\alpha$, which represents the fraction of absolute entropy lost by the solvent when going from gas to liquid phase and equally applies to the solute as it solvates into the same solvent (see equation 2.46).

$$\Delta S^2_{StdSol} = \alpha(S^o + \Delta S^1_{V1-VL}) \qquad (2.46)$$

Where $S^o$ is the absolute standard entropy of the gas solute (1 atmosphere, gas phase) and the term $(S^o + \Delta S^1_{V1-VL})$ is the remaining absolute entropy after the volume change loss. The term $\Delta S^1_{V1-VL}$ produces a negative value as a volume decrease is expected when changing phase from gas to liquid.

If one would to use this relation as a correcting factor in transition state theory, directly to adjust the free energy change between the active intermediary identified with ≠ (e.g. transition state) and the reactive complex, one would notice that, for the ideal gas assumption, the volume change dependant entropic changes would cancel out, yielding the resulting in equation 2.49.

$$\Delta\Delta S_{Sol} = (\Delta S^{\neq 1}_{V1-VL} + \Delta S^{\neq 2}_{StdSol} + \Delta S^{\neq 3}_{VL-VF})_{TS} - (\Delta S^1_{V1-VL} + \Delta S^2_{StdSol} + \Delta S^3_{VL-VF})_{RC} \qquad (2.47)$$

$$\Delta\Delta S_{Sol} = \Delta S^{\neq 2}_{StdSol} - \Delta S^2_{StdSol} = \alpha\big((S^{\neq o} + \Delta S^{\neq 1}_{V1-VL}) - (S^o + \Delta S^1_{V1-VL})\big) \qquad (2.48)$$

$$\boldsymbol{\Delta\Delta S_{Sol} = \alpha(S^{\neq o} - S^o)} \qquad (2.49)$$

Finally, the entropic contribution of solvation would result in a change in free energy that can be obtained for a given temperature in a given solvent (and corresponding $\boldsymbol{\alpha}$) from the absolute standard entropies of the active intermediary and the reaction complex by equation 2.50.

$$\Delta\Delta \boldsymbol{G_{Sol}} = \boldsymbol{\alpha T}(\boldsymbol{S^{\neq o}} - \boldsymbol{S^{o}}) \qquad (2.50)$$

## 2.10 Zero Point Correction

All DFT structural optimizations are based on the electronic structure (i.e. electronic energy) solely. However, a better thermochemical description of a reaction requires a vibrational component for entropy and enthalpy corrections, which allows one to calculate the free energy, and with this, reaction barriers and thermodynamics that can be compared to experimental values, as well as other properties, such as Kinetic Isotope Effects (KIE) or infrared (IR) spectra (Ochterski, 1999). Herein, Gaussian 09 (see references) is employed as in the inbuilt methods. Entropy (S) and heat capacity (*Cv*) are calculated from the ideal gas partition functions from the calculated vibrations and also includes the corrections from translations, rotations, and, in high spin systems, electronic motion, which is set to 0 for closed-shell systems (Ochterski, 2000). The vibrational analysis is performed by Gaussian parting from the Hessian matrix, which represents the set of second partial derivatives of the potential V (in whatever level of theory), with respect to the displacement of the atoms (Ochterski, 1999).

## 2.11 Dispersion Effects

One of the main problems with the generally used DFT functionals is that they fail to include the weak non-bonding interactions, called van der Waals, or dispersion interactions of the chemical systems. These forces are regarded as electron correlations that are normally not well described by typical DFT functionals such as B3LYP or PBE. The London dispersion effects are present on all systems, inter and intra-molecularly, however the effects are more relevant the larger the system is, and between such systems. With the obvious difficulty of calculating full electron correlation, semi-empirical dispersion corrections were developed to improve DFT methodologies. These are generally regarded as DFT-D (or DFT-D3, etc., depending on the model used), and are mostly based on an atom to atom interaction (atom pairs) approach (Grimme, 2011) as presented in equation 2.51.

$$E_{disp}^{DFT-D} = -\sum_{AB}\sum_{n=6,8,10,\dots} s_n \frac{C_n^{AB}}{R_{AB}^n} f_{damp}(R_{AB}) \qquad (2.51)$$

The terms A and B represent any pair of atoms in the system, R represents the interatomic distance, $C_n$ is a dispersion coefficient, $s_n$ is a scaling factor, and $f_{damp}$ is a damping function that avoids asymptotic effects of the dispersion energy, as well as double counting, as it instead approaches zero when R approaches 0. The empirical coefficients are calculated from first principles in modern dispersion corrections used in Grimme methods (most commonly used), and are atom pairwise specific (Grimme, 2011).

## 2.12 Molecular Mechanics and Dynamics

Molecular mechanics (MM) methods rely on classical models where the potential energy of the system is parameterized through different factors such as electrostatic potential, bond stretching potential, angle bending potential, dihedral torsion potential and non-bonding Van der Waals interactions that depend solely on the coordinates of the system, and are set thorough a collection of parameters that describe the weight and form (equations and constants). This collection of parameters is called the force field, and numerous examples exist, such as CHARMM (Brooks et.al., 1982) and AMBER (Cornell et.al., 1995). The CHARMM force field, used later herein, employs the potentials defined by equations 2.52 for the bonding potential, 2.53 for the angle potential, 2.54 for the dihedral angle potential, and 2.55 for improper torsions.

$$E_B = \sum k_b \, (r - r_0)^2 \qquad (2.52)$$

$$E_\theta = \sum k_\theta \, (\theta - \theta_0)^2 \qquad (2.53)$$

$$E_\emptyset = \sum |k_\emptyset| - k_\emptyset \cos(n\emptyset) \qquad (2.54)$$

$$E_w = \sum k_w \, (w - w_0)^2 \qquad (2.55)$$

The elements $r_0, \theta_0$, and $w_0$ represent geometric constants related to equilibrium positions at which energy is at a minimum, and $k_b$,$k_\theta$, $k_\emptyset$, $k_w$ represent force constants. All these parameters are required *a priori*, and can be obtained from different sources such as vibrational data, crystal structures, or other kind of sources and calculations. The elements $r$, $\theta$, and $w$ represent the geometric variables as a function of the coordinates at any given moment. Non-bonding interactions such as vdW and electrostatic potentials are also computed through the $r^6$ and $r^{12}$ forces and Coulomb relations respectively, and some other interactions are also possible such as hydrogen bonding interactions (Brooks et.al., 1982).

Molecular Dynamics (MD) has a special relevance in drug discovery, especially by complementing the structure based drug design methodologies, where perhaps the most relevant observable is the drug-target (e.g. drug – protein) binding affinity energy and the equilibrium constant associated with it. By effectively predicting the binding affinity one may for example improve virtual ligand screening techniques with a hybrid approach where post virtual screening ligands are subjected to MD analyses to further filter and improve experimental ligand hit rates. These binding affinities can be defined from equilibrium between target and ligand (see equation 2.56), where there exists and equilibrium defined by constant $K_a$ in equation 2.57 (De Vivo et. al. 2016).

$$t + l \leftrightarrow tl \tag{2.56}$$

$$K_a = \frac{[tl]_{eq}}{[t]_{eq}[l]_{eq}} \tag{2.57}$$

With this equilibrium interaction, there is an associated Gibbs free energy. However, for any polyatomic system, due to the large numbers of degrees of freedom, one is subject to a numerous collection of microstates that are plausible in the canonical ensemble as according to Boltzmann distribution. Therefore, on unbiased molecular mechanics, for a limited number of samples, the free Gibbs energy may be expressed as a probability function from the observed samples (see equation 2.58) (De Vivo et. al. 2016).

$$\Delta G^o = -k_B ln\left(\frac{p_{bound}}{p_{unbound}}\right) \tag{2.58}$$

Given that one must sample almost infinitely to account for all possible microstates to accurately and completely predict the energy with this approach, in theory one may require an infinitely long molecular dynamics simulation to retrieve such information. However, sacrificing some accuracy one can run a simulation for a practical amount of time and gather enough data for predicting a reliable energy. For a weak interaction a small sampling may be accurate enough and very practical with this unbiased approach. However, for stronger interactions, other schemes have been developed to overcome the limitations of Boltzmann statistics and accurately predict binding affinities with lower computational resources (De Vivo et. al. 2016).

## 2.13 QM/MM Method General Theory

As the name suggests, QM/MM are methods that combine the accuracy of quantum mechanics calculations with the advantage of the relatively low computational cost of molecular mechanics. This combined approach is practical because MM methods alone are incapable of modelling electronic structure such as bond formation and breaking, charge transfer or excited states. However, Quantum Mechanics methods are very expensive computationally, and one can only model relatively small systems under this scheme. However, a solvated enzymatic system, which is the main concern herein, may contain tens of thousands of atoms (Lin and Truhlar, 2006).

In the QM/MM method one defines QM and MM regions, specifying which atoms are to be calculated within the QM region (those where electronic structure is expected to change the most, e.g. where reaction takes place) while the rest of the atoms are treated with the simpler MM approach. The total energy of the system can be calculated by equations 2.59 and 2.60, where $E_{QM}$ stands for the energy of the QM region, $E_{MM}$ stands for the energy of the MM region, and $E_{QM/MM}$ stands for the coupling interaction of both regions. Within the coupling energy $E_{QM/MM}$ defined by equation 2.60, $E_Q$ refers to the electrostatic interaction, $E_{vdW}$ to van der Waals forces, and $E_{FF}$ to force field contributions at the boundary region (Lin and Truhlar, 2006; Kästner et.al. 2007).

$$E_{Tot} = E_{QM} + E_{MM} + E_{QM/MM} \qquad (2.59)$$

$$E_{QM/MM} = E_Q + E_{vdW} + E_{FF} \qquad (2.60)$$

A main aspect of concern in QM/MM theory is the coupling between the QM and MM regions, which depending on the treatment that is given, is regarded as through mechanical embedding or electrostatic embedding. The treatment in the boundary region deals mainly with electrostatic interactions between the regions (polarization interactions) and bonding interactions where the boundary cuts through bonded regions, which is often necessary, especially when dealing with enzymes (Lin and Truhlar, 2006; Senn and Thiel, 2007).

The mechanical embedding approach deals with the coupling region with a molecular mechanics level (bonding and nonbonding potentials), which therefore requires the appropriate parameters at the boundary region. The electrostatic embedding deals with the region by incorporating some “one electron” terms into the QM Hamiltonian and allowing the MM point charges to polarize the QM region. This may be done by the aid of a link atom (i.e. hydrogen) resembling the properties of the original bonding interaction or by the introduction of local orbitals, which provide a QM representation of the charge distribution. The local orbitals method is regarded as more accurate, however more complicated, than the link atom method (Lin and Truhlar, 2006; Senn and Thiel, 2007). Herein, we employ the approach of hydrogen link atoms and electrostatic embedding for all QM/MM calculations presented onward.

Also a concern is the optimization algorithm that deals with both regions, MM and QM. Both regions are optimized independently and different schemes are employed, with the microiterative adiabatic treatment being very popular. In this scheme, the internal QM region is not re-optimized during each step of the MM region optimization, but instead approximated by a point charge interaction energy. This interaction is kept constant until full convergence of the MM region. Then the QM region is optimized again until convergence. The cycle repeats until full convergence is obtained on both regions (Kästner et.al. 2007).

## 2.14 The QM/MM Methodology for Enzymatic Catalysis

Using QM/MM methods to study complete proteins is, unlike the common methods used for DFT models where only atom coordinates and atomic numbers are required in principle, not a straight forward approach. Special attention must be given to the preparation of the system for the later set of QM/MM calculations. The overall process employed by our group is presented in a flow diagram depicted in Figure 2.4 (Quesne et.al. 2016).

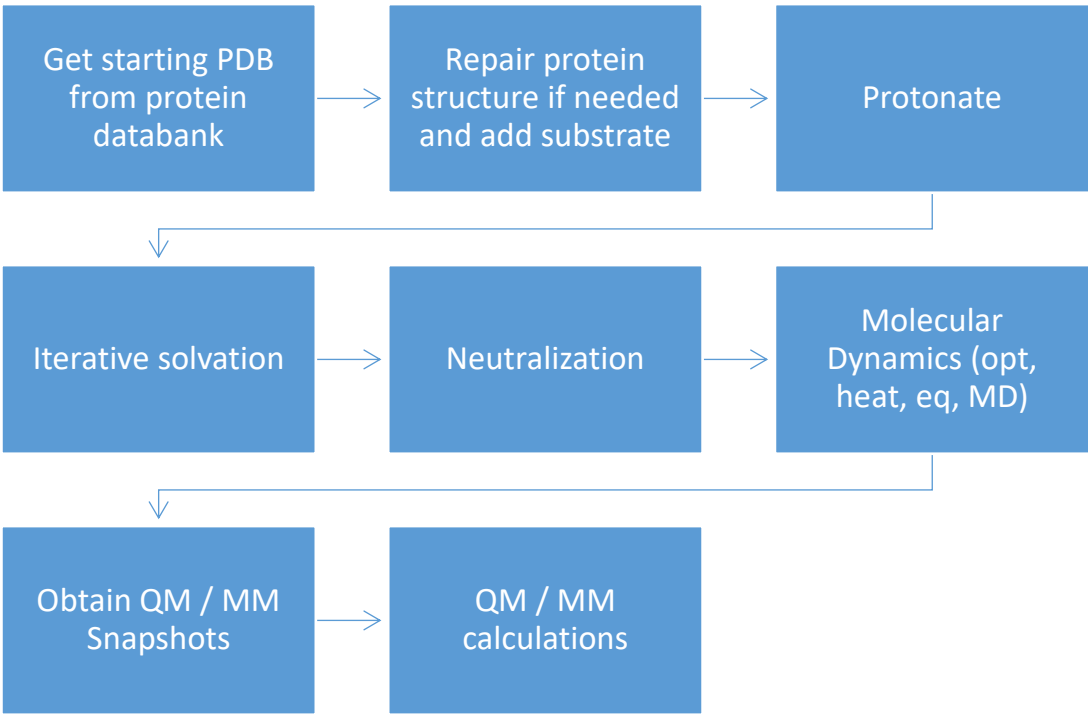


**Figure 2.4**: General Flowchart of the QM/MM Methodology.

The selection of a proper starting PDB structure for the protein of interest is not arbitrary. Special attention should be paid on the resolution of the crystal, the completeness of the structure's heavy atoms, and whether it is bound to a substrate. The protein structure often has conformational changes when bound to a substrate as compared to a free protein, and the presence of another substrate in the crystal may help to better find the right place of a new substrate (Quesne et.al. 2016).

For some proteins, although several crystal structures exist, none are complete, and the selected crystal structure should repaired, especially if the broken loops or helices are close to the reactive site or may have a structural or functional impact (Quesne et.al. 2016). Several web servers exist to generate and to model and repair the missing loops by homologous polypeptide strands from a database such as FREAD (Choi et. al. 2009). For instance, ModLoop (Fisser et.al. 2003) is a web server that models and incorporates the elsewhere generated loop strands into the protein's gap.

The substrate's position is of significant relevance for QM/MM calculations. The positioning or docking of the substrate may be done manually (with some qualitative references) or by the aid of docking methodologies, such as Swissdock (Grosdidier et.al. 2011) or AutoDock (Morris et.al. 2009), where energetically favourable substrate docking positions are produced. The user then may choose one or many convenient conformations where the substrate is in position to be activated or exert its chemical function.

Water molecules can have a very important role in the model. Thus, for a model with explicit solvent molecules, one must make sure that the molecules enter the internal cavities where they might have an impact. A common approach, and the one used herein, is an iterative solvation – equilibration method where one places the water molecules from a spherical/cubic outer shell and runs a small optimization followed by an equilibration phase to allow the added molecules to reach relevant cavities (See Fig 2.5). The new spaces created will be filled in the next solvation iteration, and after several of these steps, the number of new added water molecules should greatly decrease until a desired threshold is reached. (Quesne et.al. 2016).

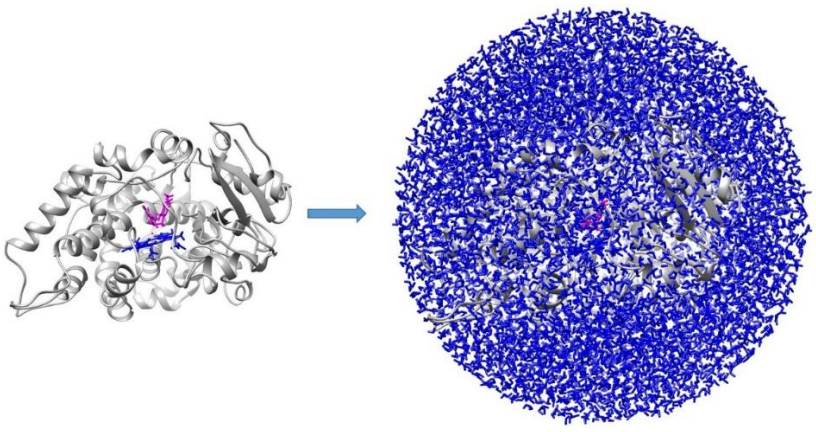

**Figure 2.5:** Solvation of P450-3A4-4D6Z system (with Docked R-Omeprazole).

Prior to molecular dynamics, the overall charge of the system is neutralized by the random addition of chlorine or magnesium ions. Then one can start the molecular dynamics, which encompasses the processes of optimization, heating (stepwise increase in velocities), equilibration (reaching an average state) and then running the free dynamics simulation of the system's motion. This allows the production of more realistic conformations of the system in order to obtain snapshots (coordinates) of the system at diverse time frames. These snapshots are thus a fairly representative sample of the ensemble. From these snapshots, the QM/MM calculations begin, where according to the previously presented theory, one defines the QM region to further calculate the desired results such as Transition States or high accuracy optimizations (Quesne et.al. 2016).

# Chapter Three

## PROJECT 1

# *Substrate Sulfoxidation by an Iron(IV)-Oxo Complex: Benchmarking Computationally Calculated Barrier Heights to Experiment.*

*Fabián G. Cantú Reinhard,[‡] Abayomi S. Faponle,[‡] and Sam P. de Visser*[*,‡]*

[‡] Manchester Institute of Biotechnology and School of Chemical Engineering and Analytical Science, The University of Manchester, 131 Princess Street, Manchester M1 7DN, United Kingdom

**Abstract.**

*High-valent metal-oxo oxidants are common reactive species in synthetic catalysts as well as heme and nonheme iron enzymes. In general, they efficiently react with substrates through oxygen atom transfer and for a number of cases experimental rate constants have been determined. However, since these rate constants are generally measured in a polar solution, it has been found difficult to find computational methodologies to reproduce experimental trends and reactivities. In this work we present a detailed computational study into para-substituted thioanisole sulfoxidation by a nonheme iron(IV)-oxo complex. A range of density functional theory methods and basis sets has been tested for their suitability to describe the reaction mechanism and compared with experimentally obtained free energies. It is found that the enthalpy of activation is reproduced well, but all methods overestimate the entropy of activation by about 50%, for which we recommend a correction factor. The effect of solvent and dispersion on the barrier heights is explored both at the single point level but also through inclusion in geometry optimizations and particularly solvent is seen as highly beneficial to reproduce experimental free energies of activation. Interestingly, in general experimental trends and Hammett plots are reproduced well with almost all methods and procedures and only a systematic error seems to apply for these chemical systems. Very good agreement between experiment and theory is found for a number of different methods, including B3LYP and PBE0, and procedures that are highlighted in the paper.*

**Published Reference:**

Cantu-Reinhard, F.G. Faponle. A.S. De Visser, S.P. 2016. Substrate Sulfoxidation by an Iron(IV)-Oxo Complex: Benchmarking Computationally Calculated Barrier Heights to Experiment. *J. Phys. Chem.* 120, 9805 – 9814.

## 3.1 Introduction.

Nonheme iron dioxygenases are versatile oxidants with a large range of biochemical functions vital for human health (Solomon et.al. 2000; Bugg, 2001; Ryle et.al. 2002; Costas et.al. 2004; Abu-Omar et.al. 2005). These functions range from catalyzing DNA repair mechanisms by, for instance, the AlkB repair enzymes (Trewick et.al. 2002; Falnes et.al. 2002; O'Brien et.al. 2006; Yi et.al. 2009), but also the detoxification of cysteine by cysteine dioxygenase (Stipanuk, 2004; Straganz et.al. 2006; Joseph et.al. 2007). Most nonheme iron dioxygenases bind the metal in a specific coordination motif and a common one in biology is the facial 2-His/1-Asp motif that links the iron atom to the protein, thereby leaving three iron ligand sites available for molecular oxygen and (co)-substrate (Que, 2000; Kovaleva et.al., 2008). Often nonheme iron dioxygenases utilize α-ketoglutarate as a co-substrate, which in a reaction with molecular oxygen gives succinate and an iron(IV)-oxo species, which is the active species of the enzyme. The latter is known to be a highly potent oxidant and often reacts with substrates through substrate hydroxylation (Meunier et.al. 2004; de Visser et.al. 2011).

To understand catalytic reaction mechanisms of nonheme iron dioxygenases, synthetic model complexes have been developed, so-called biomimetic models that have the structural features of the enzyme active site but lack the protein (Costas et.al. 2011; Bruijnincx et.al. 2008; Kryatov et.al. 2005; McDonald et.al. 2013; Nam et.al. 2014). These oxidants react in a solution phase, usually water or acetonitrile, and as such have more relevance to Industrial applications. Computational modelling, and particularly, density functional theory methods often struggle with the description of reaction processes and rate constants due to the fact that transition metal centers often have close-lying spin states (de Visser et.al. 2014; Ghosh et.al. 2003; Güell et.al. 2008). Nonheme iron(IV)-oxo complexes, specifically, have close-lying triplet and quintet spin states, whereby the ordering and relative energies are dependent on the metal-ligand system as well as environmental perturbations (Jackson et.al. 2008; Ye et.al. 2013; de Visser et.al. 2013; Tse et.al. 2014; Biswas et.al. 2015).

As the experiments often are reported in highly polar solvents, i.e. acetonitrile, methanol or water, this leads to difficulties to appropriately model these systems with, e.g., density functional theory (DFT) methods. On top of that often the entropy taken from a quantum chemical calculation is taken from gas-phase (Ideal Gas) situations and can be strongly overestimated (Cooper, 2002; Postils et.al. 2015). In order to find out how well density functional methods can reproduce experimental rate constants, we decided to do a thorough computational study into a well-characterized and studied system for which experimental rate constants and reaction conditions are known. Sastri et.al. (2005) investigated the para-Y-substituted thioanisole (Y = H, $CH_3$, Cl, $OCH_3$) sulfoxidation by $[Fe^{IV}(O)(N4Py)]^{2+}$ with N4Py = *N*,*N*-bis(2-pyridylmethyl)-*N*-bis(2-pyridyl)methylamine in water, Scheme 3.1. In particular, they measured temperature-dependent rate constants and established activation enthalpies and activation entropies for the reactions. They showed that the rate constants follow a typical Hammett plot, where the logarithm of the second-order rate constant ($k_2$) correlates linearly with the $\sigma_P$ Hammett parameter.

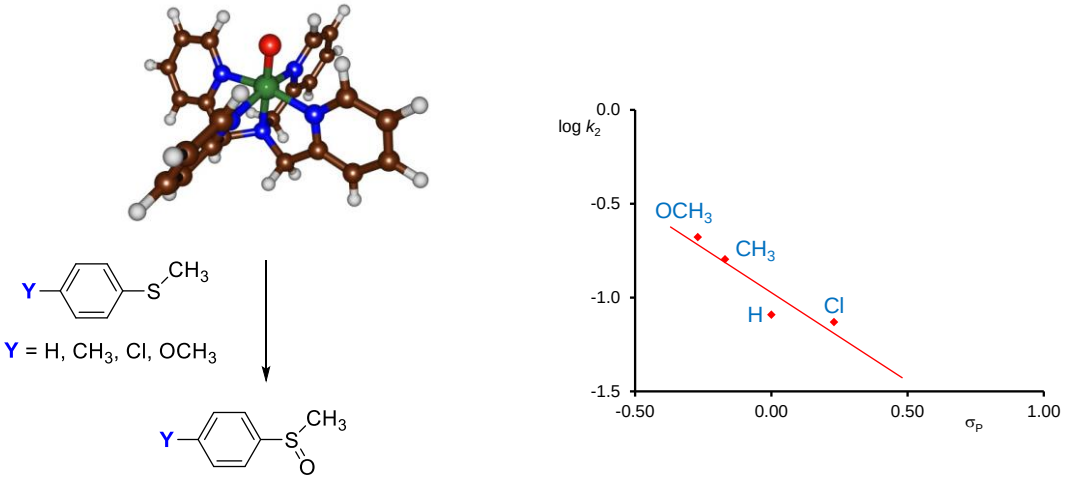


**Scheme 3.1.** Compounds and substrates investigated in this work and experimental Hammett plot with second-order rate constants from Sastri et.al. 2005.

In this work, we report a detailed computational study on the thioanisole sulfoxidation by $[Fe^{IV}(O)(N4Py)]^{2+}$ using a range of computational models, basis sets and solvent models. In general, all computational models predict the experimental reactivity trends and find a linear correlation with the $\sigma_P$ Hammett parameter. However, strong differences in absolute values of the enthalpy of activation are found depending on the use of solvent, dispersion and entropy corrections.

### 3.2 Methods.

Calculations presented in this work utilize a combination of density functional theory (DFT) methods as implemented in the Gaussian-09 software package (Frisch et.al. 2009). Our initial work focused on the properties of $[Fe^{IV}(O)(N4Py)]^{2+}$, **1**, and subsequent work investigated the mechanism and activation energy for the sulfoxidation of para-Y-substituted thioanisoles (Y = H, $CH_3$, Cl, $OCH_3$), see Scheme 3.1. We ran geometry optimizations (without constraints) for reactants and products and characterized the sulfoxidation transition states with a range of methods and procedures. All structures were confirmed as local minima or first-order saddle points through an analytical frequency calculation. The unrestricted approach was used in all chemical systems investigated here.

In a first set of calculations, we did a gas-phase geometry optimization and subsequently carried out single point calculations with a dielectric constant of $\varepsilon$ = 78.3553 mimicking water included using either the Polarized Continuum Model (PCM) (Tomasi et.al. 2005) or the Universal Solvation Model SMD (Marenich et.al. 2009). Subsequently, we ran full geometry optimizations of all structures with the PCM model included at the B3LYP, B3LYP-D3, (Becke, 1993; Lee et.al. 1988, Grimme, 2006), BP86 (Becke, 1988; Perdew 1986), PBE0 (Adamo et.al. 1999), level of theory and did SMD calculations with B3LYP. In addition, single point energy calculations on the gas-phase and PCM optimized structures obtained at B3LYP and B3LYP-D3 were performed with various density functional methods: namely, B3LYP, B3LYP-D3 BP86, PBE0, M06 (Zhao et.al. 2008), B97 (Becke, 1997), BMK (Schmider, 1998), B2PLYP(Grimme, 2006), and mPW2PLYP (Schwabe et.al., 2006).

The initial calculations utilized the Los Alamos-type double-$\zeta$ quality LANL2DZ basis set (with electron core potential, ECP) on iron and 6-31G* on the rest of the atoms (basis set BS1) (Hay et.al., 1985). To improve the energetics single point calculations with an enlarged basis set were performed, namely the LANL2DZ+ECP basis set on iron and 6-311+G** on the rest of the atoms (basis set BS2) and LACV3P+ (with ECP) on iron and 6-311+G* on the rest of the atoms (basis set BS3). To test the effect of the basis set on the obtained structures, we ran a full geometry optimization at the B3LYP/BS2, B3LYP-D3/BS2, B3LYP/BS3 and B3LYP-D3/BS3

levels of theory, which investigated the effect of basis set and dispersion on the structure and energetics along the reaction mechanism.

Free energies reported contain electronic energies, zero-point and thermal corrections as well as entropy at T = 283K, i.e, the temperature of the experimental work described by Sastri et.al. 2005. As gas-phase DFT models generally overestimate the entropy contribution with respect to solvation, it has been suggested to empirically reduce the translational and rotational components of the entropy (Harvey, J. 2010), and in this paper we use the Wertz model (Wertz, D. 1980). The gas-phase (Ideal gas obtained) entropy (S°) was taken from the frequency calculations and scaled according to Wertz's method to obtain the solvent corrected free energy at standard conditions ($\Delta G_{Wertz}^{\ddagger}$), using Eq 1 (Cooper and Ziegler, 2002; Wertz, D. 1980):

$$\Delta G_{Wertz}^{\ddagger} = \Delta G_{DFT}^{\ddagger} + (1 - 0.46)(T)(S_{TS}° - S_{RC}°) \quad (1)$$

### 3.3 Results and Discussion.

Substrate sulfoxidation by iron(IV)-oxo complexes has been extensively studied previously (Kumar, et.al. 2011; Kumar et.al. 2014; Sharma et.al. 2003, Kumar et.al. 2005; Aluri et.al. 2007), and follows a concerted reaction mechanism, whereby the sulfur atom of the substrate attacks the oxygen atom of the iron(IV)-oxo group. The reaction starts from a reaction complex (**RC**) corresponding to $[Fe^{IV}(O)(N4Py)]^{2+}$ and substrate. The group spin densities and charges show that no electron transfer has taken place in the **RC** structures and all are characterized as an iron(IV)-oxo with nearby substrate. Along the reaction coordinate a transition state ($\mathbf{TS}_{SO}$) is passed on the way to the sulfoxide product complex ($\mathbf{P}_{SO}$). We calculated the sulfoxidation reaction for para-Y-substituted thioanisoles with Y = H, $CH_3$, Cl and $OCH_3$, whereby we give the substituent of Y in the subscript label of each of the structures.

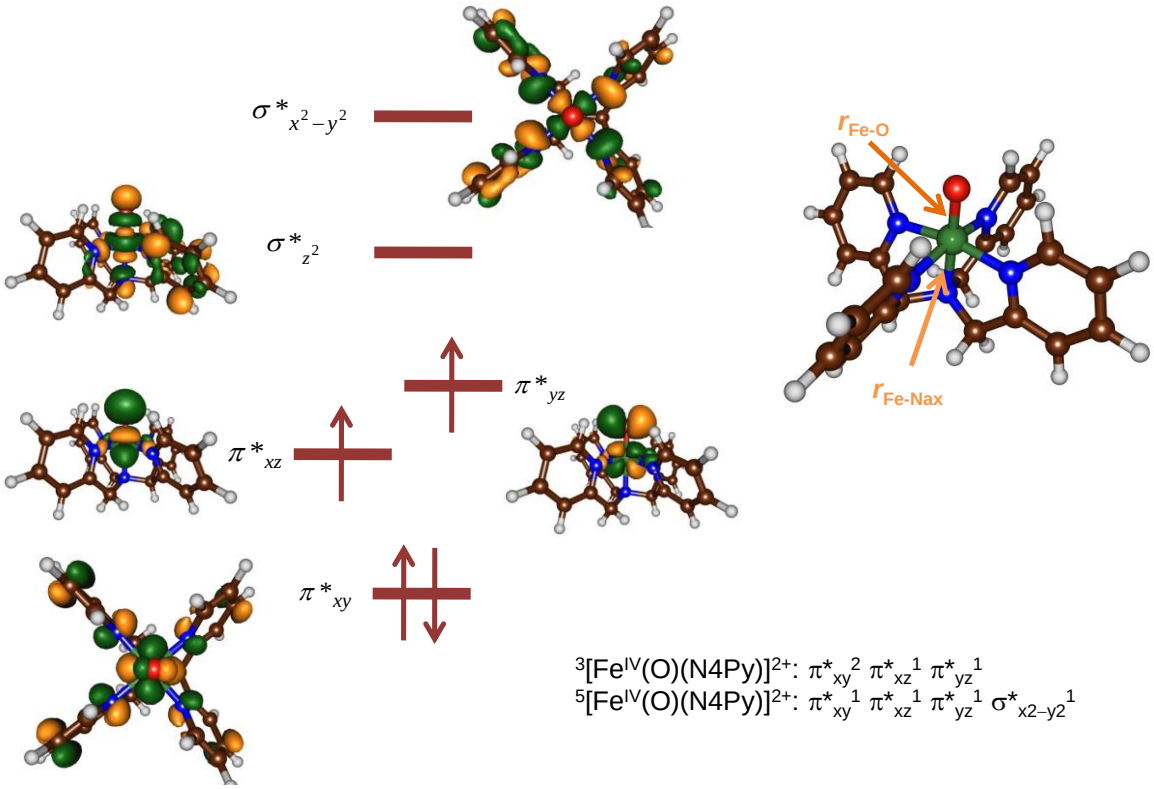


**Figure 3.1.** Relevant valence orbitals of $[Fe^{IV}(O)(N4Py)]^{2+}$ and orbital occupation in the triplet and quintet spin states. Also given are the definitions of the bond lengths $r_{Fe\text{-}O}$ and $r_{Fe\text{-}Nax}$.

Before discussing the reaction mechanism, let us go into the details of the reactant structure and the low lying spin states. Figure 3.1 displays high-lying occupied and molecular orbitals of $[Fe^{IV}(O)(N4Py)]^{2+}$ and the corresponding orbital occupation in the triplet and quintet spin states. Thus, the reactant has high-lying metal-based orbitals for the interactions of the 3d(Fe) orbitals with its ligands. There are three π*-type orbitals ($\pi^*_{xy}$, $\pi^*_{xz}$, $\pi^*_{yz}$), one is in the plane of the four nitrogen atoms of N4Py ($\pi^*_{xy}$), whereas the other two ($\pi^*_{xz}$ and $\pi^*_{yz}$) represent the antibonding interactions of the 3d(Fe) and 2p(O) atoms. In the triplet spin state these orbitals are occupied with four electrons to give a configuration $\pi^*_{xy}{}^2\ \pi^*_{xz}{}^1\ \pi^*_{yz}{}^1$. In the quintet spin state, one of the $\pi^*_{xy}$ electrons is promoted to the $\sigma^*_{x2-y2}$ orbital that reflects the antibonding interactions of the metal with the pyrrole nitrogen atoms. Higher lying and virtual is the σ* antibonding interaction of $3d_{z2}$(Fe) with a 2p orbital on oxygen and the 2p of the axial nitrogen atom. Experimental electron paramagnetic resonance studies established a triplet spin ground state for $[Fe^{IV}(O)(N4Py)]^{2+}$ (Kaizer et.al., 2004), therefore we will continue our work and focus on triplet spin reactivity only. Thus, we

investigated the sulfoxidation of para-Y substituted thioanisoles (Z = $OCH_3$, $CH_3$, H and Cl) and compare the mechanisms, reactivity trends and free energies of activation to the experimental data.

Similarly to previous studies on substrate sulfoxidation (Kumar, et.al. 2011; Kumar et.al. 2014; Sharma et.al. 2003, Kumar et.al. 2005; Aluri et.al. 2007), the reaction is concerted via a single transition state leading to products. Optimized geometries of the transition states for Y = H obtained with a range of methods and procedures are given in Figure 3.2. We initially did a gas phase geometry optimization at B3LYP/BS1 level of theory and optimizations with a solvent model included with a modest double-ζ quality basis set (BS1). With B3LYP/BS1 we did the optimizations in the gas-phase as well as with the PCM and SMD solvent models included. In addition, we tested a variety of alternative density functional methods with basis set BS1 and the PCM solvent model, namely B3LYP-D3, BP86 and PBE0. Thereafter, we investigated the effect of the basis set and improved the basis set to BS2 for the B3LYP and B3LYP-D3 calculations that includes diffuse functions and an extra Gaussian contraction function to the non-iron atoms. Finally, at B3LYP and B3LYP-D3 level of theory also calculations were done with a triple-ζ basis set on iron, i.e. BS3.

Figure 3.2 shows results of the geometry optimizations done for the sulfoxidation mechanism for Y = H as obtained with ten different methods and procedures. The same set of methods were also used for Y = $OCH_3$, $CH_3$ and Cl, but the general trends that we obtain is the same as for the data in Figure 3.2 on Y = H, see Supporting Information Tables S1 and S2. As can be seen, in general only minor differences in optimized geometries are observed. With exception of the BP86 result, all structures give an Fe–O distance ranging from 1.69 – 1.74Å, while the O–S separation is 1.98 – 2.10Å. Thus, addition of a PCM solvent model shortens the Fe–O and elongates the O–S distances, whereas the reverse effect is seen with the SMD solvent model. Dispersion corrections, by contrast, appear to have the reverse effect from solvent corrections on the optimized geometries and in addition raises the value of the imaginary frequency. No dramatic changes are seen in the optimized geometries calculated with alternative DFT methods. Group spin densities and charges (see Supporting Information Table S3) give similar results along the structures investigated here and do not show major variations. We also calculated the mechanism of

sulfoxidation of para-Y substituted thioanisoles with Y = $OCH_3$, $CH_3$ and Cl with $[Fe^{IV}(O)(N4Py)]^{2+}$ using the same methods and techniques as those displayed in Figure 3.2. However, in all cases the trends are the same and the same geometric features are found, see Supporting Information.

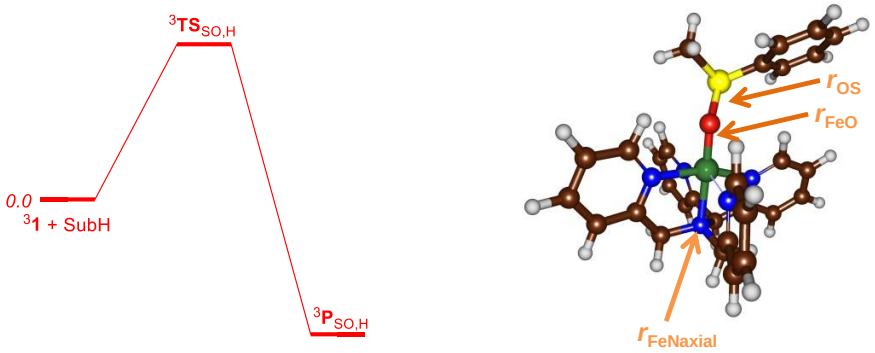


| Method | $r_{FeO}$ | $r_{OS}$ | $r_{FeNaxial}$ | Imag freq | $\Delta H^{\ddagger}$ | $\Delta S^{\ddagger}$ |
|---|---|---|---|---|---|---|
| B3LYP/BS1 | 1.702 | 2.079 | 2.124 | i352 | 0.5 | -29.9 |
| B3LYP/BS1+PCM | 1.694 | 2.104 | 2.121 | i284 | 16.7 | -31.4 |
| B3LYP/BS1+SMD | 1.712 | 2.066 | 2.099 | i433 | 17.8 | -31.0 |
| B3LYP-D3/BS1+PCM | 1.709 | 2.012 | 2.097 | i577 | 5.3 | -37.5 |
| BP86/BS1+PCM | 1.817 | 1.892 | 2.181 | i495 | 21.5 | -35.5 |
| PBE0/BS1+PCM | 1.690 | 2.043 | 2.087 | i423 | 12.4 | -31.0 |
| B3LYP/BS2+PCM | 1.717 | 2.069 | 2.115 | I424 | 16.3 | -30.2 |
| B3LYP-D3/BS2+PCM | 1.725 | 2.013 | 2.100 | i582 | 5.9 | -36.2 |
| B3LYP/BS3+PCM | 1.723 | 2.060 | 2.129 | I391 | 20.4 | -37.6 |
| B3LYP-D3/BS3+PCM | 1.739 | 1.978 | 2.099 | i680 | 9.1 | -36.0 |
| **Experimental** | | | | | **12.4** | **-19.2** |

**Figure 3.2.** DFT calculated transition states for the reaction of $[Fe^{IV}(O)(N4Py)]^{2+}$ ($^3$**1**) with para-H thioanisole (SubH). Bond lengths are in angstroms and the value of the imaginary frequency in wave numbers. Enthalpy ($\Delta H^{\ddagger}$) and entropy ($\Delta S^{\ddagger}$) of activation are reported in kcal $mol^{-1}$ and cal $mol^{-1}$ $K^{-1}$ respectively, relative to isolated reactants.

Inclusion of diffuse basis functions to the basis set and an extra set of Gaussian contractions on atoms except iron, i.e. as done in basis set BS2, has very little effect on optimized geometries and relative energies. It appears that diffuse basis functions on non-iron atoms are not essential to describe the structure and energetics of the transition states. Surprisingly, a triple-ζ basis set on iron (as in basis set BS3) gives little changes to the geometries but relative enthalpies shift by less than 1 kcal $mol^{-1}$ (Figure 3.2). Nevertheless, the same trends are observed.

These results implicate that a single point calculation with a larger basis set on a double-ζ optimized geometry will give only small changes in relative energies of potential energy surfaces.

Surprisingly, there are structurally no dramatic differences between gas-phase optimized and structures optimized with a solvent model included. In particular, the Fe–O bond length in the transition state ranges from 1.690Å (obtained at PBE0/BS1+PCM level of theory) to 1.716Å (obtained at BP86/BS1+PCM level of theory). The O–S bond formation in the transition state is found at a distance ranging from 1.978 to 2.104Å and refers to B3LYP-D3/BS3+PCM and B3LYP/BS1+PCM, respectively. Therefore, some geometric variation between the various optimization techniques is obtained as expected from pure versus hybrid density functional methods. However, as can be seen from the final columns in Figure 3.2, the different methods give dramatically different enthalpies of activation.

Using transition state theory the experimental second order rate constant for para-H thioanisole sulfoxidation by $[Fe^{IV}(O)(N4Py)]^{2+}$ is estimated to be $\Delta G^{\ddagger}$ = 17.96 kcal $mol^{-1}$ at 283K, while the corresponding Eyring plot splits this into an enthalpy and entropy of activation of $\Delta H^{\ddagger}$ = 12.4 kcal $mol^{-1}$ and $\Delta S^{\ddagger}$ = –19.2 cal $mol^{-1}$ $K^{-1}$. The method that closest approaches the experimental enthalpy of activation is the $\Delta H^{\ddagger}$ value obtained after a PBE0/BS1+PCM optimization (12.4 kcal $mol^{-1}$). Also in reasonable agreement with experiment is the $\Delta H^{\ddagger}$ value calculated at B3LYP/BS1+PCM (16.7 kcal $mol^{-1}$). All other methods either strongly underestimate the free energy of activation (B3LYP in the gas phase and B3LYP-D3/BS1+PCM) or highly overestimate it (BP86/BS1+PCM). Indeed, as also found previously (Castro et.al. 2015), solvent effects raise gas-phase barriers dramatically, whereas dispersion corrections generally lower them in energy.

Interestingly, all methods overestimate the entropy of activation strongly and give a deviation from experiment by more than 50%. It has been hypothesized previously that computational modelling overestimates entropies, and, in particular rotational and vibrational entropy due to solvent layers around a structure that prevent it from rotating well (Harvey, 2010; Wertz, [1080). In particular, Wertz has suggested to scale computational entropy with Eq 1. Indeed, when we apply the Wertz correction to the

entropy, the calculated values of the free energy of activation are considerably improved and approach the experimental data better. As such, the Wertz correction to the entropy is recommended, and, therefore, we will only discuss Wertz corrected free energies of activation in the following.

As the optimization method appears to affect the structure little, we decided to do a series of single point calculations on the gas-phase and solvent optimized structures to see if that would have a major impact on the obtained relative energies. Figure 3.3 displays calculated free energies of activation for the reaction of $[Fe^{IV}(O)(N4Py)]^{2+}$ with para-H thioanisole in comparison to the experimental free energy of activation of Sastri et al (2005), as calculated with more than 40 different computational methods. The same set of methods were used for the sulfoxidation of para-Y-thioanisole (Y = $OCH_3$, $CH_3$ and Cl) with the iron(IV)-oxo oxidant, see Supporting Information. In particular, we did single point calculations using a range of different methods, models and basis sets on the structures described above.

Entry 1 – 12 in Figure 3.3 (bars in green on the left) refer to results obtained after a gas-phase geometry optimization (designated Vac B3LYP/BS1) and followed by single point calculations using a variety of methods in either the gas-phase or with a solvent model included. The set of data compares the gas-phase versus PCM and SMD solvent models as well as the effect of the basis set and dispersion corrections at the single point level of theory.

Entry 13 – 22 in Figure 3.3 (bars in blue), on the other hand, refer to geometries optimized with the PCM solvent model included and is followed by a solvent corrected single point calculation with another method, namely B3LYP-D3, M06, B97, BMK, B2PLYP and mPW2PLYP, or improved basis set (BS2 or BS3). These studies highlight some key features of the method, basis set and procedure that affect the free energy of activation and dissect the factors that influence the transition state geometry and consequently the barrier height. Entries 23 – 28 in Figure 3.3 (bars in gold) started from a B3LYP-D3/BS1 geometry optimization and test the effect of the basis set and the density functional method on the free energy of activation. Two geometry optimizations with basis set BS2 and basis set BS3 were done at the B3LYP and B3LYP-D3 level of theory (entry 29 – 32 in Figure 3.3). Finally, two pure density

functional methods were tested for geometry optimizations including PBE0 (entry 33 – 35) and BP86 (entry 36 – 39). The results obtained with the alternative solvent model (SMD) are grouped in entries 39 – 41 in Figure 3.3.

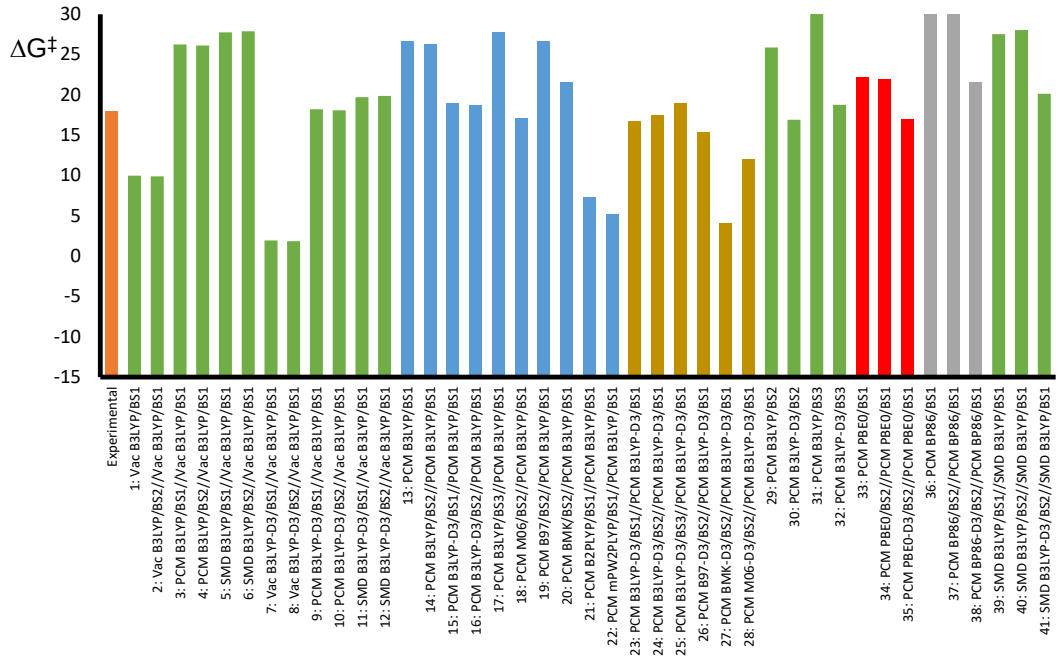


**Figure 3.3.** Free energy of activation (in kcal $mol^{-1}$) of DFT calculated para-H thioanisole sulfoxidation by $[Fe^{IV}(O)(N4Py)]^{2+}$ after a geometry optimization in vacuum (Vac) or with a PCM/SMD model included. Single point calculations with different methods, basis sets and/or solvent model were tested as well. For comparison the experimentally determined free energy of activation is given in orange on the left-hand-side.

Firstly, increasing the basis set from BS1 to BS2 on the same optimized geometry has a small effect on the obtained barrier height and in all cases where this was attempted an energy change by less than 0.5 kcal $mol^{-1}$ was found whether the optimization was done in the gas phase or with a solvent model included. Improving the basis set further to BS3 gives minor changes to the relative energies either. That is the case at single point energy level on a structure optimized with a double-ζ basis set or optimized with a larger basis set applied. Therefore, structurally and energetically little changes are observed when the basis set is increased from BS1 to either BS2 or BS3. In all cases, except the full geometry optimization B3LYP/BS3+PCM, we find barrier heights within 1 kcal $mol^{-1}$ with respect to that found after a B3LYP/BS1+PCM. Consequently, the basis set on non-transition metal atoms has little effect on the

relative energies and only increasing the basis set on iron to a triple-ζ quality basis set (LACV3P+) raises the free energy by maximally 4 kcal $mol^{-1}$.

Secondly, addition of dispersion corrections on a structure optimized without dispersion but the same method gives a lowering of the barrier by about 8 kcal $mol^{-1}$, whereas a solvent model, such as PCM, raises the gas phase barrier for that method by about 16 – 18 kcal $mol^{-1}$. These two components partially cancel each other out when applied together. This is in agreement with previous reports on DFT calculations on olefin polymerization, where solvent and dispersion corrections were found to cancel each other out (Aluri et.al. 2007).

Figure 3.4 shows the free energy of activation for the reaction of $^{3}$**1** with para-H thioanisole with entropy correction due to Wertz included for the same set of methods and procedures as described in Figure 3.3. Note that the Wertz entropy correction lowers the free energy of activation by about 5 kcal $mol^{-1}$. However, in three cases the addition of the Wertz entropy correction results in an unrealistic overall negative value for the free energy of activation, i.e. entries 7, 8 and 27. Two of these calculations refer to a dispersion corrected single point on a structure where no dispersion was included in the method. Hence these procedures are not suitable for the calculations of free energies of activation of oxygen atom transfer processes. With the Wertz correction applied, the best agreement with experiment is obtained at the PCM PBE0/BS2//PCM PBE0/BS1 level of theory with a deviation of less than 1 kcal $mol^{-1}$ from experiment (entry 33 and 34 in Figure 3.4), although a PCM B3LYP/BS2 optimization only overestimates the barrier by 3.3 kcal $mol^{-1}$. Methods that at the single point level of theory give free energies of activation within 3.5 kcal $mol^{-1}$ from experiment are SMD B3LYP-D3/BS1 or BS2//Vac B3LYP/BS1, PCM BMK/BS2//PCM B3LYP/BS1, PCM BP86-D3/BS2//PCM/BP86/BS1 and SMD B3LYP-D3/BS2//SMD B3LYP/BS1 (entries 11, 12, 20, 38 and 41). Interestingly, therefore, in these particular cases a gas-phase geometry optimization followed by solvent single point and improved basis set gives a free energy of activation at par with experiment, but probably for the wrong reasons, namely due to cancellation of errors.

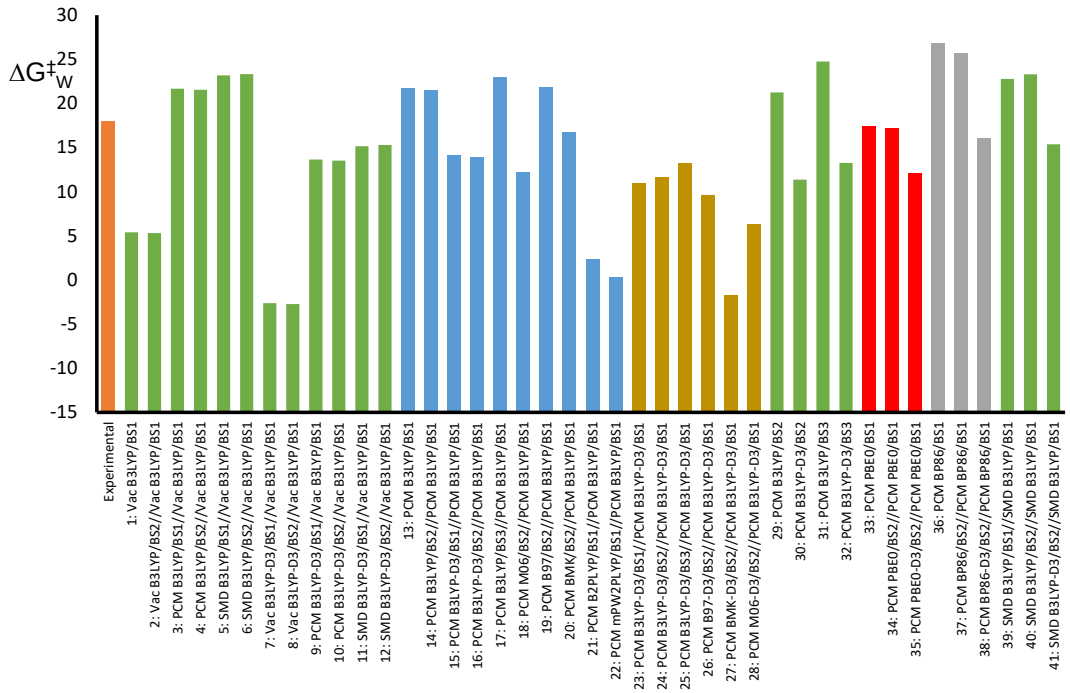


**Figure 3.4.** Free energy of activation with Wertz entropy correction (in kcal $mol^{-1}$) of DFT calculated para-H thioanisole sulfoxidation by $[Fe^{IV}(O)(N4Py)]^{2+}$ after a geometry optimization in vacuum (Vac) or with a PCM model included and the effect of single point calculations with different methods and basis sets. For comparison the experimentally determined free energy of activation is given in orange on the left-hand-side.

Subsequently, we calculated the thioanisole sulfoxidation by $^3$**1** with different para-Y substituted thioanisoles and investigated Y = H, $CH_3$, $OCH_3$ and Cl. This was again calculated with a range of different DFT methods and procedures and tested without (Supporting Information) and with the Wertz entropy correction. Due to space restrictions we will focus on the Wertz corrected free energies of activation. Figure 3.5 displays the free energies of activation of selected para-Y thioanisole sulfoxidation barriers by $^3$**1** as calculated with 25 different methods and procedures. All calculations presented in Figure 3.5 refer to a geometry optimization with the PCM model included using a specific density functional method. In several cases single point calculations with either an enlarged basis set or alternative density functional method was performed.

In general most calculations reproduce the experimental trends in $\Delta G^{\ddagger}_{W}$, which increases in value with substituent Y from $OCH_3 < CH_3 < H < Cl$. Consequently, this implies that even though the calculations may give a (large) systematic error, they reproduce experimental selectivities and product distributions and give the correct trends. Note that some of the differences in free energy of activation are calculated within 1 kcal $mol^{-1}$ and, hence, *relative energies of a series of analogous chemical reactions provide the right trends within chemical accuracy*. As such, most density functional theory methods capture the correct changes in relative reactivity patterns well and supply the right polarization or charge relay needed to reproduce an experimental trend. Indeed, work on iron-porphyrin reactivity showed that experimental regioselectivities were excellently reproduced with DFT methods regardless of the method chosen (Kumar et.al. 2004; de Visser et.al. 2009, de Visser et.al. 2006; Kumar et.al. 2009; de Visser et.al. 2011; Sainna et.al. 2015).

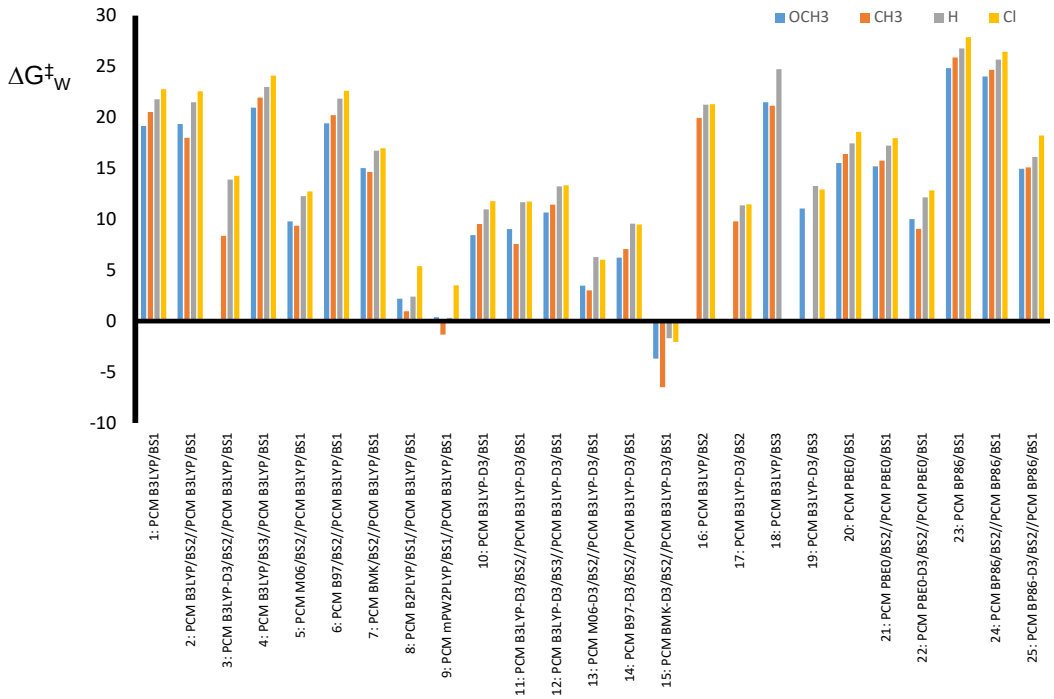


**Figure 3.5.** Free energy of activation (in kcal $mol^{-1}$) of DFT calculated para-Y thioanisole (Y = H, $CH_3$, $OCH_3$, Cl) sulfoxidation by $[Fe^{IV}(O)(N4Py)]^{2+}$ after a geometry optimization with a PCM model included and followed by a single point calculation with different method and/or basis set. All data include the Wertz entropy correction.

A number of DFT methods, however, fail to reproduce the experimental trends. Similarly to that mentioned above, also in Figure 3.5 a single point calculation with a dispersion-corrected method on a geometry calculated without dispersion fails to reproduce experimental energetics and trends, e.g entries 3 and 22. Interestingly, in a number of cases a geometry optimization using a modest basis set followed by a higher level single point calculation gives better agreement with experiment than a geometry optimization with a larger basis set, which probably is as a result of cancellation of errors and should not be relied on for too much. Also, single point calculations using a double hybrid mPW2PLYP on a B3LYP+PCM optimized geometry (entry 9) or BMK-D3/BS2 level of theory on B3LYP-D3+PCM/BS1 optimized geometry (entry 15) gives poor agreement with experiment and even leads to negative activation barriers, which are physically impossible.

In order to get a feeling as to how well computational methods reproduce the experimental values of the free energy of activation, we compared the free energy of activation of the four oxygen atom transition states for each method, namely for the reaction of para-Y substituted thioanisole (Y = H, $CH_3$, $OCH_3$, Cl) with $[Fe^{IV}(O)(N4Py)]^{2+}$ with a range of different methods and techniques. Thereafter, the mean barrier height for the four transition states ($\Delta G^{\ddagger}_{mean}$) was calculated from the mean value of these four transition states of para-Y substituted thioanisole sulfoxidation by $[Fe^{IV}(O)(N4Py)]^{2+}$ for each method. The mean value was then compared to the obtained result from experimentally determined second-order rate constants, Figure 3.6.

For the full set of four transition states, the best agreement with experimental mean is obtained at the PBE0+PCM/BS1 level of theory (entry 20) at a deviation of only 0.8 kcal $mol^{-1}$, however, the basis set used was very modest, so that this agreement may not be reproducible. At the B3LYP/BS3 level of theory (entry 18) the average deviation is 0.9 kcal $mol^{-1}$, hence an acceptable result is obtained for the set of four transition state structures. Very good agreement with the experimental trends is obtained at the PBE0+PCM/BS2//PBE0+PCM/BS1 level of theory (entry 21) with a deviation of about 1.2 kcal $mol^{-1}$ from experiment. Other methods that give encouraging results and a mean free energy of activation to within 3.5 kcal $mol^{-1}$ from experiment are B3LYP+PCM/BS2//B3LYP+PCM/BS1 (entry 2) and

B97+PCM/BS2//B3LYP+PCM/BS1 (entry 6). Similar as discussed above, single point calculations at the BMK and M06-2X level of theory on B3LYP optimized geometries give unrealistically low barrier heights (entries 13 and 15). Also, dispersion corrected single point calculations on non-dispersion optimized geometries give barrier heights that are well off from the experimental values.

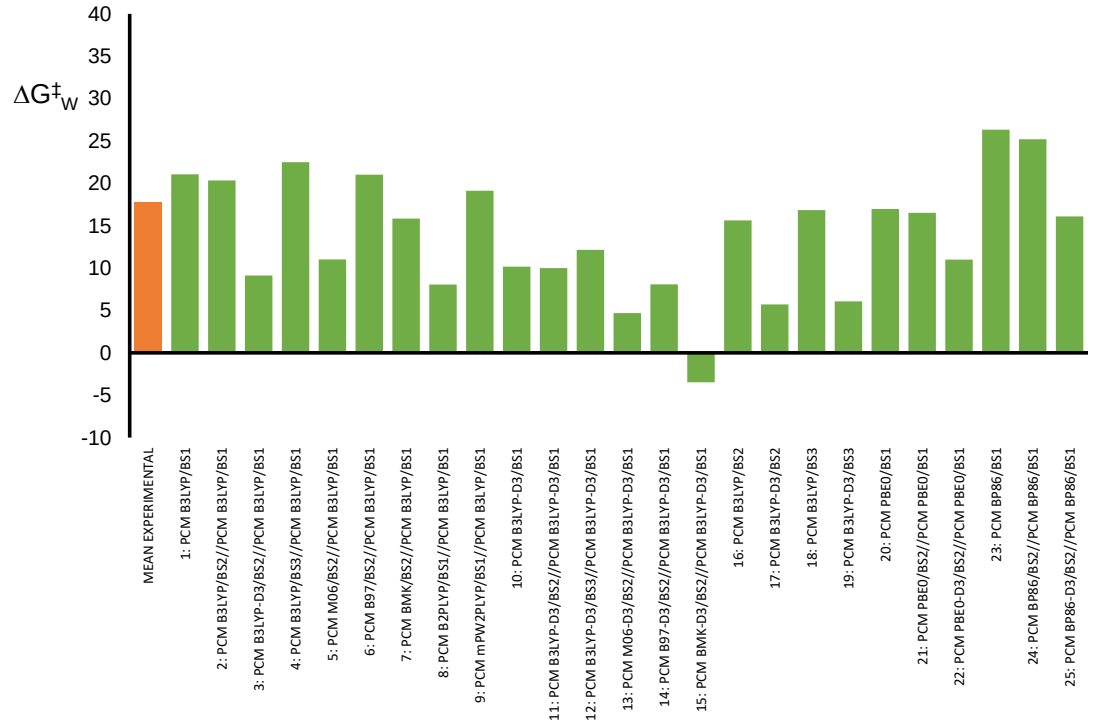


**Figure 3.6.** Mean free energies (in kcal mol$^{-1}$) for the reactions of para-Y substituted thioanisole (Y = $OCH_3$, $CH_3$, H, Cl) with $[Fe^{IV}(O)(N4Py)]^{2+}$ as calculated with DFT with a PCM model included but using a variety of methods. The corresponding value from the experimental data is given in orange. All data include the Wertz entropy correction.

The results displayed in Figure 3.6 give evidence onto the question what computational procedure (gas-phase, solvent, dispersion, density functional method, basis set) is most appropriate for the description of reactivity patterns by nonheme iron(IV)-oxo complexes. As can be seen, the mean free energy of the four sulfoxidation reactions is within a few kcal mol$^{-1}$ from the experimental value for B3LYP/BS2//B3LYP/BS1 level of theory with solvent included. Slightly closer to the experimental results are PBE0/BS1 optimized geometries and energy calculations. Clearly, B3LYP and PBE0, at least for this set of tested reactivity studies, appear to reproduce experimental rate constants the best and are our recommended methods for calculating transition states and free energies of activation.

Similarly to the notes regarding Figure 3.5, a dispersion single point calculation on a structure optimized without dispersion correction over stabilizes the energies. Surprisingly, a full geometry optimization at B3LYP-D3 with a large basis set (BS3 or BS2) gives one of the lowest free energies of activation for all methods and cannot be recommended for calculations on rate constants of transition metal complexes. This result may be due to overcorrection of the dispersion as a result of calculating the energies relative to isolated reactants. Thus, Lonsdale et al (2010) showed that for QM/MM calculations dispersion corrected methods are recommended. Indeed, in QM/MM the energy is calculated relative to a reactant complex rather than versus isolated reactants.

Interestingly, a BMK/BS2 single point on a B3LYP/BS1 optimized geometry gives matching free energies of activation with respect to experiment, whereas dispersion corrected single point and geometry optimizations give very low reaction barriers.

### 3.4 Conclusions

In this work we present an extensive benchmark study on substrate sulfoxidation by a nonheme iron(IV)-oxo complex using a large range of density functional methods and basis sets. We also tested the effect of solvent through various models and how it compares to gas-phase results. Finally, entropy corrections due to solvation effects were applied. We show that the Wertz entropy correction is essential to reproduce experimental free energy of activations. Overall it is seen that solvent optimized geometries lead to a better match between experiment and theory. Most density functional methods predict experimental trends correctly, but deviate strongly in the absolute values of the free energy of activation. Overall B3LYP and PBE0 reproduce experimental free energies of activation the best.

### Abbreviations

DFT, density functional theory; N4Py, N,N-bis(2-pyridylmethyl)-N-bis(2-pyridyl)methylamine; PCM, polarized continuum model.

# Chapter Four

# PROJECT 2

***Oxygen atom transfer using an iron(IV)-oxo embedded in a tetracyclic N-heterocyclic carbene system: How does the reactivity compare to Cytochrome P450 Compound?***

*Fabián G. Cantú Reinhard,[a] and Sam P. de Visser*[a]*

## Abstract

*N-heterocyclic carbenes (NHC) are common catalyst features in transition metal chemistry. Recently, a cyclic system containing four NHC groups with a central iron atom was synthesized and its iron(IV)-oxo characterized, [FeIV(O)(cNHC4)]2+. This tetra-cyclic NHC ligand system may give the iron(IV)-oxo species unique catalytic properties as compared to traditional nonheme iron and heme iron ligand systems. Therefore, we performed a computational study on the structure and reactivity of the [FeIV(O)(cNHC4)]2+ complex in substrate hydroxylation and epoxidation reactions. The reactivity patterns are compared with cytochrome P450 Compound I and nonheme iron(IV)-oxo models and it is shown that the [FeIV(O)(cNHC4)]2+ system is an effective oxidant with oxidative power analogous to P450 Compound I. Unfortunately, in polar solvents a solvent molecule will bind to the sixth ligand position and decrease the catalytic activity of the oxidant. A molecular orbital and valence bond analysis provides insight into the origin of the reactivity differences and makes predictions on how to further exploit these systems in chemical catalysis.*

**Published Reference:**
Cantu-Reinharrd, F.G. De Visser, S.P. Oxygen atom transfer using an iron(IV)-oxo embedded in a tetracyclic N-heterocyclic carbene system: How does the reactivity compare to Cytochrome P450 Compound I? Chem. Eur. J. 2017, 12, 2935-2944.

## 4.1 Introduction

Heme enzymes are versatile catalysts in nature and come in a large variety of shapes and structures that give them their unique biochemical functions. For instance, the heme peroxidases and catalases detoxify the body from hydrogen peroxide(Ortiz de Montellano, 1992; Raven, 2003; Poulos, 2010; Hollmann et.al. 2011; Nicholls et.al. 2000; Veitch et.al. 2000; Hersleth et.al. 2006), while the cytochromes P450 typically react as monoxygenases through oxygen atom transfer with substrates as a means to initiate the metabolism of drugs, the biodegradation of xenobiotics as well as the biosynthesis of hormones (Sono et.al. 1996; Groves, 2003; Ortiz de Montellano, 2004; Denosov et.al. 2005; Meunier et.al. 2004; Ortiz de Montellano, 2010). Heme peroxidases, catalases and monoxygenases have in common that they generate a high-valent iron(IV)-oxo heme cation radical species, called Compound I (CpdI)(Dawson, 1988; Schligting et.al. 2000; Shaik et.al. 2005). CpdI is highly reactive, but nevertheless, has been characterized in several peroxidases using a range of spectroscopic techniques, including electron paramagnetic resonance, Mössbauer and UV-Vis absorption spectroscopies (Roberts et.al. 1981; Sivaraja et.al. 1989; Goodin et.al. 1993). In P450 chemistry, CpdI has been more challenging to trap and characterize but spectroscopic studies of Rittle and Green provided evidence on its existence. Moreover, it was shown to be in a doublet spin ground state with two unpaired electrons in $\pi^*_{FeO}$ orbitals and a third unpaired electron in a heme-thiolate type orbital called $a_{2u}$. (Rittle et.al. 2010). The difference in reactivity of peroxidases and monoxygenases was assigned to the axial ligand bound to the metal (trans to the oxo group in CpdI), which is typically cysteinate in the P450s but histidine in peroxidases (Dawson et.al. 1976).

Over the years, a large number of synthetic model complexes that resemble the active site of heme enzymes have been created with the aim to gain insight into the characteristic properties of metal and ligand on structure and reactivity (Costas et.al., 2004; Bruijnincx, et.al. 2008; Abu-Omar et.al. 2005; Que, 2007; Nam et.al. 2007; Atanasov et.al. 2009). In particular, oxidants were created with heme-analogues, such as corrole, corrolazine and phthalocyanine (Aviv-Harel et.al. 2011; Thomas et.al. 2012; Abu-Omar et. al. 2011; Neu et.al. 2015; Afanasiev et.al. 2016; Isci et.al., 2015), which have differences in their aromaticity, overall charge and electron-

donating/withdrawing properties. These studies have given insight into the function and properties of the heme and how it influences reaction mechanisms and spectroscopic variables. For instance, corroles and corrolazines have an overall charge of 3– and as such can stabilize metals in high oxidation states.

One specific structural feature that is commonly used in catalysis nowadays are the N-heterocyclic carbenes (NHC)(Hopkinson et.al. 2014; Flaningan et.al. 2015; Domyati et.al. 2016). Very recently, Kühn and co-workers synthesized and characterized a tetra-cyclic NHC complex (cNHC4), whereby the four NHC components were bridged by alkyl groups (Anneser et.al. 2015; Anneser et.al. 2016). Its geometry and, in particular the one with bridging methyl groups as is studied here, shows structural similarity to a porphyrin (Por) manifold, see Scheme 4.1, although it misses the strong p-conjugation. Clearly, the $cNHC_4$ ligand is tetradentate like porphyrin, but lacks the large conjugated π-system characteristic for its absorption spectrum and responsible for electron abstraction during monoxygenation reactions. Recent studies of Meyer and co-workers spectroscopically characterized an iron(IV)-oxo species with the $cNHC_4$ ligand system and showed it to be in a triplet spin ground state (Kupper et.al. 2016). So far little is known on the catalytic properties of this tetra-cyclic NHC complex and no studies on reactivity patterns have been reported. In particular, the tetra-cyclic NHC chemical system may have catalytic properties unrivalled to in nonheme iron chemistry. To find out whether the iron(IV)-oxo species with tetra-cyclic NHC ligand would potentially be an active oxidant of oxygen atom transfer reactions we decided to do a detailed density functional theory (DFT) study. In particular, we compare two iron(IV)-oxo complexes, namely with $cNHC_4$ or Por ligand system, i.e. $[Fe^{IV}(O)(cNHC_4)X]^{2+}$ with X = no ligand or $CH_3CN$ and $[Fe^{IV}(O)(Por)(SH)]$ as a model of P450 CpdI. We hypothesized that the electron donation of the NHC groups toward iron, may affect the electron affinity of the complex and consequently its reactivity patterns with substrates. We initially investigated the iron(IV)-oxo complex with $cNHC_4$ ligand system with and without an axial solvent (acetonitrile) ligand. Thereafter, we studied the reactivity patterns for oxygen atom transfer and calculated double bond epoxidation of styrene and propene and aliphatic hydroxylation of propene and ethylbenzene (Scheme 4.1).

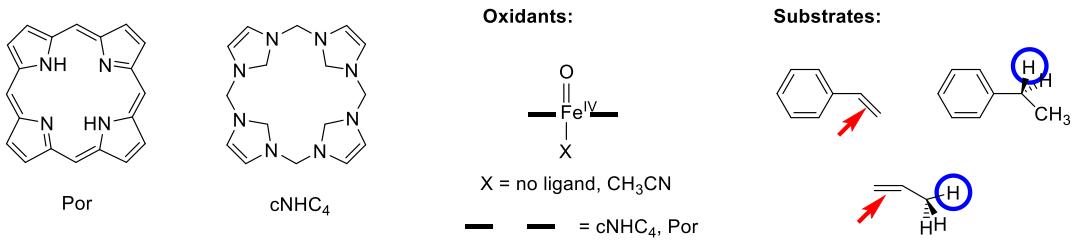


**Scheme 4.1.** Oxidants and substrates studied in this work.

The studies here are compared to previous work on iron(IV)-oxo porphyrin systems (Ogliaro et.al., 2000; Kamachi et.al. 2003; Li et.al. 2012) and nonheme iron(IV)-oxo models and shows that the $[Fe^{IV}(O)(cNHC_4)]^{2+}$ oxidant is a good oxidant that reacts with comparable rate constants as $[Fe^{IV}(O)(Por)(SH)]$ system, however, in acetonitrile a solvent molecule will bind the sixth ligand position and reduce its catalytic activity.

## 4.2 Results

Our work started off with a detailed analysis of the structure and spectroscopic properties of $[Fe^{IV}(O)(cNHC_4)]^{2+}$ ($^{3,5}$**1**) and $[Fe^{IV}(O)(cNHC_4)(CH_3CN)]^{2+}$ ($^{3,5}$**1**$_{AN}$), whereby the latter contains a solvent acetonitrile molecule in the sixth ligand position trans to the oxo group. We initially did a gas-phase geometry optimization, but later redid the work with an implicit solvent model with a dielectric constant mimicking acetonitrile, as recent studies showed this to give a better match to experimental free energies of activation (Cantu-Reinhard et.al. 2016; Yang et.al. 2016). Here we will focus on the solvent optimized geometries, whereas gas-phase results can be found in the Supporting Information. Typically for nonheme iron(IV)-oxo complexes there are two close-lying spin states, namely the triplet and quintet spin states, and dependent on the ligand environment and solvent their ordering can change (Balcells et.al., 2008; de Visser et.al. 2013; Wang et.al. 2013). Our model uses methyl bridges between the four NHC groups and optimized geometries of $[Fe^{IV}(O)(cNHC_4)]^{2+}$ (**1**) and $[Fe^{IV}(O)(cNHC_4)(CH_3CN)]^{2+}$ (**1**$_{AN}$) are given in Figure 4.1. In the quintet spin state the axial acetonitrile molecule displaces itself from the iron(IV)-oxo species and hence no stable $^{5}$**1**$_{AN}$ structure can be formed and acetonitrile (or alternative neutral molecules) will not bind in the axial position in the quintet spin state. This is most probably due to occupation of the $\sigma^*_{z2}$orbital with one electron that creates extra antibonding interactions along the O–Fe–axial ligand axis and prevents acetonitrile

from binding. The Fe–O bond lengths are around 1.62 – 1.64 Å in the triplet spin state, which are values in good agreement with previous experimental and computational studies of nonheme iron(IV)-oxo complexes (Rohde et.al., 2003; Martinho et.al. 2005).

While our study was under consideration, Kupper et.al (2005), reported an experimental report on an iron(IV)-oxo complex with tetra-cyclic NHC complex; however, their model had two bridging methyl and ethyl groups (designated complex **2**) rather than the four methyl linkages between the NHC groups as used here. The change in ligand system reduces the Fe–O distances by about 0.01Å and, consequently will affect vibrational frequencies slightly. Specifically, the two ethyl linkages used in Kupper et.al. (2005) create a stronger saddling than that seen in the structures in Figure 4.1. Despite this, there is still considerable saddling seen in the geometries with respect to a planar porphyrin ring. In particular, the two meso-methyl carbon atoms are below the iron(IV) atom as measured along the line through the iron(IV)-oxo by more than 1Å, while the other two meso-carbon atoms are located above the position of the iron atom by +0.58Å in $^3$**1** and by +0.76Å in $^3\mathbf{1}_{AN}$. Therefore, the saddling on the side of the iron(IV)-oxo group is less than that on the axial ligand side..

In structure **1**, the triplet spin state is the ground state and well separated from the quintet spin state by $\Delta E+ZPE = 15.1$ kcal mol$^{-1}$. This energy gap is considerably larger than that typically found for iron(IV)-oxo porphyrins and nonheme iron(IV)-oxo models (Rosa et.al., 2012; Neidig et.al., 2006; Hirao et.al., 2006). In particular, the latter tends to have a high-spin ground state with pentacoordinated ligands, while the triplet spin state is lower in energy in hexacoordinated environments. The group spin densities are given in Figure 4.1 and show one unpaired electron on the iron and oxo groups in the triplet spin state, although there is a small polarization toward iron radical in both cases. Very little spin density is seen on the $cNHC_4$ ligand. As the $[Fe^{IV}(O)(cNHC)_4]^{2+}$ complex, either with or without axial ligand has clearly separated triplet and quintet spin state surfaces, it makes the complex highly suitable for understanding triplet spin reactivity. In particular, since some computational studies have suggested that nonheme iron(IV)-oxo reactivity proceeds on a dominant quintet spin state, while the triplet spin surface shows sluggish reactivity.

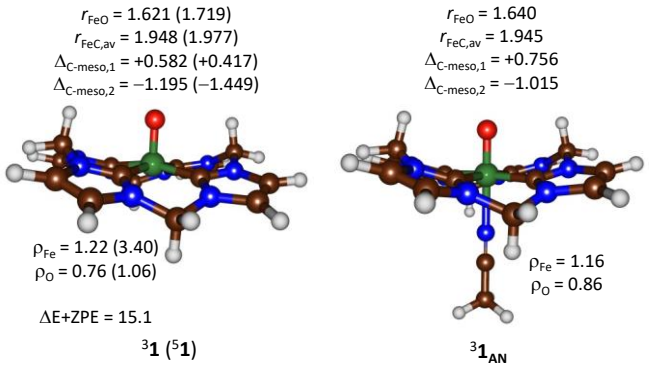


**Figure 4.1.** Optimized geometries (UB3LYP+PCM) of iron(IV)-oxo complexes with $cNHC_4$ ligand system. Bond lengths are given in angstroms, group spin densities (ρ) in atomic units and relative energies in kcal $mol^{-1}$. The saddling was estimated from the displacement of the meso-carbon with respect to the iron atom ($\Delta_{C\text{-}meso}$).

Subsequently, we analyzed the molecular orbitals of $^3$**1** in detail, see Figure 4.2. As commonly seen in iron(IV)-oxo complexes the As commonly seen in iron(IV)-oxo complexes the Fe–O interaction is described by a pair of $\pi_{xz}/\pi^*_{xz}$ and $\pi_{yz}/\pi^*_{yz}$ orbitals due to the interaction of the $3d_{xz}/3d_{yz}$ atomic orbital on iron with a $2p_x/2p_y$ orbital on oxygen. The bonding pairs are doubly occupied, while the antibonding pairs are singly occupied. In addition, there is one σ-type orbital along the Fe–O bond, i.e. $\sigma_{z2}/\sigma^*_{z2}$, for the interaction of the iron $3d_{z2}$ with the $2p_z$ on oxygen and the bonding combination is filled, whereas the antibonding is high in energy and virtual. The same is the case for the $\sigma_{x2-y2}/\sigma^*_{x2-y2}$ pair of orbitals that represent the bonding and antibonding interactions of the metal with the four carbon atoms of the NHC groups. The final set of orbitals highlighted in Figure 4.2 are the carbene orbitals of the NHC ligands that give the $\sigma_{d,xz}/\sigma_{d,yz}$ orbitals highlighted. Therefore, the electronic configuration of $^3$**1**/$^3$**1**$_{AN}$ is $\pi^*_{xy}{}^2\ \pi^*_{xz}{}^1\ \pi^*_{yz}{}^1$, whereas it is $\pi^*_{xy}{}^1\ \pi^*_{xz}{}^1\ \pi^*_{yz}{}^1\ \sigma^*_{z2}{}^1$ for $^5$**1**/$^5$**1**$_{AN}$.

As can be seen from Figure 4.2, there is a considerable energy gap for the a-set of orbitals between the p*xz/p*yz orbitals on the one hand, with the $\sigma^*_{z2}$ orbital on the other hand. This large separation of the π* and σ* orbitals stabilizes the triplet spin state over the quintet spin state in energy. Indeed, a large triplet-quintet energy gap of larger than 15 kcal mol–1 is reported above in Figure 4.1. Furthermore, a large HOMO-LUMO gap may implicate a large electron affinity and hence sluggish

reactivity with substrates as proposed previously (de Visser, 2010). Details of the reactivity patterns and a thermochemical analysis of the oxidative properties of the iron(IV)-oxo species will be discussed in detail below.

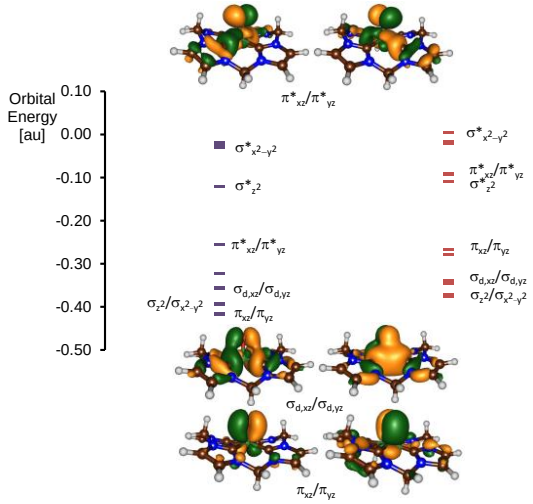


**Figure 4.2.** Orbital energy diagram of $^3$**1** as obtained at B3LYP/BS2.

Subsequently, we investigated the effect of the alkyl bridge of the tetracyclic NHC iron(IV)-oxo complexes and compared the system from this work with the one from Kupper et al. (2005) In particular, we calculated spectroscopic parameters for complexes $^3$**1** and $^3$**2**, whereby both are iron(IV)-oxo complexes with tetracyclic NHC ligand system, but **1** has four methyl bridges and **2** has two ethyl and two methyl bridges. Firstly, the extension of the bridges from methyl to ethyl has very limited effect on the Fe–O frequency, and values of 959 cm–1 for $^3$**1** and 961 cm–1 for $^3$**2** (B3LYP/BS1+PCM optimized geometry) are found. By contrast, optimized geometries for the acetonitrile ligated complexes, at the same level of theory, are 928 cm–1 for $^3$**1**$_{AN}$ and 933 cm–1 for $^3$**2**$_{AN}$. Therefore, addition of an acetonitrile molecule to the sixth ligand position leads to a major drop in Fe–O frequency (by about 30 cm–1) due to shortening of the Fe–O bond. On the other hand changing the alkyl bridge from methyl to ethyl has little effect on the Fe–O bond length and frequency.

To find out whether other spectroscopic variables are more strongly affected by the change in the NHC alkyl bridges, we calculated the Mössbauer parameters of $^3$**1** and $^3$**2**. Interestingly, the quadrupole splitting drops $\Delta E_Q$ = 3.52 mm s$^{-1}$ for $^3$**1** to 2.72 mm s$^{-1}$ for $^3$**2**, respectively. As such, the ligand system influences some spectroscopic properties strongly, whereas other factors are lesser effected.

Next, we investigated the oxygen atom transfer ability of **1** and $\mathbf{1}_{AN}$ with substrates and specifically double bond epoxidation and aliphatic C–H bond hydroxylation were studied. Firstly, we will discuss double bond epoxidation of styrene and propene and the lowest energy profile is shown in Figure 4.3. The triplet spin state is the ground state for this system and stays the lowest energy conformation throughout the full reaction mechanism. This is unique in iron(IV)-oxo chemistry as usually a spin state crossing from the triplet to the quintet spin state takes place. Nevertheless, the calculations presented here show that the triplet spin state can be reactive in substrate oxidation. The quintet spin state starts off above the triplet by 15 kcal mol–1 in the reactants and its surface, therefore, is inaccessible during the electrophilic attack that happens initially. Thus the iron(IV)-oxo attacks the terminal carbon atom via an electrophilic addition transition state $\mathbf{TS}_E$ to form a radical intermediate IE. The stepwise reaction continues with a ring-closure transition state $\mathbf{TS}_{rc}$ to form the epoxide-ring and generates the product complexes $\mathbf{P}_E$. In all cases, the rate determining step in the mechanism is the initial C–O bond formation barrier ($\mathbf{TS}_E$), which is followed by a small ring-closure transition state.

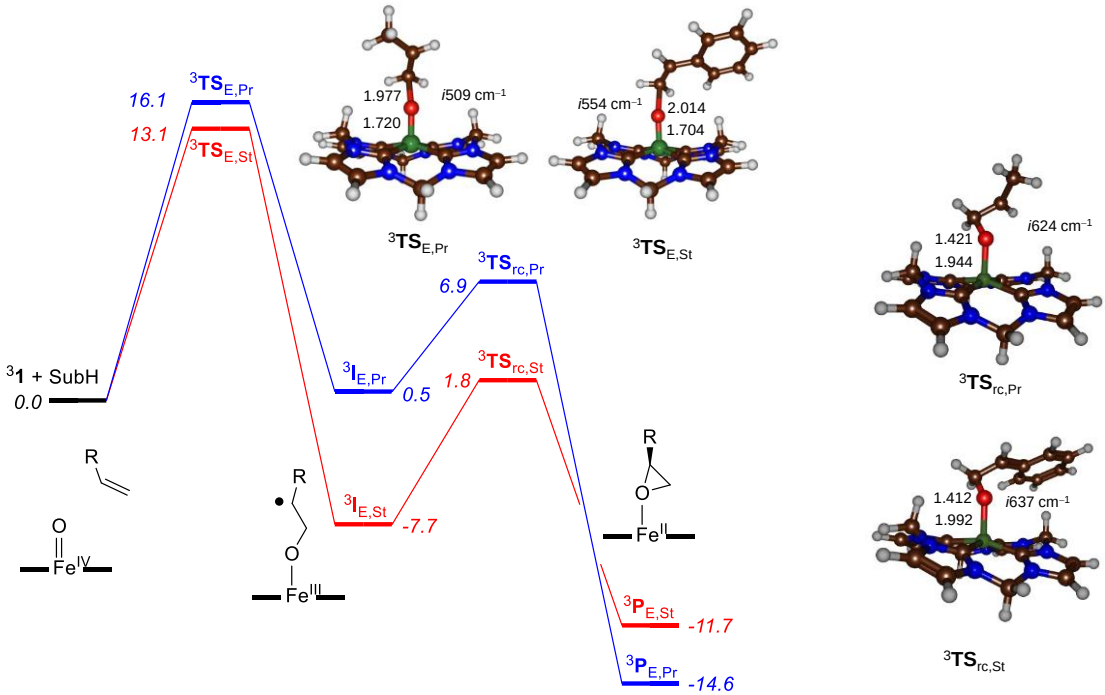


**Figure 4.3**. Potential energy surface and rate determining transition state geometries for styrene (St) and propene (Pr) epoxidation by $^3$**1** as calculated at UB3LYP/BS2+PCM//UB3LYP/BS1+PCM. Bond lengths are given in angstroms, the imaginary frequency is in cm–1 and relative energies (ΔE+ZPE+Esolv) in kcal mol$^{-1}$.

The transition states ($^3$**TS**$_E$) are characterized with a large imaginary frequency of well over 500 cm–1. These frequencies are in line with those found for substrate epoxidation by iron(IV)-oxo porphyrin and nonheme complexes that gave values typically between i250 – i500 cm–1 (Kumar et.al. 2010) .It was shown that for a set of para-substituted styrene systems, the barrier height for substrate epoxidation correlated with the imaginary frequency in the transition state (Kumar et.al. 2013), whereby large imaginary frequencies correlated with relative high activation energies for substrate epoxidation. Nevertheless, as discussed in detail later, the barrier heights for styrene and propene double bond activation by $^3$**1** are similar to those found for a P450 Compound I model.

Structures are typical for substrate epoxidation reactions and see an elongation of the Fe–O bond due to occupation of the $\sigma^*_{z2}$ orbital with one electron. Thus, the electrophilic pathway via **TS**$_E$ results in an electron transfer from substrate to iron(IV)-oxo species that occupies the virtual s*z2 orbital with one electron. This, so-called $^3\sigma$-pathway (Bernasconi et.al. 2008; Wong et.al. 2011; Sahu et.al. 2013), gives an iron(III) intermediate ($^3$**I**$_E$) with orbital occupation with three unpaired electrons with up-spin on the metal ($\pi^*_{xz}{}^1$ $\pi^*_{yz}{}^1$ $\sigma^*_{z2}{}^1$) and a down-spin radical on the carbon atom of the substrate ($\phi_{Sub}{}^1$). Group spin densities (see Supporting Information) confirm the assigned pathway.

The alternative pathway, i.e. the $^3\pi$-pathway, whereby the substrate donates an electron in the $\pi^*_{xz}$ orbital instead gives a radical intermediate $^3$**I**$_E$' with occupation $\pi^*_{xz}{}^2$ $\pi^*_{yz}{}^1$ $\sigma^*_{z2}{}^0$ $\phi_{Sub}{}^1$. However, for propene epoxidation we find the 3IE' state to be higher in energy by 10.6 kcal mol–1 than 3IE and hence did not pursue this mechanism further.

Geometrically, the electrophilic transition states have elongated Fe–O bonds of about 1.720 / 1.704 Å for $^3$**TS**$_{E,Pr}$ / $^3$**TS**$_{E,St}$, respectively, whereas the reactant structure had a distance of 1.621 Å. At the same time, the substrate approaches the oxidant under a large angle Fe–O–C of 141° / 147° in $^3$**TS**$_{E,Pr}$ / $^3$**TS**$_{E,St}$. These angles are considerably larger than those found for typical $^3\pi$-pathways that tend to give an Fe–O–C angle of about 120° instead (de Visser, 2011; Laifiti et.al. 2013). Most likely, these enlarged angles are a consequence of the non-planarity of the cNHC4 ligand, so that the substrate cannot approach the iron(IV)-oxo under an ideal angle as a result of electronic repulsions with the ligand.

After the electrophilic transition state the system relaxes to a radical intermediate ($^3$**I**$_E$), which is separated from products via a ring-closure transition state ($^3$**TS**$_{rc}$). The electron transfer from substrate to oxidant that happens in this reaction step fills the $\pi^*_{xz}$ molecular orbital with a second electron, which reduces the spin density on iron and creates an iron(II) product complex with $\pi^*_{xz}{}^2$ $\pi^*_{xz}{}^1$ $\sigma^*_{z2}{}^1$ orbital occupation. Optimized geometries of the ring-closure transition states are given in Figure 4.3. Now the bond between iron and oxo is broken and the oxygen atom inserts itself into the C–C bond to form the epoxide product. Hence, short O–C and long Fe–O distances are seen in both transition states.

The ring-closure barriers are relatively large (6.4 and 9.5 kcal mol–1 for propene and styrene, respectively), which implies that the radical intermediates will have a finite lifetime during which rearrangement process may occur leading, for instance, to stereochemical scrambling and the formation of cis-products from trans-reactants. In addition, side products leading to aldehydes or suicidal products in P450 chemistry of olefins were explained as originating from the lifetime of the radical intermediates (de Visser et.al. 2001; de Visser et.al. 2004). Nevertheless, in all cases the barrier **TS**$_E$ is rate determining.

Subsequently, we investigated the aliphatic hydroxylation pathways of two model substrates, namely ethylbenzene (EB) and propene (Pr) and the results are given in Figure 4.4. Similarly to the epoxidation mechanisms the reactions are stepwise via a radical intermediate (**I**$_H$) and consist of a hydrogen atom abstraction via transition state **TS**$_H$. The OH rebound step via transition state **TS**$_{reb}$ gives the iron(III)-alcohol product complex **P**$_H$. Again the rate-determining step is the initial barrier and the rebound

barrier is smaller. Interestingly, we could not locate a rebound transition state for ethylbenzene hydroxylation, but for propene a considerable barrier of 10.2 kcal mol–1 was found.

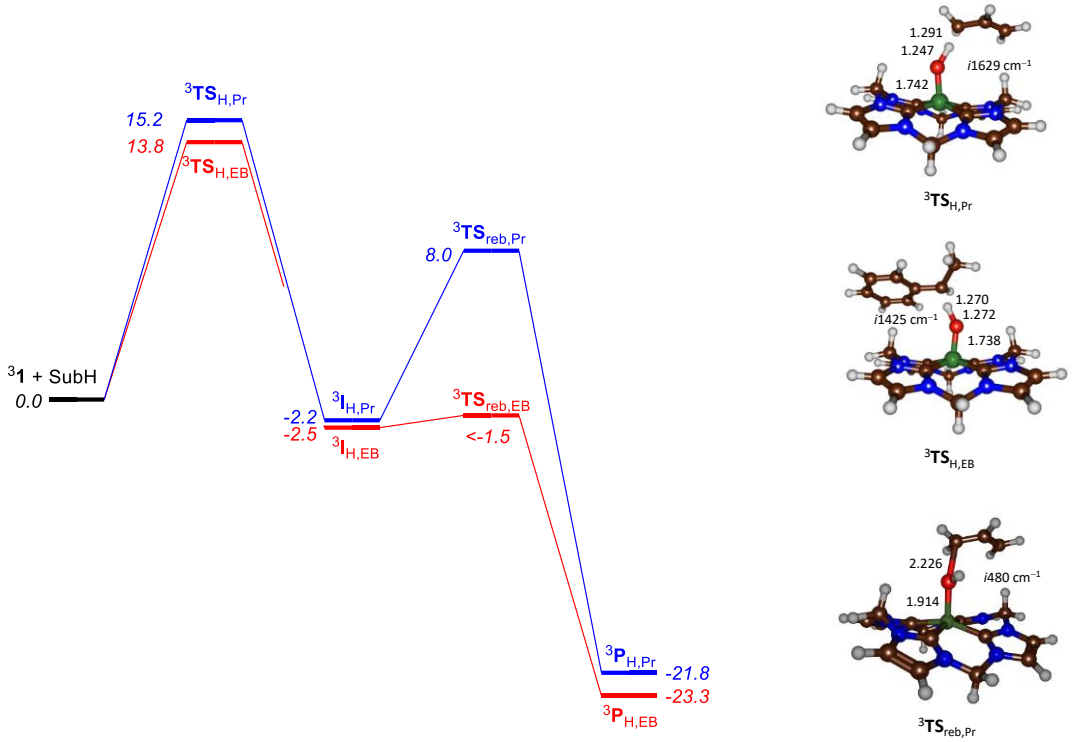


**Figure 4.4**. Potential energy surface and rate determining transition state geometries for ethylbenzene (EB) and propene (Pr) hydroxylation by 31 as calculated at UB3LYP/BS2+PCM//UB3LYP/BS1+PCM. Bond lengths are given in angstroms, the imaginary frequency is in cm–1 and relative energies ($\Delta E+ZPE+E_{solv}$) in kcal mol–1.

Geometrically, both hydrogen atom abstraction barriers are central with almost equal C–H and O–H distances that displays a large imaginary frequency of well over i1400 cm–1. An imaginary frequency of that magnitude will lead to a large kinetic isotope effect as a result of replacing the transferring hydrogen atom by deuterium. Indeed, we calculate an Eyring kinetic isotope effect ($KIE_E$) for hydrogen atom abstraction from propene and ethylbenzene of 6.6 and 6.7, respectively, whereas Wigner corrections due to tunneling raise these values to 9.3 and 9.1. These values match calculated and experimentally measured KIEs for hydrogen atom abstraction by nonheme iron(IV)-oxo and P450 Compound I models excellently (Company et.al., 2007; Park et.al. 2013; de Visser, 2006; Mandal et.al. 2016).

Similarly as the substrate epoxidation pathways, the radical intermediates $^3\mathbf{I}_H$ are characterized with an orbital occupation of $\pi^*_{xz}{}^1\ \pi^*_{yz}{}^1\ \sigma^*_{z2}{}^1\ \phi_{Sub}{}^1$ fSub1 as typical for 3s-pathways. Indeed, the Fe–O distance in the $^3\mathbf{TS}_H$ structures is very similar to those in the $^3\mathbf{TS}_E$ geometries and so are the group spin densities. Formation of the radical intermediates is slightly exothermic by 2.2 and 2.5 kcal mol–1 for propene and ethylbenzene. Under these conditions, it appears that $^3[Fe^{IV}(O)(cNHC_4)]^{2+}$ should be able to react with olefins and aliphatic groups through substrate epoxidation and hydroxylation reactions.

Next, the styrene and propene epoxidation pathways were calculated for a series of different oxidants and the results are summarized in Table 4.1. First, an axial acetonitrile molecule was added to $^3\mathbf{1}$ to give $^3\mathbf{1}_{AN}$. Second, the tetra-cyclic NHC iron(IV)-oxo complex $^3\mathbf{2}_{AN}$ with two ethyl and two methyl linkages from Kupper et.al. (2005) was studied. Thirdly, a heme and nonheme iron(IV)-oxo species were investigated, namely a small model of cytochrome P450 Compound I, 4[Fe(O)(Por+·)(SH)] (Kumar et.al. 2011; Ji et.al. 2015), and a typical nonheme iron(IV)-oxo with pentadentate ligand system N4Py (N4Py = N,N-bis(2-pyridylmethyl)-N-bis(2-pyridyl) methylamine) were studied (Vardhaman et.al. 2013; Kumar et.al. 2014).

**Table 4.1.** Barrier heights $\mathbf{TS}_E$ for styrene and propene epoxidation by various iron(IV)-oxo complexes.

| Oxidant | $\Delta E+ZPE+E_{solv}$[a] | Imag[b] | R(C–O)[c] | R(Fe–O)[c] |
|---|---|---|---|---|
| Styrene: | | | | |
| $^3\mathbf{1}$ | 13.1 | i554 | 2.014 | 1.704 |
| $^3\mathbf{1}_{AN}$ ($^3\mathbf{2}_{AN}$) | 20.7 (25.1) | i521 | 1.957 | 1.732 |
| $^4$[Fe(O)(Por$^{+\bullet}$)(SH)] | 12.4 | i543 | 2.040 | 1.687 |
| $^3[Fe(O)(N4Py)]^{2+}$ | 15.7 | i448 | 1.999 | 1.714 |
| Propene: | | | | |
| $^3\mathbf{1}$ | 16.1 | i509 | 1.977 | 1.720 |
| $^3\mathbf{1}_{AN}$ ($^3\mathbf{2}_{AN}$) | 22.8 (23.1) | i627 | 1.897 | 1.742 |
| $^4$[Fe(O)(Por$^{+\bullet}$)(SH)] | 17.1 | i558 | 1.941 | 1.726 |
| $^3[Fe(O)(N4Py)]^{2+}$ | 19.2 | i493 | 1.981 | 1.720 |

Values in kcal mol-1 calculated at UB3LYP/BS2+PCM//UB3LYP/BS1+PCM for complex $\mathbf{1}$/$\mathbf{1}_{AN}$ and UB3LYP/BS2+PCM//UB3LYP/BS1 for $\mathbf{2}_{AN}$. [b] Imaginary frequency in cm-1. [c] C-O and Fe-O distances in angstroms.

Addition of an axially ligated solvent molecule to the cNHC4 complex $^3$**1** gives a considerable rise of the transition state energies by more than 7 kcal mol-1. The same is found for hydrogen atom abstraction from propene by $^3$**1** and $^3$**1**$_{AN}$, which give $^3$**TS**$_H$ barriers of 13.2 and 21.2 kcal mol–1, respectively. This is similar to what was observed recently in m-nitrido bridged diiron porphyrin and phthalocyanine complexes that gave much higher hydrogen atom abstraction barriers with an axially ligated anion at more than 5Å from the active oxo group (Quesne et.al. 2016). As shown above in Figure 4.1 the iron atom is closer to the plane through the four carbene atoms, which destabilizes the p* orbitals and makes the electron transfer into the metal-oxo group lesser favorable. Therefore, complex $^3$**1** in an acetonitrile solution will pick up a solvent molecule to form $^3$**1**$_{AN}$. The resulting complex is a lesser good oxidant than $^3$**1** for substrate epoxidation and hydroxylation reactions than the complex in the gas phase.

Complex $^3$**1** actually gives enthalpies of activation of substrate epoxidation reactions that are close in energy to those found for P450 Compound I. For both propene and styrene the TSE barriers from $^3$**1** and 4[Fe(O)(Por+·)(SH)] are within 1 kcal mol-1. As such, the N-heterocyclic carbene structure **1** is actually a very good oxidant. Unfortunately, in an acetonitrile solution $^3$**1** will rapidly convert into $^3$**1**$_{AN}$ and lose significant catalytic activity. Interestingly, $^3$**1** is also better in activating propene and styrene than a typical iron(IV)-oxo oxidant, such as $^3[Fe^{IV}(O)(N4Py)]^{2+}$, although axial binding of acetonitrile reverses the trend and $^3$**1**$_{AN}$ reacts significantly slower than $^3[Fe^{IV}(O)(N4Py)]^{2+}$.

For two substrates (styrene and propene), we also calculated the epoxidation transition state $^3$**TS**$_E$ using the tetra-cyclic NHC complex with two bridging ethyl and two methyl groups, structure $^3$**2**$_{AN}$. In the case of propene, the epoxidation barrier is within 0.3 kcal mol–1 of that obtained for $^3$**1**$_{AN}$. However, for styrene the epoxidation barrier is raised by more than 4 kcal mol–1, which may implicate that substrate approach is hindered due to the larger saddling in $^3$**2**$_{AN}$ as compared to that of $^3$**1**$_{AN}$. Previous studies on iron(IV)-oxo porphyrins showed that substrate epoxidation barriers are affected by ligands attached to the porphyrin scaffold and cause repulsive interactions that raise substrate activation barriers (Kumar et.al. 2009).

### 4.3 Discussion

In the following, we will compare the aliphatic hydroxylation and olefin epoxidation reactions by $^3$**1** and $^3$**1**$_{AN}$ and particularly focus on the origins of the reactivity differences relative to those seen for analogous nonheme iron(IV)-oxo and iron(IV)-oxo porphyrin cation radical models. Let us first compare the effect of the environment, such as a polarized continuum model (PCM) and the addition of an axial ligand. Table 4.2 gives transition state (free) energies for styrene activation by $^3$**1** and $^3$**1**$_{AN}$ as calculated in the gas-phase and with a PCM model.

**Table 4.2.** Enthalpy of activation ($\Delta E^{\ddagger}$+ZPE) and Gibbs free energy of activation for styrene TS.

| | $\Delta E^{\ddagger}$+ZPE | | $\Delta G^{\ddagger}$ | |
|---|---|---|---|---|
| Oxidant[a] | Gas-phase | PCM | Gas-phase | PCM |
| $^3$**1** | -1.0 | 13.1 | 9.9 | 23.9 |
| $^3$**1**$_{AN}$ | 12.4 | 20.7 | 23.4 | 33.4 |

[a] Values obtained at UB3LYP/BS2//UB3LYP/BS1 in kcal mol$^{-1}$.

Similar to that seen before the free energy of activation is approximately 10 kcal mol–1 higher in value than the enthalpy of activation due to entropic effects with respect to isolated reactants (Bernasconi et.al. 2013; Sainna et.al.2015). Interestingly, a solvent model increases the barriers by 8.3 kcal mol–1 (for $^3$**1**$_{AN}$) and 14.1 kcal mol–1 (for $^3$**1**), which is probably the result of the charge of the chemical system, which is more polarized in the gas-phase. Furthermore, an axial ligand, such as a solvent molecule like acetonitrile, bound in the axial position of the iron(IV)-oxo complex raises the barriers drastically by 13.4 kcal mol–1. This is in contrast to iron(IV)-oxo heme cation radical complexes, where the axial ligand is involved in key interactions to the metal and its electron-donating properties affect the electron affinity of the oxidant and consequently its oxygen atom transfer ability (Sastri et.al. 2005; Sastri et.al. 2007; Mekmouche et.al. 2001; Kurahashi et.al. 2009).

These studies implicate that the $^3[Fe^{IV}(O)(cNHC_4)]^{2+}$ will be an effective oxidant in the gas phase and probably apolar solvents, but becomes a significantly weaker oxidant in polar solvents that bind as sixth ligand to the complex. Nevertheless, a solvent molecule is only weakly bound to the iron(IV)-oxo complex and a binding strength of $\Delta E+ZPE+E_{solv}$ = 9.5 kcal mol–1 was calculated for removal of an acetonitrile molecule from $^3\mathbf{1}_{AN}$.

To understand the reactivity differences of of $^3\mathbf{1}$ and $^3\mathbf{1}_{AN}$ on the one hand with iron(IV)-oxo porphyrin cation radical and nonheme iron(IV)-oxo models, on the other hand, we set up a valence bond/molecular orbital diagram on the orbital forming and breaking processes that take place during the rate determining step of the reaction. In particular, we recently proposed a two-parabola model to predict barrier heights of oxygen atom transfer reactions (Barman et.al.2016; Cantu-Reinhard et.al. 2016), see right-hand-side of Figure 4.5 for details. This model considers the reactants and products to reside in the minimum point of a parabola at a reaction coordinate x = 0 (reactants, **R**) and x = 1 (products). The two parabolas cross in a point just above the actual transition state at a reaction coordinate of x = ½ and the energy of the crossing point ($\Delta E_{cross}$) can then be described from the two parabola functions ($y_R$ and $y_P$). Specifically, we derived previously that the energy at the crossing point is a function of the driving force from reactants to products ($\Delta E_{rp}$) and the Franck-Condon energy between the two curves at x = 0 ($E_{FC,\mathbf{R}}$), Eq 4.1.

$$\Delta E_{cross} = \frac{1}{4} E_{FC,\mathbf{R}} + \frac{3}{4} \Delta E_{rp} \qquad (4.1)$$

The actual transition state is located slightly below the crossing point and using valence bond modelling Shaik (2010) predicted that it is lower by a contribution due to the resonance energy B. It was further estimated that B is one half of the weakest bond that is either broken or formed during a hydrogen atom abstraction reaction.

For the oxidants reported in Table 4.1, we estimated the crossing point for hydrogen atom abstraction from propene and consequently the barrier height ($\Delta E^{\ddagger}_{VB,H,Pr}$) from empirical values. Figure 4.5 also shows the relevant bonding orbitals in Lewis structures along the hydrogen atom abstraction pathway by $^3\mathbf{1}$ (top left) and $^4[Fe^{IV}(O)(Por^{+\bullet})SCys]$ (bottom left) as a model of P450 Compound I. Thus, upon hydrogen atom abstraction the substrate C–H orbital ($\sigma_{CH}$) needs to be broken into

atomic orbitals ($2p_C$ and $1s_H$) and the $1s_H$ then forms a new O–H orbital ($\sigma_{OH}$) with a $2p_O$ atomic orbital on the oxo group. This atomic $2p_O$ orbital originates from the $\pi_{xz}/\pi^*_{xz}$ pair of orbitals along the Fe–O bond that is split back into atomic orbitals. As the $\pi_{xz}/\pi^*_{xz}$ pair of orbitals is occupied with three electrons, after breaking these bonds one electron stays on oxygen ($2p_O$), while the other two move to the iron: One electron occupies the now non-bonding $3d_{xz}$ orbital, whereas the other electron is transferred into the $\sigma^*_{z2}$ orbital.

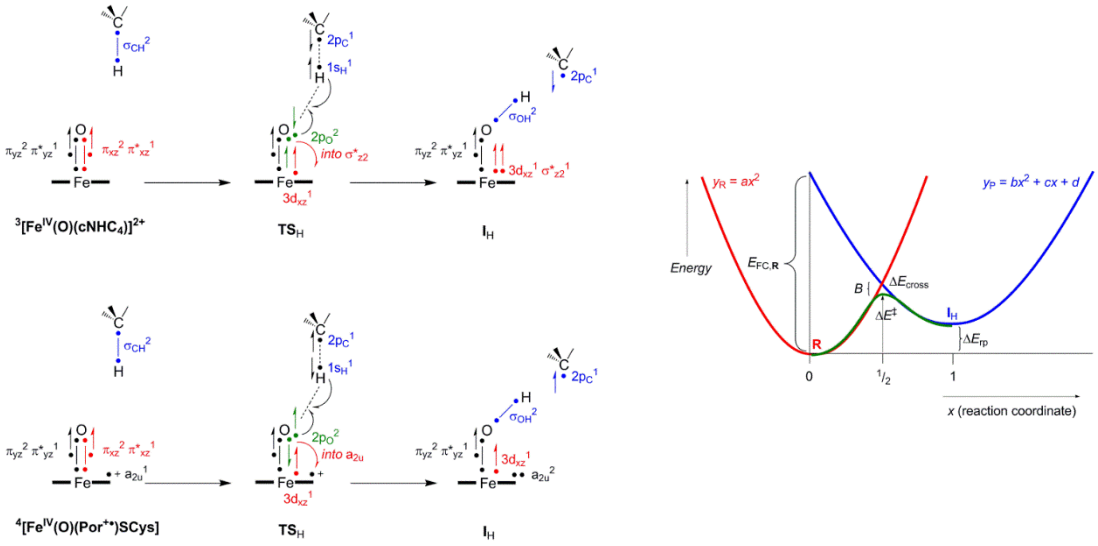


**Figure 4.5.** Electron distribution over key orbitals during the hydrogen atom abstraction process in $^3$**1** (top) and $^4$[Fe$^{IV}$(O)(Por$^{+\bullet}$)(SCys)] (bottom). A line with two dots represents a bonding orbital with two electrons.

Therefore, the orbital processes that happen in the hydrogen atom abstraction by $^3$**1** are: (1) The breaking of the $\sigma_{CH}$ orbital into atomic orbitals, (2) The formation of a $\sigma_{OH}$ orbital from atomic orbitals, (3) The breaking of the $\pi_{xz}/\pi^*_{xz}$ pair of orbitals into atomic orbitals, and (4) The excitation of an electron from $3d_{xz}$ to $\sigma^*_{z2}$. As such, the Franck-Condon energy ($E_{FC,1}$)in the reactants for the hydrogen atom abstraction by $^3$**1** can be described by Eq 4.2. In this equation the breaking of the $\pi_{xz}/\pi^*_{xz}$ pair of orbitals is given as $E_{\pi/\pi^*xz}$ and the excitation energy from $3d_{xz}$ to $\sigma^*_{z2}$ is $E_{Exc,xz\rightarrow\sigma^*zz}$. Finally, the bond dissociation energies of the C–H bond of the substrate and the O–H bond of the iron(III)-hydroxo product are described by $BDE_{CH}$ and $BDE_{OH}$, respectively. We estimated the $\pi_{xz}/\pi^*_{xz}$ energy gap and the $\pi_{xz}$ to $\sigma^*_{z2}$ excitation energy from the individual molecular orbitals in the reactant complexes and give the obtained values in Table 4.3. In addition, we calculated the $BDE_{OH}$ values from the difference in

energy between the iron(III)-hydroxo complex and the sum of the iron(IV)-oxo and a hydrogen atom and also present the electron affinity (EA) of the complexes in Table 4.3.

**Table 4.3.** Calculated intrinsic properties of oxidants and predicted and DFT calculated propene hydrogen atom abstraction barriers.

| Oxidant[a] | EA | $BDE_{OH}$ [b] | $E_{\pi/\pi^*xz}$ | $E_{Exc}$ | $\Delta E^{\ddagger}_{VB,H,Pr}$ | $\Delta E^{\ddagger}_{DFT,H,Pr}$ |
|---|---|---|---|---|---|---|
| $^3$**1** | 87.9 | 84.0 | 99.1 | 134.2 | 15.3 | 15.2 |
| $^3\mathbf{1}_{AN}$ | 77.1 | 77.2 | 95.6 | 154.9 | 26.4 | 21.2 |
| $^4$[Fe(O)(Por$^{+\bullet}$)(SH)] | 114.2 | 83.2 | 83.1 | 108.4 | 5.6 | 17.1 |
| $^3$[Fe(O)(N4Py)]$^{2+}$ | 93.3 | 83.0 | 84.5 | 163.3 | 19.9 | 20.7 |

[a] All values are in kcal mol–1 and include ZPE and solvent corrections. [b] Adiabatic value.

$$E_{FC,\mathbf{1}} = E_{\pi/\pi^*xz} + E_{Exc,xz\rightarrow\sigma^*zz} + BDE_{CH} - BDE_{OH} \quad (4.2)$$

The driving force for the hydrogen atom abstraction is simply taken as the difference in energy between $BDE_{CH}$ and $BDE_{OH}$. Indeed, a difference of -2.1 kcal mol$^{-1}$ is found, which is almost identical to the value of the radical intermediate from isolated reactants (see Figure 4.4). The VB model predicts hydrogen atom abstraction barriers of 15.3 (propene) and 15.1 (ethylbenzene) kcal mol–1 from empirical values. These values are in excellent agreement with the DFT barriers reported in Figure 4.4 and confirm the individual electronic components that contribute to the hydrogen atom abstraction barrier.

Addition of an axial acetonitrile ligand to form $^3\mathbf{1}_{AN}$ has a dramatic effect on the hydrogen atom abstraction barriers and leads to a VB predicted barrier of 26.4 kcal mol$^{-1}$, which is in reasonable agreement with the DFT result from Table 4.1. The reason the barriers go up in energy is mostly due to a considerable increase of the $\pi_{xz} \rightarrow \sigma^*_{z2}$ excitation energy. Thus, addition of an axial ligand lowers the metal into the plane of the four carbene atoms, which affects the $\sigma^*_{z2}$ orbital dramatically and raises it in energy by more than 20 kcal mol$^{-1}$. In addition, there are further destabilizing effects of the $\mathbf{TS}_H$ as a result of a smaller $BDE_{OH}$ value, which of course, also affects the driving force. Therefore, binding an axial solvent molecule to $^3\mathbf{1}$ reduces the oxidative power of the system and makes it a weaker oxidant as an electron is transferred into a higher energy orbital.

Using the same model, as reported previously (Quesne et.al. 2016), the same model can be applied to hydrogen atom abstraction by P450 CpdI. The Franck-Condon value for CpdI is described in a similar way as that for $^3$**1** and $^3$**1**$_{AN}$ and depends as well on the $\pi_{xz}/\pi^*_{xz}$ energy gap, the $BDE_{CH}$ and $BDE_{OH}$ values, Eq 3. In addition, the excitation energy from $\pi_{xz}$ into the $a_{2u}$ orbital, which is much lower in energy than $\sigma^*_{z2}$ and should cost lesser energy. Consequently, this lower excitation will lead to a reduction in the Franck-Condon energy, although other components may balance it.

$$E_{FC,\mathbf{1}} = E_{\pi/\pi^*xz} + E_{Exc,xz\rightarrow a2u} + BDE_{CH} - BDE_{OH} \qquad (4.3)$$

As seen from the data in Table 4.3, VB predicts a low barrier for hydrogen atom abstraction from propene, which is somewhat lower than the DFT calculated value probably because the pairing energy of the two electrons in a2u is not included in the model. Nevertheless, the trend is reproduced well and highlights the components contributing to the hydrogen atom abstraction barrier.

In summary, the VB/MO modelling highlights the key intrinsic properties of the oxidants that drive hydrogen atom abstraction reactions and show that a lower lying orbital is filled by P450 CpdI as compared by the nonheme iron(IV)-oxo analogs. However, the electron affinity of the CpdI model is significantly higher than those of the tetra-cyclic NHC complexes **1** and **1**$_{AN}$.

## 4.4 Conclusions

In this work we report a computational study on substrate hydroxylation and epoxidation of four model substrates by a set of iron(IV)-oxo complexes. In particular, two iron(IV)-oxo complexes with tetra-cyclic NHC ligand system were investigated with and without an axial acetonitrile ligand. The work is compared with reactivity of P450 CpdI and a nonheme iron(IV)-oxo complex with pentadentate N4Py ligand system. The work shows that the pentacoordinate system **1** is an excellent oxidant of olefin epoxidation and aliphatic hydroxylation reactions and reacts with rate determining barriers that are similar to those found for P450 CpdI models. Addition of an axial ligand, however, reduces the activity and raises the barriers dramatically in energy, although they are low enough to take place at room temperature. The differences are analyzed by molecular orbital and valence bond methods and shown to originate from differences in molecular orbital energy levels. Specifically, the $\sigma^*_{z2}$ orbital is raised from $^3$**1** to $^3$**1**$_{AN}$ and is the dominant reason for the slowing down of the reaction. By contrast, P450 CpdI has a lower lying $a_{2u}$ orbital that is accessible and thereby enjoys lower barriers for hydrogen atom abstraction. Overall, the tetra-cyclic NHC ligated iron(IV)-oxo complex is a unique chemical system with reactivity patterns at par with porphyrin complexes. Moreover, the $[Fe^{IV}(O)(cNHC)_4]^{2+}$ complex has well separated triplet and quintet spin state surfaces, whereby the quintet is so much higher in energy that it cannot take a role in catalysis. As such this system enables for spin-selective studies on triplet spin states in oxygen atom transfer reactions.

## 4.5 Experimental Section

Computational methods and procedures follow previously described studies from our group (de Visser, 2014) and utilize density functional theory methods as implemented and run in the Gaussian-09 software package (Frish et.al. 2009). All structures described here are the result of a full geometry optimization (without constraints) with the unrestricted B3LYP hybrid density functional methodology (Becke et.al. 1993; Lee et.al. 1988). Although, the initial structures were optimized in the gas-phase, we followed up our studies with full geometry optimizations using a self-consistent reaction-field (SCRF) model with a dielectric constant mimicking acetonitrile (Tomasi et.al. 2005). In previous work we showed that this model matches experimental structures and reaction mechanisms and rate constants better than gas-phase geometry optimizations, particularly since the system has an overall charge of +2 (Cantu-Reinhard et.al., 2016; Yang et.al. 2016). Details of the gas-phase results are given in the Supporting Information, while we focus here on the solvent corrected data only. Geometry optimizations use an LANL2DZ (+ core potential) on iron and 6-31G* on all other atoms: basis set BS1 (Hay et.al. 1985; Hehre et.al. 1972). Single point energy calculations on the optimized geometries were done with a more elaborate LACV3P+ (+ core potential) basis set on iron and 6-311+G* on the rest of the atoms: basis set BS2, including the implicit solvation model. Vibrational frequencies reported here are unscaled.

We created a tetra-cyclic-NHC ligand from a porphyrin analogue by replacing carbon and nitrogen atoms and adding hydrogens. Iron(IV)-oxo was then inserted into the ligand to create $[Fe^{IV}(O)(cNHC_4)]^{2+}$ or **1**. Complex **1** was investigated in the triplet and quintet spin states with and without an axial acetonitrile molecule bound. Subsequently, the reactivity in oxygen atom transfer, i.e. double bond epoxidation and C–H hydroxylation, was studied with styrene, propene (hydroxylation and epoxidation) and ethylbenzene.

Kinetic isotope effects for the replacement of hydrogen atoms by deuterium were initially calculated using the Eyring equation ($KIE_E$) by taking the free energy of activation ($\Delta G^{\ddagger}$) difference of the systems with all hydrogen atoms and the structure where one or more hydrogen atoms were replaced by deuterium atoms (de Visser 2016; Kumar et.al. 2004).

The free energy difference was then converted into a rate constant ratio ($k_H/k_D$) by taking the natural logarithm over the free energy difference divided by the gas constant (R) and the temperature (T = 298K), Eq 4.4.

$$KIE_E = \exp\{(\Delta G^{\ddagger}_D - \Delta G^{\ddagger}_H)/RT\} \qquad (4.4)$$

The effect of tunnelling on the kinetic isotope effects was calculated from the Wigner correction to the KIE by multiplication with the tunnelling ratio (QtH/QtD) taken from the change in imaginary frequency (n) in the transition state, Eqs 4.5 and 4.6.

$$KIE_W = KIE_E \times Q_{tH}/Q_{tD} \qquad (4.5)$$

$$Q_t = 1 + \frac{1}{24}\left(\frac{h\nu}{kT}\right)^2 \qquad (4.6)$$

In Eq 4.6, k is the Boltzmann constant and h is Planck's constant.

Mössbauer parameters were calculated in Orca for $^3$**1** and $^3$**2** on the B3LYP/BS1 optimized geometries (Neese, 2009) These calculations use approaches discussed before (Tchesnokov et.al. 2016) with the unrestricted B3LYP employed with basis set CP(PPP) with effective core potential on iron and SV(P) on the rest of the atoms

Keywords: iron(IV)-oxo • epoxidation • hydroxylation • NHC • density functional theory

# Chapter Five

# PROJECT 3

# *A systematic account on aromatic hydroxylation by a cytochrome P450 model Compound I: A low-pressure mass spectrometry and computational study*

*Fabián G. Cantú Reinhard,[a]† Mala A. Sainna,[a]† Pranav Upadhayay,[b] G. Alex Balan,[a] Devesh Kumar,[b] Simonetta Fornarini,*[c] Maria Elisa Crestoni,*[c] and Sam P. de Visser*[a]*

## Abstract

*Cytochrome P450 enzymes are heme containing mono-oxygenases that mainly react through oxygen atom transfer. Specific features of substrate and oxidant that determine the reaction rate constant for oxygen atom transfer are still poorly understood and, therefore, we did a systematic gas-phase study on reactions by iron(IV)-oxo porphyrin cation radical structures with arenes. We present here the first results obtained by using Fourier transform-ion cyclotron resonance mass spectrometry and provide rate constants and product distributions for the assayed reactions. Product distributions and kinetic isotope effect studies implicate a rate determining aromatic hydroxylation reaction that correlates with the ionization energy of the substrate and no evidence of aliphatic hydroxylation products is observed. To further understand the details of the reaction mechanism, a computational study on a model complex was performed. These studies confirm the experimental hypothesis of dominant aromatic over aliphatic hydroxylation and show that the lack of an axial ligand affects the aliphatic pathways. Moreover, a two parabola valence bond model is used to rationalize the rate constant and identify key properties of the oxidant and substrate that drive the reaction. In particular, the work shows that aromatic hydroxylation rates correlate with the ionization energy of the substrate as well as with the electron affinity of the oxidant.*

**Published Reference:**

Cantu-Reinharrd, F.G. Sainna, M.A. Upadhayay, P. Balan, A. Kumar, D. Fornarini, S. Crestoni, M.E. De Visser, S.P. 2016. A Systematic Accunt on Aromatic Hydroxilation by a Cytochrome P450 Model Compound I: A Low pressure mass spectrometry and computational study. *Chem. Eur. J.* 2016, 51, 18608-18619.

## 5.1 Introduction

Aromatic hydroxylation is a challenging catalytic reaction because a very strong C–H bond of a substrate needs to be broken in the process. Several enzymes in nature have developed procedures to enable an aromatic hydroxylation or even a deoxygenation (Costas et.al. 2004; Abu-Omar et.al. 2007; Comba et.al. 2009; de Visser et.al. 2011). Among those are the nonheme iron dioxygenases that regio- and stereospecifically dihydroxylate an aromatic substrate into a catechol (Solomon et.al. 2000; Kryatov et.al. 2005; Bruijnincx et.al. 2008; Costas, 2011; McDonald et.al. 2013; Nam e.al. 2014). Highly relevant for environmental purposes are, for instance, the naphthalene dioxygenases that have functions in biotechnology that include the cleaning up of oil-spills and removal of aromatic compounds from soil (Karlsson et.al. 2003). Also, in the human body applications of heme and nonheme iron dioxygenases are found, for instance, for the biodegradation of aromatic amino acids starting with a mono- or dihydroxylation reaction (Bugg, 2003; Kovaleva et.al.2007; Fetzner et.al. 2010). Further arene activating enzymes in the body include the thiolate-ligated heme mono-oxygenases called cytochromes P450 (P450) that have been shown to hydroxylate arenes to phenols as a means to metabolize drugs as well as xenobiotic molecules in the liver (Sono et.al. 1996; Groves, 2003; Meunier et.al. 2004; Ortiz de Montellano, 2005; Munro et.al. 2007; Grogan et.al. 2011; Kadish et.al. 2010; Poulos, 2014).

The full details of the mechanism of the latter processes are still shrouded in many mysteries and so far no experimental reaction rates have been obtained. Progress in understanding the P450-type reaction mechanisms has been made in the fields of computational chemistry and low-pressure mass spectrometry (Shaik et.al. 2005; Blomberg et.al. 2014; Lanucara et.al. 2011; Crestoni et.al. 2005; Chiavarino et.al. 2008; Crestoni et.al. 2009; Crestoni et.al. 2010). In particular, some of us have utilized Fourier transform-ion cyclotron resonance mass spectrometry (FT-ICR MS) to trap and characterize a pentacoordinated model complex of the active species of P450 enzymes (Compound I, CpdI) (Crestoni et.al. 2007). We have utilized this experience and measured low-pressure thermal rate constants of aromatic hydroxylation by this CpdI model for the first time and present these results here.

P450 CpdI is a high-valent iron(IV)-oxo heme cation radical, which is bound to the enzyme through a thiolate bridge of a conserved cysteinate residue. It has been spectroscopically trapped and characterized at low temperature for one specific isozyme, but for only very few substrates experimental rate constants could be determined due to its short lifetime (Rittle et.al. 2010). As such much has to be gained from understanding the reactivity patterns of CpdI with substrates and particularly on the regioselectivity and bifurcation patterns leading to a variety of products. On the other hand, CpdI and its reactivity patterns with substrates have been extensively studied with computational methods and detailed mechanisms of aromatic and aliphatic hydroxylation as well as sulfoxidation were established (Green, 1999; Ogliaro et.al. 2000; Li et.al. 2012; de Visser et.al. 2012).

Figure 5.1 shows the active site description of P450 CYP120A1 with the heme and its link to $Cys_{391}$ highlighted. These crystal structure coordinates contain retinoic acid as substrate in the vicinity of the heme on its distal site (Kuhnel et.al. 2008). CpdI was shown to be a versatile oxidant and to react efficiently with a variety of different substrates. In our previous work we reported a combined mass spectrometric and computational study on a biomimetic model of CpdI, where the protoporphyrin IX was replaced by 5,10,15,20-tetrakis(pentafluorophenyl) porphyrin (TPFPP), Figure 5.1b (Sainna et.al. 2015). The ensuing $[Fe^{IV}(O)(TPFPP^{+\bullet})]^{+}$ cation was trapped in the cell of an FT-ICR mass spectrometer and its reactivity studied with a selection of olefins.

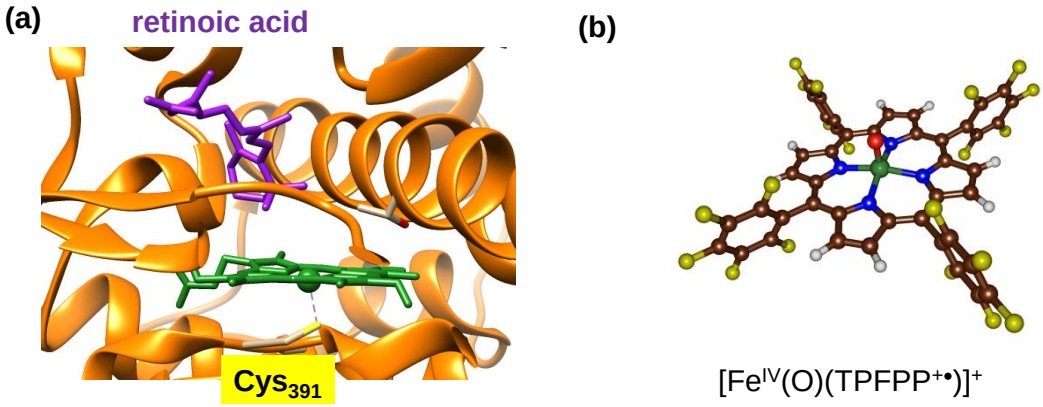


**Figure 5.1.** Enzymatic and biomimetic models of cytochrome P450 CpdI. (a) Active site structure as taken of substrate bound-resting state P450 from the 2VE3 pdb file. (b) Biomimetic model investigated here.

These studies established rate constants for olefin epoxidation showing them to correlate with the ionization energy (IE) of the substrate that is activated. Subsequently, density functional theory (DFT) calculations confirmed the observed trend and using a valence bond (VB) scheme highlighted the major components of the oxidant and substrate that contribute to the free energy of activation. To gain further insight into the reactivity patterns of CpdI model complexes using a combined FT-ICR MS and DFT approach, we decided to follow up our studies with work on aromatic hydroxylation. We propose a nucleophilic addition pathway as rate determining reaction step, whereby the rate is determined by the ionization potential of the substrate and the $\pi/\pi^*$ energy splitting of the CpdI models as well as electron reorganization energies within the complex. Furthermore, it is found that the removal of the axial cysteinate ligand as in the FT-ICR MS model used here raises the energies of the aliphatic hydroxylation pathways dramatically and prevents these product channels. The studies, therefore, give evidence of the axial ligand to be crucial in determining the activity and potential of the reactive oxidant of P450 enzymes.

## 5.2 Results

### 5.2.1 Experiment

In previous work, we established working procedures for the trapping of high-valent transition metal-oxo intermediates in an FT-ICR MS (Lanucara et.al. 2011; Crestoni et.al. 2005; Chiavarino et.al. 2008; Crestoni et.al. 2009; Crestoni et.al. 2010; Sainna et.al. 2015) These studies identified structures with m/z 1044 in the mass spectrum representing $[Fe^{IV}(O)(TPFPP^{+\bullet})]^+$ ions in good abundance and with long enough lifetime to enable ion-molecule reactions in the gas-phase. These procedures enabled us to do a systematic study into olefin epoxidation by these ions (Sainna et.al. 2015) which established reactivity trends and a model that accounts for the observed reactivity. We decided to follow the study up with a systematic account on arene hydroxylation processes. In particular, a series of 16 aromatic substrates were investigated and their second-order rate constants ($k_{exp}$) in a reaction with $[Fe^{IV}(O)(TPFPP^{+\bullet})]^+$ determined. Note that due to bifurcation processes multiple reaction channels and products are possible leading to aromatic and aliphatic hydroxylation products. Using ADO theory (see Methods), the experimental rate constants were converted into reaction efficiencies ($\Phi$) that represent the fraction of reactive collisions.

Table 5.1 summarizes the experimentally determined reaction rates for all substrates as well as their individual product distributions. Also included are ionization energies (IE) taken from the NIST database (See NIST[1] in references). Thus, the reaction of $[Fe^{IV}(O)(TPFPP^{+\bullet})]^{+}$ with arenes typically gives two reaction channels, namely oxygen atom transfer (OAT) and an addition process (Add), see Scheme 5.1. The OAT reaction leads to the formation of $[Fe^{III}(TPFPP)]^{+}$ ions with m/z 1028, and, consequently release of oxygenated substrate. In addition, in several cases an adduct complex is observed with mass corresponding to $[Fe^{III}(TPFPP)(SubO)]^{+}$, whereby Sub represents the substrate.

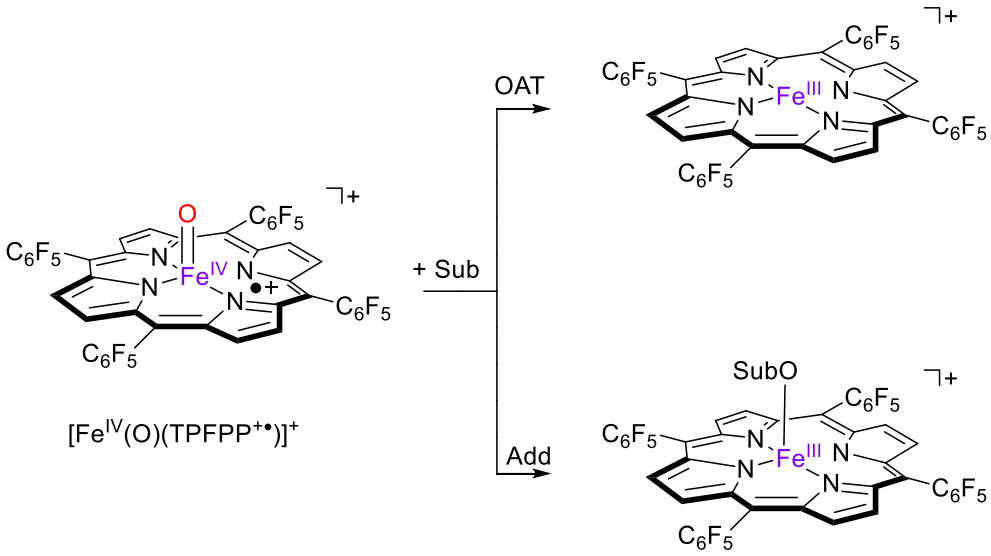


**Scheme 5.1.** Reaction products observed from the reaction of [FeIV(O)(TPFPP+•)]+ with arenes (Sub).

**Table 5.1.** FT-ICR MS reactivity of $[FeIV(O)(TPFPP^{+\bullet})]^{+}$ with arenes: Second-order rate constants, reaction efficiencies and product distributions (OAT and Add)

| Substrate | IE [a] | $k_{exp}$ [b, c] | $k_{ADO}$ [b] | $\Phi_{OAT}$ | $\Phi_{Add}$ | %OAT | %Add |
|---|---|---|---|---|---|---|---|
| benzaldehyde | 9.50 | 0.15 | 11.4 | – | 1.3 | 0 | 100 |
| α-[$D_1$]-benzaldehyde | 9.50 | 0.14 | 11.4 | – | 1.2 | 0 | 100 |
| benzene | 9.20 | 0.012 | 8.8 | 0.14 | – | 100 | – |
| toluene | 8.80 | 0.36 | 9.2 | 3.1 | 0.78 | 80 | 20 |
| ethylbenzene | 8.77 | 0.58 | 9.5 | 4.3 | 1.8 | 70 | 30 |
| [$D_5$]-ethylbenzene | 8.77 | 0.56 | 9.5 | 4.2 | 1.7 | 72 | 28 |
| [$D_{10}$]-ethylbenzene | 8.77 | 0.57 | 9.5 | 4.4 | 1.6 | 73 | 27 |
| i-propylbenzene | 8.73 | 1.2 | 10.0 | 7.8 | 4.2 | 65 | 35 |
| t-butylbenzene | 8.68 | 1.0 | 10.0 | 9.5 | 0.5 | 95 | 5 |
| o-xylene | 8.56 | 1.4 | 9.5 | 9.5 | 5.2 | 65 | 35 |
| [$D_4$]-o-xylene | 8.56 | 1.4 | 9.5 | 9.1 | 5.6 | 62 | 38 |
| [$D_6$]-o-xylene | 8.56 | 1.3 | 9.5 | 8.9 | 4.8 | 65 | 35 |
| m-xylene | 8.55 | 1.6 | 9.5 | 15.8 | 1.2 | 93 | 7 |
| p-xylene | 8.44 | 1.3 | 8.9 | 9.4 | 5.1 | 65 | 35 |
| mesitylene | 8.40 | 1.9 | 9.0 | 12.6 | 8.4 | 60 | 40 |
| naphthalene | 8.14 | 0.93 | 9.1 | 7.6 | 2.4 | 76 | 24 |

[a] from NIST database, in eV. [b] second-order rate constants (kexp) in units of $10^{-10}$ $cm^3$ $molecule^{-1}$ $s^{-1}$, at the temperature of the FT-ICR cell (300K). [c] The estimated error is ±30%; the internal consistency of the data is within ±10%.

Figure S1 in the Supplementary Information shows an example of a mass spectrum recorded along the kinetic run for the reaction of $[Fe^{IV}(O)(TPFPP^{+\bullet})]^{+}$ with toluene at 3.8 x $10^{-8}$ mbar and displays signals at 120 s reaction time for the reactant $[Fe^{IV}(O)(TPFPP^{+\bullet})]^{+}$ centered at m/z 1044, product ions $[Fe^{III}(TPFPP)]^{+}$ at m/z 1028, and $[Fe^{III}(TPFPP)(SubO)]^{+}$ at m/z 1136.

The actual formation of an oxidation product remaining in the coordination sphere of $[Fe^{III}(TPFPP)]^+$ assigned to the $[Fe^{III}(TPFPP)(SubO)]^+$ ion at m/z 1136 has been verified by isolating the complex and submitting it to low-energy collision induced dissociation. As shown in Figure S2, the ion at m/z 1136 undergoes fragmentation releasing $[Fe^{III}(TPFPP)]^+$ by loss of SubO, namely the oxidation product of toluene. Additional evidence for the formation of a SubO ligand is inferred from a reaction that is observed at longer reaction times whereby the $[Fe^{III}(TPFPP)(SubO)]^+$ ion undergoes a ligand substitution process by a Sub molecule, the neutral present in the FT-ICR cell, to give $[Fe^{III}(TPFPP)(Sub)]^+$. This process is clearly observed for the reaction of benzaldehyde. In this case, one finds that the efficiency for the $[Fe^{III}(TPFPP)(SubO)]^+$ + Sub → $[Fe^{III}(TPFPP)(Sub)]^+$ + SubO reaction is less than 1.3% (this value represents the efficiency for the $[Fe^{IV}(O)(TPFPP^{+\bullet})]^+$ + Sub → $[Fe^{III}(TPFPP)(SubO)]^+$ reaction, with Sub equal to benzaldehyde).

On this basis, an indirect probe for the structure of $[Fe^{III}(TPFPP)(SubO)]^+$ ions has been sought by forming distinct model complexes and studying their gas phase reactivity towards benzaldehyde. In methanol solution $[Fe^{III}(TPFPP)]^+$ reacts with both (m/p)-hydroxy-benzaldehyde and benzoic acid to give an addition complex which is delivered by electrospray ionization (ESI) into the gas phase, led into the ICR cell and tested for bimolecular reactivity with benzaldehyde. The complex with benzoic acid is found to be substantially more reactive in the ligand transfer process than both complexes with (m/p)-hydroxy-benzaldehyde (reaction efficiencies are equal to 14% and ca. 0.60%, respectively, Eq 5.1 – 5.3). This result is indicative that the gas phase oxidation of benzaldehyde by $[Fe^{IV}(O)(TPFPP^{+\bullet})]^+$ is directed at the aromatic ring rather than at the formyl group. The same experiment could not be extended to other substrates, given the scant ligand transfer reactivity typically displayed by arenes, but this outcome in the favorable case of benzaldehyde suggests that $[Fe^{IV}(O)(TPFPP^{+\bullet})]^+$ prefers attack at the aromatic ring rather than at a side chain substituent.

$[Fe^{III}(TPFPP)(C_6H_5COOH)]^+ + C_6H_5CHO$
$\rightarrow [Fe^{III}(TPFPP)(C_6H_5CHO)]^+ + C_6H_5COOH$, $\Phi$ = 14% (5.1)

$[Fe^{III}(TPFPP)(p\text{-}OH\text{-}C_6H_4CHO)]^+ + C_6H_5CHO$
$\rightarrow [Fe^{III}(TPFPP)(C_6H_5CHO)]^+ + p\text{-}OH\text{-}C_6H_4CHO$, $\Phi$ = 0.64% (5.2)

$[Fe^{III}(TPFPP)(m\text{-}OH\text{-}C_6H_4CHO)]^+ + C_6H_5CHO$
$\rightarrow [Fe^{III}(TPFPP)(C_6H_5CHO)]^+ + m\text{-}OH\text{-}C_6H_4CHO$, $\Phi$ = 0.56% (5.3)

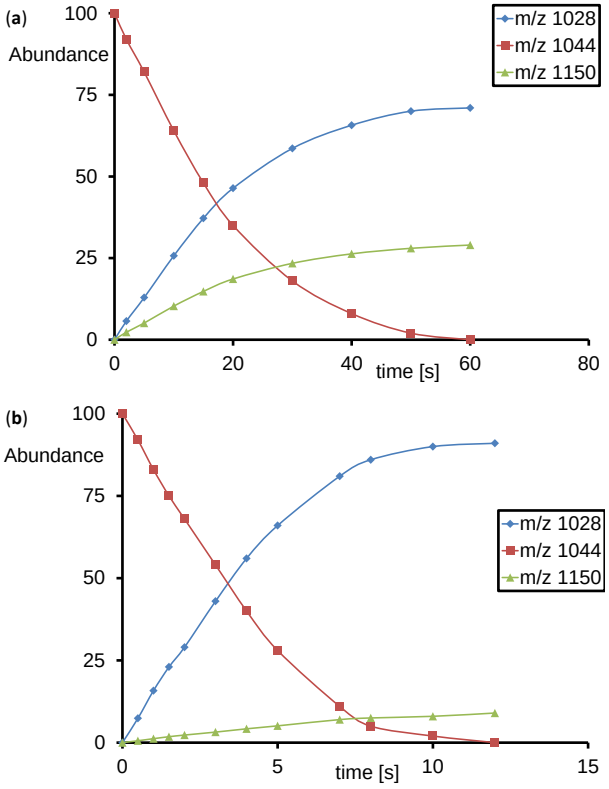


**Figure 5.2.** Ion distributions as a function of time for the reaction of $[Fe^{IV}(O)(TPFPP^{+\bullet})]^+$ with (a) ethylbenzene and (b) m-xylene.

As follows from Table 5.1 the rate constant ranges from 0.012 x $10^{-10}$ $cm^3$ $s^{-1}$ for the reaction of $[Fe^{IV}(O)(TPFPP^{+\bullet})]^+$ with benzene increasing to a value of 1.9 x$10^{-10}$ $cm^3$ $s^{-1}$ for the one with mesitylene. As such a spread of two orders of magnitude in rate constant is found for the series of substrates investigated here. In all cases (except for benzaldehyde) the dominant product complex obtained is the $[Fe^{III}(TPFPP)]^+$ ion representing the OAT channel. However, addition products are obtained in significant amounts with percentages of up to 40% (with mesitylene), whereas for benzaldehyde this is the sole reaction channel. Figure 5.2 displays the reactant and product abundancies as a function of time for the reaction of $[Fe^{IV}(O)(TPFPP^{+\bullet})]^+$ with ethylbenzene and m-xylene. The reactant ion abundance decays according to pseudo first-order kinetics as expected for a bimolecular reaction in the gas-phase. Thus, the

ion abundance at m/z 1044 decays slowly as a function of time as the $[Fe^{IV}(O)(TPFPP^{+\bullet})]^{+}$ reacts away and the decay patterns were used to establish the experimental second-order rate constants $k_{exp}$. In the case of ethylbenzene as a substrate (Figure 5.2a) two products are formed with m/z 1028 and m/z 1150 representing the OAT and Add channels. The shape of the curves shown in Figure 5.2 is used to determine the efficiencies $\Phi_{OAT}$ and $\Phi_{Add}$ described in Table 5.1. As follows the ratio of the abundancies of the OAT and Add channels are constant as a function of time for ethylbenzene as well as m-xylene with ratios of m/z 1028:m/z 1150 of 2.5 and 13, respectively. This implies that these products originate from the same source and most probably, product release from the iron(III) complex is a slow process.

To find out whether the reactivities and, in particular, the product distributions relate to aromatic or aliphatic hydroxylation pathways, we repeated some of the reactions with deuterated substrates. Thus, we tested ethylbenzene with all aliphatic hydrogen atoms replaced by deuterium ($[D_5]$-ethylbenzene) and fully deuterated ethylbenzene ($[D_{10}]$-ethylbenzene). As can be seen from Table 5.1, the substrate deuteration has a small but non-significant effect on the reaction efficiencies and product distributions. Therefore, it can be concluded that the reaction between $[Fe(O)(TPFPP^{+\bullet})]^{+}$ and ethylbenzene does not proceed with a rate-determining hydrogen atom abstraction. The indication is rather that these reactions with deuterated substrates strongly implicate an aromatic hydroxylation of substrates. The product ratios also suggest that an ethylphenol product (as obtained from ethylbenzene) is more strongly bound to the iron(III) complex than the dimethylphenol product obtained from m-xylene.

To further confirm the reactions as aromatic hydroxylation, we investigated o-xylene with all aromatic hydrogen atoms replaced by deuterium ($[D_4]$-o-xylene) and all aliphatic hydrogen atoms replaced by deuterium ($[D_6]$-o-xylene). Table 5.1 gives the product distributions and reaction efficiencies for o-xylene, $[D_4]$-o-xylene and $[D_6]$-o-xylene. Within our experimental error margin all reaction efficiencies, rate constants and product distributions are the same, which gives evidence that in the reaction of $[Fe(O)(TPFPP^{+\bullet})]^{+}$ with o-xylene no rate determining hydrogen atom abstraction takes place.

### 5.2.2 Theory

To support the experiments and gain insight into the details of the reaction mechanism, we followed the work up with an extensive density functional theory (DFT) study to establish reactivity trends. Our initial work was aimed at the aromatic hydroxylation mechanism of arenes by $^{4,2}[Fe^{IV}(O)(TPFPP^{+\bullet})]^{+}$, although we utilized a model without porphyrin substituents here, i.e. porphyrin (Por). The investigated arenes in this work were mesitylene (**1**), toluene (**2**), ethylbenzene (**3**), fluorobenzene (**4**), chlorobenzene (**5**), naphthalene (**6**), i-propylbenzene (**7**) and t-butylbenzene (**8**). Test calculations with the full TPFPP model were also performed but found to give only minor differences in structure and reactivity with respect to the smaller porphyrin complex without side groups (see Supporting Information). Figure 5.3 shows the aromatic hydroxylation reaction of the para-position of toluene (PhMe; henceforth indicated with the subscript 2 beside the label of the structure) by the doublet and quartet spin states of $[Fe^{IV}(O)(Por^{+\bullet})]^{+}$ as calculated with DFT as an example. Thus, the reaction starts with an electrophilic attack of the oxo group on the para-carbon atom of the substrate that via a transition state **TS1** leads to the intermediate **I1**. As shown previously by calculations on P450 model complexes, the ipso-proton is abstracted by the porphyrin group via transition state **TS2** to form the protonated porphyrin structure **I2**. Finally, the proton is relayed to the phenolate group via transition state **TS3** to form phenol products (**P**) (de Visser et.al. 2003; de Visser et.al. 2011).

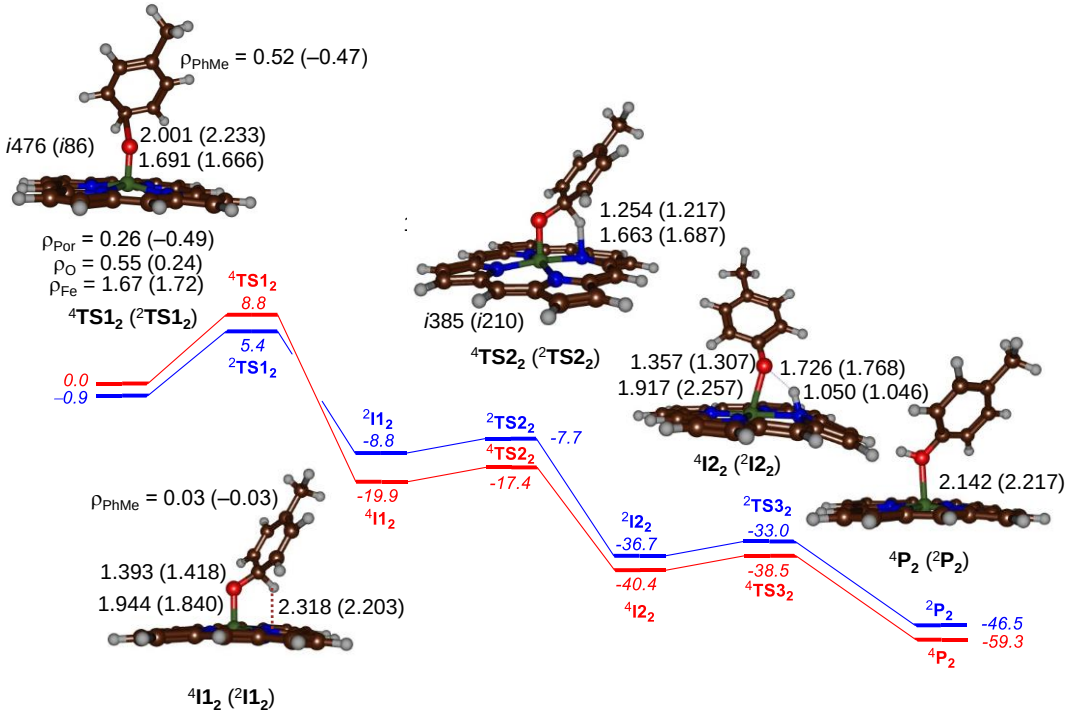


**Figure 5.3.** Potential energy profile (in kcal mol–1) of aromatic hydroxylation of toluene (PhMe) by $[FeIV(O)(Por^{+\bullet})]^{+}$ as calculated with DFT at UB3LYP/BS2//UB3LYP/BS1 level of theory. All data include ZPE corrections and are calculated relative to isolated reactants. Bond lengths are given in angstroms and group spin densities (ρ) in atomic units.

An analysis of the group spin densities and charges establishes the intermediates **I1** as cationic on the substrate moiety ($\rho_{PhMe}$ = 0.03/–0.03 in $^{4}$**I1**$_2$/$^{2}$**I1**$_2$), which implies that two electrons have transferred from substrate to oxidant. We made several attempts to find radical intermediates through the swapping of molecular orbitals, but in all of these cases the wave functions converged back to the cationic intermediates instead. Recent experimental studies of Asaka and Fujii found experimental evidence of fast electron transfer during the C–O bond formation step and hence support the formation of a cationic intermediate (Asaka et.al. 2016). After the cationic intermediates (**I1**) the substrate loses its ipso-proton to the porphyrin ring via a small reaction barrier of 2.5 kcal mol$^{-1}$ on the quartet spin state and 1.1 kcal mol$^{-1}$ on the doublet spin surface. This proton-transfer intermediate (**I2**) then relays the proton back to the phenolate oxygen atom to form phenol products via another transition state **TS3** lying close in energy to **I2**.

The rate determining step in the reaction mechanism, however, is the electrophilic addition step via **TS1**, which elongates the Fe–O bond to 1.691/1.666 Å in $^{4,2}$**TS1**$_2$ and has the substrate in an almost upright position. An analysis of the group spin densities ($\rho$) establishes it as a radical-type transition state with spin densities of 2.22 (1.96), 0.26 (–049) and 0.52 (–0.47) on the FeO, Por and PhMe groups, respectively, in $^4$**TS1**$_2$ ($^2$**TS1**$_2$). As the reactant state has an electronic configuration $\pi^*_{xz}{}^1\ \pi^*_{yz}{}^1\ a_{1u}{}^1$ with spin density of about 2 on the FeO group and 1 on the porphyrin ring, this implies that radical character on the porphyrin manifold is lost in the transition state. In particular, an electron transfer from substrate into the $a_{1u}$ orbital has occurred to create a transition state with configuration approximating $\pi^*_{xz}{}^1\ \pi^*_{yz}{}^1\ a_{1u}{}^2\ \phi_{PhMe}{}^1$.

After the transition state the system relaxes to the cationic intermediate **I1**, which involves a second electron transfer from the substrate to the metal to generate an intermediate with orbital occupation $\pi^*_{xz}{}^1\ \pi^*_{yz}{}^1\ \sigma^*_{z2}{}^1\ a_{1u}{}^2\ \phi_{PhMe}{}^0$. Geometrically, this second electron transfer and the single occupation of the $\sigma^*_{z2}$ orbital results in considerable lengthening of the Fe–O bond from 1.691 Å in $^4$**TS1**$_2$ to 1.944 Å in $^4$**I1**$_2$. At the same time the C–O distance shortens from 2.001 Å in the transition state to 1.393 Å in the intermediate.

In the subsequent step we located transition states for proton transfer from the ipso-position to one of the nitrogen atoms of the porphyrin ligand in the doublet and quartet spin states. These proton transfer barriers have a relatively small imaginary frequency, i385 cm$^{-1}$ ($^4$**TS2**$_2$) and i210 cm$^{-1}$ ($^2$**TS2**$_2$), as compared to typical hydrogen atom abstraction transition states where values of well over i1000 cm$^{-1}$ were found (Kumar et.al. 2014; Ji et.al. 2015).

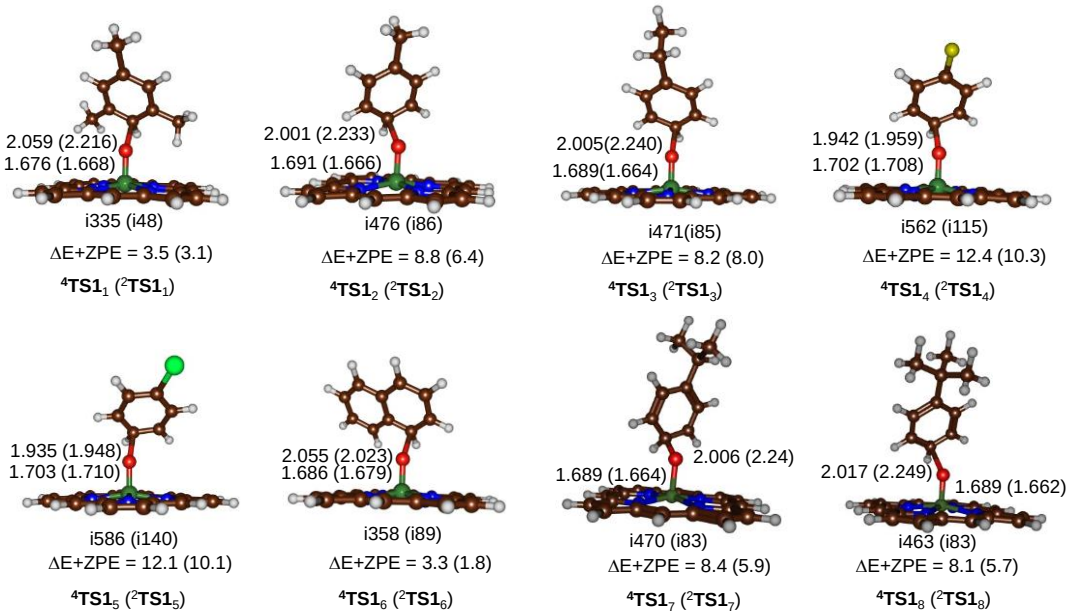


**Figure 5.4.** Optimized electrophilic addition transition states for the reaction of $^{4,2}[Fe^{IV}(O)(Por^{+\bullet})]^{+}$ with arenes. Barrier heights (in kcal mol$^{-1}$) given are relative to isolated reactants and calculated at UB3LYP/BS2//UB3LYP/BS1 level of theory. Bond lengths are in angstroms and imaginary frequencies in wave numbers.

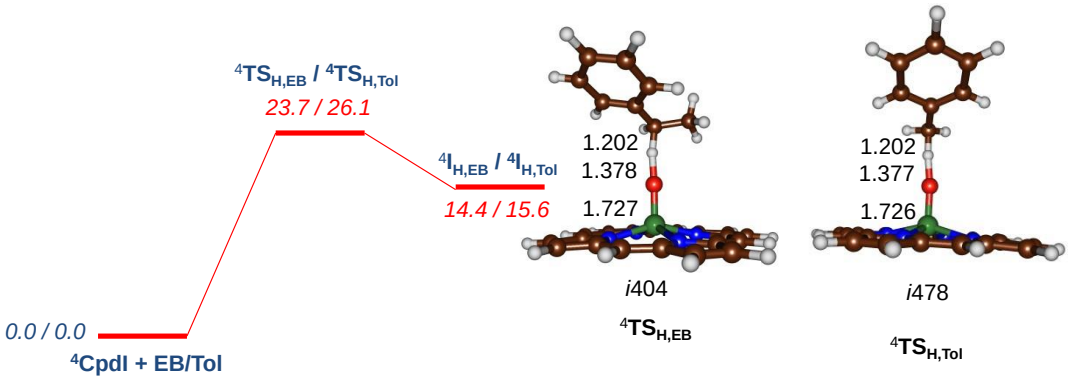


**Figure 5.5.** Aliphatic hydroxylation potential energy landscape as calculated at UB3LYP/BS2//UB3LYP/BS1 level of theory. Energies are in kcal mol$^{-1}$ and include ZPE correction, while geometries give bond distances in angstroms and the imaginary frequency in wave numbers.

From the **I2** intermediates another proton transfer leads to the phenol product complexes with high exothermicity. A small barrier **TS3** is obtained in both spin states. Overall, the aromatic hydroxylation reaction is stepwise with a rate determining electrophilic addition step with a barrier of $\Delta E^{\ddagger}$+ZPE = 8.8 (5.4) kcal mol$^{-1}$ on the quartet (doublet) spin states. These values compare well with previous studies of aliphatic and aromatic hydroxylation by iron(IV)-oxo porphyrin cation radical complexes (Sainna et.al. 2015; Kumar et.al. 2014; Pratter et.al. 2013).

Thereafter, we completed the investigation of $^{4,2}[Fe^{IV}(O)(Por^{+\bullet})]^{+}$ and its aromatic hydroxylation of a range of arenes and initially calculated the full landscape for chlorobenzene hydroxylation by $^{4,2}[Fe^{IV}(O)(Por^{+\bullet})]^{+}$, see Supporting Information for details. The landscape gives the same pattern as that seen for toluene in Figure 5.3 with a rate-determining electrophilic addition barrier **TS1**$_5$ leading to a cationic intermediate **I1**$_5$. Similarly to the toluene data reported above, $^{2}$**TS1**$_5$ is below $^{4}$**TS1**$_5$ as seen before in aromatic hydroxylation by P450 CpdI models (de Visser et.al. 2003; de Visser et.al. 2011). In addition, we calculated $^{4,2}$**TS1** and $^{4,2}$**I1** for the following substrates: mesitylene, ethylbenzene, fluorobenzene, naphthalene, i-propylbenzene and t-butylbenzene, whereby we give the label as a subscript after the structure name. In general, the same structural trends are observed in the quartet and doublet spin states and the mechanism is the same.

As can be seen strong geometric differences are found upon changing the para-substituent of the arene, whereby the $^{4}$**TS1** structures for fluorobenzene gives Fe–O and O–C distances of 1.703 and 1.942 Å, while with ethylbenzene these distances change to 1.689 and 2.005 Å, respectively. Similar differences are seen for the other complexes as well as in the value of the imaginary frequency in the transition state. Nevertheless, all **TS1** structures shown in Figure 5.4 represent the same electronic transition of electron transfer from arene to $a_{1u}$ and the accumulation of radical character on the arene group. Moreover, the transition state structures are geometrically alike with the substrate in virtually the same orientation in all cases. The occurrence of an electron transfer equilibrium preceding aromatic hydroxylation by a compound I model within a solvent cage has been highlighted (Asaka et.al. 2016). The electrophilic addition transition states shown in Figure 5.4 differ strongly in the barrier height and values of $\Delta E^{\ddagger}$+ZPE range from 1.8 kcal mol$^{-1}$ for $^{2}$**TS6** (naphthalene) to 12.4 kcal mol$^{-1}$ for $^{4}$**TS1**$_4$ (fluorobenzene). Nevertheless, all of them are radical type transition states with group spin densities similar to those reported for $^{4,2}$**TS1**$_2$ reported above in Figure 5.3.

To ascertain that the lowest energy pathway indeed is aromatic hydroxylation rather than aliphatic hydroxylation, we also calculated the aliphatic hydroxylation mechanisms of toluene and ethylbenzene by $^4[Fe^{IV}(O)(Por^{+\bullet})]^+$, see Figure 5.5. These reactions are also stepwise with an initial hydrogen atom abstraction via transition state $^4\mathbf{TS}_H$ that leads to a radical intermediate $^4\mathbf{I}_H$. In both aliphatic hydrogen atom abstraction transition states significant radical character ($\rho$ = –0.52 for both) is obtained. In a subsequent radical rebound barrier the OH group is transferred to substrate to form alcohol product complexes $^4\mathbf{P}_H$. The hydrogen atom abstraction is rate determining and has a relatively central transition state with elongated C–H distances of 1.202 Å for both toluene and ethylbenzene. In both structures the Fe–O bond has elongated to well over 1.7 Å.

Energetically, the hydrogen atom abstraction barriers are higher than the arene activation barriers **TS1** shown in Figure 5.4 by well over 15 kcal mol$^{-1}$. Therefore, the dominant pathway is expected to be aromatic hydroxylation of arenes by $[Fe^{IV}(O)(Por^{+\bullet})]^+$ and little or no aliphatic hydroxylation products should be observed. The $[Fe^{IV}(O)(Por^{+\bullet})]^+$ system, as a consequence, reacts sluggishly with aliphatic groups, in contrast to iron(IV)-oxo porphyrins with an anionic axial ligand. Previously, we and others showed that the barrier heights of aliphatic hydroxylation reactions correlate with the bond dissociation energy ($BDE_{OH}$) for the formation of the iron(IV)-hydroxo species from the iron(IV)-oxo species and a hydrogen atom (Meyer, J.M., 1998; de Visser, S.P., 2010). This implies that the $BDE_{OH}$ of the $[Fe^{IV}(O)(Por^{+\bullet})]^+$ system will be considerably smaller than that of P450 CpdI and unable to react via hydrogen atom abstraction. Indeed, we calculate a $BDE_{OH}$ for the reaction of $^3[Fe^{III}(OH)(Por^{+\bullet})]^+$ into CpdI and a hydrogen atom of $\Delta E+ZPE$ = 66.3 kcal mol$^{-1}$, whereas for a P450 CpdI model a value of 88.9 kcal mol$^{-1}$ was obtained (de Visser et.al. 2008). In aliphatic hydroxylation the energy of the hydrogen atom abstraction step is equal to the difference in $BDE_{CH}$ of the substrate and the $BDE_{OH}$ of the oxidant. The $BDE_{CH}$ of ethylbenzene is 82.5 kcal mol$^{-1}$ (de Visser et.al. 2011). In the case of $[Fe^{IV}(O)(Por^{+\bullet})]^+$, therefore, hydrogen atom abstraction from ethylbenzene will be endothermic by 16.2 kcal mol$^{-1}$, whereas the P450 CpdI model should give an exothermic hydrogen atom abstraction by –6.4 kcal mol$^{-1}$.

Indeed, the radical intermediate $^4\mathbf{I}_H$ for ethylbenzene as a substrate is 14.4 kcal mol$^{-1}$ higher in energy than reactants and, therefore, matches the difference in energy between $BDE_{OH}$ and $BDE_{CH}$ of oxidant and substrate. The endothermicity for the hydrogen atom abstraction reactions of substrates by $[Fe^{IV}(O)(Por^{+\bullet})]^+$ is too high and, therefore; this process will not be able to compete with lower energy reaction channels, such as substrate epoxidation and aromatic hydroxylation.

Thus, the efficiency and reaction rate constant of aliphatic hydroxylation was shown to be linearly correlated with $BDE_{OH}$ (de Visser, S.P., 2010), hence, the system without axial ligand, i.e. $[Fe^{IV}(O)(Por^{+\bullet})]^+$, has reduced catalytic efficiency for aliphatic hydroxylation. Clearly, the axial cysteinate ligand in P450 enzymes affects the reactivity properties of the oxo group and, thereby makes it a better oxidant. Electrophilic reactions, such as aromatic hydroxylation and epoxidation, however, tend to connect with the ionization energy of the substrate and the electron affinity of the oxidant (Kumar et.al. 2010), which is appropriate for $[Fe^{IV}(O)(Por^{+\bullet})]^+$ to perform these reactions.

### 5.3 Discussion

In this work a comprehensive overview of arene activation by $[Fe^{IV}(O)(Por^{+\bullet})]^+$ and $[Fe^{IV}(O)(TPFPP^{+\bullet})]^+$ is given as mimics of P450 CpdI reactivity with substrates. As some of the substrates have aliphatic substituents to the arene, our initial work focused on establishing the nature of the reaction products. Unfortunately, aliphatic and aromatic hydroxylation of arenes gives products with equal mass and as such cannot be distinguished by mass spectrometry. Moreover, the fragmentation patterns of the products did not give direct evidence of what pathway was followed either. Hence, FT-ICR MS cannot distinguish the two products directly. We, therefore, repeated the experiments with deuterium labelled compounds, which gave only minor changes to the rate constants and implicated that the rate determining step does not include a hydrogen atom abstraction.

To gain further insight into the details of the reaction mechanism and the bifurcation processes computational modelling was performed. In particular, DFT studies on the relative barriers for aliphatic versus aromatic hydroxylation reactions were performed (Figures 5.4 and 5.5) and confirmed the latter to be well lower in energy. As such, in

the gas-phase the $[Fe^{IV}(O)(TPFPP^{+\bullet})]^{+}$ complex will preferentially react via aromatic hydroxylation over aliphatic hydroxylation with substrates. Nam et.al. (Song et.al. 2005) studied the aliphatic versus aromatic hydroxylation of ethylbenzene by $[Fe^{IV}(O)(TPFPP^{+\bullet})(X)]$ with X = $Cl^{-}/CF_3SO_3^{-}$ in dichloromethane. Aliphatic hydroxylation products were obtained with $[Fe^{IV}(O)(TPFPP^{+\bullet})(Cl)]$ as an oxidant, whereas aromatic hydroxylation products were detected in a reaction with $[Fe^{IV}(O)(TPFPP^{+\bullet})(CF_3SO_3)]$. Subsequent computational modelling showed that the axial ligand affects the electron affinity and O–H bond strength (bond dissociation energy, $BDE_{OH}$) and hence affected the relative barriers of aliphatic versus aromatic hydroxylation (de Visser et.al. 2011; de Visser, S.P., 2006). To gain further insight into the intricate details of the bifurcation processes, below we will show a molecular orbital and valence bond interpretation of the mechanisms, but first we will discuss the experimental reaction trends.

To find trends and a rationale in the obtained rate constants and particularly find evidence on the properties of the catalyst/oxidant that determines the reaction process, we decided to search for physicochemical properties of substrate and oxidant in correlation with the rate constant. These analyses should give insight into the fundamental properties of P450 CpdI and how it is able to activate arenes. To this end, we decided to plot the natural logarithm of the rate constant against physical chemical properties of the substrate and oxidant, including the ionization energy of the substrate. Thus, previously it was shown that reactions starting with a rate-determining hydrogen atom abstraction generally correlate with the strength of the C–H bond that is broken, i.e. the bond dissociation energy ($BDE_{CH}$) (Mayer, J.M., 2004; Kaizer, et.al. 2004; Yoon et.al. 2009; Goldberg, D.P., 2007; Kang et.al. 2009; Shaik et.al. 2011; Kumar et.al. 2012). However, aromatic hydroxylation pathways by metal-oxo complexes were shown to connect to the ionization energy (IE) of the substrate (Shaik et.al. 2011; Kumar et.al. 2012).

Figure 5.6 displays plots of the natural logarithm of the experimentally determined rate constant versus the ionization energy of the substrate (part a) and the $BDE_{CH}$ value of the aliphatic group of the substrate (part b). As can be seen from Figure 5.6, the ionization energy of the substrate follows a linear correlation with the ln $k_{exp}$ value with an $R^2$ value of 0.88. Interestingly, the rate constants for benzene and naphthalene activation by $[Fe^{IV}(O)(TPFPP^{+\bullet})]^{+}$ do not fit the trend. This may be due to the fact that

these substrates approach the oxidant differently and give extra interactions with the oxidant. Aromatic hydroxylation, similarly to double bond epoxidation, therefore, gives rate constants that are proportional to the IE of the substrate involved (Shaik et.al. 2011; Kumar et.al. 2012) This means that any oxidant reacting with a substrate containing an arene and a double bond as a separate group will give preferential aromatic hydroxylation rather than double bond epoxidation.

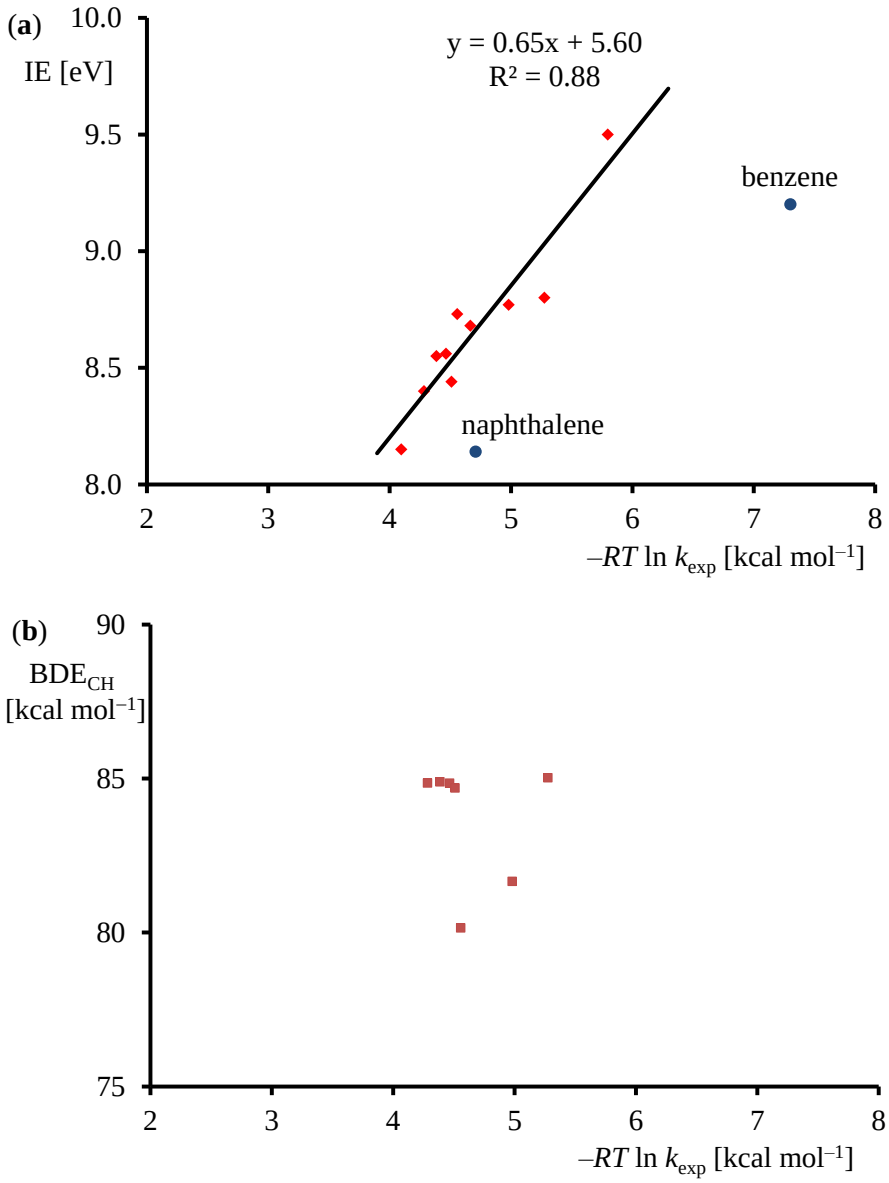


**Figure 5.6.** Correlation of the natural logarithm of the rate constant with (a) ionization energy from the substrate. (b) $BDE_{CH}$ value of the aliphatic group of the substrate. Ionization energies taken from the NIST Database (NIST). $BDE_{CH}$ values calculated with DFT at B3LYP/BS2//UB3LYP/BS1 including ZPE corrections.

For the set of substrates with aliphatic substituents also a plot of ln $k_{exp}$ versus $BDE_{CH}$ was attempted (Figure 5.6b), however, no correlation is found. Based on this evidence the aliphatic hydroxylation pathway can be ruled out as a viable mechanism for arene activation by $[Fe^{IV}(O)(TPFPP^{+\bullet})]^{+}$ and based on the reactivity trends as well as the KIE values, the dominant pathway is aromatic hydroxylation.

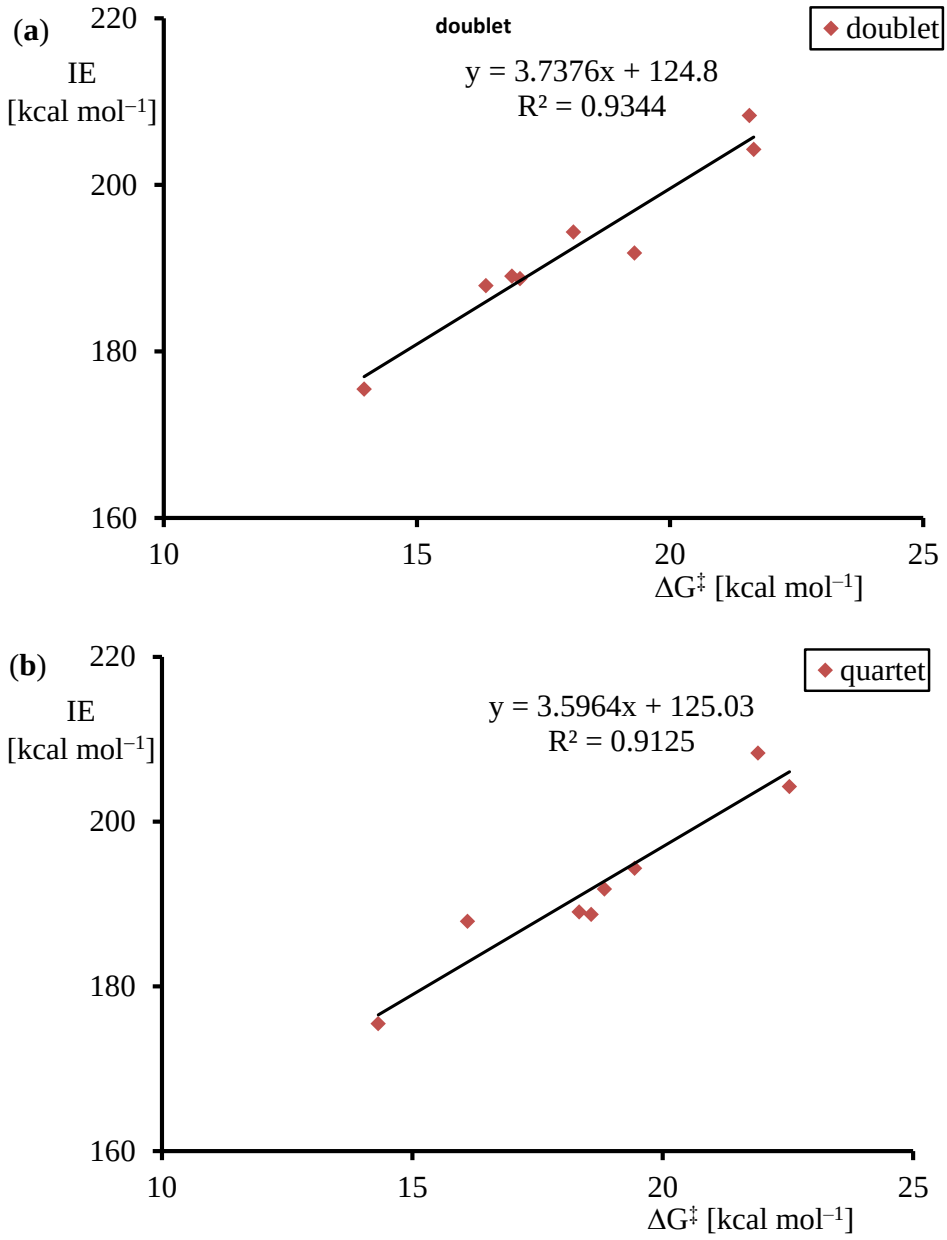


**Figure 5.7.** Correlation of the computationally determined free energy of activation of aromatic hydroxylation (**TS1**) with calculated ionization energy of the substrate.

Figure 5.7 gives the corresponding plot for the correlation between the ionization energy and the computationally determined aromatic hydroxylation free energy of activation calculated for the various $^{4,2}$**TS1** structures for the substrates in Figure 5.4. In agreement with the experimental result, a linear correlation between barrier height and ionization energy is found with an $R^2 = 0.91$ (quartet) and 0.93 (doublet). As such, both experimental reaction rates and computational barrier heights implicate a linear correlation between the natural logarithm of the rate constant and ionization energy. As both experiment and theory give the same correlation, of course, the experimental rates also correlate linearly with the computational barrier heights. Moreover, using the found trends, this enables us to predict reaction rates of alternative substrates. For instance, the rate constants for aromatic hydroxylation of chlorobenzene and fluorobenzene could not be measured. However, the trend from Figures 5.6a and 5.7a enable us to predict their values as 4.8 and $5.0 \times 10^{-11}$ ($cm^3$ $molecule^{-1}$ $s^{-1}$) respectively. Similarly, we predict barrier heights at B3LYP level of theory from the experimental trend in Figure 6a of $\Delta G$ = 19.5, 19.9 and 24.4 kcal $mol^{-1}$ for i-propylbenzene, t-butylbenzene and benzaldehyde, respectively, whereas values of $\Delta G$ = 18.8, 19.2 and 19.3 kcal $mol^{-1}$ are expected for m-, o-, and p-xylene. As such the two plots from Figure 5.6 and 5.7 enable one to predict experimental rates from computational trends or computational barriers from experimental trends. To verify the accuracy of this procedure we predicted the DFT barriers for toluene, ethylbenzene and mesitylene from the trend in Figure 5.6a and find values of $\Delta G$ = 22.3, 21.2 and 16.4 kcal $mol^{-1}$, respectively, which are within a mean error of 2.8 kcal $mol^{-1}$ of the DFT calculated results (Supporting Information).

Electronically, the fact that the trends correlate with ionization energy implicate that the electron transfer from substrate to oxidant will determine the reaction rate. The trends in reactivity also imply that none of the products observed in the mass spectra can correlate with aliphatic hydroxylation products. Therefore, the product ions with m/z 1028 and m/z 1150 (Figure 5.2) originate from the aromatic hydroxylation of substrates. Clearly, product release from the iron(III) complex is a slow process and a mixture of metal ligated and free phenol products are obtained.

Evidently, the rate constant and reactivity patterns of the iron(IV)-oxo porphyrin complex with arenes is dependent on key properties of the oxidant and substrate. In order to improve catalyst design and find novel oxidants for this reaction process, we delineated the transition state barrier into fundamental properties of oxidant and substrate. This analysis identifies the origin of the reaction mechanism and explains how the oxidant can be further improved for better catalysis.

To understand the obtained trends and correlations we used a parabolic approximation of previously described VB models to explain the reaction barrier (Shaik, S.S., 1981; Shaik, S.S., 2010). Figure 5.8 displays the basic features of the two-parabola crossing model, where we assume the reactant complex (**R**) to reside in a local minimum that can be described by a parabola with function $y_R = ax^2$ with $y_R$ being the energy function of the reactant complex, $x$ the reaction coordinate and $a$ is a constant that describes the curvature of the reaction coordinate function. The reactant complex is defined as the starting point of the reaction with coordinates $x_R = 0$ and $y_R = 0$. For the product complex we describe the potential energy surface with another parabola that is shifted from the reactant parabola and hence has function $y_P = bx^2 + cx + d$ with $b$, $c$, and $d$ some constants that describe the curvature and extremes of the parabola. We now assume that the product local minimum is located at a reaction coordinate with value $x = 1$ and the transition state at the half-way point ($x = ½$). That means the two curves for $y_R$ and $y_P$ will cross at $x_{cross} = ½$ and create a crossing point, at energy $y_P(½) = \Delta E_{cross}$, which will ultimately lead to an avoided crossing and a transition state for the reaction. One can see from Figure 5.8 that $y_P(0) = d = E_{FC,\mathbf{R}}$, whereby $E_{FC,\mathbf{R}}$ represents the Franck-Condon energy at the reactant geometry. Furthermore, $y_P(1)$ is equal to the driving force for the reaction ($\Delta E_{rp}$). Using the information for the first derivative of $y_P$ at the point $x = 1$, i.e. $y_P'(1) = 0$, we can now derive Eq 5.4 for $y_P(½)$ as a function of the driving force for the reaction and the Franck-Condon energy at the reactants geometry.

$$y_P(½) = \Delta E_{cross} = \frac{1}{4} E_{FC,\mathbf{R}} + \frac{3}{4} \Delta E_{rp} \qquad (5.4)$$

The actual transition state, however, with energy $\Delta E^{\ddagger}$ will be below the crossing point by an amount $B$ that represents the resonance energy, Eq 5.5.

$$\Delta E^{\ddagger} = \Delta E_{cross} - B \qquad (5.5)$$

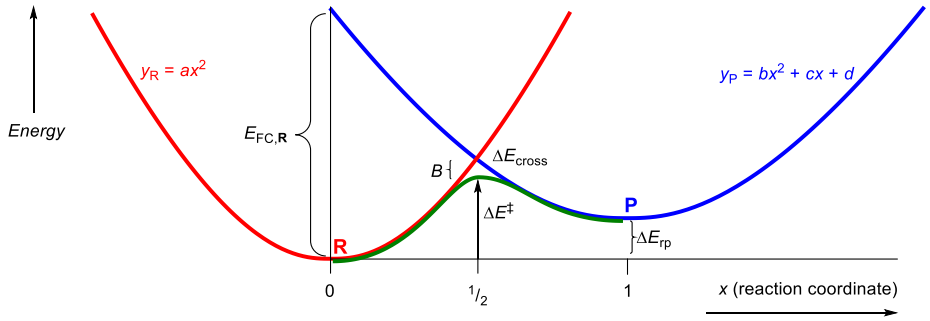


**Figure 5.8.** Two-parabola curve crossing model for the prediction of barrier heights.

Using Eqs 5.4 and 5.5 we can predict the barrier height for the reaction in terms of the driving force for the reaction ($\Delta E_{rp}$), the change in electronic configuration between the reactant and product state in the geometry of the reactants ($E_{FC,\mathbf{R}}$) and the resonance energy $B$. Values for the driving force are taken as the difference in energy ($\Delta E$+$ZPE$) between reactant complex (**R**) of $^4$CpdI and substrate with the radical intermediate $^4$**I1**.

**Figure 5.9** shows the curve crossing diagram with key valence bond (VB) structures of critical points along the reaction mechanism. The difference in VB structure between the reactant and product structures in the geometry of the reactants will determine the value of $E_{FC,\mathbf{R}}$. These diagrams have been used previously to rationalize barrier heights of chemical reactions and explain what features of substrate and oxidant affect the value of the barrier height (Kumar et.al. 2010; Shaik et.al. 2008; Kumar et.al. 2013).

The diagram starts on the bottom-left with the reactant configuration of $[Fe^{IV}(O)(Por^{+\bullet})]^{+}$ and arene. Thus, in the ground state the system has three unpaired electrons distributed over the $\pi^*_{xz}$, $\pi^*_{yz}$ and $a_{1u}$ molecular orbitals. The $\pi_{xz}/\pi^*_{xz}$ and $\pi_{yz}/\pi^*_{yz}$ molecular orbitals represent the bonding and antibonding combinations of 3d orbitals on Fe with 2p orbitals on oxygen.

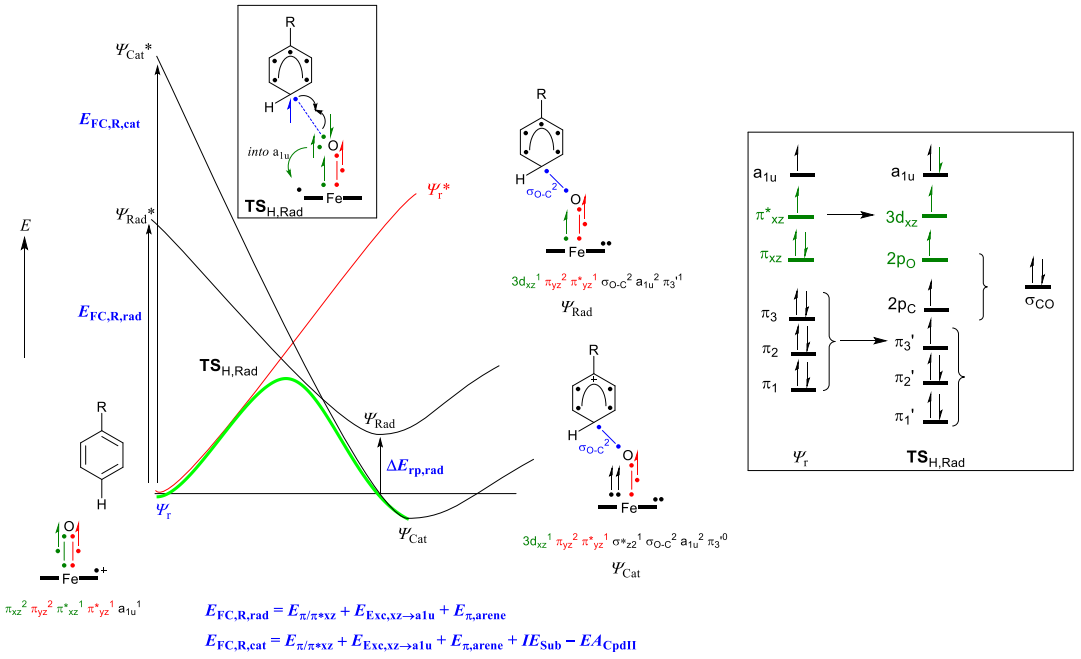


**Figure 5.9.** Valence bond curve crossing diagram and orbital/bonding changes along the electrophilic addition pathway of arene activation by $[Fe^{IV}(O)(Por^{+\bullet})]^{+}$. Valence bond structures give electrons as dots. Orbital occupation and hybridization changes are indicated with the orbital diagram.

The $a_{1u}$ orbital is a nonbonding π-orbital on the porphyrin ring and is close in energy to the $a_{2u}$ orbital. In previous work on $[Fe^{IV}(O)(Por^{+\bullet})]^{+}$ we found several close-lying electronic states with either doublet or quartet spin and single occupation of $a_{1u}$ or $a_{2u}$ (Sainna et.al. 2015). The three green dots along the Fe–O bond in Figure 5.9 represent the $\pi_{xz}/\pi^*_{xz}$ electrons, while the ones in red are the $\pi_{yz}/\pi^*_{yz}$ electrons. Both set of $\pi/\pi^*$ orbitals form a three-electron bond along the Fe–O group. Upon formation of the intermediate complex either a radical or cationic structure is formed. In both cases the C–O bond is formed from one of the electrons of the π-cloud of the substrate plus an electron from the $\pi_{xz}/\pi^*_{xz}$ system. This means that electrophilic addition will result in the breaking of the π–system of the substrate and the set of six electrons in the substrate π--system ($\pi_1$, $\pi_2$ and $\pi_3$ orbitals), will be split into a $2p_C$ atomic orbital for one carbon and a conjugated π-system over the remaining five carbon atoms with orbitals $\pi_1$', $\pi_2$' and $\pi_3$'. Breaking the π-cloud of the substrate, will cost the system an energy $E_{\pi,arene}$. Of course, the breaking of the π-cloud will also be correlated to the excitation energy in the π-system as well as the ionization energy for removal of an electron from one of the π-orbitals.

As such, the barrier height and the driving force for the reaction are likely to correlate with the ionization energy of the substrate as indeed shown in Figure 5.6a and 5.7. By contrast, the cationic pathway will more likely be connected to the second ionization energy of the substrate as apart from the breaking of the π-orbitals of the substrate also an electron will have to transfer to the oxidant.

In the calculations presented in Figures 5.3 and 5.4 the intermediates are of a cationic nature with an electronic configuration of $3d_{xz}^1\ \pi_{yz}^2\ \pi^*_{yz}{}^1\ \sigma^*_{z2}{}^1\ a_{1u}^2\ \pi'^0_3$ with spin density of less than 0.1 on the aromatic ring and a value of about 3 on the FeO unit. Interestingly, the transition states gives significant radical character on the aromatic ring, typically 0.50 – 0.70, so that these transition states should be considered as radical-type transition states connecting the reactants with the radical intermediates. For the estimation of the barrier heights from the VB structures, therefore, we will use the driving force to reach the radical intermediates, $\Delta E_{rp,rad}$. On the oxidant side of the reaction, a number of electron transfer and orbital reorganizations happen, which enable us to predict the value for $E_{FC,\mathbf{R},rad}$. Firstly, the $\pi_{xz}/\pi^*_{xz}$ set of orbitals (highlighted in green in the VB structures for the reactant and the transition state) split back into atomic orbitals ($3d_{xz}$ and $2p_O$), which will cost the system $E_{\pi/\pi^*xz}$ in energy. One of the electrons of $2p_O$ pairs up with the single electron in $2p_C$ and forms the new C–O bonding orbital $\sigma_{CO}$. The value of $E_{\pi/\pi^*xz}$ is determined from the relative energies of the two orbitals in the reactant complex and is 85.2 kcal mol$^{-1}$. The remaining two electrons stay on the metal-porphyrin side of the system and one of those electrons is promoted into the $a_{1u}$ orbital to fill it with a second electron with excitation energy $E_{Exc,xz\rightarrow a1u}$. From the relative energies of the $\pi_{xz}$ and $a_{1u}$ orbitals in the reactant complex a value of 51.5 kcal mol$^{-1}$ is obtained. Finally, the Franck-Condon energy between the reactant and the radical state is dependent on the breaking of the π-system of the arene, $E_{\pi,arene}$. The overall Franck-Condon energy for the transition from the reactant to the radical state is given in Eq 5.6.

$$E_{FC,\mathbf{R},rad} = E_{\pi/\pi^*xz} + E_{Exc,xz\rightarrow a1u} + E_{\pi,arene} \qquad (5.6)$$

Using Eqs 5.4 – 5.6 we have estimated VB predicted barrier heights of ΔE+ZPE = 12.5, 12.1, 5.1 and 6.2 kcal $mol^{-1}$ for the reaction of $[Fe^{IV}(O)(Por^{+\bullet})]^{+}$ with chlorobenzene, fluorobenzene, toluene and ethylbenzene, respectively. These values are in good quantitative agreement with those obtained from full DFT optimizations and shown in Figures 5.3 and 5.4 above. As such, the two-parabola curve crossing diagram gives a good quantitative representation of the reaction mechanism and the kinetics obtained. Moreover, the model gives hints on the key electronic properties of oxidant and substrate that determine the rate determining reaction step.

Eq 5.6 shows that the barrier height for aromatic hydroxylation should be proportional to the excitation energy of the π-cloud of the substrate arene, which, of course, is proportional to the ionization energy. Indeed that is what we observe above in Figures 5.6 and 5.7. The fact that the rate constants for benzene and naphthalene do not fit the trend displayed in Figure 5.6 could be explained as those systems following a cationic pathway rather than a more radical pathway and hence should correlate with $E_{FC,\mathbf{R},cat}$ rather than $E_{FC,\mathbf{R},rad}$.

In the case of electrophilic addition, however, there is also a pathway leading to a cationic intermediate with wave function $\Psi_{Cat}$. This electronic configuration can be formed from the radical intermediate through an electron transfer from the substrate π-system into the $\sigma^*_{z2}$ orbital of the metal. As such, we expect there to be a direct transition state leading to the radical intermediate as well as one to form the cationic intermediate, although the latter is higher in energy. These transition states will be proportional to the Franck-Condon energy from the reactant state to the excited state representing the product electronic configuration. Figure 5.8 gives descriptions for the Franck-Condon energies reaching the radical state ($E_{FC,\mathbf{R},rad}$) and the one leading to the cationic state ($E_{FC,\mathbf{R},cat}$). Based on the electronic differences between ground and excited state configurations, we established the individual contributions determining these excitation energies. As it happens, the excitation energy leading to the cationic state contains all features of the one leading to the radical state plus two additional terms, namely the ionization energy of the substrate ($IE_{Sub}$) and the electron affinity of the metal in the radical intermediate, which is the reduced form of the iron(IV)-oxo species, namely $EA_{CpdII}$. Therefore, in the transition state the cationic process is higher in energy and only after the barrier a crossover from radical to cationic pathway will be observed leading to the cationic intermediate and fast conversion to phenol products.

The DFT and VB models, therefore, implicate a rate determining electrophilic addition step with a radical-type transition state. However, upon C–O bond formation *en route* to the intermediate a state crossing occurs to the lower lying cationic intermediate. In summary, the VB diagram highlights the factors of the substrate and oxidant that affect the barrier height and predicts that the rate constant is proportional to the ionization energy of the substrate regarded that the oxidant stays the same.

## 5.4 Conclusions

A combined FT-ICR MS and DFT study is performed on the reactivity of arenes with a model of P450 CpdI without axial ligand. It is shown that removal of the axial ligand gives a dominant aromatic hydroxylation pathway and no evidence of aliphatic hydroxylation is found. In general, the natural logarithm of the rate constant of aromatic hydroxylation links linearly with the ionization energy of the substrate. The explanation of this finding is supported within the framework of a Valence Bond model.

## 5.5 Experimental Section

### 5.5.1 Materials

All chemicals and solvents used for this work were research grade and purchased from commercial sources. Iodosylbenzene was used as a terminal oxidant for the synthesis of the iron(IV)-oxo complex and was generated according to a literature procedure (Bowers, M.T., 1979), and subsequently stored at –20°C prior to usage.

### 5.5.2 Instrumental

A Bruker BioApex FT-ICR mass spectrometer was used for all experiments described here, which includes a cylindrical infinity cell, a 4.7 T superconducting magnet and an Apollo I electrospray ionization (ESI) source. Analyte solutions of reactants were infused into the mass spectrometer through a fused-silica capillary with internal diameter of 50 μm at a continuous flow rate of 120 μL $h^{-1}$ by a syringe pump. Ions were desolvated by applying an $N_2$ counter current drying gas heated at 380K and then accumulated for 0.8 seconds in a radiofrequency-only hexapole ion guide. Thereafter, the ions were pulsed into the ICR cell that is held at room temperature (300 K). The

ions of interest, $[Fe^{IV}(O)(TPFPP^{+\bullet})]^+$ at m/z 1044, were mass selected by ion ejection procedures and ion-molecule reactions were studied by inserting neutral collision gases and monitoring the abundance of product ions as a function of time. Neutral reagents were admitted into the FT-ICR cell at stationary pressures (in the range from $1.0 – 15 \times 10^{-8}$ mbar) by a needle valve. The pressure in the FT-ICR cell was measured with a cold-cathode sensor (IKR Pfeiffer Balzers S.p.A., Milan, Italy) and calibrated against the rate constant of proton transfer from methane cation radical to methane, Eq 5.7, which is known to have a rate constant k = 1.1 x $10^{-9}$ $cm^3$ $s^{-1}$ (Bowers, M.T., 1979).

$$CH_4^{+\bullet} + CH_4 \rightarrow CH_5^+ + CH_3^{\bullet} \qquad (5.7)$$

In the mass spectra, corrections for $^{13}C$ isotopic contributions were applied in order to reveal possible species deriving from a hydrogen atom transfer channel, namely $[Fe^{IV}(OH)(TPFPP)]^+$ ions at m/z 1045, presenting a formally protonated ferryl unit.

Ion abundances were monitored as a function of time and pseudo first-order rate constants were obtained from the slope of the semi-logarithmic plots. These values, determined at least in triplicate, were then converted into second-order rate constants ($k_{exp}$) by dividing the parent ion abundances by the substrate concentration at 300 K. Reaction efficiencies ($\Phi$) were calculated from the ratio of the second-order rate constant and the collision rate constant ($k_{ADO}$), Eq 5.8. Values for $k_{ADO}$ were calculated using the parametrized trajectory theory (Su et.al. 1982).

$$\Phi = k_{exp}/k_{ADO} \text{ x } 100\% \qquad (5.8)$$

Product ion branching ratios and reaction efficiencies were found to be independent of the pressure in the ICR cell. The error in the estimated second-order rate constants ($k_{exp}$) is to within 10% with an absolute error of ±30%, caused largely by the uncertainty affecting the pressure of the neutral (Angelelli et.al. 2005).

### 5.5.3 Sample preparation

The $[Fe^{IV}(O)(TPFPP^{+\bullet})]^{+}$ ion was synthesized in a methanol/dichloromethane (1:1) mixture by adding iodosylbenzene (0.5 mM) to the corresponding iron(III)chloride complex, 10 μM of $[Fe^{III}(TPFPP)Cl]$, and cooled to –40°C. The iron(IV)-oxo complex remained stable at this temperature for at least 1 hour. The ESI FT-ICR mass analysis of the reaction mixture gave a prominent peak centered at m/z 1044 with isotopic pattern conforming to an iron(IV)-oxo complex, $[Fe^{IV}(O)(TPFPP^{+\bullet})]^{+}$, together with the reduced form $[Fe^{III}(TPFPP)]^{+}$ at m/z 1028. Nonetheless, the ion population at m/z 1044 comprises a fraction of isomeric species, likely corresponding to an isobaric ion oxidized on the porphyrin ring, and unable to attain any oxidation process. This fraction was titrated by its complete trapping by NO yielding the $[Fe^{III}(TPFPP–O)(NO)]^{+}$ adduct, in analogy with the reduced form, $[Fe^{III}(TPFPP)]^{+}$. The presence of this unreactive form was taken into account in treating the kinetic data.

### 5.5.4 Computation

To support the experimental observations and determine further trends and features of the reaction mechanism, we did a detailed DFT study on aromatic hydroxylation by $[Fe^{IV}(O)(Por^{+\bullet})]^{+}$, where Por represents an unsubstituted porphyrin ligand. We also tested the full $[Fe^{IV}(O)(TPFPP^{+\bullet})]^{+}$ system but found very little differences in geometry, electronic description and reactivity with respect to the $[Fe^{IV}(O)(Por^{+\bullet})]^{+}$ system (Supporting Information Figure S4), hence the latter was used here. All calculations were performed in Gaussian-09 (Frish et.al. 2009), and implemented DFT methods. Test calculations with a range of density functional methods show little sensitivity of the amount of exchange and correlation to optimized geometries and the potential energy landscape gives the same pattern (Supporting Information Tables S1 – S20), therefore, we will show results obtained with the B3LYP (Becke, A.D., 1993) density functional method only as that will enable a direct comparison with our previous work (Sainna et.al. 2015).

Initial geometry optimizations and constraint geometry scans were performed at the UB3LYP/BS1 level of theory: BS1 is LACVP on iron (with core potential) and 6-31G on the rest of the atoms (Hay et.al. 1985; Hehre et.al. 1972). The maxima of the geometry scans were then used as starting points for the transition state searches,

which established first-order saddle points with a single imaginary frequency for the correct mode. Improved energies were obtained through single point calculations at the UB3LYP/BS2 level of theory: BS2 is LACV3P+ on iron (with core potential) and 6-311+G* on the rest of the atoms. Free energies are reported at a temperature of 298K and 1atm pressure and include zero-point, thermal and entropic corrections under standard conditions. Although the experiments were performed in the gas-phase, we also tested the effect of solvent on the obtained rate constants from single point calculations using the polarized continuum model in Gaussian with a dielectric constant mimicking acetonitrile. All structures represent full geometry optimizations without constraints and were characterized with a frequency calculation as either a local minimum (real frequencies only) or a first-order saddle point.

## 5.6 Acknowledgements

MAS and FGCR thank the Petroleum Technology Development Fund and the Conacyt Mexico for a studentship. SdV acknowledges cpu time support from the National Service of Computational Chemistry Software (NSCCS). The EU-COST Network Explicit Control Over Spin-states in Technology and Biochemistry (ECOSTBio, CM1305) is acknowledged for support. MEC and SF are grateful to the Università di Roma „La Sapienza“ for funding of the FT-ICR MS work.

# Chapter Six

# PROJECT 4

***Hydrogen atom versus hydride transfer in cytochrome P450 oxidations: A combined mass spectrometry and computational study***

*Fabián G. Cantú Reinhard, Simonetta Fornarini*, Maria Elisa Crestoni* and Sam P. de Visser**

## Abstract

*Biomimetic models of short-lived enzymatic reaction intermediates can give useful insight into the properties and coordination chemistry of transition metal complexes. In this work we investigate a high-valent iron(IV)-oxo porphyrin cation radical complex, namely* $[Fe^{IV}(O)(TPFPP^{+\bullet})]^{+}$ *where TPFPP is the dianion of 5,10,15,20-tetrakis(pentafluorophenyl) porphyrin. The* $[Fe^{IV}(O)(TPFPP^{+\bullet})]^{+}$ *ion was studied by ion-molecule reactions in a Fourier transform-ion cyclotron resonance mass spectrometer through reactivities with 1,3,5-cycloheptatriene, 1,3-cyclohexadiene and toluene. The different substrates give dramatic changes in reaction mechanism and efficiencies, whereby cycloheptatriene leads to hydride transfer, while cyclohexadiene and toluene react via hydrogen atom abstraction. Detailed computational studies point to major differences in ionization energy as well as C–H bond energies of the substrates that influence the hydrogen atom abstraction versus electron transfer pathways. The various variables that determine the pathways for hydride transfer versus hydrogen atom transfer are elucidated and discussed.*

## Published Reference:

Cantu-Reinhard, F.G. Fornarini, S. Crestoni, M.E. De Visser, S. Hydrogen Atom vs. Hydride Transfer in Cytochrome P450 Oxidations: A Combined Mass Spectrometryand Computational Study. *Eur. J. Inorg. Chem.* **2018**, 1854-1865.

## 6.1 Introduction

Cytochrome P450 enzymes are versatile catalysts in the human body that detoxify the liver from foreign compounds, such as drugs and some of their metabolites as well as other xenobiotics (Soto et.al. 1996; Ortiz de Montellano, 2005; Ortiz de Montellano, 2010; Kadish et.al. 2010). Structurally, the P450s contain an iron(III)-heme deeply embedded into a protein matrix, where the substrate binds into a pocket of varying size depending on the P450 isozyme (Nelson, 2009; Poulos, 2014). The P450 catalytic cycle uses molecular oxygen, two reduction and two protonation equivalents in order to convert the iron(III)-heme(water) resting state into its active form, namely the high-valent iron(IV)-oxo porphyrin cation radical species called Compound I (CpdI) (Meunier et.al. 2004; Denisov et.al. 2005; Rittle and Green, 2010). CpdI is known as one of the most efficient and versatile oxidants in Nature and generally reacts with substrates through oxygen atom transfer. For instance, it converts aliphatic groups through a hydroxylation process into alcohols, but also can activate aromatic C–H bonds into phenols and sulfides into sulfoxides (Soto et.al. 1996; Ortiz de Montellano, 2005; Ortiz de Montellano, 2010; Kadish et.al. 2010; Nam, 2007; Watanabe et.al. 2007). In particular, substrate hydroxylation has been the topic of many studies and controversies have been posed whether it is initiated by a rate-determining hydrogen atom abstraction (HAT) or a hydride transfer (HT), as explained in Scheme 6.1 (Nam et.al. 2014; Asaka et.al. 2016; Ji et.al. 2014).

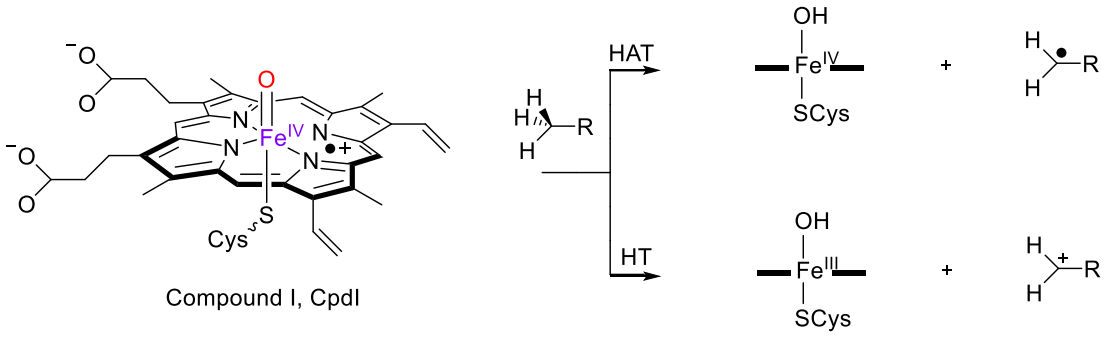


**Scheme 6.1.** Products obtained from a reaction of CpdI with an aliphatic group.

Thus, computational modelling on hydrogen atom abstraction reactions by P450 enzymes with common aliphatic substrates, such as alkanes or alkylbenzenes, revealed a stepwise mechanism with an initial hydrogen atom abstraction followed by radical rebound to form alcohol product complexes (Ogliaro et.al. 2000; Shaik et.al. 2005; Li et.al. 2012; Blomberg et.al. 2014). However, experimental studies of a synthetic iron(IV)-oxo porphyrin in a reaction with the substrate 10-methyl-9,10-dihydroacridine ($AcrH_2$) gave hydride transfer instead (Jeong et.al. 2008; Fukuzumi et.al. 2008). Computational modelling on these reaction mechanisms implicated that hydride and hydrogen atom transfer pathways could both be feasible under certain reaction conditions, but are determined by the thermochemical properties of the oxidants, intermediates and substrates (Tahsini et.al. 2009). To gain more insight into the mechanisms leading to hydride transfer by CpdI of P450, we pursued a combined mass spectrometry and computational study on the hydride versus hydrogen atom abstraction patterns of model substrates. In particular, we compare the reactivity patterns of these CpdI models with substrates that are likely to react via either hydride or hydrogen atom transfer. Thus, 1,3,5-cycloheptatriene (CHT) is used as a model substrate for hydride transfer reactions and 1,3-cyclohexadiene (CHD) and toluene are considered for aliphatic hydrogen atom transfer. We present here a detailed joint mass spectrometric and computational study on substrate activation by a synthetic CpdI model and establish the origin of hydride versus hydrogen atom transfer pathways. Furthermore, a detailed thermochemical and valence bond analysis explains the intrinsic properties of substrate and oxidant that determine hydride transfer versus hydrogen atom transfer by metal-oxo oxidants.

## 6.2 Results

### 6.2.1 Mass spectrometry results.

The preparation of a high-valent iron(IV)–oxo porphyrin cation radical complex, $[Fe^{IV}(O)(TPFPP^{+\bullet})]^{+}$ with TPFPP being the dianion of 5,10,15,20-tetrakis(pentafluorophenyl) porphyrin, was done by treatment of $[Fe^{III}(TPFPP)]Cl$ with iodosylbenzene as oxygen atom donor, in a methanol/dichloromethane solution at –40°C as previously reported (Crestoni et.al. 2009). The reaction mixture sampled by electrospray ionization (ESI) and characterized by high resolution Fourier transform-ion cyclotron resonance (FT-ICR) mass spectrometry contains substantial

amounts of an ion cluster centered at m/z 1044.0116, revealing the incorporation of one oxygen atom by the reactant species $[Fe^{III}(TPFPP)]^+$.

**Table 6.1.** Thermodynamic and kinetic data and product distributions for the reaction of selected hydrocarbons with $[Fe^{IV}(O)(TPFPP^{+\bullet})]^+$.

| Compound (A) | IE [a] | $BDE_{CH}$ [b] | $IE_{radical}$ [a] | $k_{exp}$ [c] | Φ (%) | %$[A–H]^+$ [d] | %$[Fe^{III}(TPFPP)]^+$ | %ADD |
|---|---|---|---|---|---|---|---|---|
| Toluene | 8.828 | 87.9 | 7.242 [e] | 0.36 | 3.9[h] | – | 80 | 20 |
| CHT | 8.0–8.3 | 72.9 | 6.28 [f] | 2.67 | 30 | 40 | 60 | – |
| CHD | 8.25 | 72.9 | 6.82 [g] | 1.58 | 17 [i] | – | 100 | – |

[a] In eV. [b] In kcal $mol^{-1}$. [c] Second-order rate constant in units of $10^{-10}$ $cm^3$ $molecule^{-1}$ $s^{-1}$, at the temperature of the FT-ICR cell of 300K. [d] product ion at *m/z* value for substrate minus $H^-$. [e] Data from NIST. [f] The reaction of cycloheptatriene-7-[$D_1$] displays a H/D kinetic isotope effect of 2.5, resulting from the time independent ratio of the abundances of the $C_7H_6D^+$ and $C_7H_7^+$ product ions. [g] Data from Krechkivska et.al. 2014. [h] Data from Cantu-Reinhard et.al.[2], 2016. [i] Data from Sainna et.al. 2015.

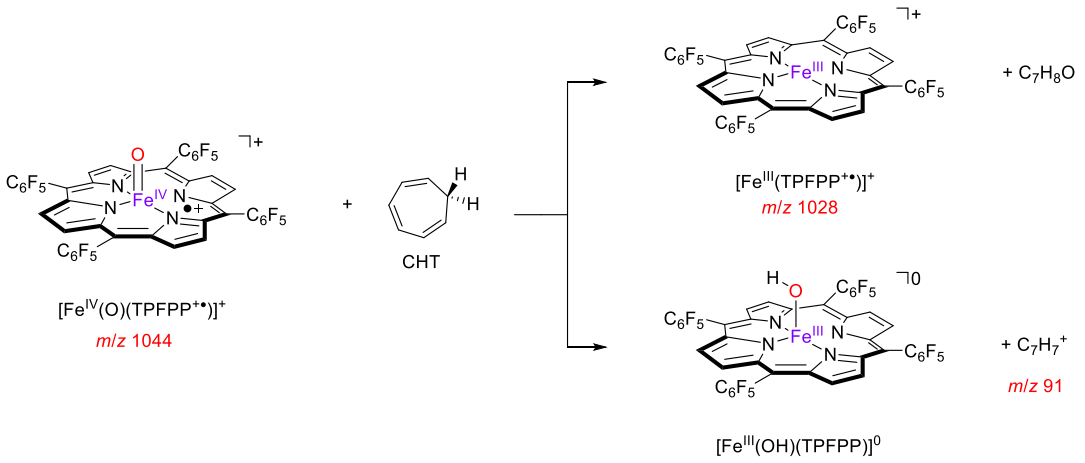


**Scheme 6.2.** Reaction channels observed for the reaction of [FeIV(O)(TPFPP+•)]+ with 1,3,5-cycloheptatriene in the FT-ICR cell.

When trapped in the FT-ICR cell, mass-selected ions with m/z 1044.0116 are remarkably stable toward unimolecular dissociation (kdiss ≤ 0.001 s–1) and their fragmentation patterns and isotope patterns characterize them as $[Fe^{IV}(O)(TPFPP^{+\bullet})]^+$. Moreover, when exposed to stationary concentrations of candidate reductants, they react with a wide variety of compounds, including NO, $NO_2$, aromatics, olefins, sulfides, amines, and phosphites (Chiavarino et.al.2008; Crestoni et.al. 2007; Crestoni et.al. 2005).

A comprehensive combined mass spectrometric and computational approach recently succeeded in unveiling the full details of multiple reaction channels and product distribution in olefin epoxidation (Sainna et.al. 2015) and aromatic hydroxylation (Cantu-Reinhard et.al. 2016), in the gas-phase, i.e. in a solvent-free environment. In this context, we have become keenly interested in gaining further information on the Compound I-like reactivity of $[Fe^{IV}(O)(TPFPP^{+\bullet})]^{+}$ with CHT, that has been assessed and is described herein. CHT is an isomer of toluene, although it lacks aromatic stabilization. Therefore, the two compounds possess quite different physical and chemical properties. In particular, CHT is characterized by a markedly lower ionization energy (IE): 8.0 – 8.3 eV for CHT versus 8.828 eV for toluene (Hunter et.al. 2017). Also significantly smaller for CHT versus toluene is its C–H bond dissociation energy (BDECH) for removal of a hydrogen atom from the methylene group. Thus, the BDECH of methylene C–H bond of CHT is 72.9 kcal $mol^{-1}$ whereas it is 87.9 kcal mol–1 for the cleavage of the H–CH2C6H5 bond in toluene (Lide, 2010). However, the most notable reactivity feature in the reactive behavior of CHT is the drive towards formation of $c\text{-}C_7H_7^{+}$, i.e. the tropylium ion, which has aromatic character and hence is relatively stable. This species plays an important role in the oxidation of CHT and CHT-derivatives and the process has interesting synthetic applications, namely in anodic oxidation, oxidation by photoinduced electron transfer, and chemoenzymatic studies (Shono et.al. 1991; Jacobi et.al. 1999; Xu et.al. 1997).

Because of the peculiar features of cycloheptatriene, we envisaged a detailed gas phase reactivity study towards $[Fe^{IV}(O)(TPFPP^{+\bullet})]^{+}$ would be interesting and could contribute to elucidation of the intrinsic factors that determine the reactivity behavior of this model of P450 Cpd I. An interesting comparison may as well arise from the reaction of $[Fe^{IV}(O)(TPFPP^{+\bullet})]^{+}$ with 1,3-cyclohexadiene (CHD) as it has a comparable IE and also similar C–H BDECH for the methylene group (IE and BDECH values are equal to 8.25 eV and 72.9 kcal $mol^{-1}$, respectively), see Table 6.1 (Hunter et.al. 2017; Shono et.al. 1991; Jacobi et.al. 1999; Xu et.al. 1997; Krechkivska et.al. 2014). However, ionization of the so-formed radical is remarkably easier for $c\text{-}C_7H_7\bullet$ when compared to the c-C6H7• radical from 1,3-cyclohexadiene (6.28 vs. 6.82 eV, respectively). Table 6.1 gives a summary of all cited thermochemical data (Hunter et.al. 2017; Shono et.al. 1991; Jacobi et.al. 1999; Xu et.al. 1997; Krechkivska et.al. 2014).

The thermal reactivity of $[Fe^{IV}(O)(TPFPP^{+\bullet})]^+$ towards CHT occurs along two reaction channels, namely a process that yields the reduced $[Fe^{III}(TPFPP)]^+$ ion and oxidized (neutral) substrate, and a formal hydride transfer (HT) pathway, whereby $C_7H_7^+$ as ionic product is released together with (neutral) $[Fe^{III}(OH)(TPFPP)]$, Scheme 6.2. Thus, upon isolation of the ion at m/z 1044 representing the $[Fe^{IV}(O)(TPFPP^{+\bullet})]^+$ complex, ion abundances were measured as a function of time in the presence of a stationary concentration of CHT. Indeed, the abundance of ions at m/z 1044 decayed as a function of time and two new peaks in the spectrum appeared at m/z 1028 and m/z 91. These two peaks correspond to the products $[Fe^{III}(TPFPP)]^+$ and $C_7H_7^+$, resulting from oxygen atom transfer and hydride transfer from the reaction of $[Fe^{IV}(O)(TPFPP^{+\bullet})]^+$ with cycloheptatriene. The reaction is fast and characterized by a reaction efficiency of $\Phi = 30\%$ (see Table 6.1). Semi-logarithmic plots of the reactant ion abundance as a function of time obtained at varying CHT concentration enabled us to calculate the second-order rate constants for both reaction processes, as displayed in Figure S1 in the Supporting Information.

The reaction of $[Fe^{IV}(O)(TPFPP^{+\bullet})]^+$ with cycloheptatriene-7-[D1] gives a mixture of hydrogen and deuterium transfer and results in the formation of both $C_7H_6D^+$ and $C_7H_7^+$ ions in the product mixture. The abundance ratio of $C_7H_6D^+$ and $C_7H_7^+$ product ions is about 2.5 and is independent of the reaction time. Therefore, the ratio of the abundances of $C_7H_6D^+$ versus $C_7H_7^+$ corresponds to the H/D kinetic isotope effect for competing hydride versus deuteride abstraction from cycloheptatriene-7-[D1]. The kinetic plot for the reaction of $[Fe^{IV}(O)(TPFPP^{+\bullet})]^+$ with cycloheptatriene-7-[D1] is given in Figure 6.1 showing the profiles of ion abundances as a function of time.

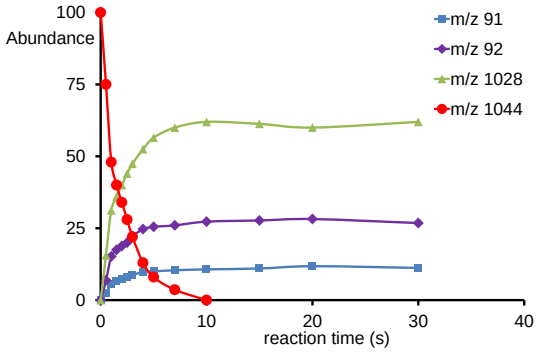


**Figure 6.1.** Ion abundances as a function of time after isolation of m/z 1044 ions, i.e. [FeIV(O)(TPFPP$^{+\bullet}$)]$^+$, in the FT-ICR cell in the presence of 5 × 10–8 mbar cycloheptatriene-7-[D1] at room temperature.

It is interesting to note that the HT path is specific for CHT, while formation of the reduced $[Fe^{III}(TPFPP)]^+$ ion is commonly observed in the reactivity of both olefins and aromatic compounds (Sainna et.al. 2015; Cantu-Reinhard et.al.[b] 2016). In order to find out how the reactivity of $[Fe^{IV}(O)(TPFPP^{+\bullet})]^+$ with CHT differs to that with aliphatic substrates, we decided to compare the reactivity of $[Fe^{IV}(O)(TPFPP^{+\bullet})]^+$ with CHD and toluene. Thus, P450 Cpd I models typically react with CHD through dehydrogenation and the formation of benzene (Kumar et.al. 2009; Latifi et.al. 2013), or alternatively by oxygen atom transfer to form the corresponding epoxide. On the other hand, using toluene as a substrate a mechanism was found starting with hydrogen atom abstraction and followed by OH rebound to form phenylmethanol products (de Visser et.al. 2004; Latifi et.al. 2012). As follows, the aromatic $C_7H_8$ isomer of CHT, namely toluene, displays exclusive formation of the reduced $[Fe^{III}(TPFPP)]^+$ ion with a markedly lower efficiency of only 4%, which includes also a formal addition path leading to a complex at m/z value corresponding to the sum of oxidant and substrate (ADD pathway), Table 6.1. Also 1,3-cyclohexadiene, with conjugated double bonds, undergoes exclusively an oxygen atom transfer process (OAT) with 17% efficiency, which could implicate substrate epoxidation (Sainna et.al. 2015). Thus, in aromatic hydroxylation and double bond epoxidation reactions studied for analogous systems poxidation (Sainna et.al. 2015; Cantu-Reinhard et.al.[b] 2016; Chiavarino et.al. 2010; Lanucara et.al. 2011), OAT is the common product ion, and hence would implicate epoxidation of CHD.

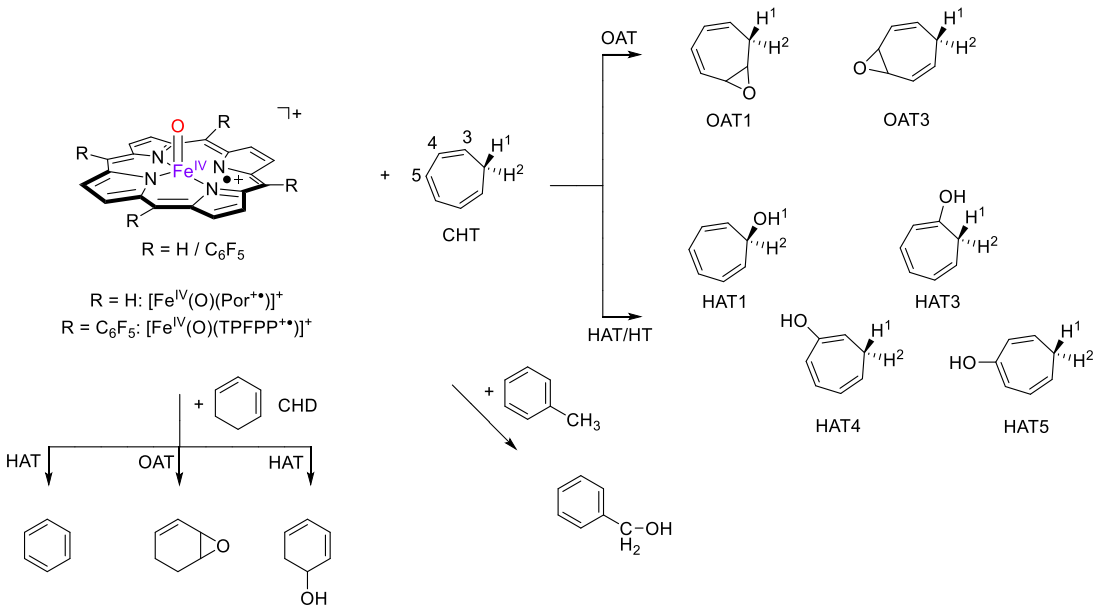


**Scheme 6.3.** Mechanisms considered in this work for the reactions of **1** and **2** with CHT, CHD and toluene and the products obtained.

### 6.2.2 Computational modelling

To support the experiments and gain insight into the reaction pathways for 1,3,5-cycloheptatriene activation by $[Fe^{IV}(O)(TPFPP^{+\bullet})]^{+}$ we performed a computational study on the mechanisms and pathways leading to the various products for activation of CHT. As a comparison, we also included computational studies using CHD and toluene as substrates, since the experimental studies with these substrates have considerably different product distributions (Table 6.1). Initial calculations using the CHT substrate utilized a TPFPP scaffold abbreviated to porphyrin (Por) without side chains, $^{2,4}$**1**. However, in a second set of calculations the full system (TPFPP, $^{2,4}$**2**) was also studied for the full reaction pathway of the predominant hydroxylation reactions, on the quartet and doublet spin states (see Scheme 6.3). In the case of CHT substrate technically, oxygen atom transfer can lead to various isomeric epoxides, namely at positions 3 or 5 (Scheme 6.3) or alternatively a hydroxylation process can lead to alcohols from H1, H3, H4 and H5. Hydrogen atom abstraction from position H2 was also attempted but led to the same transition state and local minimum as the one from H1. We decided to investigate all these mechanisms using established procedures reported recently (Sainna et.al. 2015; Cantu-Reinhard et.al.[b] 2016).

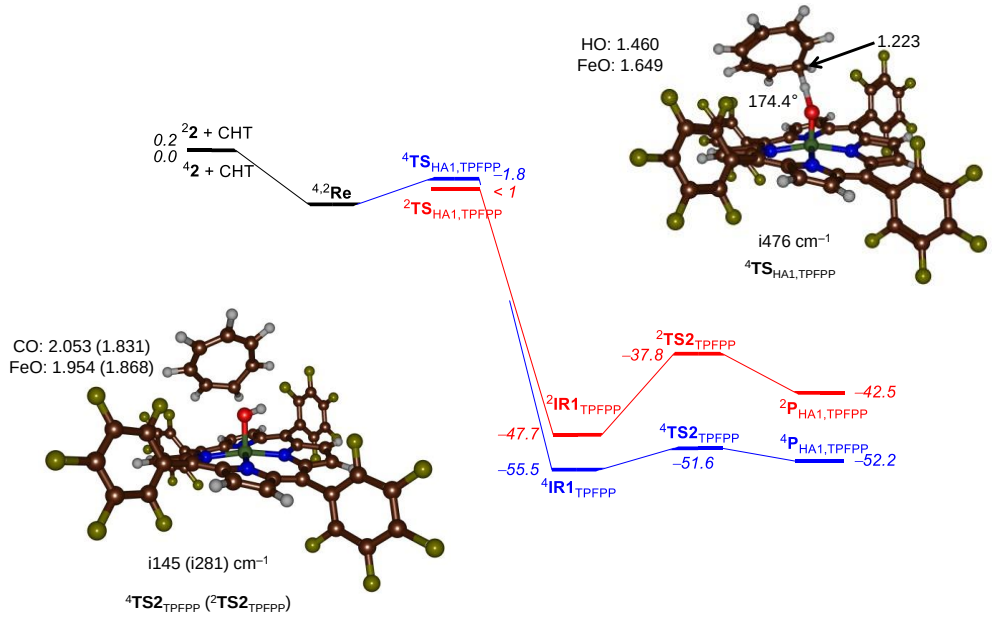


**Figure 6.2.** Free energy landscape for oxidation reactions of cycloheptatriene by $^{4,2}$**2**. Free energies use electronic energies at UB3LYP/BS2//UB3LYP/BS1 in kcal mol$^{-1}$ and contain zero-point, entropic and thermal corrections to 298K. Also given are optimized geometries of $^{4}$**TS**$_{HA1}$ and $^{4,2}$**TS2**$_{TPFPP}$ with bond lengths in angstroms, angles in degrees and the imaginary frequency in cm$^{-1}$.

A detailed benchmark study aimed at reproducing experimental reaction free energies of activation of substrate sulfoxidation reactions by an iron(IV)-oxo species showed that PBE0 and B3LYP were the preferred density functional theory methods to reproduce experimental data and activation enthalpies to within 3 – 4 kcal $mol^{-1}$ from experiment were obtained for a series of substrates (Cantu-Reinhard et.al[a] 2016; Yang et.al. 2016; Vardhaman et.al. 2013). Furthermore, for several chemical systems we calculated bifurcation pathways and predicted the correct product distributions. For instance, we calculated the hydrogen atom abstraction pathways from the six possible hydrogen atoms of a proline residue in a peptide chain by prolyl-4-hydroxylase and found a low-energy pathway for the formation of R-4-hydroxyproline, in agreement with experimental observation (Timmins et.al. 2017; Timmins and de Visser, 2017). Furthermore, for the cytochrome P450 peroxygenase reaction pathways were calculated for fatty acid decarboxylation and hydroxylation and the predicted product distributions matched experiment very well (Faponle et.al. 2016). As such we utilized these methods in this work.

To gain further insight into hydride transfer versus hydrogen atom transfer pathways, we included calculations for the full mechanism of 1,3-cyclohexadiene and toluene, see Scheme 6.3. The full set of results is documented in the Supporting Information (Tables S1 – S16; Figures S2 – S10), while we focus on the main trends here. Note that hydride transfer is not always a feasible mechanism as will be discussed later; however, molecular orbital swaps were attempted in all cases to estimate the energy difference between hydrogen atom and hydride transfer pathways. Further details on the possibilities of hydride transfer follow in the thermochemical analysis of structures in the Discussion section.

Let us start with a description of a typical reaction mechanism of oxygen atom transfer, namely of cycloheptatriene activation at its methylene group by the iron(IV)-oxo model. In the following, we will add the label for the reaction process as a subscript to the molecule. Calculations were done starting from the isoelectronic doublet and quartet spin state structures of $[FeIV(O)(Por^{+\bullet})]^{+}$, $^{4,2}\mathbf{1}$. Similarly to our previous work on this chemical system as well as reports on P450 CpdI (Watanabe et.al. 2007; Cantu-Reinhard[b] et.al. 2016; Green, 1999; De Visser et.al. 2003; de Visser and Tan, 2008;

Cantu-Reinhard and de Visser 2017), we find the doublet and quartet spin states of the reactant complex to be within 0.5 kcal mol$^{-1}$ for $^{4,2}$[FeIV(O)(Por$^{+\bullet}$)]$^{+}$ as well as for $^{4,2}$[FeIV(O)(TPFPP$^{+\bullet}$)]$^{+}$: $^{4,2}$**2**.

Figure 6.2 gives the potential energy landscape for cycloheptatriene activation on one of the aliphatic C–H bonds by $^{4,2}$**2**. The substrate and oxidant initially form a reactant complex ($^{4,2}$**Re**) and then react with a fast hydrogen atom abstraction leading to a very low-energy intermediate. Although the $^{4}$**TS**$_{HA1,TPFPP}$ barrier is lower in energy than isolated reactants, it is slightly higher in energy than the reactants complex. Therefore, the hydrogen atom abstraction will be fast. On the doublet spin state, we were unable to locate the structure of the hydrogen atom transition states as all attempts led to the product complexes instead. Similarly to previous calculations on aliphatic hydroxylation by P450 CpdI, the doublet and quartet spin states are close in energy and only at the products stage they diverge due to differences in orbital occupation (Watanabe et.al. 2007; Shaik et.al. 2005; Wang et.al. 2007; Ji et.al. 2015; Cantu-Reinhard and de Visser, 2017).

The group spin densities of $^{4}$**TS**$_{HA1,TPFPP}$ give $\rho_{FeO}$ = 2.16, $\rho_{TPFPP}$ = –0.06 and $\rho_{SubH}$ = 0.90, which points to a hydrogen atom abstraction transition state coupled to a triplet spin iron(IV)-oxo group. Interestingly, the intermediate ($^{4}$**IR1**$_{TPFPP}$) that connects to this transition state has spin densities corresponding to $\rho_{FeO}$ = 2.96, $\rho_{TPFPP}$ = 0.02 and $\rho_{Sub}$ = 0.02, which implies that the intermediate is an ion-molecule complex of $C_7H_7^+$ with a neutral [Fe(OH)(TPFPP)]$^0$ molecule. Therefore, the mechanism starts with a fast hydrogen atom abstraction, but en route to the intermediate another electron transfer takes place to form the overall hydride transfer intermediate $^{4,2}$**IR1**. In the next stage of the reaction the OH– rebound gives alcohol product complexes (P) via the rebound transition state **TS2**. As can be seen from Figure 6.2, the rebound encounters a barrier of 3.9 kcal mol$^{-1}$ in the quartet spin state, but 9.9 kcal mol$^{-1}$ in the doublet spin state. These barriers, particularly the one in the doublet spin state are relatively high and may implicate dissociation of the complex into individual $C_7H_7^+$ and [Fe(OH)(TPFPP)]$^0$. Indeed, the experimental measurements observed $C_7H_7$+ products alongside the reduced complex [Fe(TPFPP)]$^+$. It could very well be that the latter is formed through the low-barrier high-spin reaction mechanism, whereas the low-spin mechanism leads to dissociation of the intermediate delivering free $C_7H_7^+$ ions.

Apart from calculations on the full structure $^{4,2}$**2** and its mechanism with substrates, we did a more comprehensive study using the smaller model $^{4,2}$**1**, whereby mechanisms for various hydrogen atom abstractions and oxygen atom transfer processes were investigated. In general, the hydrogen atom abstraction mechanism is the same for $^{4,2}$**1** as compared to $^{4,2}$**2**. The $^{4,2}$**TS**$_{HA1}$ barriers are relatively early on the potential energy surface with short C–H and long O–H bonds (1.189 and 1.143 Å and 1.560 and 1.762 Å, respectively) indicative of a fast reaction process (see Figure 6.3). Although generally aliphatic hydroxylation mechanisms are stepwise via a radical intermediate; for the small model no stable radical and/or cationic intermediates could be located, which implies a fast and efficient rebound to alcohol products. Therefore, the small model is not good enough to mimic the experimental system. Further evidence that the small model fails to capture the chemical properties of the meso-substituents follows from the calculated bond dissociation energies (BDEOH) of the O–H bond of the $[Fe^{IV}(OH)(Por)]^+$ versus $[Fe^{IV}(OH)(TPFPP)]^+$ complexes.

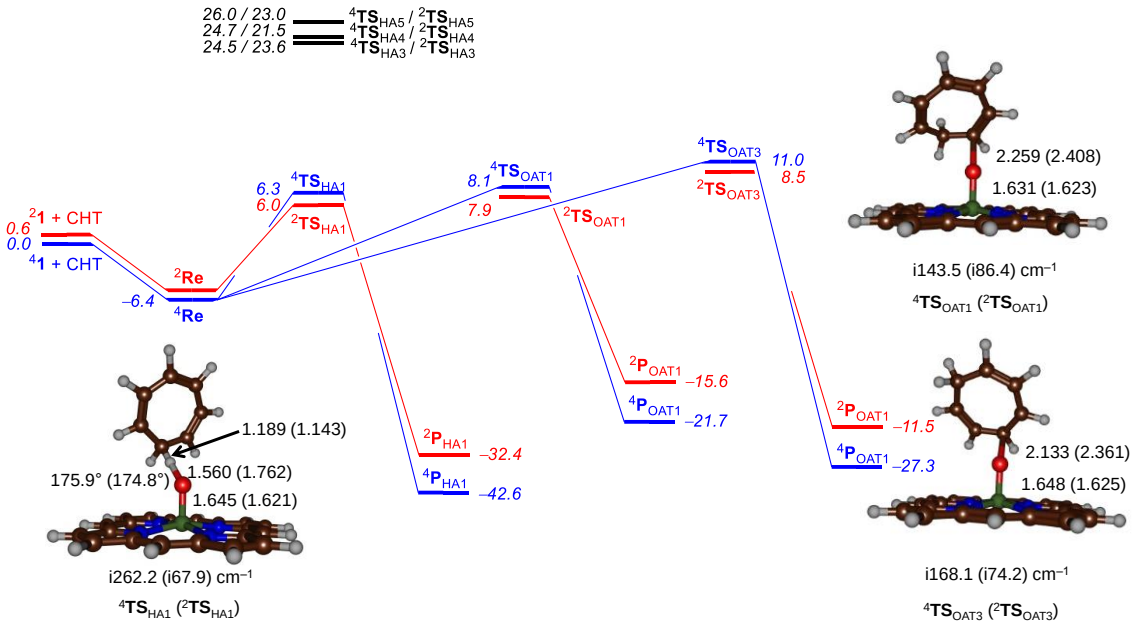


**Figure 6.3.** Free energy landscape for HAT and OAT reactions from cycloheptatriene by $^{4,2}$**1**. Free energies use electronic energies at UB3LYP/BS2//UB3LYP/BS1 in kcal mol$^{-1}$ and contain zero-point, entropic and thermal corrections. Also given are optimized geometries of $^{4,2}$**TS**$_{HAT1}$, $^{4,2}$**TS**$_{OAT1}$ and $^{4,2}$**TS**$_{OAT3}$ with bond lengths in angstroms, angles in degrees and the imaginary frequency in cm$^{-1}$.

In particular, we calculate an energy difference between the iron(IV)-hydroxo and the sum of the iron(IV)-oxo porphyrin cation radical model and a hydrogen atom of 42.8 kcal mol$^{-1}$ for [Fe$^{IV}$(OH)(TPFPP)]$^{+}$ and 83.6 kcal mol$^{-1}$ for [Fe$^{IV}$(OH)(Por)]$^{+}$. This difference results from a change of 8.0 kcal mol–1 in the electron affinity of the iron(IV)-oxo species and 32.2 kcal mol$^{-1}$ drop in pKa value of the iron(IV)-hydroxo species. As a consequence of this, the small model reacts with lesser exothermicity and higher hydrogen atom abstraction barriers with substrates with aliphatic groups than the large system.

The barriers for hydrogen atom abstraction for both the small and large models ($^{4,2}$**1** and $^{4,2}$**2**) are relatively small. Previously, a series of hydrogen atom abstraction barriers with a range of aliphatic substrates showed early transition states to correspond to lower reaction barriers (Shaik et.al. 2008; Latifi et.al. 2009). Indeed, $^{4,2}$**TS**$_{HA1}$ are low in energy and only $\Delta G^{\ddagger}$ = 6.0/6.3 kcal mol$^{-1}$ above the energy of reactants in the doublet/quartet spin state. Note also that the imaginary frequency in the transition state is relatively low (i262 cm$^{-1}$ for $^{4}$**TS**$_{HA1}$ and i476 cm$^{-1}$ for $^{4}$**TS**$_{HA1,TPFPP}$). Typical values of the imaginary frequency for hydrogen atom abstraction barriers are well over i1500 cm$^{-1}$, which usually leads to a major kinetic isotope effect (KIE) for the replacement of the transferring hydrogen atom by deuterium (Quesne et.al. 2016; Barman et.al. 2016). We calculate a value of KIE = 2.7, which matches the experimental rate constant ratio perfectly. Nevertheless, typical KIE values of hydrogen atom abstraction barriers are well above 10 for analogous systems (Abu-Omar et.al. 2005; Atanasov et.al. 2009; Bruijnincx et.al. 2008; Costas et.al. 2004).

For all the smaller models dealing with $^{4,2}$[FeIV(O)(Por$^{+\bullet}$)]$^{+}$, after passing the hydrogen atom abstraction transition states, the system directly collapses to the alcohol product complex and no stable radical intermediates could be located and hence a concerted hydroxylation process is predicted. In previous work on P450 model complexes (Watanabe et.al. 2007; Ogliaro et.al. 2000; Shaik et.al. 2005; Li et.al.2012; Blomberg et.al. 2014; Wang et.al. 2007; Ji et.al. 2015; Cantu-Reinhard and de Visser 2017; Shaik et.al. 2008; Latifi et.al. 2009), most HAT pathways showed a shallow intermediate that was separated with a small barrier to products (typically less than 1 kcal mol$^{-1}$ on the doublet spin state surface and less than 5 kcal mol$^{-1}$ on the high-spin surface); however, no such local minimum could be located here and all attempts

converged to the product complexes instead. Therefore, the absence of a radical intermediate may have to do with the lack of meso-substituents in the model that affects the electron affinity and hydrogen atom abstraction ability of the complex as will be discussed in the thermochemical section later.

The group-spin densities for the doublet and quartet intermediates give most radical character on the FeO group and virtually no spin density is seen on the substrate. Consequently, these intermediates correspond to a formal hydride transfer from substrate to oxidant. The reaction is highly exothermic and $^{4,2}$**IR1** are below reactants by $\Delta G$ = 55.5 (quartet) and 47.7 (doublet) kcal mol$^{-1}$. Clearly, the small model does not capture the properties of the intermediate state well even though the hydrogen atom abstraction barriers are similar in structure and electronic configuration.

In contrast to the intermediates $^{4,2}$**IR1**, the hydrogen atom abstraction transition states have significant radical character on the substrate. To be specific, a spin density of 0.88 (–0.73) is found on the $C_7H_8$ unit in $^{4,2}$**TS$_{HA1}$**. Therefore, during the transition state a hydrogen atom is transferred, which is quickly followed by another electron transfer before reaching the intermediate state.

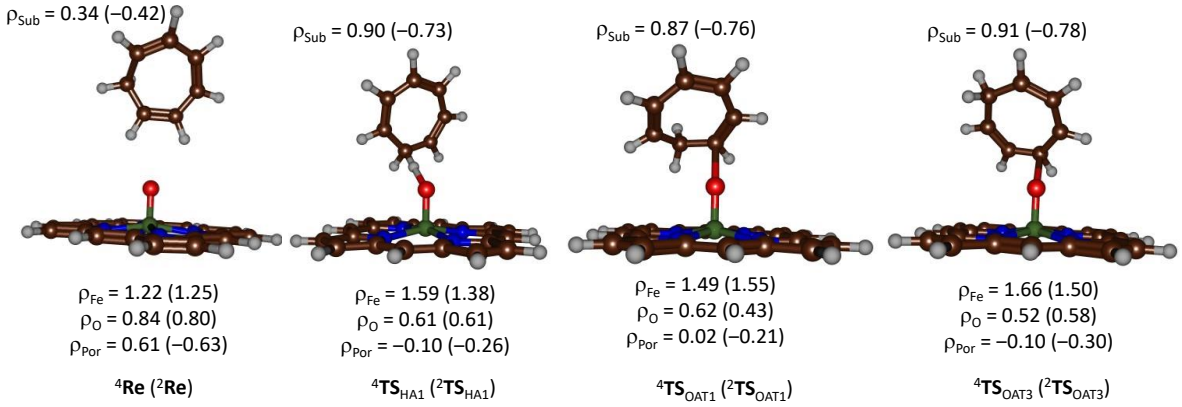


**Figure 6.4.** Group spin densities of reactant complexes and low-energy transition states for the reaction of $[Fe^{IV}(O)(Por^{+\bullet})]^+$ with CHT as calculated at UB3LYP/BS2//UB3LYP/BS1.

The last step, then, refers to an $OH^-$ transfer from [FeIII(OH)( TPFPP)] to $C_7H_7^+$ to form the alcohol product complex. Subsequently, we calculated hydrogen atom abstraction by $^{4,2}$**1** at position H3, H4 and H5 and the doublet and quartet barrier heights are given in Figure 6.3 as well. As follows, all these hydrogen atom

abstraction barriers are well over 20 kcal $mol^{-1}$ and will not be competitive with hydrogen atom abstraction from H1 or H2. This is not surprising as hydrogen atom abstraction from aromatic centers (or olefins) generally requires a lot of energy and does not give a stable radical (de Visser and Shaik 2003).

We then studied C–O activation through an electrophilic attack of the oxo group onto the carbon atom at position 3 and 5. Similarly to the aliphatic hydroxylation reported in Figure 6.3, the reaction is concerted with a C–O bond formation barrier that directly leads to epoxide product complexes without the formation of a radical intermediate. The two pathways are competitive and only a small energy difference on the C–O bond formation barrier is seen between attacks on position 3 versus 5. Therefore, the oxygen atom transfer on position 3 and 5 will be competitive, although their barriers are higher in energy than that for aliphatic hydrogen atom abstraction. Similarly to the aliphatic hydroxylation barriers, also the oxygen atom transfer barriers are early on the potential energy surface with long C–O and short Fe–O distances (Figure 6.3).

Thereafter, we investigated the mechanistic landscapes for oxygen atom transfer of $[Fe^{IV}(O)(TPFPP^{+\bullet})]^{+}$ with toluene and 1,3-cyclohexadiene (CHD) on both spin states. In particular, we focused on aliphatic hydroxylation of toluene and CHD, and hydroxylation/dehydrogenation of CHD and epoxidation of CHD. Toluene undergoes the expected HAT with a free energy of activation of 13.4 kcal $mol^{-1}$ on the doublet spin state and 16.3 kcal $mol^{-1}$ on the quartet states (Figure S9, Supporting Information). In both cases a radical intermediate is formed representing $[Fe^{IV}(OH)(TPFPP)]^{+}$-$C_7H_7^{\bullet}$]. However, it is expected its lifetime will be short as the reaction is completed with an OH• rebound to form the final alcohol products with negligible barrier. Finally, the reaction of $^{4,2}[Fe^{IV}(O)(TPFPP^{+\bullet})]^{+}$ with CHD was investigated computationally leading to either epoxidation, hydroxylation or dehydrogenation products. Interestingly, all reactions have very small barriers of less than 1.2 kcal $mol^{-1}$ for concerted reaction mechanisms leading to products directly. As such, the reaction of $^{4,2}[Fe^{IV}(O)(TPFPP^{+\bullet})]^{+}$ with CHD should lead to a mixture of products. This is surprising as CHD as a substrate with iron(IV)-oxo or manganese(V)-oxo complexes in solution typically gives dehydrogenation to benzene as the sole product(Song et.al. 2006; Prokopet.al. 2010). Our gas-phase model, therefore, has properties significantly deviating from solution-based oxidants and consequently gives different reactivity patterns, which we analyze in detail below. Most probably the lack of an axial ligand in our $[Fe^{IV}(O)(TPFPP^{+\bullet})]^{+}$ model gives it significantly different chemical properties and results in reactivity differences.

## 6.3 Discussion

In order to understand the mechanistic details of the reaction pathways and find the origin of hydride versus hydrogen atom abstraction processes, we did a detailed analysis of the electronic and thermochemical properties of reactants and intermediates. Let us start with a look at the spin density distribution of reactant complexes and rate determining transition states, see Figure 6.4. As can be seen from the spin densities in the reactant complexes of $[Fe^{IV}(O)(Por^{+\bullet})]^{+}$ with CHT, designated $^{2,4}$Re, there is considerable spin density found on the substrate moiety, i.e. $\rho_{Sub}$ = 0.34 (–0.42) in $^{4}$Re ($^{2}$Re), respectively. The systems with TPFPP as equatorial ligand give analogous spin density distributions, see Tables S11 and S12 (Supporting Information). Similar spin density distributions are also seen for the reactant complexes containing cyclohexadiene and toluene. Therefore, upon approach of the substrate to the iron(IV)-oxo species, a considerable charge transfer happens from the substrate to the porphyrin group, which thereby loses radical character. This type of charge transfer in the reactant complexes is not seen in similar iron(IV)-oxo complexes bearing an axial ligand (de Visser et.al. 2004; Latifi et.al. 2012; Shaik et.al. 2008; Latifi et.al. 2009).

In one previous study (Vardhaman et.al. 2013; Kumar et.al. 2014) of a nonheme iron(IV)-tosylimido complex with CHD also electron transfer in the reactant complexes was observed due to the large electron affinity of the iron(IV)-tosylimido group as compared to P450 CpdI, where this electron transfer is not seen. The group spin densities of **$TS_{HA,CHT}$** and **$TS_{OAT,CHT}$** are also given in Figure 6.4 and display even more charge-transfer from substrate to porphyrin as compared to the reactant complexes. In particular, in **$^{4,2}TS_{HA,CHT}$** a spin density of $\rho_{Sub}$ = 0.90 (–0.73) is found for the quartet (doublet) spin state and hence almost a full electron transfer has taken place at this stage, so that the transition state corresponds to hydrogen atom abstraction.

However, the subsequent intermediates **IR1** for either the **Por** or **TPFPP** ligand systems have no radical on the substrate group, hence are cationic. Therefore, along the pathway from **$TS_{HA}$** to **IR1** an extra electron transfer has occurred to give an overall hydride transfer leading to the local minimum **IR1**. As such, even though **IR1** mimics a hydride transfer local minimum, in fact the reaction proceeds via an initial

hydrogen atom transfer in the transition state followed by a fast electron transfer en route to the intermediate **IR1**. Clearly, the hydride transfer is split into a hydrogen atom transfer followed by an electron transfer and these two processes are not simultaneous, namely the hydrogen atom transfer happens first, i.e. in the TS, and the subsequent electron transfer happens after the TS. As a result of this, the subsequent OH rebound will refer to an $OH^-$ transfer to the substrate cation. The early second electron transfer will lower the energy of the iron-hydroxo intermediate in the mechanism. As a matter of fact the energy of $^{4,2}$**IR1** is lower than that of the alcohol product complexes with a substantial rebound barrier in the low-spin state. It is, therefore, likely that $C_7H_7^+$ will be released from **IR1** as is also detected in the mass spectrum. The calculated mechanism and the obtained charge and spin distributions clearly support the experimental observations and explain the various product distributions.

To understand the obtained potential energy profiles and reaction mechanisms of the reaction of $[Fe^{IV}(O)(TPFPP^{+\bullet})]^+$ with CHT substrate, we set up a valence bond (VB) curve crossing diagram to gain insight into the electronic changes during the reaction. In the past, we used these valence bond diagrams to understand the electronic features of reactants that determine the transition states. Thus, we showed that in hydrogen atom abstraction transition states by metal(IV)-oxo oxidants, the rate determining barrier correlates with either the strength of the C–H bond that is broken or the O–H bond that is formed (de Visser et.al. 2004; Latifi et.al. 2012; Shaik et.al. 2008; Latifi et.al. 2009; de Visser, 2010). Furthermore, these VB diagrams explained the electronic origin of regioselectivities and bifurcation pathways (Yang et.al. 2016; Timmins et.al. 2017, Timmins and de Visser, 2017; Faponle et.al. 2016; Ji et.al. 2015; Li et.al. 2017). Note that in the following all calculations represent the large model as its thermochemistry was seen to be slightly different from the small model (compare Figures 6.2 and 6.3).

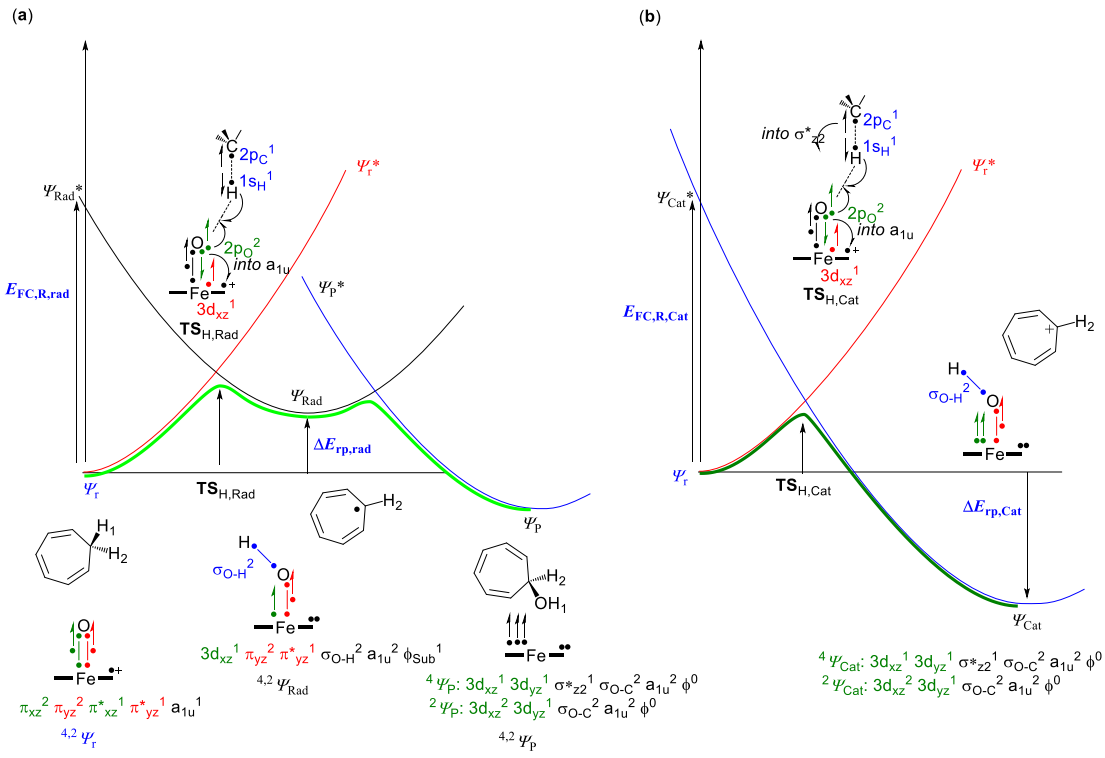


**Figure 6.5.** Valence bond curve crossing diagrams for a stepwise hydroxylation (a) and concerted hydroxylation (b) pathways. Dots represent electrons and a line in between two dots is a bonding orbital with two electrons.

The VB diagram explain the difference between stepwise and concerted reaction mechanisms and gives the various electron transfer processes and, in particular, highlights how hydrogen atom transfer and hydride transfer differ (Figure 6.5). Previously, a stepwise mechanism for substrate hydroxylation for aliphatic hydroxylation by **CpdI** of P450 was reported with a VB landscape similar to the one shown on the left-hand-side of Figure 6.5 (Shaik et.al. 2008; Latifi et.al. 2009; de Visser, 2010; Li et.al. 2017; Hernandez-Ortega et.al. 2015). Thus, in VB theory the reactant configuration has wave function $\Psi_r$ and connects to an excited state in the product geometry with wave function $\Psi_r$*. The product wave function is $\Psi_P$ in the product geometry and connects to an excited state in the reactant geometry with wave function $\Psi_P$*.

In our model the reaction starts from $[Fe^{IV}(O)(TPFPP^{+\bullet})]^+$, which is an iron(IV)-oxo porphyrin cation radical species with orbital occupation $\pi_{xz}^2\ \pi_{yz}^2\ \pi^*_{xz}{}^1\ \pi^*_{yz}{}^1\ a_{1u}{}^1$.[11] Occupation of the $\pi_{xz}$ and $\pi^*_{xz}$ orbitals with three electrons means there is a two-center three-electron bond located in the xz-plane along the Fe–O axis. In addition, there is another two-center three-electron bond in the yz-plane due to occupation of $\pi_{yz}$ and $\pi^*_{yz}$

with three electrons (shown in red in Figure 6.5). In addition, $[Fe^{IV}(O)(TPFPP^{+\bullet})]^{+}$ has a singly occupied orbital with a1u symmetry on the porphyrin ligand. Upon activation of the substrate, a hydrogen atom abstraction transition state results in breaking of the σC–H orbital in the substrate into atomic orbitals ($2p_C$ and $1s_H$). Furthermore, the $\pi_{xz}^2$ $\pi^*_{xz}^1$ pair of orbitals revert to atomic orbitals $2p_O^2$ $3d_{xz}^1$, whereby one electron from the $2p_O$ orbital is promoted to the $a_{1u}$ orbital. Finally, the remaining $2p_O$ electron pairs up with the $1s_H$ electron to form the $\sigma_{O-H}$ orbital. Consequently, the hydrogen atom abstraction barrier ($E_{TS(H,Rad)}$) is determined by the strength of the C–H bond that is broken ($BDE_{CH}$), the strength of the O–H bond that is formed ($BDE_{OH}$), the strength of the $\pi_{xz}/\pi^*_{xz}$ orbitals that are broken ($E_{\pi/\pi^*xz}$) and the excitation energy from $2p_O$ to the porphyrin group ($E_{exc}$), Eq 6.1.[24c,32]

$$E_{TS(H,Rad)} \propto BDE_{CH,CHT} - BDE_{OH} + E_{\pi/\pi^*xz} + E_{exc} \qquad (6.1)$$

In the concerted mechanism (Figure 6.5b) these same bond breaking and bond forming reactions occur. However, at the same time, an electron is promoted from the $2p_C$ orbital of the CHT group into the metal-type orbitals, i.e. into the $\sigma^*_{z2}$ orbital in the quartet spin state and into $3d_{xz}$ in the doublet spin state. Therefore, the barrier ($E_{TS(H,Cat)}$) for the concerted mechanism will be dependent on the energy to break the C–H bond ($BDE_{CH}$), the energy to form the O–H bond ($BDE_{OH}$), the energies to split the $\pi_{xz}/\pi^*_{xz}$ pair of orbitals into atomic orbitals ($E_{\pi/\pi^*xz}$), the electron transfer from $2p_{O,x}$ to $a_{1u}$ ($E_{exc}$) and from $2p_C$ to $\sigma^*_{z2}/3d_{xz}$. The latter excitation refers to the ionization energy of CHT ($IE_{Sub}$) and the electron affinity of the iron(IV)-oxo complex ($EA_{FeO}$), Eq 6.2.

$$E_{TS(H,Cat)} \propto BDE_{CH,CHT} - BDE_{OH} + E_{\pi/\pi^*xz} + E_{exc} + IE_{Sub} + EA_{FeO} \qquad (6.2)$$

Consequently, the VB analysis highlights the fundamental differences between hydrogen atom and hydride transfer processes. In particular, it shows that hydride transfer is only possible if the second electron transfer is an exothermic reaction. Therefore, the hydrogen atom abstraction barrier is always lower in energy than the hydride transfer barrier unless the energy difference between the ionization energy of the substrate (IESub) and the electron affinity of the oxidant EAFeO is negative. To find out if that is the case for substrates CHT, CHD and toluene, we estimated values for all these individual contributions from adiabatic electron and hydrogen atom transfer energies or the molecular orbital differences in the reactant complexes.

Figure 6.6 gives the enthalpic differences for individual electron, hydrogen atom and hydride transfer processes from CHT to iron(IV)-oxo porphyrin cation radical. Thus, the reactions from left to right represent electron transfer to form $[Fe^{IV}(O)(TPFPP)]^0$ and $C_7H_8^{+\bullet}$ and has a small endothermic driving force of $\Delta H_{ET}$ = 6.6 (6.2) kcal mol$^{-1}$ in the doublet (quartet) spin states. Therefore, a long-range electron transfer between oxidant and substrate will not happen. Furthermore, the difference between radical and cationic pathways displayed in Figure 6.5 implicated that the radical pathway would be lower for an endothermic electron transfer. As this is the case, the combination of VB and thermochemical modelling predicts a rate-determining hydrogen atom abstraction first.

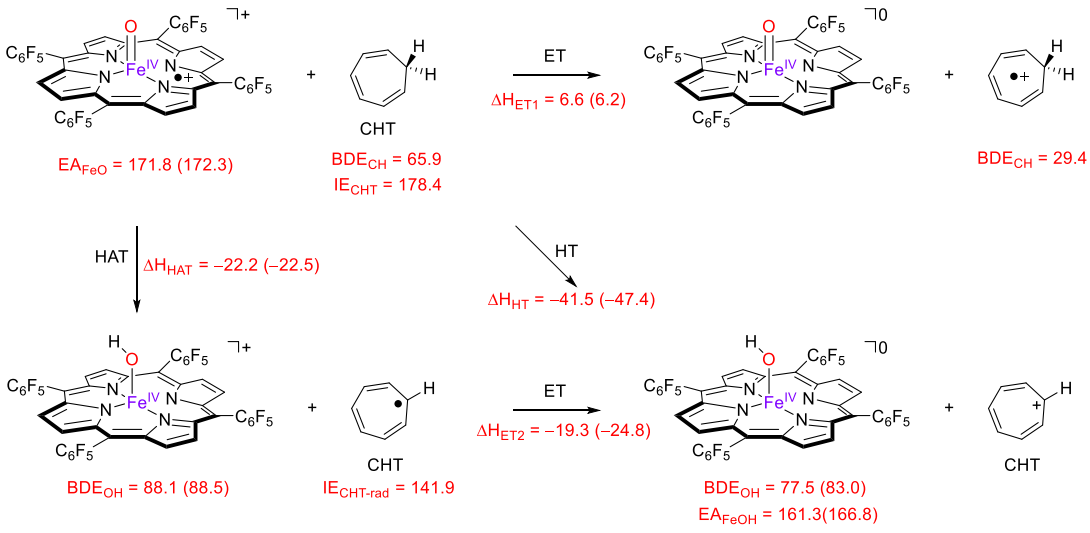


**Figure 6.6.** Thermochemical reaction scheme for individual electron, proton and hydride transfer from iron(IV)-oxo and iron(IV)-hydroxo complexes. Data represent reaction enthalpies (in kcal mol$^{-1}$) as calculated at UB3LYP/BS2//UB3LYP/BS1 with ZPE corrections included. Quartet spin data in parenthesis, doublet spin data out of parenthesis.

By contrast, the enthalpy of reaction for hydrogen atom abstraction is calculated as $\Delta H_{HAT}$ = –22.2 (–22.5) kcal mol$^{-1}$ in the doublet (quartet) spin states. Consequently, approach of substrate on [$Fe^{IV}$(O)(TPFPP$^{+\bullet}$)]$^{+}$ will lead to a hydrogen atom abstraction and the formation of [$Fe^{IV}$(OH)(TPFPP)]$^{+}$ and $C_7H_7^{\bullet}$ rather than electron transfer. However, the electron transfer between [$Fe^{IV}$(OH)(TPFPP)]$^{+}$ and $C_7H_7^{\bullet}$ has an exothermic driving force of $\Delta H_{ET}$ = –19.3 (–24.8) kcal mol$^{-1}$ for the doublet (quartet) pathways. This means that although no electron transfer will take place between reactants, as soon as the hydrogen atom transfer has taken place it becomes energetically feasible and will happen quickly. Indeed, the DFT calculations reported above give a mechanism whereby an initial hydrogen atom abstraction took place followed by a fast electron transfer in an overall hydride transfer process.

If we now calculate the reaction enthalpies for Figure 6.6 but with cyclohexadiene or toluene as a substrate, we find an analogous result, whereby the long-range electron transfer is energetically unfavorable over hydrogen atom transfer but by an even larger amount. In the case of cyclohexadiene, the electron transfer from $C_7H_7^{\bullet}$ to [$Fe^{IV}$(OH)(TPFPP)]$^{+}$ is still exothermic by 6.0 kcal mol$^{-1}$, while it is endothermic for toluene. Therefore, cyclohexadiene is expected to also react via an overall hydride transfer with an initial hydrogen atom abstraction followed by electron transfer, whereas no such electron transfer will be expected for toluene.

## 6.5 Conclusions

In this work a combined mass spectrometry and density functional theory study is presented on the reactivity of [$Fe^{IV}$(O)(TPFPP$^{+\bullet}$)]$^{+}$ with CHT and selected substrates. We find a reaction mechanism whereby electron transfer is determined by the intermediate structure. Thus, although a formal hydride transfer is thermochemically favorable, actually the initial step is hydrogen atom transfer with a subsequent electron transfer. As such, hydride transfer processes should be seen as consecutive hydrogen atom and electron transfer processes, where an initial hydrogen atom abstraction is followed by a quick electron transfer as also reported previously for the reactivity of analogous heme and nonheme iron(IV)-oxo oxidants. Our thermochemical modelling shows that the original reactant cannot react via electron transfer as it is endothermic; however, the subsequent intermediate, namely the iron(IV)-hydroxo species, has a sufficiently large electron affinity to abstract electrons from the substrate. This

mechanism may have relevance to enzymatic and biomimetic reactivity work where often hydride transfer processes are proposed and explains the intrinsic properties of substrate and oxidant that determines the reaction mechanism.

## 6.6 Experimental Section

### 6.6.1 Experiment

All chemicals and solvents were research grade products purchased from commercial sources and used as received. For the synthesis of the iron(IV)-oxo porphyrin cation radical complex, a reaction of (5,10,15,20-tetrakis(pentafluorophenyl)porphinato) iron(III) chloride, [$Fe^{III}$(TPFPP)]Cl was applied with iodosylbenzene ($C_6H_5IO$), which was synthesized according to a literature procedure (Saltzman and Sharefkin, 1973) and stored at –20 °C. The cycloheptatriene-7-[D1] was prepared by the reduction of 7-acetoxynorbornadiene with $LiAlD_4$ in tetrahydrofuran as described in the literature (Franzus and Snyder, 1963). Subsequently, it was purified by preparative GLC using a 3 m column filled with Chromosorb 80/100 W-AW coated with a base deactivated polyethyleneglycol stationary phase, mounted on a Carlo Erba FRACTOVAP Mod ATC/f series 410 gas chromatograph. The identification, purity and deuterium content was obtained by GLC-MS analyses on a Hewlett-Packard 5890 gas chromatograph coupled with a model 5989B quadrupole mass spectrometer, by using a 50 m long, 0.2 mm i.d. fused silica capillary column, coated with cross-linked methylsilicone film. The extent of D-incorporation in cycloheptatriene-7-[D1] was found equal to 98.0 atom %D.

### 6.6.2 Instrumental

All procedures and methods follow those from our previous studies on these chemical systems (Sainna et.al. 2015; Cantu-Reinhard[b] et.al. 2016). Mass spectrometric studies were performed on a Bruker BioApex Fourier transform-ion cyclotron resonance (FT-ICR) mass spectrometer, which is implemented with a cylindrical infinity cell, a 4.7 T superconducting magnet and an Apollo I electrospray ionization (ESI) source. Analyte solutions were infused into the mass spectrometer at a continuous flow rate of 120 μL $h^{-1}$ by a syringe pump through a 50 μm i.d. fused-silica capillary. Subsequently, ions were desolvated by applying an N2 counter current of drying gas heated at 400 K, trapped and accumulated in a radiofrequency-only hexapole ion guide for 0.8 seconds,

and then pulsed into the ICR cell (held at room temperature, 300 K). An ion ejection procedure was used to select the ions of interest, namely $[Fe^{IV}(O)(TPFPP^{+\bullet})]^+$ with m/z 1044, and their reactivity and fragmentation patterns were studied through ion-molecule reactions by inserting neutral collision gases to the ICR cell at stationary pressures (in the range 1.0 – 15 × $10^{-8}$ mbar) by a needle valve. The product ion abundances were monitored as a function of time and analyzed. The pressure readings, obtained from a cold-cathode sensor (IKR Pfeiffer Balzers S.p.A., Milan, Italy), were calibrated against the rate constant of proton transfer from methane cation radical to methane, Eq 6.3, for which the rate constant has been accurately determined at k = 1.1 × $10^{-9}$ $cm^3$ $s^{-1}$ and weighted by using individual response factors (Meot-Ner, 1979; Bartmess, 1983).

$$CH_4^{+\bullet} + CH_4 \rightarrow CH_5^+ + CH_3^{\bullet} \qquad (6.3)$$

Rate constants for the reaction processes were derived from the ion abundance of the reactant ion, $[Fe^{IV}(O)(TPFPP^{+\bullet})]^+$, monitored as a function of time at each selected pressure. The slope of these semi-logarithmic plots gave us the pseudo first-order rate constants for the disappearance of $[Fe^{IV}(O)(TPFPP^{+\bullet})]^+$, then divided by the substrate concentration to obtain second-order rate constants ($k_{exp}$) at 300 K. All measurements were done at least in triplicate and averaged. Whereas the reproducibility of $k_{exp}$ values is within 10%, the estimated error in the absolute rate constants is estimated to be ±30%. The ratio of the second-order rate constant and the collision rate constant ($k_{ADO}$), as described in Eq 6.4, enabled us to estimate the reaction efficiencies (Φ). Values for $k_{ADO}$ were calculated using the parametrized trajectory theory (Su and Chesnavich, 1982).

$$\Phi = k_{exp}/k_{ADO} \times 100\% \qquad (6.4)$$

### 6.6.3 Sample preparation.

The $[Fe^{IV}(O)(TPFPP^{+\bullet})]^{+}$ ion was synthesized by adding iodosylbenzene (0.5 mM) to 10 μM of $[Fe^{III}(TPFPP)]Cl$ in a methanol/dichloromethane (1:1) mixture and was stable for about 1 h, if kept cooled at –40°C. The high-resolution ESI FT-ICR mass analysis of the reaction mixture gave a prominent peak centered at m/z 1044 with isotopic pattern conforming to an iron(IV)-oxo complex, $[Fe^{IV}(O)(TPFPP^{+\bullet})]^{+}$, as well as a signal for the reduced form $[Fe^{III}(TPFPP)]^{+}$ at m/z 1028. As already described in previous contributions (Chiavarino et.al. 2008; Sainna et.al. 2011; Cantu-Reinhard[b] et.al. 2016), the synthetic procedure leads to the formation of an additional fraction of isomeric species, most likely corresponding to a four-coordinate iron(III) complex oxidized on the porphyrin ring and unable to perform any oxidation reactions. This portion, quantified by its complete trapping by NO gives the $[Fe^{III}(TPFPP\text{-}O)(NO)]^{+}$ adduct, similarly to the reduced form, $[Fe^{III}(TPFPP)]^{+}$, and was discarded from the kinetic analysis.

### 6.6.4 Density functional theory modelling

Calculations were done using density functional theory methods as implemented in Gaussian-09 (Frisch et.al. 2015), and follow methods and procedures as reported and tested previously on analogous complexes and reactions (Cantu-Reinhard[a] et.al. 2016, Yang et.al. 2016; Vardhaman et.al. 2013, Cantu-Reinhard[b] et.al. 2017). In general, the unrestricted B3LYP hybrid density functional theory is used for all geometry optimizations and frequencies (Becke, 1993; Lee et.al. 1988). All structures were optimized in the gas phase with an LACVP basis set on iron (with core potential) and 6-31G on the rest of the atoms (H, C, N, O): basis set BS1 (Hay and Wadt, 1985). Single points using a triple-ζ quality basis set on iron (with core potential), i.e. LACV3P+, and 6-311+G* on the rest of the atoms were done to correct the energies: basis set BS2. All stationary points had real frequencies and transition states were characterized with a single imaginary frequency for the correct mode. Energies reported here are UB3LYP/BS2//UB3LYP/BS1 with zero-point energy included. Previous studies showed little differences in optimized geometries and reaction kinetics between geometry optimizations at UB3LYP/BS2 and UB3LYP/BS1 level of theory (Sainna et.al. 2015; Cantu-Reinhard[b] et.al. 2016), hence the latter was used here.

Kinetic isotope effects are calculated from the free energy of activation difference between hydrogen atom abstraction transition state and isolated reactants ($\square G^{\ddagger}_{HA}$) between the substrate with all hydrogen atoms and the one with one or more hydrogen atoms replaced by deuterium, according to Eq, 6.5, with R being the gas constant and T the estimated temperature (300K) (Kumar et.al. 2004; de Visser, 2006).

$$KIE = \exp((\Delta G^{\ddagger}_{HA,D} - \Delta G^{\ddagger}_{HA,H})/RT) \quad (6.5)$$

**Acknowledgements**

FGCR thanks the Conacyt Mexico for a studentship. The COST Action (CM1305 ECOSTBio, Explicit Control Over Spin-States in Technology and Biochemistry) is acknowledged for support.

**Keywords**: High-valent iron(IV)-oxo • Porphyrin • density functional theory • FT-ICR MS • reaction mechanisms

# Chapter Seven

# PROJECT 5

## *Biodegradation of cosmetics products: A computational study of Cytochrome P450 metabolism of phthalates*

*Fabián G. Cantú Reinhard,[‡] and Sam P. de Visser*[*,‡]*

[‡] Manchester Institute of Biotechnology and School of Chemical Engineering and Analytical Science, The University of Manchester, 131 Princess Street, Manchester M1 7DN, United Kingdom

**Abstract.**

*The cytochromes P450s are a broad class of enzymes in the human body with important functions for human health that include the metabolism and detoxification of compounds in the liver. Phthalates are a type of compounds commonly found in the environment from pollution. This work discusses the possible degradation mechanisms of phthalates by the cytochromes P450 in the liver through computational modelling using 2-ethylhexyl-phthalate as a model substrate. In particular, we focus on the mechanisms for O-dealkylation, aliphatic hydroxylation and aromatic hydroxylation processes. Thus, in their catalytic cycle the P450s form a high-valent iron(IV)-oxo heme cation radical as the active species (called Compound I) that reacts with substrates. We set up model complexes of Compound I with substrate and investigate the reaction mechanism to products with a phthalate model. The reactions are subsequently studied with density functional theory and quantum mechanics/molecular mechanics on enzymatic structures. The work shows that several reaction barriers in the gas-phase are close in energy leading to a mixture of products. However, when we try to dock substrate into a P450 isozyme some of those channels are inaccessible due to unfavorable substrate positions. Product distributions are discussed under various reaction conditions and rationalized with valence bond and thermodynamic models.*

**Published Reference:**

Cantu-Reinhard, F.G. De Visser, S. Biodegradation of cosmetics products: A computational study of Cytochrome P450 metabolism of phthalates. *Inorganics* **2017**, 5, 77.

## 7.1. Introduction

Phthalates are commonly used chemicals in a variety of products including cosmetics. Although no clear evidence exists, they actually may be harmful compounds to Biosystems and, for instance, may lead to breast cancer in humans. It is believed that phthalates can be biodegraded in the human liver and most likely the cytochromes P450 are involved in this process. However, as some of these products may be toxic metabolites, we decided to do a computational study on the most likely products obtained from the reaction of a P450 active site model with phthalate. Thus, cytochrome P450 enzymes are a superfamily of heme-containing monoxygenases found in most biological systems including mammals, insects, fungi as well as bacteria (Sono et.al. 1996; Ortiz de Montellano, 2004; Meunier et.al. 2004; Denisov et.al. 2005; Munro et.al. 2007; Ortiz de Montellano, 2010). It is believed to be the most abundant enzyme family in the plant kingdom (Xu et.al. 2015). As of 2017, there have been over 39,400 sequences assigned across 236 species (Fujikura et.al. 2015), and with many genomes yet to be sequenced, these numbers are projected to increase significantly over the next few years (Ortiz de Montellano, 2010; Xu et.al. 2015).

The P450s display a large range of substrate activation reactions and, hence, they are well studied and applications of these enzymes are being sought in biotechnology and medicine. In general, the P450s are heme enzymes that bind molecular oxygen on the heme-iron and their most common reaction mechanism with substrates happens through oxygen atom transfer to substrate (Meunier et.al. 2004; Groves et.al.2003; Watanabe et.al. 2007; de Visser and Nam, 2010). Figure 7.1 displays the active site structure of P450 as taken from the 4L40 protein databank (pdb) file (Belcher et.al. 2014). The catalytic cycle of P450 enzymes has an iron(III)(heme)(water) with the metal in six-coordination ligand environment that is linked to the protein backbone through a chemical bond of the iron with the sulfur atom of a cysteinate residue (Cys365). The pdb file also contains the substrate, i.e. a linear fatty acid that is located in a pocket on the distal side of the heme and held in position through a salt-bridge with an active site Arg residue.

Upon entering of substrate into the binding pocket and approach to the heme, the water molecule is released from iron and a spin-state change triggers an electron transfer from the P450 reduction partner. Subsequently, molecular oxygen binds to the heme, is reduced and protonated to form an iron(III)-hydroperoxo species called Compound 0 (Cpd0). A final protonation step leads to an iron(IV)-oxo heme cation radical species called Compound I (CpdI). The latter reacts with substrates, for instance, through an aliphatic hydroxylation reaction. Experimental evidence for this catalytic cycle comes from spectroscopy (UV-Vis absorption, electron paramagnetic resonance and Mössbauer spectroscopy) studies that characterized P450 CpdI (Rittle et.al. 2010) as well as Cpd0 (Daydov et.al. 2005). Computational modelling revealed that CpdI has two close-lying spin states, namely doublet and quartet spin, that are degenerate and hence the structure and reactivity is dependent on the abundances of both spin states.

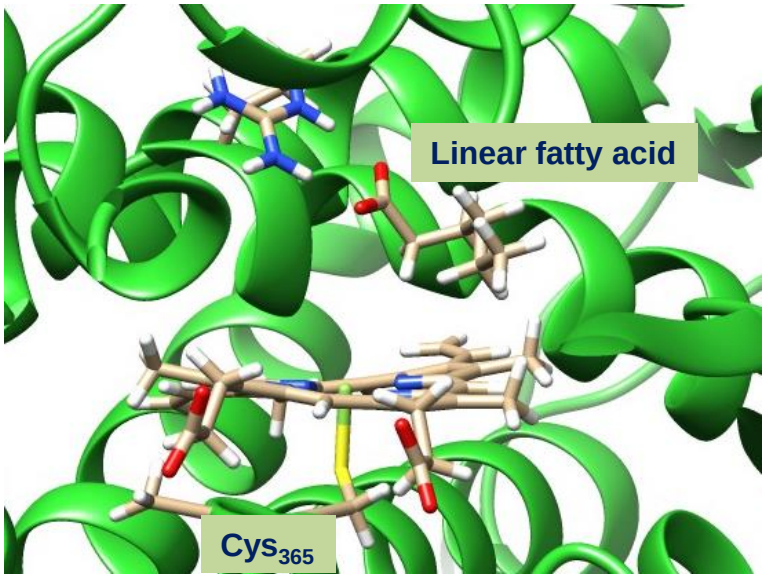


**Figure 7.1.** Active site structure of the substrate bound resting state of P450 as taken from the 4L40 pdb file.

The mechanism of these oxygen atom transfer reactions has been studied in detail with a range of computational techniques (Shaik et.al. 2005; Blomberg et.al. 2014). An overview of commonly catalyzed reactions by P450 isozymes is given in Figure 7.2. The most extensively studied reaction pathway is aliphatic hydroxylation (Oligaro et.al. 2000; Kamachi et.al. 2003; de Visser et.al. 2004; Li et.al. 2017) that happens via a stepwise mechanism with an initial hydrogen atom abstraction to form an iron(IV)-hydroxo intermediate following rebound to give the alcohol product complexes. With most substrates, the hydrogen atom abstraction step is rate-determining, while the

rebound barrier is much smaller (Shaik et.al. 2004). In particular, the doublet spin state mechanism tends to have negligible rebound barriers, while they are generally higher on the quartet spin state surface. This is due to electron transfer into a virtual orbital in the quartet spin state, whereas the electron can move into a lower lying orbital in the doublet spin state. P450s are also known to convert C=C double bonds into olefins (de Visser et.al. 2001; de Visser et.al. 2002; Kumar et.al. 2010; Sainna et.al. 2015), sulfides into sulfoxides (Sharma et.al. 2003; Kumar et.al. 2005; Kumar et.al. 2011) and arenes into phenols (de Visser et.al. 2003; Kumar et.al. 2012; Cantú-Reinhard et.al. 2016) (pathways II, III and IV in Figure 7.2). Apart from sulfoxidation, which is a concerted process, all other oxygen atom transfer reactions are stepwise via at least one intermediate that is usually a radical.

In recent years; however, alternative mechanisms have been established that lead to desaturation or ring-closure processes (pathways V, VI and VII in Figure 7.2). In particular, ring-closure reactions are part of natural product biosynthesis of antibiotics and hormone compounds (Tang et.al. 2017). Other forms of desaturation processes refer to the conversion of aliphatic groups to olefins (pathway V) or the decarboxylation of fatty acids to terminal olefins (pathway VI). Thus, desaturation reactions have been observed in the activation of drug molecules, for instance in ethylcarbamate and valproic acid, by P450 isozymes (Rettie et.al.1987; Lee et.al. 1998) but also in the biosynthesis of ergosterol in the human body (Guengerich et.al. 1991). Computational studies on the mechanism of substrate desaturation showed these desaturation reactions by CpdI to start with a hydrogen atom abstraction similarly to aliphatic hydroxylation. However, in contrast to rebound of the OH group to the radical as happens in substrate hydroxylation mechanisms, in desaturation processes instead a second hydrogen atom abstraction by the iron(IV)-hydroxo group gives iron(III)-water and an olefin product (Kumar et.al. 2004; Ji et.al. 2015). As such the mechanism can bifurcate in the radical intermediates that can lead to both hydroxylation and desaturation products. Recently, a P450 isozyme was discovered (P450 $OleT_{JE}$) that binds long-chain fatty acids and convert them to terminal olefins through a decarboxylation reaction (Rude et.al. 2011; Grant et.al. 2015). A detailed quantum mechanics/molecular mechanics (QM/MM) study on the mechanism leading to decarboxylation and α- and β-hydroxylation of the linear fatty acid was performed (Faponle et.al. 2016) and gave insight into the origins of the bifurcation pathways.

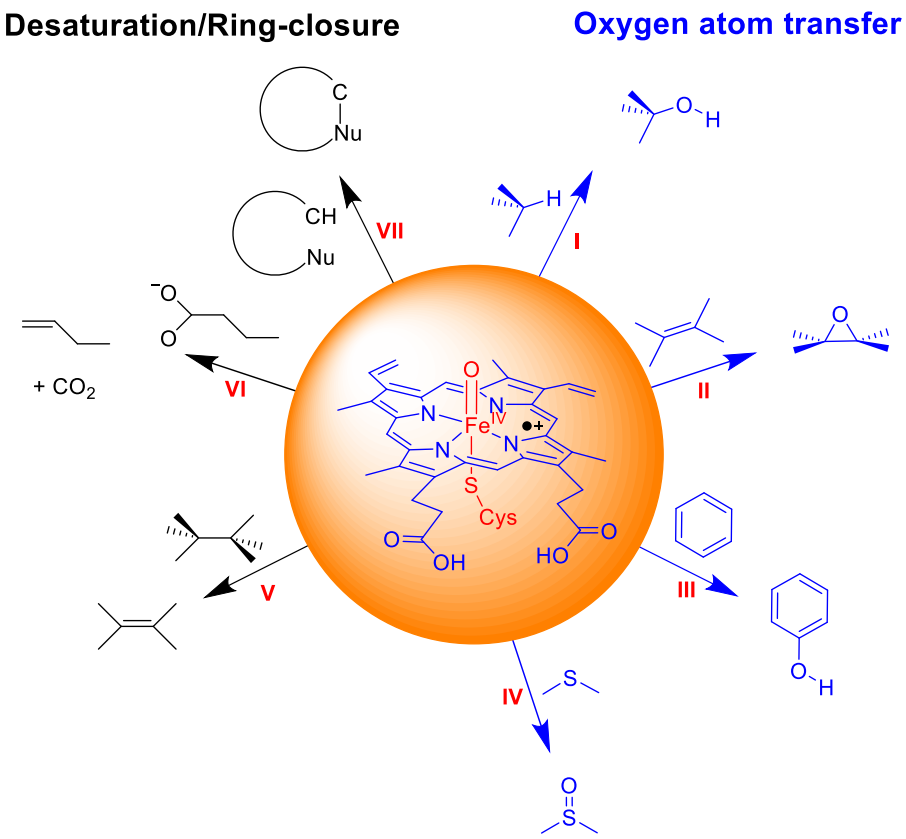


**Figure 7.2.** Reaction mechanisms catalyzed by P450 Compound I.

Clearly, P450 enzymes react via a diverse set of chemical reactions with substrates and the origins of the product distributions are not always clear. To gain insight into how P450 enzymes metabolize phthalate substrates, we decided to do a computational study, which is presented in this work.

### 7.2. Results

Following previous benchmark and calibration studies, we started the work with enzyme active site model complexes of P450 CpdI with substrate (Ogliaro et.al. 2001; de Visser et.al.2003; Cantú-Reinhard et.al. 2017). The model (see Figure 7.3) contains the iron(IV)-oxo group embedded in a porphyrin without side chains, while the axial cysteinate ligand is abbreviated to SH–. As a model substrate we investigated the ester of phthalate with 2-ethylhexanol (SubH) and studied the mechanisms leading to aliphatic hydroxylation, O-dealkylation, epoxidation and aromatic hydroxylation, which are suggested products obtained for the reaction of phthalates with P450s (Choi et.al. 2012). Specifically, we focus on aliphatic hydroxylation at the $C^5$ position of the alkyl chain of the substrate and expect it to start with a hydrogen atom abstraction (via transition state **$TS_A$**) to give a radical intermediate **IA**. Radical rebound (via transition

state **TS**$_{rebA}$) with then give the alcohol product complex **PA**. The mechanism tested for O-dealkylation starts with a hydrogen atom abstraction from atom C$^{1}$ (via transition state **TS**$_{B}$) to give a radical intermediate **IB**. Subsequently, radical rebound (via transition state **TS**$_{rebB}$) gives the alcohol product (structure **IB2**). The latter transfer the alcoholic proton to the carboxylate group and splits into phthalate and an aldehyde (product **PB**). The third mechanism tested is epoxidation of the aromatic ring, where an electrophilic attack of the oxo group on one of the aromatic carbon atoms takes place (via transition state **TS**$_{C}$) to form an intermediate **IC**. A ring-closure transition state (**TS**$_{rcC}$) then leads to the epoxide product complexes **PC**. The final mechanism is aromatic hydroxylation, which also starts with an electrophilic attack of the oxo group on one of the aromatic carbon atoms (via the same transition state **TS**$_{C}$) to form an intermediate **IC**. However, a bifurcation of the latter leads to the loss its ipso-proton to the porphyrin ring via a protonated porphyrin intermediates **ID** that reshuttles its proton to the oxygen atom to form phenol products **PD**.

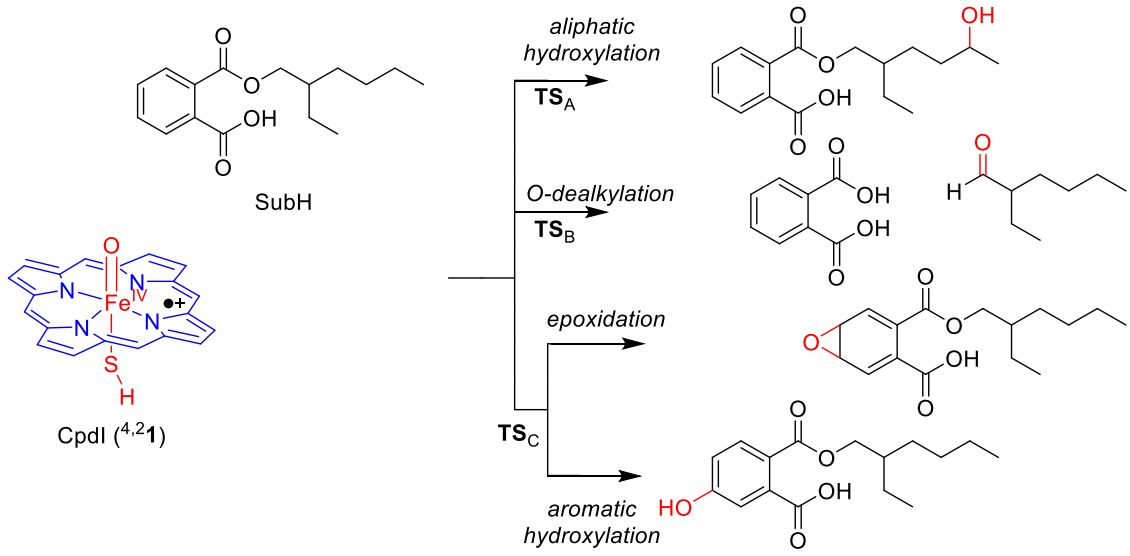


**Figure 7.3.** P450 model and reaction mechanisms studied in this work.

In the next few sections, we will discuss each of these mechanisms in detail, but first start with a comprehensive analysis of the reactant complex, namely CpdI.

### *7.2.1. CpdI structure and electronic configuration*

CpdI has been characterized experimentally as a triradical system with unpaired electrons on the iron(IV)-oxo and heme groups in an antiferromagnetic manner (Rittle et.al. 2010). Early density functional theory (DFT) calculations (Ogliaro et.al. 2001; de Visser et.al. 2003; Green et.al.1999) as well as subsequent QM/MM studies (Schöneboom et.al. 2002; Bathelt et.al. 2008; Porro et.al. 2009) predicted this electronic configuration already but showed that CpdI has close-lying doublet and quartet spin states of almost equal energy. Figure 7.4 displays the relevant valence orbitals of P450 CpdI. The left-hand-side of Figure 7.4 gives the metal dominated orbitals. The lowest three orbitals shown are the bonding-type orbitals along the Fe–O bond and include the $\sigma_{z2}$ for the overlap of $3d_{z2}$ on iron with $2p_z$ on oxygen and the degenerate pair of $\pi_{xz}$ and $\pi_{yz}$ molecular orbitals for the bonding interaction between the $3d_{xz}$ (or $3d_{yz}$) on iron with the $2p_x$ (or $2p_y$) atomic orbital on oxygen. The antibonding combination of this pair of orbitals ($\pi^*_{xz}$ and $\pi^*_{yz}$) are higher in energy and both are singly occupied. In between those two pairs of orbitals is the doubly occupied $\delta_{x2-y2}$ orbital, which is non-bonding and located in the plane of the heme/porphyrin. High in energy and virtual are the two $\sigma^*$ antibonding orbitals: One along the O–Fe–S axis (the z-axis), namely $\sigma^*_{z2}$, and the other one in the plane of the porphyrin ring for the antibonding interactions of the metal with $2p_x/2p_y$ orbitals on the nitrogen atoms of the porphyrin ($\sigma^*_{xy}$). Note, that in this nomenclature, we took the x- and y-axis through an Fe–N bond. If the x- and y-axis instead are drawn in between two Fe–N bonds this results in the change of the labels xy and $x^2–y^2$.

On the right-hand-side of Figure 7.4 are given two high-lying $\pi$-orbitals on the porphyrin manifold, namely $a_{1u}$ and $a_{2u}$. The $a_{2u}$ orbital has electron density on the porphyrin nitrogen atoms as well as the meso-carbon atoms. As a result of this, these $\pi$-orbitals interact with the axial ligand orbitals and as it happens the $a_{2u}$ mixes somewhat with a $\pi$-orbital on sulfur, which destabilizes it in energy (Ogliaro et.al. 2000). Consequently, the $a_{2u}$ is high-lying and is easier to reduce than if this interaction is not present resulting in a low electron affinity for P450 CpdI (de Visser et.al. 2010).

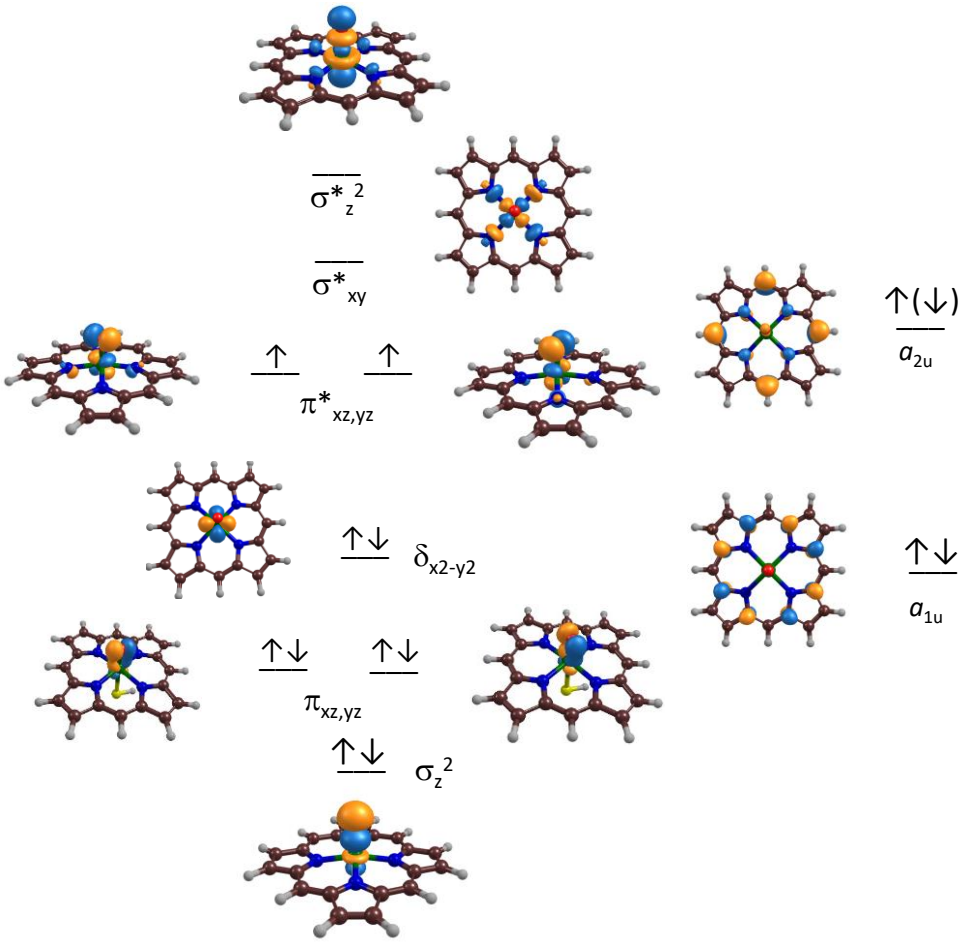


**Figure 7.4.** Relevant molecular orbitals of P450 CpdI and orbital occupation in the quartet and doublet spin states.

Our optimized geometries of $^{4,2}$CpdI matches previous structures well with Fe–O distances of 1.626 (1.624) Å and Fe–S distances of 2.570 (2.581) Å for $^{4}$**1** ($^{2}$**1**), respectively. Both structures correspond to an electronic configuration of $\pi_{xz}^2\ \pi_{yz}^2\ \delta_{x2-y2}^2\ \pi^*_{xz}{}^1\ \pi^*_{yz}{}^1\ a_{1u}^2\ a_{2u}^1$, whereby the unpaired $a_{2u}$ electron is up-spin in the quartet spin state, but down-spin in the doublet spin state. Energetically, the two spin states are within 1 kcal mol$^{-1}$ but their exact ordering and energy differences are dependent on whether solvent, entropy and external perturbations are taken into account.

### *7.2.2. Phthalate hydroxylation.*

Next, we investigated the reaction mechanism of aliphatic hydroxylation at the $C^5$ position and the obtained potential energy profile is given in Figure 7.5. The reaction is stepwise via a radical intermediate leading to alcohol products in a highly exothermic process. The hydrogen atom abstraction barrier is rate-determining with values of ΔE+ZPE = 19.9 (18.2) kcal $mol^{-1}$ on the quartet (doublet) spin states. The imaginary frequency for the hydrogen atom abstraction barriers are large (i1750 and i1549 for $^4$**TS**$_A$ and $^2$**TS**$_A$, respectively), which is typical for hydrogen atom abstraction barriers (de Visser et.al. 2010; Barman et.al. 2016; Timmins et.al. 2017) and usually means they are affected by replacement of hydrogen by deuterium that gives a large kinetic isotope effect (de Visser et.al. 2006).

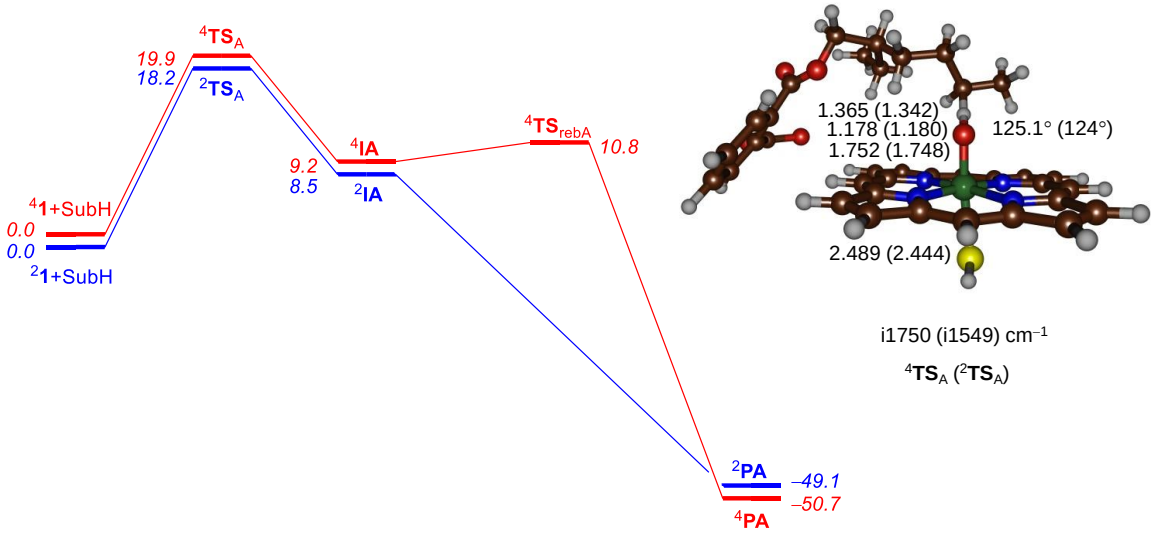


**Figure 7.5.** Potential energy landscape (B3LYP/BS1 optimized) of phthalate hydroxylation by P450 CpdI at the C5 position. Relative energies contain zero-point corrections and taken from B3LYP/BS2//B3LYP/BS1 in kcal $mol^{-1}$. Optimized geometries give bond lengths in angstroms, the Fe–O–C angle in degrees and the imaginary frequency in the transition state in $cm^{-1}$.

The optimized geometries of $^{4,2}$**TS**$_A$ put the transferring hydrogen atom close to the acceptor oxygen atom (1.178 and 1.180 Å for $^4$**TS**$_A$ and $^2$**TS**$_A$, respectively) indicating that the transition states are late on the potential energy surface. In general, late transition states correspond with higher barriers on the potential energy surface than earlier transition states in agreement with lower barriers (de Visser et.al. 2004). In both cases a radical intermediate is formed and spin density is starting to accumulate on the substrate $C^5$ atom in both cases ($\rho_{SubH}$ is 0.98 and 0.77 for the quartet and doublet spin states). At the same time the spin density on the FeO group is polarized toward iron.

Formation of the radical intermediates is energetically costly and is overall endothermic by 9.2 and 8.5 kcal $mol^{-1}$ in the quartet and doublet spin states. In the hydrogen atom abstraction step, in analogy to previous work (Shaik et.al. 2005; Ogliaro et.al. 2000, Kamachi et.al. 2003; de Visser et.al. 2004, Li et.al. 2017; Shaik et.al. 2002; Sharma et.al. 2003; Singh et.al. 2015), the doublet and quartet spin state surfaces are close in energy and virtually degenerate. After the radical intermediate, however, the two pathways bifurcate and a radical rebound barrier of 1.6 kcal $mol^{-1}$ needs to be crossed on the quartet spin state surface whereas the mechanism is barrierless on the low-spin surface. Attempts were made to find a rebound transition state on the doublet spin state surface, but all our geometry scans showed facile pathways with barriers less than 1 kcal mol–1 to form product complexes. The overall reaction leading to alcohol products is highly exothermic by around 50 kcal mol–1 on both spin state surfaces.

### *7.2.3. Phthalate O-dealkylation.*

Subsequently, we considered the reaction mechanism for O-dealkylation of our phthalate substrate and the obtained potential energy landscape is given in Figure 7.6. Similarly to the aliphatic hydroxylation reaction described in the previous section, the reaction is stepwise with an initial hydrogen atom abstraction via a radical intermediate leading to alcohol products in a highly exothermic process. However, the alcohol is not the final product and with a proton transfer step via transition state $\mathbf{TS}_{dealk}$ the alkyl group comes off as an aldehyde. Also for O-dealkylation, the hydrogen atom abstraction barrier is the rate-determining barrier in the reaction process with values of $\Delta E+ZPE$ = 19.3 (20.3) kcal mol–1 on the quartet (doublet) spin states. The imaginary frequency for the hydrogen atom abstraction barriers are large (i1775 and i1726 for $^{4}\mathbf{TS}_{B}$ and $^{2}\mathbf{TS}_{B}$, respectively), which is similar to those reported above for $^{4,2}\mathbf{TS}_{A}$.

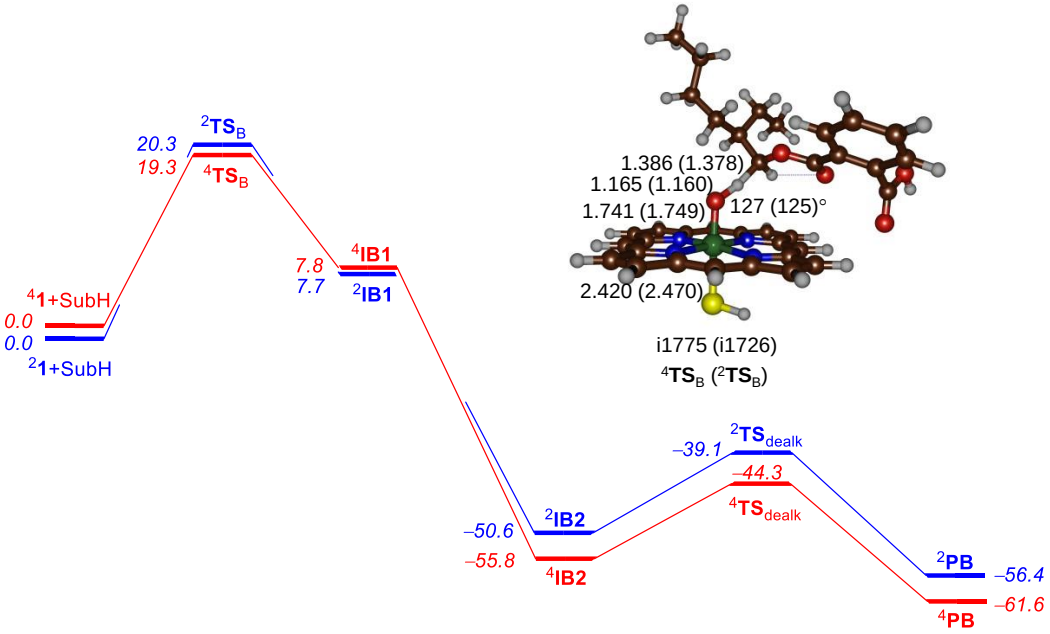


**Figure 7.6.** Potential energy landscape (B3LYP/BS1 optimized) of phthalate O-dealkylation by P450 CpdI. Relative energies contain zero-point corrections and taken from B3LYP/BS2//B3LYP/BS1 in kcal mol$^{-1}$. Optimized geometries give bond lengths in angstroms, the Fe–O–C angle in degrees and the imaginary frequency in the transition state in cm$^{-1}$.

The hydrogen atom abstraction transition state geometries ($^{4,2}$**TS**$_B$) are similar in structure to $^{4,2}$**TS**$_A$ with long C–H and short O–H distances: C–H bonds of 1.386 and 1.378 Å and O–H bonds of 1.165 and 1.160 Å are found for $^4$**TS**$_B$ and $^2$**TS**$_B$, respectively, indicating that the transition states are also late on the potential energy surface. Intermediates **IB1** are radicals with considerable spin density on the substrate C$^2$ atom ($\rho_{SubH}$ is 0.97 for both the quartet and doublet spin states). Similarly to the aliphatic hydroxylation pathway from the previous section the radical intermediates $^{4,2}$**IB1** are above reactants by about 7 – 8 kcal mol$^{-1}$. On both spin state surfaces we failed to obtain a rebound transition state, but geometry scans point to a facile and fast process with a barrier of less than 1 kcal mol$^{-1}$ leading to intermediate $^{4,2}$**IB2**. The radical disappears upon formation of the alcohol intermediate $^{4,2}$**IB2** en route to O-dealkylation product $^{4,2}$**PB**. The last step of dealkylation happens away from the P450 active site and can be catalyzed by a solvent water molecule. Thus, when we add a bridging water molecule to the substrate alcohol position a dealkylation barrier of 11.5 kcal mol$^{-1}$ is obtained for proton relay from the alcohol group to the carbonyl of the ester bond. This breaks the ester bond and releases *ortho-phthalic* acid in a process that is exothermic by 5.8 kcal mol$^{-1}$. Subsequent inclusion of water molecules in the model may even bring the barrier further down as evidenced in previous studies on P450 catalyzed dealkylation (Schyman et.al. 2010).

### *7.2.4. Phthalate epoxidation and aromatic hydroxylation.*

The final two pathways of phthalate oxidation by P450 CpdI that were considered are substrate epoxidation and aromatic hydroxylation that both start with an electrophilic attack of the oxo group on one of the carbon atoms of the aromatic ring to form a radical intermediate $^{2,4}$**IC**. From this intermediate the landscape is seen to bifurcate into two directions (Figure 7.7). Firstly, a ring-closure transition state $\mathbf{TS}_{rcC}$ leads to epoxide product complexes **PC**. Secondly, from **IC** the ipso-proton can transfer from the benzene ring to one of the nitrogen atoms of porphyrin to form intermediate **ID** in a highly exothermic reaction step. A small proton-reshuttle barrier $\mathbf{TS}_{PT}$ of less than 1 kcal mol$^{-1}$ transfers the proton to the oxygen atom to form phenol products PD. An alternative proton transfer pathway from $^{4,2}$**ID** leads via a significantly higher barrier to ketone products.

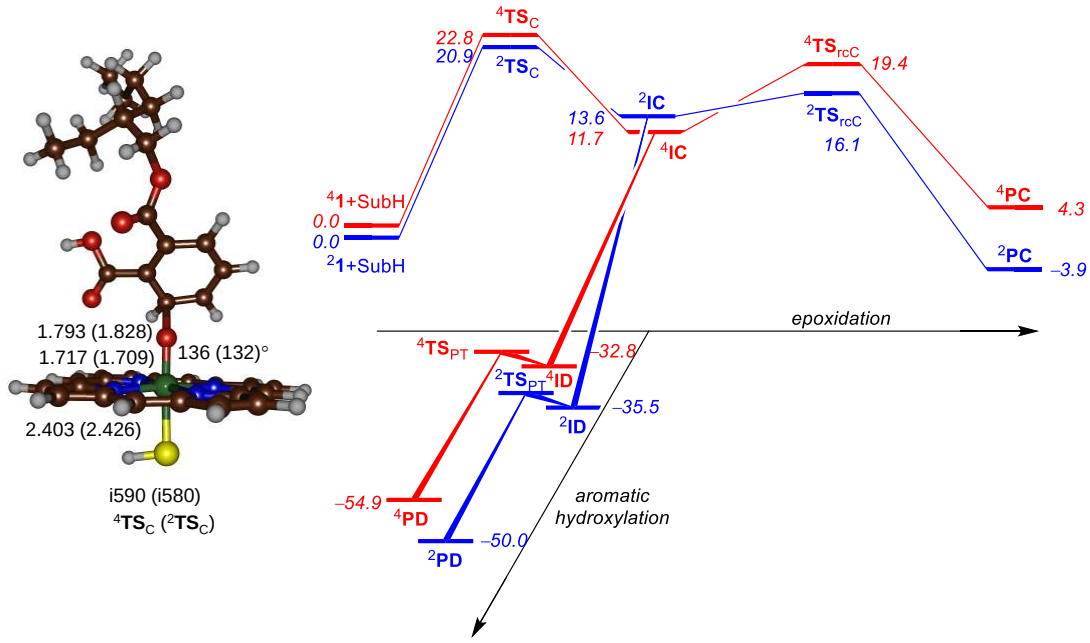


**Figure 7.7.** Potential energy landscape (B3LYP/BS1 optimized) of epoxidation and aromatic hydroxylation of phthalate by P450 CpdI. Relative energies contain zero-point corrections and taken from B3LYP/BS2//B3LYP/BS1 in kcal mol$^{-1}$. Optimized geometries give bond lengths in angstroms, the Fe–O–C angle in degrees and the imaginary frequency in the transition state in cm$^{-1}$.

The electrophilic attack of the oxo group on the aromatic ring carbons passes transition states 4,2TSC at a cost of 20.9 (22.8) kcal $mol^{-1}$ on the doublet (quartet) spin states. These transition states have elongated Fe–O bond lengths of 1.717 (1.709) Å and long O–C bond lengths of 1.793 (1.828) Å for $^{4}$**TS**$_{C}$ ($^{2}$**TS**$_{C}$), respectively. The potential energy surface is broad and hence a small imaginary frequency of well below i600 $cm^{-1}$ is found. Geometrically, the structure is upright with an Fe–O–C angle of 136° (132°) and matches earlier calculated structures of aromatic hydroxylation mechanism by P450 CpdI using different substrates (de Visser et.al. 2003; Kumar et.al. 2012; Cantú-Reinhard et.al. 2016; de Visser et.al. 2006; de Visser et.al. 2009).

After the transition state, the system relaxes to a radical intermediate $^{4,2}$**IC** with spin density of $\rho_{FeO}$ = 2.31 and $\rho_{SubH}$ = 1.01 in the quartet spin state. Both spin states remain degenerate along the pathway from reactants to **IC** as seen above for the other mechanisms as well and are higher in energy than reactants by 13.6 (11.8) kcal $mol^{-1}$ for $^{4}$**IC** ($^{2}$**IC**). Similar to aliphatic rebound, also the ring-closure barriers leading to epoxide products are well higher in energy on the quartet spin state than on the doublet spin state, (7.7 versus 2.5 kcal $mol^{-1}$).This is as a result of promotion of an electron from substrate into the $\pi^*_{xz}$ orbital in the doublet spin state, whereas in the quartet spin state the electron moves to the higher energy $\sigma^*_{z2}$ instead. Overall, epoxidation is a thermoneutral process and at our level of theory it is slightly endothermic in the quartet spin state (by 4.3 kcal $mol^{-1}$), while it is slightly exothermic in the doublet spin state (by 3.9 kcal $mol^{-1}$). Structures along the epoxidation pathway are similar to those calculated before on alternative substrates (de Visser et.al. 2001; de Visser et.al.2002[a]; Kumar et.al. 2010; Sainna et.al. 2015; Kumar et.al. 2005; Kumar et.al. 2013; de Visser et.al. 2001; de Visser et.al. 2002[b]).

Proton shuttle from the ipso-carbon atom to the porphyrin ring is virtually barrierless and leads in highly exothermic process to intermediate $^{4,2}$**ID** and is followed by another small proton transfer barrier (**TS**$_{PT}$) that gives ortho-phenol products (**PD**). As the barrier height for the conversion of the radical intermediates $^{4,2}$**IC** into proton-transfer intermediates $^{4,2}$**ID** is significantly smaller than the barrier for ring-closure, it can be concluded that substrate epoxidation is an unlikely process and will not be able to compete with aromatic hydroxylation under these conditions. However, it may come into play in a constraint substrate situation such as an enzyme active site where the substrate orientation stabilizes this process.

## 7.3. Discussion

To understand the regioselectivity patterns of phthalate activation by P450 CpdI, we calculated the mechanisms leading to aliphatic hydroxylation at the $C^5$ position of the aliphatic chain, the O-dealkylation, aromatic hydroxylation of the ortho-carbon atom and epoxidation of the aromatic ring. In the next few sections, we will discuss the patterns and the consequences of phthalate activation by the P450s.

### *7.3.1. Regioselectivity of phthalate oxidation by P450 CpdI.*

Table 7.1 gives a summary of the rate determining barriers for hydrogen atom abstraction from the C5 position ($^{4,2}$**TS**$_A$), hydrogen atom abstraction from the $C^1$ position ($^{4,2}$**TS**$_B$) and electrophilic addition to the *ortho*-position at the aromatic ring ($^{4,2}$**TS**$_C$). As can be seen all barriers at the ΔE+ZPE level of theory fall inside a window of 4.6 kcal mol$^{-1}$ with the lowest one through $^2$**TS**$_A$ at 18.2 kcal mol$^{-1}$. This implies that the dominant reaction pathway ideally should lead to C5 activation on the doublet spin state, but the other barriers for $C^5$ and $C^1$ activation are within 2 kcal mol$^{-1}$ and hence will be competitive. The same trends and transition state ordering is found at the free energy level of theory. The only difference between ΔE+ZPE and ΔG is a raise of the value for the latter due to the addition of entropy. Nevertheless, the entropy effect appears to be similar for all transition state and pathways covered.

**Table 7.1.** Calculated rate determining barrier heights for various oxidation reactions.

| barrier | doublet [1] | quartet [1] |
|---|---|---|
| $^{4,2}$**TS**$_A$ | 18.2 (32.4) | 19.9 (33.6) |
| $^{4,2}$**TS**$_B$ | 20.3 (34.2) | 19.3 (32.6) |
| $^{4,2}$**TS**$_C$ | 20.9 (34.8) | 22.8 (36.8) |

[1] ΔE+ZPE (ΔG) values in kcal mol$^{-1}$.

Although the energy differences between aliphatic hydrogen atom abstraction at the $C^5$ and $C^1$ position are very small and also close in energy to the electrophilic addition transition state in our model system, this not necessarily means $C^5$ hydroxylation is the dominant process in the enzyme. Experimental studies on phthalate activation by a range of P450 isozymes showed that the product distributions were strongly dependent on the isozyme (Choi et.al.2012). Since, each P450 isozyme has a characteristic substrate binding pocket (Poulos et.al. 2014), the substrate orientation inside P450 isozymes may be different and consequently the activation of the substrate will give other products. Thus, the work of Choi et. al. (2012) showed

that in P4503A1 and P4502C12, the dominant product is $C^5$ hydroxylation, whereas in $P450_{2D6}$ mostly O-dealkylation was found. Yet, in $P450_{3A4}$, $P450_{2C6}$ and $P450_{3A5}$ a mixture of products originating from O-dealkylation and $C^5$-hydroxylation was found. Our computational modelling gives a small energy difference in the rate determining barrier heights of $C^5$ hydrogen atom abstraction versus $C^1$ hydrogen atom abstraction (for O-dealkylation) with a small preference of about 1 kcal $mol^{-1}$ in favor of $C^5$ activation. Consequently, under ideal conditions the dominant product should be C5 hydroxylation, but if that pathway is hindered due to substrate positioning alternative mechanisms may become available. To understand the preferences better, we took a P450 structure of a liver P450 isozyme from the protein databank (Berman et.al. 2000), i.e. the 1TQN pdb file (Yano et.al.2004), which is a $P450_{3A4}$ isozyme. The active site was modified to a CpdI model by addition of an oxo group and docked our substrate into the substrate-binding pocket and shows several plausible conformations of substrate in the $P450_{3A4}$ pocket in Figure 7.8 (Grosdidier et.al. 2011).

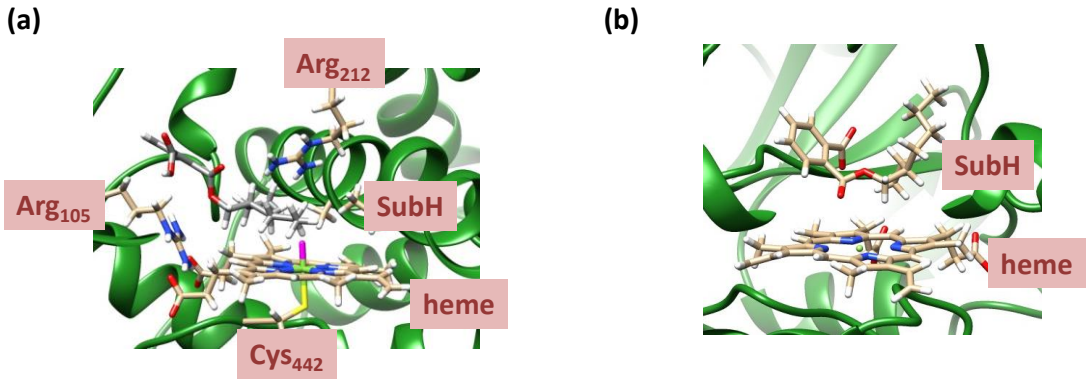


**Figure 7.8.** Two plausible conformations of the Cytochrome $P450_{3A4}$ structure with phthalate substrate (SubH) docked into the substrate binding pocket: (a) pro-$C^5$-hydroxylation binding. (b) pro-O-dealkylation binding.

We find two low-energy conformations as shown in Figure 7.8; one with the substrate in a pro-$C^5$-hydroxylation conformation and one with the substrate in a pro-O-dealkylation conformation. In the pro-C5-hydroxylation binding conformation, the docked structure (Figure 7.8a) is in a conformation with the aliphatic chains in close approach to the iron(IV)-oxo group in a crown-shaped orientations with the protons of the $C^5$ and $C^3$ positions of the hexyl group as well as the terminal hydrogen atom from the ethyl group ($C^8$) pointing towards the oxo group. In particular distances are found of $C^5$H--O of 2.10Å, $C^3$H--O of 2.06Å and $C^8$H--O of 3.07Å. Clearly, the aliphatic group fits into the cavity nearby the iron(IV)-oxo species well and should

lead to aliphatic hydroxylation products. This means that the most likely substrate activation positions in this binding configuration will be on the terminus of the aliphatic chain, i.e. the $C^5$ position for which we calculate a low-energy barrier height. On the other hand, the aromatic ring is positioned far away from CpdI and as such we do not expect significant aromatic hydroxylation products.

In the alternative conformation in Figure 7.8b, we positioned the $C^1$ carbon in close distance to the oxo group, while the aromatic ring and the alkyl chains are pointing away from the heme group. In this orientation, the ester bond is in hydrogen bonding interactions with the positive side chain of $Arg_{212}$, which may facilitate the O-dealkylation process through charge stabilization. Moreover, in this binding position, O-dealkylation will be the dominant process and no aliphatic hydroxylation on the side chains will take place.

Consequently, substrate activation by the P450s is a subtle balance of thermochemical and kinetical possibilities with substrate binding and orientation that go hand-in-hand. To understand the thermochemistry better, in the next section we discuss aliphatic C–H bond activation in more detail.

### *7.3.2. Features of the hydrogen atom abstraction step.*

To understand the intrinsic properties related to the hydrogen atom abstraction step, we devised valence bond models to explain the features of the reaction pathway following procedures described previously (de Visser et.al.2006; Kumar et.al. 2014; Quesne et.al. 2016). Figure 7.9 displays a valence bond (VB) description of the electronic configurations of reactants, hydrogen atom abstraction transition state and radical intermediate. Thus, in the reactants CpdI has two 3-electron bonds along the Fe–O interaction due to occupation of the $\pi_{xz}^2\ \pi_{yz}^2\ \pi^*_{xz}{}^1\ \pi^*_{yz}{}^1$ with six electrons, which gives two unpaired electrons at the FeO group and a spin density of about 1 on Fe and O. CpdI has a third unpaired electron in a2u and the C–H bond of the substrate is the $\sigma_{CH}$ bond with two electrons. Upon approach of CpdI on substrate, the C–H bond orbital is broken and the two electrons revert to atomic orbitals, i.e. $2p_C$ and $1s_H$. At the same time, the 3-electron bond in the xz-plane breaks back to atomic orbitals, namely $2p_O^2\ 3d_{xz}^1$. One of the electrons from $2p_O$ pairs up with the incoming hydrogen atom to form the O–H bonding orbital $\sigma_{OH}$. The second electron from $2p_O$ is then promoted into the $a_{2u}$ orbital.

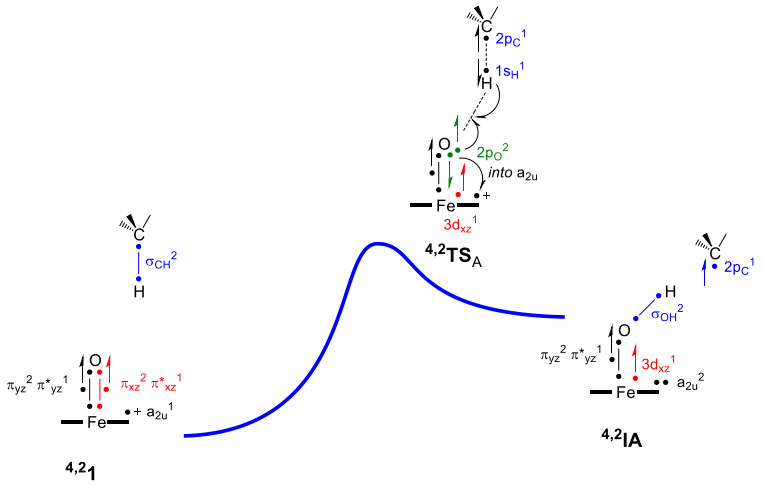


**Figure 7.9.** Valence bond description of hydrogen atom abstraction from a substrate. Dots represent electrons and a line between two dots is a bond with two electrons.

Therefore, the hydrogen atom abstraction barrier will be related to the strength of the $\sigma_{CH}$ orbital that needs to be broken, the strength of the $\sigma_{OH}$ orbital that is formed, the strength of the 3-electron $\pi_{xz}/\pi^*_{xz}$-orbitals that need to be broken and the promotion energy from $2p_O$ to $a_{2u}$. Indeed, previous studies of ours showed that the hydrogen atom abstraction barriers for a series of substrates correlated with the bond dissociation energy (BDE) of the C–H bond that was broken (de Visser et.al. 2004; de Visser et.al. 2010; Shaik et.al. 2008; Karamzadeh et.al. 2010). To gain insight into the relative C–H bond strengths of the various aliphatic positions of the phthalate substrate we calculated the BDECH for all aliphatic positions as the diabatic energy between substrate and the sum of the substrate minus a hydrogen atom and a hydrogen atom, see Figure 7.10.

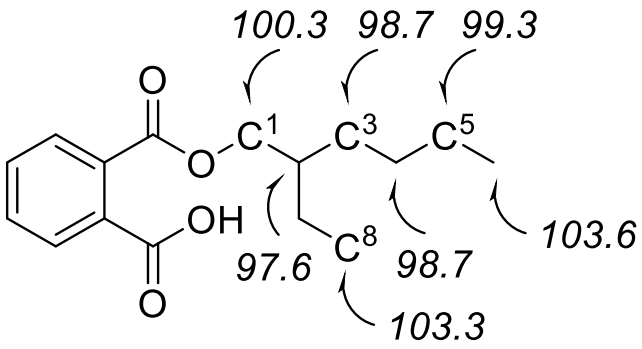


**Figure 7.10.** $BDE_{CH}$ values (in kcal $mol^{-1}$) of aliphatic C–H positions of phthalate substrate.

The data in Figure 7.10 shows that most C–H bonds of secondary carbon atoms have a strength that ranges from 98.7 kcal $mol^{-1}$ (for the $C^3$ and $C^4$ positions) to 100.3 kcal $mol^{-1}$ (for the $C^1$ position). By contrast, the primary carbon atoms, i.e. the terminal methyl groups have a C–H bond strength of 103.3 kcal $mol^{-1}$ (at $C^8$) and 103.6 kcal $mol^{-1}$ (at $C^6$), whereas the tertiary carbon atom $C^2$ has a C–H bond strength of only 97.6 kcal $mol^{-1}$. As the full set of $BDE_{CH}$ values spans a range of only 5 kcal $mol^{-1}$, it is obvious that a large mixture of products will be obtained for aliphatic hydroxylation of the alkyl chains. Moreover, substrate positioning will have a major contribution to the product formation and a low-energy binding conformation may block certain C–H bonds from being activated by the enzyme. For instance, the substrate binding position in Figure 9b gave only one specific C–H bond in close distance to the heme, namely C1 and consequently will lead to dominant C-dealkylation. On the other hand, the structure shown in Figure 9a will lead to a mixture of aliphatic hydroxylation products probably mostly at $C^3$ and $C^5$.

### 7.4. Materials and Methods

Active site models were selected like before (Karamzadeh et.al. 2010; Ogliaro et.al. 2001) as an iron embedded in protoporphyrin IX without side chains and linked to $SH^-$ as a mimic of cysteinate and with oxo in the distal position. The phthalate substrate (2-ethylhexyl-phthalate) was selected in the charged-neutral state and all complexes of CpdI with substrate were calculated in the lowest lying doublet and quartet spin states.

Calculations were performed in Gaussian-09 (Frisch et.al. 2016) using density functional theory methods that have been calibrated and benchmarked against experimental rate constants previously (Vardhaman et.al. 2011; Vardhaman et.al. 2013; Hernández-Ortega et.al. 2015; Cantú-Reinhard et.al. 2016). In general, the UB3LYP (Becke et.al.1993; Lee et.al. 1988) hybrid density functional was used for all calculations. Geometry optimizations, frequencies and reaction coordinate scans were done with a modest LACVP basis set with core potential on iron (Hay et.al.1985) and 6-31G* on the rest of the atoms (Hehre et.al.1972): basis set BS1. More accurate energies were obtained through a single point calculation on the optimized geometry using an LACV3P+ basis set with core potential on iron and 6-311+G* on the rest of the atoms: basis set BS2, which also includes an implicit solvent model mimicking the dielectric constant of water (Tomasi et.al. 2005).

## 7.5. Conclusions

A computational study on phthalates binding and activation by cytochrome P450 liver enzymes is presented here. Initial calculations use active site models of P450 Compound I in its reaction with the ester of phthalate and 2-ethylhexanol, whereby patterns for $C^5$ hydroxylation, O-dealkylation, aromatic ring epoxidation and ortho-aromatic ring hydroxylation patterns are reported. Aliphatic hydroxylation and O-dealkylation start with hydrogen atom abstraction followed by rebound to give an alcohol product complex. In O-dealkylation, we find the alcohol product to react with an assisted solvent water molecule by O-dealkylation. Epoxidation and aromatic hydroxylation mechanisms are electrophilic and lead to a radical intermediate where the oxo group forms a single bond with one carbon atom of the aromatic ring. This radical can form the epoxide through ring-closure; however, that pathway incurs a significant barrier height. A lower energy pathway leads through proton shuttle from ipso-proton to heme and back to the phenolate to give phenol products. All pathways were analyzed and rationalized with thermochemical, valence bond and kinetic models.

**Acknowledgments:** FGCR thanks the Conacyt Mexico for a studentship.

**Author Contributions:** F.G.C.R. and S.P.d.V. conceived and designed the experiments and analyzed the data; F.G.C.R. performed the experiments; S.P.d.V. wrote the paper

**Conflicts of Interest:** The authors declare no conflict of interest.

# Chapter Eight

# PROJECT 6

***Catalytic mechanism of nogalamycin monoxygenase: How does nature synthesize antibiotics without metal cofactor?***

*Fabián G. Cantú Reinhard,[‡] Jennifer L. DuBois[†] and Sam P. de Visser*[*,‡]*

[‡] Manchester Institute of Biotechnology and School of Chemical Engineering and Analytical Science, The University of Manchester, 131 Princess Street, Manchester M1 7DN, United Kingdom

† Department of Chemistry and Biochemistry, Montana State University, Bozeman, Montana 59715-3400, USA.

## Abstract

*Nogalamycin monoxygenase (NMO) is a member of a family of enzymes that catalyze a key step in the biosynthesis of tetracycline antibiotics, using molecular oxygen for substrate oxidation but without an apparent cofactor. As most monoxygenases and dioxygenases contain a transition metal center (Fe/Cu) or flavin, this begs the question how NMO catalyzes this unusual oxygen atom transfer reaction from molecular oxygen to substrate directly. We performed a detailed computational study on the mechanism and catalytic cycle of NMO using density functional theory and quantum mechanics/molecular mechanics (QM/MM) on the full protein. We considered the substrate in various protonation states and its reaction with oxidant $O_2$ as well as $O_2^{-\bullet}$ through either electron transfer, proton transfer or hydrogen atom transfer. The lowest energy pathway for the models presented here is a reaction of the neutral substrate with a superoxo anion radical. In the absence of available free superoxo anions; however, the alternative neutral pathway between $^3O_2$ and substrate may be accessible at room temperature although the barrier is higher in energy by about 20 kcal mol$^{-1}$ and therefore the reaction will be much slower. In contrast to previous experimental findings for both the enzymatic and uncatalyzed reactions, the mechanisms with the substrate in its deprotonated state were found to be high in energy, therefore new mechanistic suggestions are proposed. A thermodynamic analysis shows that the substrate has a very weak C–H bond that is easily activated by an oxidant and hence a metal cofactor may not be needed for oxidizing this particular substrate. Finally, site-directed mutations were studied where active site Asn residues were replaced and highlight the function of these residues in guiding oxygen to the $C^{12}$-position of the substrate. Overall, NMO shows a versatile reactivity pattern, where substrate can be activated by several low-energy pathways with oxidant and substrate in various oxidation and protonation states.*

***Draft Paper Submitted for Publication***

## 8.1 Introduction.

Monoxygenases are widely distributed enzymes that utilize molecular oxygen and transfer one oxygen atom to a substrate, with the second oxygen atom typically leaving as a water molecule. Because of the triplet nature of molecular oxygen, its reactivity with organic substrates is usually poor. Most often monoxygenation reactions will take place with the aid of a cofactor, for example, reduced flavin, copper, or iron (Costas et.al. 2004; Abu-Omar et.al. 2005; Krebs et.al. 2007; Bruijininex et.al. 2008; Solomon et.al. 2013). For example, the cytochromes P450 are monoxygenases that are active in all forms of life, including the human body, where they operate mainly in the liver for the detoxification of xenobiotics and the biosynthesis of hormones, such as estrogen (Sono et.al. 1996; Poulos, T.L. 2014; Guengerich, F.P., 2001; Huang et.al. 2017). The P450s undergo a catalytic cycle that is initiated with substrate binding and the reduction of the iron(III) center to enable dioxygen binding. A further reduction and two protonation steps then gives a high-valent iron(IV)-oxo heme cation radical active species that reacts with substrates through oxygen atom transfer (Meunier et.al. 2004; Denisov et.al. 2005; Ortiz de Montellano, P.R., 2010; Li et.al. 2012; Blomberg et.al. 2014; de Visser et.al. 2011).

Interestingly, in Nature several mono- and dioxygenase families operate without the inclusion of a cofactor. The recently discovered, 1-H-3-hydroxy-4-oxoquinaldine 2,4-dioxygenase (HOD) from *Arthrobacter nitroguajacolicu*s Rü61a, reacts as a ring-cleaving intradiol dioxygenase without the aid of metal or organic cofactors (Bauer et.al. 1996; Steiner et.al. 2010; Fetzner et.al. 2010; Thierbach et.al. 2014). In a combined kinetics and computational study, details of the catalytic cycle of HOD were established and it was confirmed that $O_2$ reacts directly with substrate (Hernández-Ortega et.al. 2014; Hernández-Ortega et.al. 2015). In particular, it was shown that the aromatic substrate in a reaction with $^3O_2$ formed an arene-peroxo intermediate and through a spin-crossing from the triplet to the singlet spin state formed N-acetyl-anthranilate and CO products.

Structurally and evolutionarily distinct families of cofactor-independent monooxygenases are also known. The antibiotic biosynthesis monoxygenases (ABMs) are a large family of enzymes that catalyze a step in the biosynthetic pathways of several structurally distinct tetracycline antibiotics, including tetracenomycin, daunomycin, actonorhodin, and nogalomycin (Sciara et.al. 2003; Taguchi et.al. 2013;

Kendrew et.al. 1997; Rafanan et.al. 2001; Ye et.al. 1994). These molecules have widespread clinical use as antibiotics, anti-cancer agents, and anti-psoriasis drugs. The monoxygenase acts as a so-called decorating enzyme in conjunction with polyketide synthetases, inserting an O-atom into the growing tetracycline scaffold. The same ABM family also includes oxygenases that are not associated with antibiotics synthesis, most importantly, the bacterial non-canonical heme oxygenases. These catalyze the $O_2$-dependent ring opening of the tetrapyrrole. The activated nature of the ABM substrates suggests that they, like the substrate of HOD, facilitate the initial steps of their reactions with $O_2$. The enzyme environment serves both to direct these reactions toward specific products and to accelerate their rates by several thousand-fold, relative to the uncatalyzed processes.

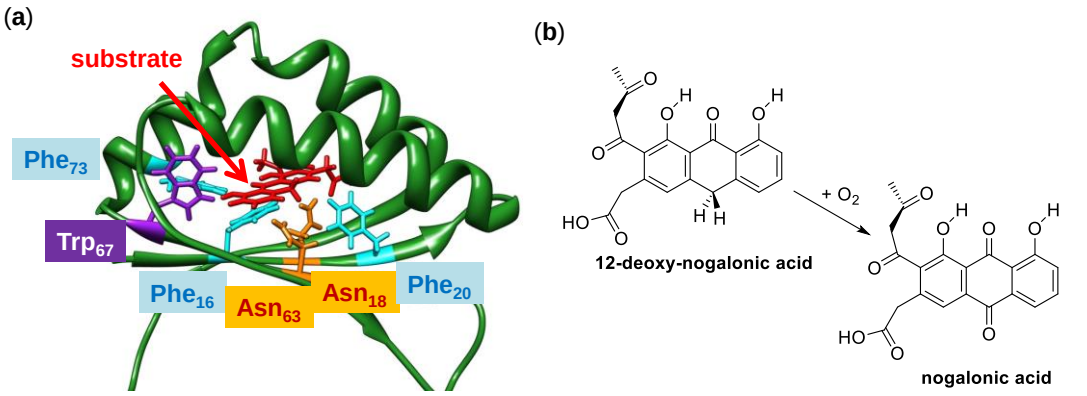


**Figure 8.1.** (a) Crystal structure (PDB ID: 3KNG) of NMO, encoded by the gene *SnoaA*, with substrate (12-deoxy-nogalonic acid) modeled in the active site pocket in the place of a molecule of bound crystallization solvent. (2) Reaction catalyzed by NMO.

Nogalamycin monoxygenase (NMO) is an antibiotic biosynthesis monoxygenase from *Staphylococcus nogalater* that catalyzes the conversion of 12-deoxy-nogalonic acid to nogalonic acid (Figure 8.1) (Siitonen et.al. 2012; Machovina et.al. 2016). A 1.9Å resolution crystal structure has been measured for the enzyme with a molecule of ethylene glycol bound, which has been replaced by a model of the native substrate in the left-hand-side of Figure 8.1 (Grocholski et.al. 2010). The substrate pocket is lined with aromatic amino acid residues, e.g., $Phe_{16}$, $Phe_{20}$, $Phe_{73}$ and $Trp_{67}$, which may have functions related to either π-stacking with the substrate or electron transfer. In addition, a number of polar residues potentially involved in hydrogen bonding interactions with substrate are located in the substrate binding pocket and the most prominent ones are $Asn_{18}$ and $Asn_{63}$.

Clearly, there is an urgent need for a detailed computational study on the mechanism of substrate oxidation by NMO enzymes and a detailed comparison with HOD. In this paper, we present recent results using quantum mechanics/molecular mechanics (QM/MM) on the reactivity of $O_2$ inside the NMO complex, where we investigated several oxidation and protonation states of dioxygen and substrate 12-deoxy-nogalonic acid.

**8.2 Methods**.

The QM/MM model of NMO was set up using previously developed methods and procedures (Faponle et.al. 2016; Quesne et.al. 2016). We initially did exploratory density functional theory (DFT) calculations on small model complexes containing substrate and dioxygen. However, later we also employed QM/MM on the full enzyme including models with active site amino acid residues in the QM region. We will focus in the main text on the QM/MM results, but will show some of the small model results in the discussion. Full details of all calculation can be found in the Supporting Information.

**8.2.1 Model set-up.**

A QM/MM model was set up starting from the crystal structure coordinates with protein databank code 3KNG (Grocholski et.al. 2010), whereby 12-deoxy-nogalonic acid was replaced by the substrate-analog dithranol. Dithranol was manually created and geometry optimized in Gaussian 09 (Frisch et.al. 2013) at the B3LYP/6-31G* level of theory (Becke, A. 1993; Lee et.al. 1988; Ditchfield et.al. 1971). CHARMM parameters for dithranol were generated with SwissParam (Zoete et.al. 2011). Subsequently, the substrate and dioxygen were docked into the protein structure at a low-energy conformation as determined in SwissDock (Grossdidier et.al. 2011). Dioxygen was placed in a position near the active site Asn residues. A standard procedure was followed for the subsequent set-up of the system, as described in more detail elsewhere (Faponle et.al. 2016; Quesne et.al.2016; Quesne et.al. 2014; Faponle et.al. 2017; Timmins et.al.[1] 2017; Timmins et.al.[2] 2017), and briefly summarize here.

The substrate bound enzyme structure with dioxygen bound was protonated to pH 7 with the PROPKA method using the PDB2PQR web service (Dolinsky et.al. 2007). Thereafter, an iterative solvation procedure was implemented through 20 cycles of solvation with a water sphere of 35 Å of radius (Supporting Information Figure S1). The fully solvated system consisted of 21,441 atoms, including 6,658 TIP3P water molecules. The system was neutralized with 10 $Mg^{2+}$ and 18 $Cl^-$ ions randomly spaced in the solvent layer surrounding the protein.

Subsequently, the model was heated and equilibrated to room temperature using the CHARMM forcefield with the protein backbone atoms fixed (Brooks et.al. 1983). Finally, an 800 ps molecular dynamics (MD) simulation was carried out in CHARMM with an unconstrained protein. We maintained a fixed water molecule close to the substrate for further studies. Snapshots were obtained after 450, 500, 550 and 600 ps, designated $Sn_{450}$, $Sn_{500}$, $Sn_{550}$ and $Sn_{600}$, respectively. The full mechanistic study of the reaction mechanism was performed at one snapshot only per case. In addition to studies of the wildtype (WT) structure, we also investigated a double mutant (Asn18Ala/Asn63Ala), whereby Asn was manually replaced by Ala and the molecular dynamics simulations were repeated. Snapshots were again taken at 450, 500, 550 ps and 600 ps.

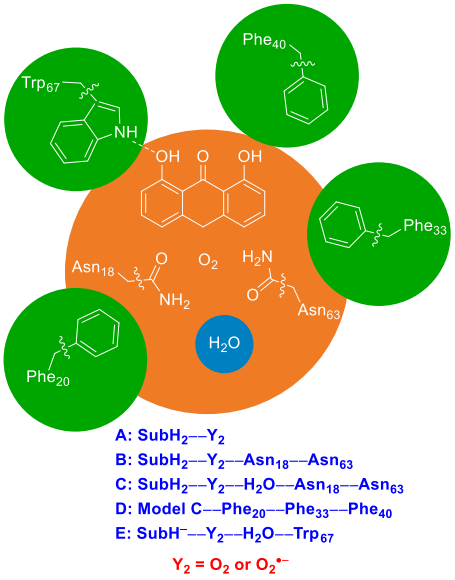


**Figure 8.2.** QM regions selected for the QM/MM calculations with either $Y_2 = O_2$ or $O_2^{-\bullet}$ as oxidant. Wiggly lines represent the border between the QM and MM regions and dithranol is abbreviated as $SubH_2$ ($SubH^-$ if deprotonated) in the model descriptions.

### 8.2.2 QM/MM Calculations.

As the border between QM and MM region and the size of the QM model can affect the structure and energetics of reaction mechanisms, we tested several QM regions as shown in Figure 8.2. The smallest QM model contained only substrate and $O_2$ (QM region **A**) and was used as a DFT-only model. In addition, calculations were done where QM region **A** was expanded with two Asn side chains (QM region **B**). Then a larger QM region tested contained the full substrate, $O_2$, one crystallographically placed water molecule and both Asn side chains (QM region **C**). In another set of calculations, we added three active site Phe side chains to QM region **C** to give QM region **D**. Finally, a potential role of close lying hydrogen-bonding $Trp_{67}$ was explored in the deprotonated substrate pathway in QM region **E**. In the mutant structures, the two proximal asparagine functional groups were replaced by alanine side chains. The border regions between the QM and MM regions of the asparagine (alanine in the mutants) residues were defined with hydrogen link-atoms and the interaction of the QM and MM systems was treated by electrostatic embedding.[20] In addition to the presented models, a larger neutral system encompassing all relevant amino acids in the QM region **F** ($Asn_{18}$, $Asn_{63}$, $Phe_{20}$, $Phe_{33}$, $Phe_{40}$, and $Trp_{67}$) was also optimized as a reactant complex, although no mechanistic investigations were performed at that size.

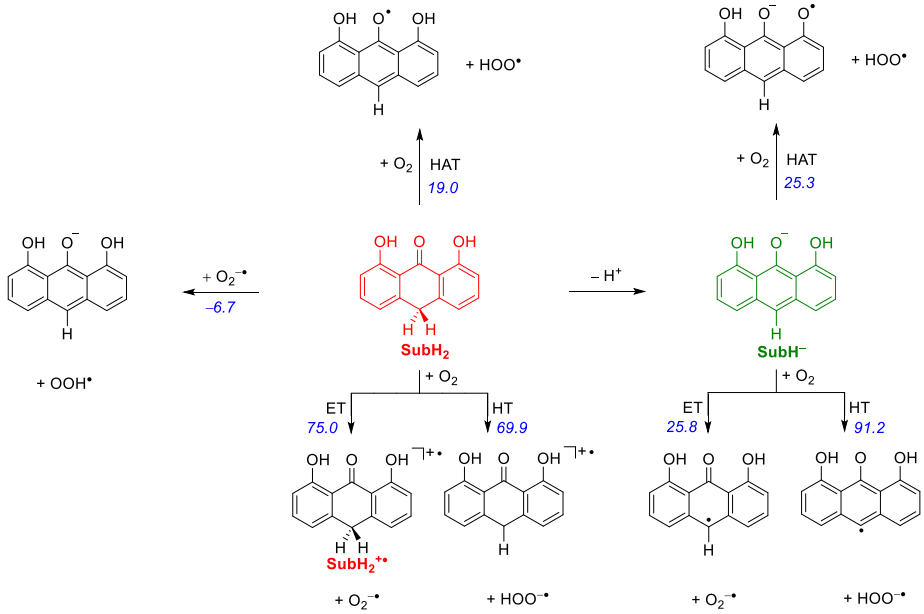


**Figure 8.3.** Possible pathways for proton, electron, hydrogen atom and hydride transfer of dithranol in NMO as calculated with gas-phase model structure A. Reaction free energies ($\Delta G_{reaction}$ in kcal $mol^{-1}$) calculated using DFT models in water at UB3LYP/6-31G* in Gaussian at 298K based on isolated reactant and product structures.

The QM section was calculated with Turbomole[21] at the unrestricted B3LYP[13] level of theory, whilst the MM region was calculated with the CHARMM forcefield in the CHARMM software package as implemented in DL-Poly (Brooks et.al. 1983; Smith and Forester, 1997; Todorov et.al. 2006). The QM and MM software packages were interfaced by Chemshell (Sherwood et.al. 2003). We did a full geometry optimization of reactants, intermediates, products and transition states at the B3LYP/SV(P) level of theory (Becke, A. 1993; Lee et.al. 1988; Shafer et.al.1992). To establish the nature of the transition states and make sure they indeed connect to reactants and products, we ran extensive geometry scans whereby one degree of freedom was fixed while all other degrees of freedom were minimized. The energetics of the optimized structures was improved through single point calculations at the B3LYP/def-TZV(P) level of theory, BS2. For one set of calculations, we also did full geometry optimizations using B3LYP/BS2, but the results were similar to those obtained with the smaller basis set. See Supporting Information.

**8.3 Results and Discussion**.

**8.3.1Protonation state of oxidant and substrate**

Our initial studies were focused on establishing computationally the most likely protonation and oxidation states of substrate (dithranol) and oxidant. In addition, reactions were considered for substrate with $O_2$ via either electron transfer (ET), hydrogen atom transfer (HAT) or hydride transfer (HT). Figure 8.3 summarizes all possible reaction pathways for dithranol in a reaction with molecular oxygen, protons, electrons and/or hydride anions. These studies should give insight into the electronic configuration of the dioxygen-bound structure of NMO and the likely protonation state of the substrate. Focusing first on the neutral substrate ($SubH_2$, highlighted in red in Figure 3), DFT calculations on small model complexes calculated at the B3LYP/6-31G* level of theory with a polarized continuum model mimicking water find an endergonic driving force for the electron transfer reaction for reaction 8.1 of $\Delta G$ = 75.0 kcal $mol^{-1}$.

$$^3O_2 + SubH_2 \rightarrow {}^2O_2^{-\bullet} + SubH_2^{+\bullet} \quad (8.1)$$

Indeed, a large active site model complex that contains the substrate, $O_2$ and several protein residues calculated with DFT gives an electronic configuration that represents a neutral $O_2$ molecule nearby $SubH_2$ rather than a charge transfer complex of superoxo with substrate cation radical. To make sure that the results were not affected by the choice of the density functional method, we employed CCSD(T) single points on the optimized geometries. The latter gave an electronic configuration similar to the one at DFT with a $^3O_2$ nearby a neutral substrate. Finally, an orbital swap was attempted at CCSD(T) level of theory to create the charge-transfer state; however, this calculation failed to converge and hence the charge-transfer state is well higher in energy than the neutral state. Therefore, based on gas-phase DFT models we do not expect electron transfer to happen between a neutral substrate and $O_2$. This observation is similar to what was recently found for cofactor independent dioxygenase HOD, where also no electron transfer took place in the neutral reactant complex (Hernández-Ortega et.al. 2014; Hernández-Ortega et.al. 2015). However, our results conflict experimental studies (Kralj et.al. 2015; Müller et.al. 1987; Müller, K. 1997) on NMO enzymes that proposed an electron transfer from substrate to $O_2$ upon its entrance into the substrate binding pocket. To find out whether the contradiction is due to the choice of the model, we continued our studies with a full protein model (see below). In addition to the electron transfer we considered direct hydride abstraction from dithranol by $O_2$, but a large energy of reaction of 69.9 kcal $mol^{-1}$ was found; hence is unfeasible. On the other hand, a direct hydrogen atom abstraction (HAT) has a free energy driving force of 19.0 kcal $mol^{-1}$ and may be accessible in the protein.

Subsequently, we considered a neutral substrate in reaction with superoxo radical anion ($^2O_2^{-\bullet}$). Much lower driving forces are found in a reaction of neutral dithranol with $O_2^{-\bullet}$ instead, where an exergonic driving force for proton transfer of –6.7 kcal $mol^{-1}$ is found. At the same level of theory we calculate an electron affinity (EA as defined in Eq 8.2) of $^3O_2$ of 12.8 kcal $mol^{-1}$.

$$^3O_2 + e^- \rightarrow {}^2O_2^{-\bullet} \qquad (8.2)$$

Therefore, an ionizable side chain such as the imidazolium group of an active site tryptophan could hypothetically relay electrons from a reduction partner to $^3O_2$ in the active site and generate superoxo anion radical (Figure 8.1). Surprisingly, no reductase partner is known for the reaction *in vivo*, in which the enzyme, $O_2$, and the organic substrate appear to be sufficient for yielding the oxygenated product and water. As such, we decided to continue the work with QM/MM and consider the effect of the protein on the reaction mechanism.

Next, we considered the possibility of dithranol being deprotonated prior to dioxygen binding (right-hand-side of Figure 8.3). Experimental work above the single-protonation p$K_a$ of the enzyme-substrate complex (6.9) showed that oxygenation is the dominant process, whereas in acidic environments the reaction appeared to undergo a net one-electron/one-proton oxidation to yield a dimeric product (Machovina et.al. 2016). The latter is an unwanted side product in the biological context, as it is off the pathway leading ultimately to the antibiotic. As such, the reaction processes for electron transfer, hydrogen atom abstraction and hydride transfer were repeated using $SubH^-$ as the substrate (right-hand-side of Figure 8.3).

Electron transfer from deprotonated dithranol ($SubH^-$) to $^3O_2$ has a much lower energy of reaction than that of dithranol to $^3O_2$ (+25.8 versus 75.0 kcal $mol^{-1}$). Hence, the electron transfer is still considerably endothermic and will be difficult to achieve in the gas phase model. Furthermore, hydride transfer from deprotonated dithranol is also unlikely to take place as it has a very high energy of reaction of well over 90 kcal $mol^{-1}$. Alternatively, a hydrogen atom transfer from deprotonated substrate to $O_2$ may occur to form the hydroperoxyl radical, although a relatively large driving force of 25.3 kcal $mol^{-1}$ is required.

The results in Figure 8.3 consequently implicate that the most reactive gas phase form of dithranol is the protonated state, i.e. $SubH_2$, and a hydrogen atom abstraction reaction can take place by either $O_2$ or $O_2^{-\bullet}$ via low-energy pathways. The availability of $O_2^{-\bullet}$ in the protein will depend on the presence of a reduction partner that can deliver the needed electrons. These results suggest that the protein environment is critical for stabilizing the deprotonated $SubH^-$ form of the substrate and guiding its reaction with $O_2$. We therefore undertook a full QM/MM investigation on the full protein with models containing either $O_2$ or $O_2^{-\bullet}$. However, for completeness, the hydrogen atom transfer process pathway of the deprotonated substrate was also investigated in full, whereby a Trp residue was included in the QM region because of its hydrogen bonding interaction with the OH group.

### 8.3.2 QM/MM studies on $O_2/O_2^{-\bullet}$ binding

First, a full QM/MM calculation on the ternary dioxygen- and neutral dithranol-bound complex of NMO was performed. Figure 8.4 displays the QM/MM optimized geometry of the reactant complex ($^3$**Re**$^0$) in the overall triplet spin state. The pocket in between the $Asn_{18}$ and $Asn_{63}$ amino acid residues fits molecular oxygen well, but during the solvation and dynamics set-up procedures also one water molecule entered. The substrate binding pocket contains three aromatic phenylalanine and one tryptophan residue, which may interact with the substrate. In the reactant complex, all spin density is located on dioxygen and no spin density is seen on the dithranol substrate. Thus, the QM/MM model shows that in agreement with the small DFT gas phase model complexes and CCSD(T), the reactant complex corresponds to $^3O_2$ in the vicinity of dithranol ($SubH_2$) and no electron transfer between the two groups has taken place. Dioxygen and water form hydrogen bonding interactions with the Asn side chains.

Optimized geometries show little differences between the various snapshots. Figure 8.4 displays the interactions between $O_2$ and the nearest protons of $Asn_{63}$ (distance $R_1$) and $Asn_{18}$ (distance $R_2$) as well as the distance between $O_2$ and one of the hydrogen atoms bound to carbon $C^{12}$ (distance $R_3$). Obviously, inclusion of the Asn side chains into the QM region affects the hydrogen bonding interactions between these groups but in all cases the interaction remains weak and $R_1$ and $R_2$ are well over 2.5Å in $^3$**Re**$^0$. A similar result was obtained by using the larger QM region (model **F**) whereby only unpaired spin density on the oxygen molecule was found.

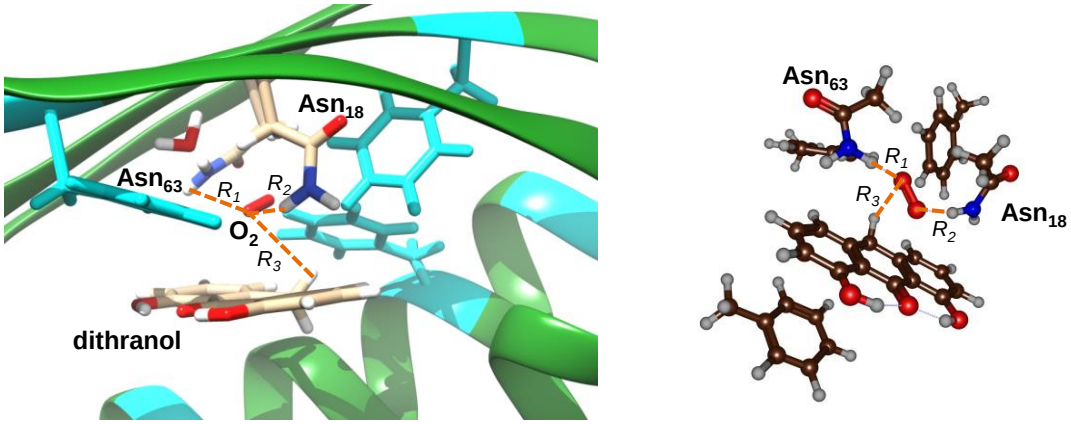


| | Charge | $R_1$ | $R_2$ | $R_3$ | $\rho(O_2)$ |
|---|---|---|---|---|---|
| $Sn_{450}$ | 0 | 2.70 (2.65) | 2.39 (2.69) | 2.83 (2.96) | 2.0 (2.0) |
| $Sn_{500}$ | 0 | 2.50 (2.64) | 2.71 (2.66) | 2.83 (3.00) | 2.0 (2.0) |
| $Sn_{550}$ | 0 | 2.65 (2.64) | 2.57 (2.74) | 2.78 (2.89) | 2.0 (2.0) |
| $Sn_{450}$ | –1 | 1.77 (1.72) | 1.79 (1.76) | 2.27 (2.56) | 1.1 (1.0) |
| $Sn_{500}$ | –1 | 1.79 (1.69) | 1.86 (1.79) | 1.83 (2.48) | 1.0 (1.0) |
| $Sn_{550}$ | –1 | 1.89 (1.94) | 1.84 (1.86) | 2.09 (2.23) | 1.1 (1.1) |

**Figure 8.4.** QM/MM optimized geometries of the neutral and anionic reactant complexes ($^3Re^0$ and $^2Re^-$) as obtained in Turbomole:CHARMM. Bond lengths are defined in the Figure and displayed in angstroms. Dioxygen spin densities are in au. Values reported are for obtained geometries with QM region B (D) for $Y_2 = O_2/O_2^{\bullet-}$.

Therefore, the different snapshots give some flexibility in the position of $O_2/O_2^{\bullet-}$ binding, but the electronic configuration varies little between the various snapshots. Thus, both DFT model complexes (Figure 8.3) as well as QM/MM on the full protein show that a complex of $SubH_2$ with $^3O_2$ does not lead to electron transfer. Our work contrasts experimental suggestions that upon $O_2$ binding a spontaneous electron transfer takes place (Siitonen et.al. 2012; Machovina et.al. 2016). Recent QM/MM calculations on the firefly luciferin reaction it was found that $O_2$ upon binding nearby a luciferin-adenylate led to spontaneous electron transfer (Berraud-Pache et.al. 2018). Clearly, the ionization potential of $SubH_2$ used here is considerably different from luciferin-adenylate and consequently no electron transfer is possible. We, therefore, considered different protonation states of the substrate as well as oxidation states.

Next, we did a series of QM/MM calculations with the QM region with overall charge −1 and an overall doublet spin state: $^{2}$**Re**$^{-}$. These systems have the charge and spin fully located on the $O_2$ moiety and hence can be characterized as [$SubH_2$---$O_2^{-\bullet}$] complexes. Bond lengths $R_1$, $R_2$ and $R_3$ are considerably shorter with superoxo bound then with molecular oxygen by at least 0.5Å and in some cases even 1Å. Therefore, superoxo will be able to approach the substrate more closely and is more likely to react via hydrogen atom abstraction. Clearly, the negatively charged $O_2^{-\bullet}$ is held more tightly in position by the Asn side chain groups that are set up for selective hydrogen atom abstraction.

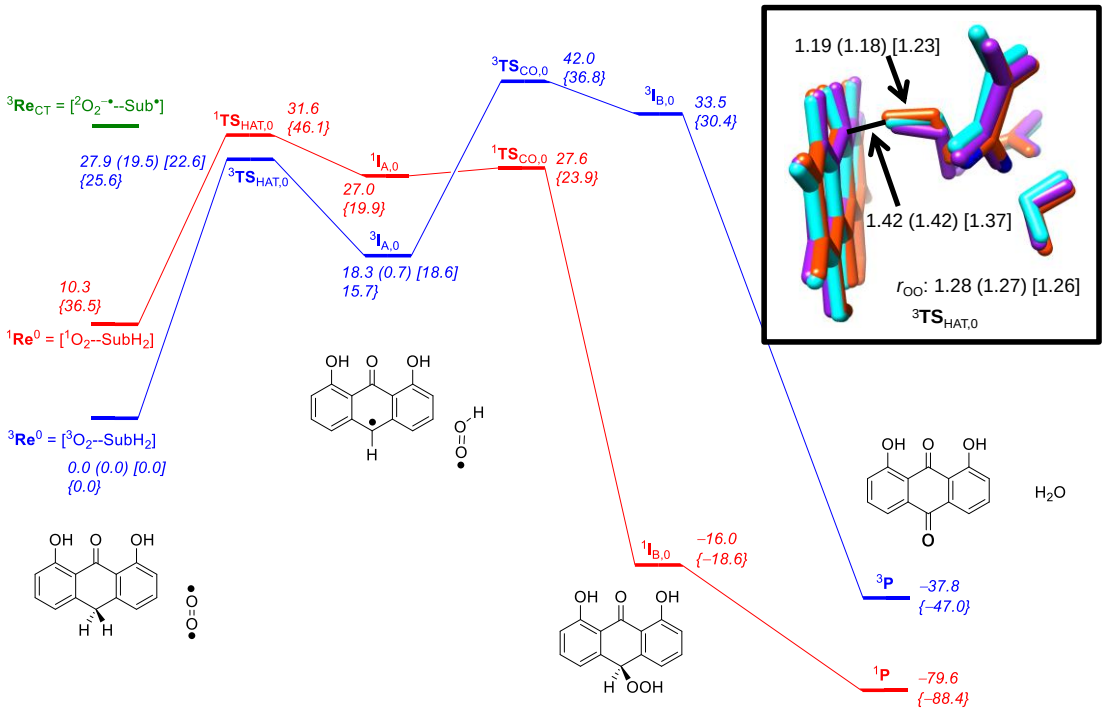


**Figure 8.5.** Potential energy landscape (with values in kcal mol$^{-1}$) for dithranol ($SubH_2$) activation by $^{3}O_2$ inside NMO as calculated with QM/MM. Formation of the monoxygenase product is depicted. Energies obtained with QM/MM at the UB3LYP/BS1 level of theory with QM region C for snapshots $Sn_{450}$ ($Sn_{500}$) [$Sn_{550}$]. Values in curly brackets obtained with basis set BS2. The inset gives an overlay of the optimized geometries of $^{3}TS_{HAT,0}$ for the three snapshots containing substrate, $O_2$ and the side-chains of the two Asn residues with bond lengths in angstroms.

### 8.3.3 Reaction of $SubH_2$ with $^3O_2$

Subsequently, we investigated the reaction mechanism of oxygen atom transfer to substrate starting from the $^3$**Re**$^0$ and $^2$**Re**$^-$ complexes, whereby approach of $^3O_2$ or $^2O_2^{-\bullet}$ initiates the reaction. These represent the reactions expected to occur below pH 6.9, i.e. the p$K_a$ of the NMO-substrate complex (Siitonen et.al. 2012; Machovina et.al. 2016). The mechanism for this reaction was not studied experimentally; however, it was shown that the monoxygenation product (dithranone) was a minor product; the major product was bisanthrone, the dimerized form of the neutral substrate radical.

Figure 8.5 displays the mechanism starting from $^3$**Re**$^0$ for oxygenation of dithranol as obtained with QM/MM using QM region **C**, which includes dithranol, oxidant, the two active site Asn groups and one water molecule. We calculated the full mechanism on the triplet and singlet spin states for snapshot $Sn_{450}$, but did an additional set of calculations for the rate-determining step in snapshots $Sn_{500}$ and $Sn_{550}$.

We will first cover the results on the full mechanism as calculated with snapshot $Sn_{450}$. The triplet spin state is the ground state and the lowest energy singlet spin state is higher in energy by 10.3 kcal mol$^{-1}$ (as calculated with QM region **C** and snapshot $Sn_{450}$). In agreement with the predictions from gas phase DFT model complexes (Figure 8.3), the initial hydrogen atom abstraction from $SubH_2$ by $O_2$ is high in energy with barriers $^3$**TS**$_{HAT,0}$ and $^1$**TS**$_{HAT,0}$ of 27.9 and 31.6 kcal mol$^{-1}$ in the triplet and singlet spin states ($Sn_{450}$), respectively. The same triplet/singlet spin state ordering is observed in the radical intermediates $^{1,3}$**I**$_{A,0}$, which represents an OOH radical nearby SubH$^\bullet$. In the next step the OOH radical attacks SubH$^\bullet$ and a covalent C–O bond is formed to generate the Sub(H)OOH intermediate **I**$_{B,0}$ via transition state **TS**$_{CO,0}$. This step is high in energy on the triplet spin state surface and a spin-state crossing from the triplet to the singlet spin state will be required to form $^1$**I**$_{B,0}$. Failure of the intermediate to undergo the spin-state crossing could yield the neutral substrate radical and OOH radical products, which diffuse from the active site and ultimately lead to bisanthrone as the major product. Alternatively, formation of $^1$**I**$_{B,0}$ following the spin crossing is highly exothermic. In a final reaction step the hydroperoxo group abstracts the other hydrogen atom from carbon atom $C^{12}$ and dissociates a water molecule from the complex via **TS**$_{W,0}$ to form products **P**$_0$. The last step is highly exothermic and may be further stabilized by access of additional water molecules or other hydrogen bonding groups.

The reaction mechanism shown in Figure 8.5 proceeds via a high energy hydrogen atom abstraction barrier and is followed by a high energy spin-state crossing from the triplet to the singlet spin-state. Consequently, this mechanism will correspond to a kinetically slow process. This is consistent with what was observed for the NMO-catalyzed reaction at acidic pH. The hydrogen atom abstraction step was calculated for three snapshots ($Sn_{450}$, $Sn_{500}$ and $Sn_{550}$) at B3LYP/BS1:CHARMM and for snapshot $Sn_{450}$ also at the B3LYP/BS1:CHARMM/ /B3LYP/BS2:CHARMM level of theory. The two energy values for $Sn_{450}$ are within a few kcal $mol^{-1}$ from each other and therefore appear to have little effect on the mechanism and conclusions. Group spin densities and charges (Supporting Information) implicate all $^3\mathbf{TS}_{HAT}$ barriers to represent hydrogen atom abstraction barriers with no excess charge on the substrate and a charge neutral $O_2$ group.

An overlay of the three optimized geometries of the QM region of these $^3\mathbf{TS}_{HAT,0}$ transition states are given in the inset of Figure 8.5. As can be seen, the transition states are late with long C–H and short O–H distances. The optimized geometries of the various snapshots give structures that are very much alike; however, the energies fluctuate strongly. In particular, $Sn_{500}$ gives a hydrogen atom abstraction transition state of 19.5 kcal $mol^{-1}$, whereas it is 27.9 and 22.6 kcal $mol^{-1}$ for $Sn_{450}$ and $Sn_{550}$, respectively. These differences are relatively large and may indicate that the protein has a high degree of flexibility. It appears, therefore, that NMO has a range of low- and high-energy enzyme conformations and in some of those the reactivity is faster than in others. Our results implicate the structure of snapshot $Sn_{500}$ to be more reactive than snapshots $Sn_{450}$ and $Sn_{550}$.

To test whether the size of the QM region has an effect on the reaction mechanism and rate constant of hydrogen atom abstraction, we ran additional QM/MM calculations without the bridging water molecule in the QM region, QM region **B**. These studies for snapshots $Sn_{450}$, $Sn_{500}$ and $Sn_{550}$ gave $^3\mathbf{TS}_{HAT,0,B}$ barrier heights of 27.2, 26.5 and 28.1 kcal $mol^{-1}$ at B3LYP/BS1:CHARMM level of theory, whereas with a large basis set of BS2 a barrier height of 27.5 kcal $mol^{-1}$ was obtained (Supporting Information). As such, the four QM/MM geometry optimizations give an average of 27.3 ± 0.7 kcal $mol^{-1}$ and therefore the standard deviation for this set is very small. A comparison of the structure and energetics of the hydrogen atom abstraction from $SubH_2$ by $^3O_2$ shows only minor differences upon inclusion of the water molecule in the QM region. Consequently, water molecules in the substrate binding pocket are there to stabilize the structure, but do not appear to have a direct catalytic function.

### 8.3.4 Reaction of $SubH_2$ with $^2O_2^{-\bullet}$

Even though the experimental work argued against the availability of a reduction partner, we considered the reaction of $SubH_2$ with superoxide, particularly since the thermochemical analysis from Figure 8.3 implicated an exergonic energy for the reaction between dithranol and $O_2^{-\bullet}$. We consequently calculated the mechanism of substrate activation from that reactant complex, i.e. $^2\mathbf{Re}^-$, with QM/MM, see Figure 8.6. As can be seen from Figure 8.6, the hydrogen atom abstraction barrier is small with an average value of 2.9 ± 0.2 kcal $mol^{-1}$ for the four snapshots leading to the radical intermediates in an almost thermoneutral reaction process. Energetically, the hydrogen atom abstraction as calculated with QM/MM, therefore, is similar to what was seen from DFT model complexes (Figure 8.3) and hence the effect of the protein and the local environment is small. The subsequent C–O bond formation step to form the hydroperoxodithranol intermediate $^2\mathbf{I}_{B,-1}$ is negligible as is the water release to form products. In conclusion, the reaction between superoxo and dithranol is a low energy process that will lead to products efficiently at little energetic costs.

Geometrically (inset of Figure 8.6), the transition states for the reaction of $O_2^{-\bullet}$ with $SubH_2$ are more central with C–H distances of 1.32 – 1.39Å and O–H distances ranging from 1.23 – 1.31Å for the four snapshots. Therefore, structurally and energetically the four transition states are alike. Furthermore, the effect of a basis set with more polarization functions appears to be limited and does not seem to improve the structure and energetics to what was obtained with B3YP/BS1. Accordingly, a superoxo anion can react efficiently with dithranol through oxygen atom transfer with release of a water molecule.

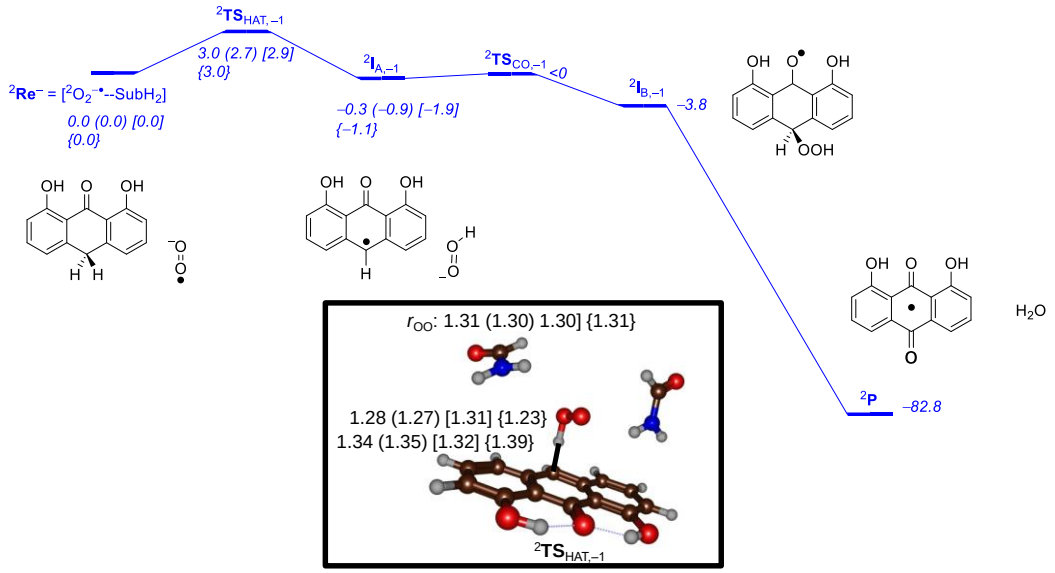


**Figure 8.6.** Potential energy landscape (with values in kcal mol$^{-1}$) for dithranol activation by $^2O_2^{-\bullet}$ inside NMO as calculated with QM/MM. Energies obtained with QM/MM at the UB3LYP/BS1 level of theory with QM region B for snapshots $Sn_{450}$ ($Sn_{500}$) [$Sn_{550}$]. Values in curly brackets are the result of a full geometry optimization with basis set BS2. The inset gives an overlay of the optimized geometries of $^2TS_{HAT,-1}$ for the three snapshots with bond lengths in angstroms.

### 8.3.5 Reaction of SubH$^-$ with $^3O_2$

Finally, we investigated three alternative reaction mechanisms (Scheme 8.1), whereby dioxygen enters the pocket containing deprotonated dithranol (SubH$^-$). These mechanisms represent possible reaction pathways describing the reaction at neutral and higher pH. Importantly, the reaction of $O_2$ with the NMO-SubH$^-$ complex uniquely leads to the biologically observed desirable monoxygenated species as the major product. This reaction is moreover ~2000-fold faster than the reaction of NMO-$SubH_2$ and $O_2$ to generate primarily bisanthrone.

Alongside DFT model complex calculations, we also performed a full QM/MM study on a structure containing deprotonated substrate and $^3O_2$ ($^3$**Re**$^0$-H$^+$) and the mechanism of substrate activation. A geometry optimization at either the QM/MM level of theory or on an active site model with DFT gives a [SubH$^-$--$^3O_2$] configuration with two unpaired electrons on dioxygen and a negative charge on deprotonated dithranol. Therefore, similarly to the reactant complexes discussed above, no electron transfer takes place upon approach of $^3O_2$ on deprotonated substrate. This confirms the results from small model complexes (Figure 8.3) that predicted an endothermicity for electron transfer of 25.8 kcal mol$^{-1}$. As such, the model predicts that the protein environment

does not stabilize the products sufficiently to make electron transfer feasible. Interestingly, experimental work using superoxide dismutase superoxide scavengers indicated a role for superoxide (or its protonated form) in the formation of the monoxygenase product at alkaline pH and hence our proposed mechanism may not represent alkaline chemical systems.

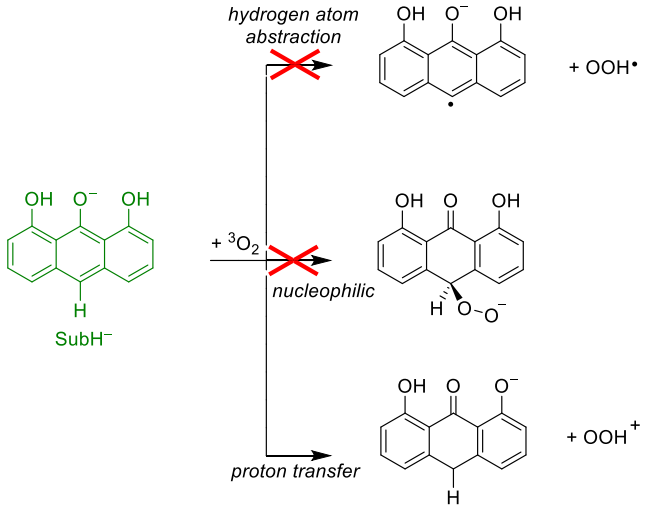


**Scheme 8.1.** Reactions tested for deprotonated substrate with dioxygen using QM region B.

Subsequently, three reaction mechanisms were explored starting from this reactant complex ($^3$**Re**$^0$-H$^+$): hydrogen atom abstraction, electrophilic addition of dioxygen to carbon C$^{12}$ as well as proton transfer from the phenol group (Scheme 8.1). Supporting Information Tables S16 and S17 give details of the geometry scans of hydrogen atom abstraction and electrophilic addition. We initially ran constraint geometry scans with QM/MM using QM region **B** to explore the potential energy profile and find information on the likelihood of the mechanism, whereby in stepwise geometry optimizations substrate and oxidant were brought closer together. However, these scans gave continuous increase of the energy upon shortening the distances. Hence, neither the aromatic nor phenolic hydrogen atom abstraction processes by SubH$^-$ is a feasible reaction mechanism.

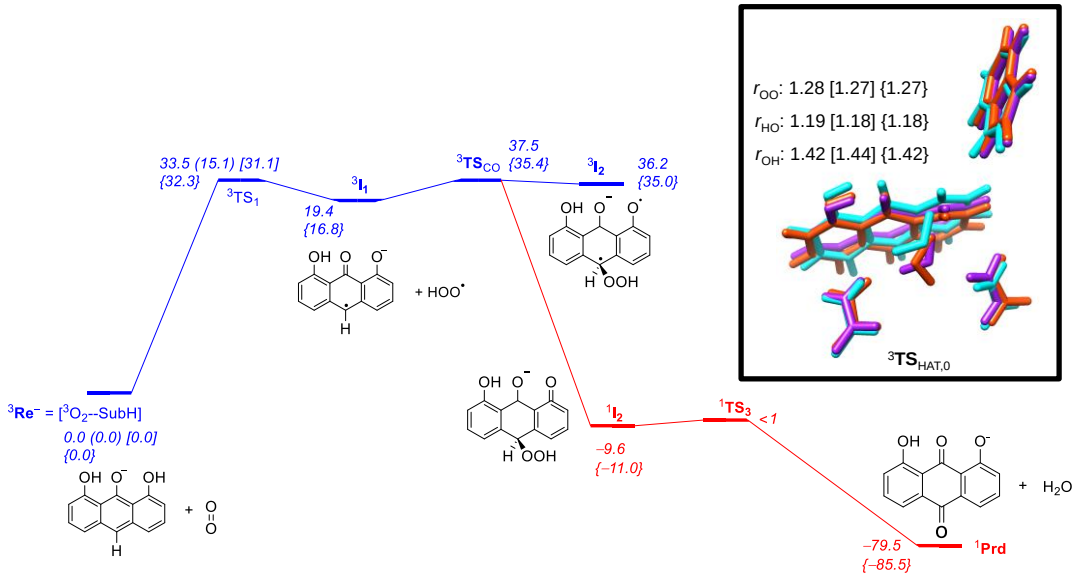


**Figure 8.7:** Potential energy landscape (with values in kcal mol$^{-1}$) for dithranol anion activation by $^3O_2$ inside NMO as calculated with QM/MM. Energies obtained with QM/MM at the UB3LYP/BS1 level of theory with QM region E for snapshots $Sn_{500}$ ($Sn_{550}$) [$Sn_{600}$]. Values in curly brackets obtained with basis set BS2. The inset gives an overlay of the optimized geometries of $^3TS_{HAT,0}$ for the three snapshots with bond lengths in angstroms.

The final mechanism considered for this model was hydrogen atom abstraction from the phenol group to $^3O_2$, Figure 8.7. The phenol proton is linked in a hydrogen bonding interaction with the indole nitrogen atom of $Trp_{67}$. Therefore, we selected a model where the QM region included this $Trp_{67}$ residue, namely QM region **E**. Figure 8.7 displays details of the calculated reaction mechanism and gives optimized geometries of key transition states for proton transfer.

As can be seen from Figure 8.7, a mechanism is obtained and a transition state for proton transfer could be located in all three snapshots. An analysis of the group spin densities, however, shows that these steps correspond to a hydrogen atom abstraction from the phenol group. Thus, the transition states give spin density distributions of approximately 1 on $O_2$ and 1 on substrate, so that the proton transfer simultaneously has resulted in an electron transfer. Energetically these proton transfer barriers fluctuate dramatically and in snapshots $Sn_{500}$ and $Sn_{600}$ they are high in energy with a magnitude of 33.5 and 31.1 kcal mol$^{-1}$. Therefore, in these snapshots the proton transfer will not be feasible at room temperature. On the other hand, in snapshot $Sn_{550}$ a low-energy transition state is found of only 15.1 kcal mol$^{-1}$. It is unclear what the origin of the low energy of the $Sn_{550}$ proton transfer transition states is. Optimized

geometries of the three proton transfer transition states are given in Figure 7 and look very similar. Probably as discussed above, this protein is small and has a large and open substrate binding pocket whereby small changes in conformation and hydrogen bonding interactions can lead to major energetic fluctuations.

The subsequent mechanism after hydrogen atom transfer leads to an intermediate $^3\mathbf{I_1}$ at 16.8 kcal mol$^{-1}$ above reactants. Similar to the electronic configuration of the transition state has a spin density of 1 on the OOH unit and 1 on the organic substrate. Attempts were made to swap molecular orbitals and find the proper proton transfer intermediate as described in Scheme 8.1; however, it was considerably higher in energy. Finally, the reaction proceeds past a second transition state $\mathbf{TS_{CO}}$ that costs an additional 18.6 kcal mol$^{-1}$ in energy leading to the biradical intermediate $^3\mathbf{I_2}$. A spin state crossing to the open-shell singlet intermediate gives an exergonic process. A very low barrier (<1 kcal mol$^{-1}$) will then release a water molecule to form the anionic product. The results obtained with snapshot $Sn_{500}$ were reproduced well with $Sn_{600}$ and calculations with a larger basis set also did not lead to major changes. Interestingly, the third snapshot ($Sn_{550}$) gives a proton transfer barrier of only 15.1 kcal mol$^{-1}$, which would be a thermochemically accessible barrier at room temperature. However, even this barrier is well higher than the ones from Figure 8.6 for the reaction of superoxo anion radical with substrate.

### 8.3.6 Effect of $Asn_{18}$ and $Asn_{63}$ residues

The calculations presented in this work show that two Asn residues ($Asn_{18}$ and $Asn_{63}$) in the substrate binding pocket can hold and guide molecular oxygen to the $C^{12}$ position of dithranol for site-selective hydroxylation. To examine their effect in catalysis, we mutated both residues to Ala and reevaluated the reaction mechanism with QM/MM. The two Asn groups were replaced by Ala groups manually and the set-up of the protein structure and particularly the solvation step was redone. In the absence of the Asn groups in the substrate binding pocket, their function is taken over by additional water molecules that are involved in key hydrogen bonding interactions. From the mutant molecular dynamics simulation, we took three snapshots and repeated the full acidic substrate activation mechanism for $SubH_2$ with $O_2$ with QM/MM. Optimized geometries of the rate-determining hydrogen atom abstraction transition states $^3\mathbf{TS}_{HAT,0,mutants}$ are given in Figure 8.8 for three snapshots obtained from MD simulation after 500, 550 and 600 ps. As can be seen geometrically and

energetically the structures are very similar to each other, but also do not deviate much from the ones given above in Figure 8.5 for the WT reaction. This is not surprising as in none of the above mentioned calculations significant radical character or charge was found on the Asn side chains. As a result, the hydrogen atom abstraction barrier heights are of similar energy to those found for WT ranging from 27.8 to 30.4 kcal $mol^{-1}$ for $^{3}\mathbf{TS}_{HAT,0,mutants}$ in the three individual snapshots. Consequently, little energetic and geometric differences are seen for the hydrogen atom abstraction barriers as compared to the studies reported in the previous sections. The hydrogen atom abstraction barriers are late on the potential energy profile with long C-H and short O-H distances and hence resemble the radical intermediate structures in geometry. As seen before, late transition states usually correspond with high hydrogen atom abstraction barriers, which indeed is the case for our system (Kumar et.al. 2010; Kumar et.al. 2013).

In conclusion, the Asn amino acids in the substrate binding pocket do not appear to have a strong catalytic function. They form hydrogen bonding interactions with dioxygen/superoxo that may guide it into the right direction and set up for attack on position $C^{12}$ of dithranol. The increase of the catalytic rates observed experimentally may be too small to be captured accurately with our computational models. However, the presence of Asn residues appears to influence the electron affinity of the reactant complex and lower it slightly.

### 8.3.7 Substrate C–H bond strength versus oxidant O–H strength

The QM/MM and DFT calculations implicate that although with low rate constants and therefore relatively slow, actually $^{3}O_2$ can abstract a hydrogen atom from neutral dithranol substrate. As there are few substrates $^{3}O_2$ is known to react directly with, we decided to investigate the C–H bond strength of dithranol and compare it to typical aliphatic C–H bond strengths. To this end we calculated the bond dissociation free energy (BDFE) of the C–H bond of a range of aliphatic molecules according to Eq 8.3 by taking the difference in free energy between the substrate (SubH), a hydrogen atom, and the substrate with one hydrogen atom less (Sub$^{\bullet}$). Previously, it was shown that the BDFE of either the bond that is broken or the bond that is formed correlates with the driving force of the reaction as well as with the activation free energy and consequently the natural logarithm of the rate constant (Friedrich, L.E. 1983; Bordwell and Cheng, 1991; Mayer, J.M. 1998). Further computational modelling on either one

oxidant with a range of aliphatic substrates or one substrate with a range of iron(IV)-oxo species confirmed the correlation between free energy of activation and $BDFE_{CH}/BDFE_{OH}$ (Shaik et.al. 2008; Latifi et.al. 2009, de Visser, S. 2010).

$$SubH \rightarrow Sub^{\bullet} + H^{\bullet} + BDFE_{CH} \qquad (8.3)$$

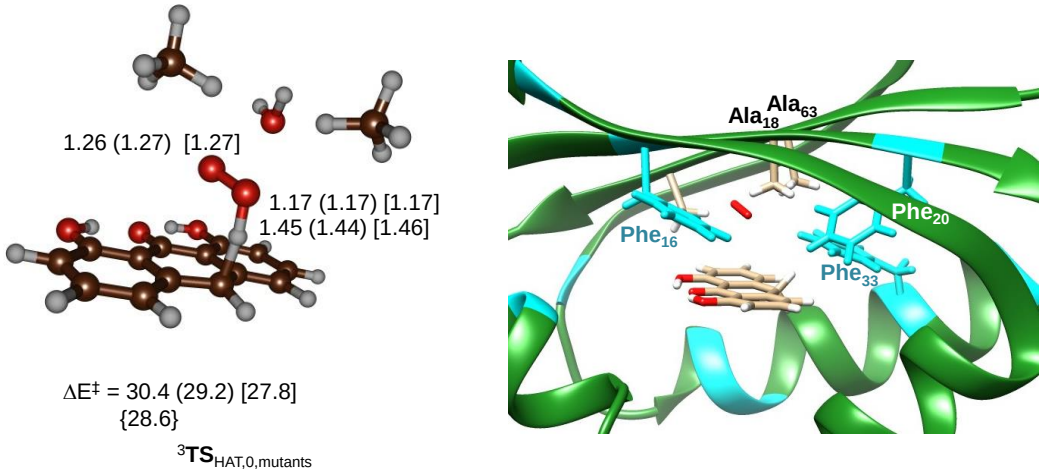


**Figure 8.** QM/MM optimized geometries of hydrogen atom abstraction transition states $^{3}TS_{HAT,0,mutants}$ of the Asn18Ala/Asn63Ala double mutant of NMO for the reaction of $SubH_2$ with $^{3}O_2$ using QM region C. Data obtained at UB3LYP/BS1:CHARMM for $Sn_{500}$ ($Sn_{550}$) and [$Sn_{600}$] and at UB3LYP/BS1:CHARMM//UB3LYP/BS2:CHARMM for {$Sn_{500}$}. Bond lengths are in angstroms and relative energies in kcal $mol^{-1}$.

Table 8.1 compares DFT calculated $BDFE_{CH}$ values of a range of aliphatic substrates. As follows from Table 1, the C–H bond strength of dithranol is extremely weak and is of similar strength to that found for the aliphatic C–H bonds of 1,3-cyclohexadiene and dihydroanthracene. Therefore, even a weak C–H bond oxidant will be able to activate dithranol efficiently. Indeed, molecular oxygen, which is not known to react with many C–H bonds directly can activate this bond. The reaction of $^{3}O_2$ with a hydrogen atom calculated using the same methods form $^{\bullet}OOH$ radical with a reaction free energy of 41.4 kcal $mol^{-1}$, which is the $BDFE_{OH}$ of the $^{\bullet}OOH$ radical. As shown above in Figure 8.3, the combination of the $BDFE_{OH}$ with the $BDFE_{CH}$ of dithranol predicts an endothermic hydrogen atom abstraction of 19.2 kcal $mol^{-1}$, which compares well with the reaction energy found between $^{3}\mathbf{Re}^{0}$ and $^{3}\mathbf{I}_{A,0}$ reported in Figure 8.5.

**Table 8.1.** DFT calculated $BDFE_{CH}$ values for selected aliphatic substrates

| **Substrate** | **$BDFE_{CH}$** [a] |
|---|---|
| Methane | 96.2 |
| Ethane | 90.4 |
| Toluene (aliphatic) | 81.5 |
| 9,10-Dihydroanthracene | 65.2 |
| 1,3-cyclohexadiene | 62.7 |
| 10-Methyl-9,10-dihydroacridine | 61.0 |
| Dithranol | 60.6 |

[a] in kcal $mol^{-1}$.

## 8.4 Conclusions.

In summary, we present a detailed DFT, QM/MM and thermochemical analysis on the reaction mechanism of substrate activation by NMO enzymes. At acidic pH, the weak C–H bond of the neutral substrate is shown to undergo direct hydrogen atom transfer to $^3O_2$, a reaction that is accelerated if superoxide anion is used as the co-substrate. The lowest energy though still endergonic pathway for the biologically relevant reaction of the substrate anion and $^3O_2$ was likewise net hydrogen atom transfer to yield a substrate anion radical and OOH radical pair. In addition, we investigate the mechanism of substrate and oxidant in various protonation and oxidation states. In general, the most effective reaction is of substrate with $O_2^{-\bullet}$; how this species could be formed experimentally would need to be investigated in the future. The lack of a clearly exergonic pathway for the reaction of the substrate anion is puzzling, given that it occurs at a much higher rate than the reaction of $SubH_2$.

## AUTHOR INFORMATION

### Corresponding Author

* sam.devisser@manchester.ac.uk (SPdV); jdubois@chemistry.montana.edu (JD).

### Author Contributions

The manuscript was written through contributions of all authors.

## ACKNOWLEDGMENT

FGCR thanks the Conacyt Mexico for a studentship. We thank Prof Robert Szilaghi (University of Montana, USA) for fruitful discussions on possible substrate protonation states and isomeric structures.

## ABBREVIATIONS

P450, cytochrome P450; HOD, 1-H-3-hydroxy-4-oxoquinaldine 2,4-dioxygenase; NMO, nogalamycin monoxygenase; DFT, density functional theory; QM/MM, quantum mechanics/molecular mechanics; ET, electron transfer; PT, proton transfer; HAT, hydrogen atom transfer; HT, hydride transfer; pdb, protein databank file.

**‘Blank page’**

## 9 Concluding Remarks

The primary metabolism of drugs is a vital aspect to understand on some very important fields of research and development, from drug discovery and design to the health science implications of currently marketed drugs. A good drug candidate should not produce toxic metabolites that may result in liver damage or other secondary effects, but it should also last long enough in the blood stream for a good therapeutic effect with good potency. To attend such problems, a combination of experimental and computational approaches are generally used. Hence, a rational approach to drug-candidate optimization is desirable, where a key investigation surrounds the elucidation and understanding of the mechanisms of reactions involved in the formation of primary metabolites. This process mostly happens by action of P450 enzymes in the liver. Biomimetic models of P450 enzymes either through CpdI models or other Fe(IV) oxo models present a critical means to better understand the drug-enzyme relationship.

We presented here an extensive study on the mechanisms of reaction of P450 enzymes, or the active species "Compound I", as well as some reaches and limitations of the currently used models and methods, mainly, QM and QM/MM. Throughout the results some key aspects relevant to drug metabolism are discussed and shown. First, a DFT iron-oxo catalyst model may very accurately predict activation barriers against experiment if the right methods are used (functionals, basis set, solvation, dispersion) as shown by a N4PY-Fe(IV)-Oxo benchmark study. Moreimportantly, trends are mostly conserved across methods, even if barrier heights are poorly represented by some methods. This shows that there is a high reliability on the qualitative interpretation of DFT data, or relative barrier comparison, which is an essential component for studying drug metabolism, where regio-selectivity and activation mechanisms are crucial features.

A novel Fe(IV)-oxo model is also studied, a N-Heterocyclic embedded iron(IV)-oxo system. Unlike CpdI, this compound is stable in its active form and shows similar mechanistic behaviour to P450, CpdI. Such a trait, as with other biomimetic models, is a window into the studying of P450 chemistry. However, with an expectedly different electronic structure and a weaker catalytic action, it is not the best biomimetic candidate of P450. Nevertheless, we have shown that DFT modelling is essential in

the understanding of the electronic structure of CpdI or its mimetic catalysts and the mechanisms by which they react.

A following set of collaborative experimental and theoretical studies on a metalloporphyrin Fe(IV)-Oxo model displays evidence and rationalization for the mechanisms involved in the hydroxylation of several aromatic compounds. Key aspects are highlighted such as the Electron Affinity (which correlates to aromatic hydroxylation) or BDE of Hydrogen-Carbon, which is unrelated to reaction kinetics, *au contraire* of what one would expect on an aliphatic hydroxylation by P450 or CpdI. A followup on this electron deficient oxidant explores the debate on hydrogen versus hydride transfers on the activation of aliphatic hydrogen atoms of some common substrates and the difference expected with this model versus a normal CpdI oxidant, giving greater insight into the electronic properties of Cpd I models.

In a more applied set of projects, a comprehensive study on P450 mediated metabolism is performed on a common phthalate derivate and its many potential metabolites resulting in several sites of activation. The effectiveness of DFT methods on toxicological and metabolic analysis is explored, where the model effectively predicts common derivates; however stereoselective effects are weak and additional tools such as docking and conformational sampling may be needed for greater experimental correspondences. Lastly a QM/MM and DFT comprehensive study on the chemistry of NMO biosynthesis via a cofactorless independent oxidation is explored. Empploying a mixture of mechanistic investigations and thermochemical cycles, many factors are explored and discussed, expanding our understanding of such processes under varying conditions.

Cytochrome P450 mediated Drug metabolism as well as other biological functions thus can greatly benefit from DFT and QM/MM methods for the analysis and rationalization of biomimetic models of Cpd I and its chemistry with common or specific substrates. By understanding and exploring CpdI reaction mechanisms, the relevance of electronic structure and discrete thermodynamic factors such as EA, as well as regioselectivity, performing VB analysis and other whole enzyme studies where necessary one can get a better understanding of complex metabolic processes with implications on several drug metabolism related areas from basic biology and chemistry, pharmacokinetics, or even drug discovery, design and development.

## 10 References

Some molecular graphics and analyses were performed with the UCSF Chimera package. Chimera is developed by the Resource for Biocomputing, Visualization, and Informatics at the University of California, San Francisco, funded by grants from the National Institutes of Health National Center for Research Resources (2P41RR001081) and National Institute of General Medical Sciences (9P41GM103311).

ChemCraft was used for some visualizations: http://www.chemcraftprog.com

Protein Crystal Structures were obtained from the RCSB Protein Data Bank.

Some images were made with VMD software support. VMD is developed with NIH support by the Theoretical and Computational Biophysics group at the Beckman Institute, University of Illinois at Urbana-Champaign. Link to http://www.ks.uiuc.edu/.

1. Abelo, A. Andersson,T. Antonsson, M. Naudot, I.S. Weidolf, L. Stereoselective metabolism of Omeprazole By Human Cytochrome P450 Enzymes. *Drug Metabolism and Disposition*. **2000**, 28, 966-972.
2. Abu-Omar, M. M.; Loaiza, A.; Hontzeas, N. Reaction Mechanisms of Mononuclear Non-heme Iron Oxygenases. *Chem. Rev.* **2005**, 105, 2227–2252.
3. Abu-Omar, M. M. High-valent iron and manganese complexes of corrole and porphyrin in atom transfer and dioxygen evolving catalysis. *Dalton Trans.* **2011**, 40, 3435–3444.
4. Adamo, C.; Barone, V. Toward reliable Density Functional Methods without Adjustable Parameters: The PBE0 model. *J. Chem. Phys.* **1999**, 110, 6158–6169.
5. Afanasiev, P. Sorokin, A. B. μ-Nitrido Diiron Macrocyclic Platform: Particular Structure for Particular Catalysis. *Acc. Chem. Res.* **2016**, 49, 583–593.
6. Agranat, I. Caner, H. Caldwell, J. 2002. Putting Chirality to Work: The Strategy of Chiral Switches. *Nature Reviews: Drug Discovery.* **2002**, 1, 753 - 768.
7. Ahmad, N. Mukhtar, H. Cytochrome P450: A Target for Drug Development for Skin Diseases. *Journal of Investigative Dermatology.* **2004**, 123, 417 – 425.

8. Ahlrichs, R.; Bär, M.; Häser, M.; Horn, H.; Kölmel, C. Electronic structure calculations on workstation computers: The program system turbomole. *Chem. Phys. Lett*. **1989**, 162, 165–169.
9. Aluri, S.; de Visser, S. P. The Mechanism of Cysteine Oxygenation by Cysteine Dioxygenase Enzymes. *J. Am. Chem. Soc*. **2007**, 129, 14846–14847.
10. Angelelli, F. Chiavarino, B. Crestoni, M. E. J Binding of gaseous Fe (III)-heme cation to model biological molecules: Direct association and ligand transfer reactions. *Am. Soc. Mass Spectrom*. **2005**, 16, 589–598.
11. Anneser, M. R. Haslinger, S. Pöthig, A. Cokoja, M. Basset, J.M. Kühn, . F. E. Synthesis and Characterization of an Iron Complex Bearing a Cyclic Tetra-N-heterocyclic Carbene Ligand: An Artifical Heme Analogue? *Inorg. Chem.* **2015**, 54, 3797–3804.
12. Anneser, M. R. Haslinger, S. Pöthig, A. Cokoja, M. D'Elia, V. Högerl, M. P. Basset, J.M. Kühn, F. E. Binding of molecular oxygen by an artificial heme analogue: investigation on the formation of an Fe–tetracarbene superoxo comple. *Dalton Trans*. **2016**, 45, 6449–6455.
13. Asaka, M.; Fujii, H. Participation of Electron Transfer Process in Rate-Limiting Step of Aromatic Hydroxylation Reactions by Compound I Models of Heme Enzymes *J. Am. Chem. Soc.* **2016**, 138, 8048–8051.
14. Asharanov, Y. Amandan, J. Vaidman, L. 1993. Meaning of the Wave Function. *Physical Review A.* **1993,** 47, 4616-4626.
15. Atanasov, M. Comba, P. Hausberg, S. Martin, B. Cyanometalate-bridged oligonuclear transition metal complexes—Possibilities for a rational design of SMMs. *Coord. Chem. Rev*. **2009**, 253, 2306–2314.
16. Atkins, P.W., Friedman, R.S. Molecular Quantum Mechanics. Third Edition, Oxford Press **1997**, 277 -278.
17. Aviv-Harel, I. Gross, Z. Coordination chemistry of corroles with focus on main group elements. *Coord. Chem. Rev*. **2011**, 255, 717–736.
18. Bach, R. Dmitrenko, O. 2010. Transient Inverted Metastable Iron Hydroperoxides in Fenton Chemistry: A Nonenzymatic Model for Cytochrome P450 Hydroxylation. *The Journal of Organic Chemistry*. **2010,** 75, 3705-30714.

19. Bakowies, D.; Thiel, W. *J.* Hybrid Models for Combined Quantum Mechanical and Molecular Mechanical Approaches. *Phys. Chem.* **1996**, *100*, 10580–10594.
20. Balcells, D. Raynaud, C. Crabtree, R. H. Eisenstein, O. A rational basis for the axial ligand effect in C− H oxidation by [MnO (porphyrin)(X)]+(X= H2O, OH−, O2−) from a DFT study. *Inorg. Chem*. **2008**, 47, 10090–10099.
21. Banse, F. Girerd, J.J. Robert, V. You have full text access to this contentNonheme "FeIVO" Models: Ab Initio Analysis of the Low-Energy Spin State Electronic Structures. *Eur. J. Inorg. Chem*. **2008**, 4786–4791.
22. Barbusinski, K. 2009.Fenton Reaction – Controversy concerning The Chemistry. *Ecological Chemistry and Engineering S.* **2009,** 16, 347 – 358.
23. Barman, P. Upadhyay, P. Faponle, A.S. Kumar, J. Nag, S. S. Kumar, D. Sastri, C.V. de Visser, S.P. Deformylation Reaction by a Nonheme Manganese (III)–Peroxo Complex via Initial Hydrogen-Atom Abstraction. *Angew. Chem. Int. Ed*. **2016**, 55, 11091–11095.
24. Bartmess, J. E. Georgiadis, R. M. Empirical methods for determination of ionization gauge relative sensitivities for different gases. *Vacuum* **1983**, 33, 149–154.
25. Bathelt, C.M.; Mulholland, A.J.; Harvey, J.N. QM/MM modeling of benzene hydroxylation in human cytochrome P450 2C9. *J. Phys. Chem. A* **2008**, 112, 13149–13156.
26. Bauer, I.; Max, N.; Fetzner, S.; Lingens, F. 2,4-Dioxygenases Catalyzing N-Heterocyclic-Ring Cleavage and Formation of Carbon Monoxide. *Eur. J. Biochem*. **1996**, *240*, 576–583.
27. Becke, A. D. Density-functional Exchange-Energy Approximation with Correct Asymptotic Behavior. *Phys. Rev*. A **1988**, 38, 3098–3100.
28. Becke, A. D. Density-functional thermochemistry. III. The Role of Exact Exchange. J. *Chem. Phys.* **1993**, 98, 5648–5652.
29. Becke, A. D. Density-Functional Thermochemistry. V. Systematic Optimization of Exchange-Correlation Functionals. *J. Chem. Phys*. **1997**, 107, 8554-60.
30. Belcher, J.; McLean, K.J.; Matthews, S.; Woodward, L.S.; Fischer, K.; Rigby, S.E.J.; Nelson, D.R.; Potts, D.; Baynham, M.T.; Parker, D.A.; Leys, D.; Munro, A.W. Structure and biochemical properties of the alkene producing

cytochrome P450 OleTJE (CYP152L1) from the Jeotgalicoccus sp. 8456 bacterium. *J. Biol. Chem*. **2014**, 289, 6535–6550.

31. Berman, H. Westbrook, J. Feng, Z. Gilliland, G. Bhat, T. Weissig, H. Shindyalov, I. Bourne, P. The Protein Data Bank. *Nucleic Acids Research.* **2000**, 28, 235-242.
32. Bernadou, J. Meunier, B. Biomimetic Chemical Catalysts in the Oxidative Activation of Drugs. *Adv. Synth. Catal.* **2004**, 346, 171 – 184.
33. Bernasconi, L. Baerends, E.J. The EDTA Complex of Oxidoiron(IV) as Realisation of an Optimal Ligand Environment for High Activity of FeO2+. *Eur. J. Inorg. Chem*. **2008**, 1672–1681.
34. Bernasconi, L. Baerends, E. J. A Frontier Orbital Study with ab Initio Molecular Dynamics of the Effects of Solvation on Chemical Reactivity: Solvent-Induced Orbital Control in FeO-Activated Hydroxylation Reactions. *J. Am. Chem. Soc*. **2013**, 135, 8857–8867.
35. Berraud-Pache, R.; Lindh, R.; Navizet, I. QM/MM Study of the Formation of the Dioxetanone Ring in Fireflies through a Superoxide Ion. *J. Phys. Chem. B* **2018**, *122*, 5173–5182.
36. Bertz, R.J, Granneman G.R. Use of *in vitro* and *in vivo* data to estimate the likelihood of metabolic pharmacokinetic interactions. *Clin. Pharmacokinet*. **1997**, 32, 210–258.
37. Best, R.B., Zhu, X., Shim, J., Lopes, P.E.M., Mittal, J., Feig, M., and MacKerell Jr., A.D. "Optimization of the additive CHARMM all-atom protein force field targeting improved sampling of the backbone phi, psi and side-chain chi1 and chi2 dihedral angles," *Journal of Chemical Theory and Computation*, **2012**, 8, 3257-3273.
38. Binkly, J. Pople, J. Hehre, W. 1980. Self-consistent Molecular Orbital Methods. 21. Small Split-Valence Basis Sets for First-Row Elements. *J. Am. Chem. Soc.* **1980,** 102, 939 -947.
39. Biswas, A. N.; Puri, M.; Meier, K. K.; Oloo, W. N.; Rohde, G. T.; Bominaar, E. L.; Münck, E.; Que Jr, L. Modeling TauD-J: a High-spin Nonheme Oxoiron(IV) Complex With High Reactivity Toward C-H Bonds. *J. Am. Chem. Soc*. **2015**, 137, 2428–2431.

40. Blomberg, M. R. A. Borowski, T. Himo, F. Liao, R.Z. Siegbahn, P. E. M. Quantum Chemical Studies of Mechanisms for Metalloenzymes. *Chem. Rev.* **2014**, 114, 3601–3658.
41. Boese, A. Martin, L. 2004. Development of Density Functionals for Thermochemical Kinetics. *J. Chem. Phys.*, **2004,** 121, 3405-16.
42. Bordwell, F. G.; Cheng, J.-P. Substituent effects on the stabilities of phenoxyl radicals and the acidities of phenoxyl radical cations. *J. Am. Chem. Soc*. **1991**, *113*, 1736–1743.
43. Borovik, A.S. Bioinspired hydrogen bond motifs in ligand design: the role of noncovalent interactions in metal ion mediated activation of dioxygen. *Acc. Chem. Res.* **2005**, 38, 54–61.
44. Bowers, M.T. (Ed) In Gas Phase Ion Chemistry, Academic Press, New York, **1979**; Vol. 1.
45. Boys, S. F. 1950. Electronic Wave Functions. I. A General Method of Calculation for the Stationary States of Any Molecular System. *Proc. R. Soc. Lond. A.* **1950,** 200, 542 – 554.
46. Brink, A. Pahler, A. Funk, S. Schadt, S. Mimicking the Risk of chemically reactive metabolite formation of new drug candidates: Implications for preclinical drug design. *Drug Discovery Today*. **2017**, 22, 751 – 756.
47. Brooks, B. Bruccoleri, R. Olafson, B. States, D. Swaminathan, S. Karplus, M. 1982. CHARMM: A Program for Macromolecular Energy, Minimization, and Dynamics Calculations. *Journal of Computational Chemistry.* **1983,** 2 , 187 – 217.
48. Bruijnincx, P. C. A.; van Koten, G.; Klein Gebbink, R. J. M. Mononuclear Non-heme Iron Enzymes With the 2-His-1-carboxylate Facial Triad: Recent Developments in Enzymology and Modeling Studies. *Chem. Soc. Rev.* **2008**, 37, 2716–2744.
49. Bugg, T. D. H. Oxygenases: Mechanisms and Structural Motifs for O(2) Activation. *Curr. Opin. Chem. Biol*. **2001**, 5, 550–555.
50. Bugg, T. D. H. Dioxygenase enzymes: catalytic mechanisms and chemical models. *Tetrahedron* **2003**, 59, 7075–7101
51. Cantú-Reinhard[a], F.G. Faponle, A.S. de Visser, S. P. Substrate Sulfoxidation by an Iron(IV)-Oxo Complex: Benchmarking Computationally Calculated Barrier Heights to Experiment. *J. Phys. Chem*. A **2016**, 120, 9805–9814.

52. Cantú Reinhard[b], F. G. Sainna, M. A. Upadhyay, P. Balan, G. A. Kumar, D. Fornarini, S. Crestoni, M. E. de Visser, S.P. A Systematic Account on Aromatic Hydroxylation by a Cytochrome P450 Model Compound I: A Low-Pressure Mass Spectrometry and Computational Study. *Chem. Eur. J.* **2016**, 22, 18608–18619.
53. Cantú-Reinhard[a], F. G. De Visser, S. Biodegradation of Cosmetics Products: A Computational Study of Cytochrome P450 Metabolism of Phthalates. *Inorganics.* **2017.** 5(4), 77.
54. Cantú-Reinhard, F.G. De Visser, S. Oxygen Atom Transfer Using an Iron(IV)-Oxo Embedded in a Tetracyclic N-Heterocyclic Carbene System: How Does the Reactivity Compare to Cytochrome P450 Compound I? *Chem. Eur.J.* **2017**, 23, 2935 –2944.
55. Cantú-Reinhard, F.G. Barman, P. Mukherjee, G. Kumar, J. Kumar, D. Sastri, C.V. de Visser, S. Keto–Enol Tautomerization Triggers an Electrophilic Aldehyde Deformylation Reaction by a Nonheme Manganese(III)-Peroxo Complex. **2017**. *J. Am. Chem. Soc.* 139, 50, 18328–18338.
56. Cantú-Reinhard, F.G. Fornarini, S. Crestoni, M.E. De Visser, S. Hydrogen Atom vs. Hydride Transfer in Cytochrome P450 Oxidations: A Combined Mass Spectrometry and Computational Study. Eur. J. Inorg. Chem. **2018**, 1854–1865.
57. Castro, L.; Kirillov, E.; Miserque, O.; Welle, A.; Haspeslagh, L.; Carpentier, J.; Maron, L. Are Solvent and Dispersion Effects Crucial in Olefin Polymerization DFT Calculations? Some Insights from Propylene Coordination and Insertion Reactions with Group 3 and 4 Metallocenes. *ACS Catal*. **2015**, 5, 416–425.
58. Cavasotto, C. **2016**. In Silico Drug Discovery and Design: Theory, Methods, Challenges, and Applications. CRC Press.
59. Chaudhary, K.R. Batchu, S.N. Seubert, J.M. Cytochrome P450 Enzymes and the Heart. *IUBMB Life.* 10, **2009**, pp. 954 – 960.
60. Chiavarino, B. Cipollini, R. Crestoni, M. E. Fornarini, S. Lanucara, F. Lapi, A. Probing the compound I-like reactivity of a bare high-valent oxo iron porphyrin complex: the oxidation of tertiary amines. *J. Am. Chem. Soc*. **2008**, 130, 3208–3217.

61. Chiavarino, B. Crestoni, M.E. Formarini, S., Lanucara, *F. Eur. J. Mass. Spectrom*. **2010**, 7, 407-414.
62. Cho, K.B., Kim, E.J., Seo, M.S., Shaik, S., Nam, W. 2012. Correlating DFT-Calculated Energy barriers to Experiments in Nonheme Octahedral FeIVO Species. *Chem. Eur. J.* **2012,** 18, 10444-10453.
63. Choi, K. Joo, H. Campbell, J.L. Clewell, R.A. Andersen, M.E. Clewell III, H.J. *In Vitro* metabolism of di(2-ethylhexyl) phthalate (DEHP) by various tissues and cytochrome P450s of human and rat. *Toxicology in Vitro*. **2012,** 26, 315 – 322.
64. Choi, Y. Deane, C. FREAD Revisited: Accurate Loop structure prediction using a database search algorithm. *Proteins*. **2009**, 78 (6),1431 – 1440.
65. Chuanprasit, P. Goh, S.H. Hirao, H. Benzyne Formation in the Mechanism-Based Inactivation of Cytochrome P450 by 1-Aminobenzotriazole and N-Benzyl-1-Aminobenzotriazole: Computational Insights. *ACS Catal.* **2015**, 5 (5), 2952–2960
66. Comba, P. Kerscher, M. Computation of structures and properties of transition metal compounds. *Coord. Chem. Rev.* **2009**, 253, 564–574.
67. Cooper, J. Ziegler, T. 2002. A Density Functional Study of SN2 Substitution at Square-Planar Platinum (II) Complexes. *Inorganic Chemistry.* **2002,** 41, 6614 – 6622.
68. Company, A. Gómez, L. Güell, M. Ribas, X. Luis, J. M. Que Jr, L. Costas, M. Alkane Hydroxylation by a Nonheme Iron Catalyst that Challenges the Heme Paradigm for Oxygenase Action. *J. Am. Chem. Soc*. **2007**, 129, 15766–15767.
69. Costas, M.; Mehn, M. P.; Jensen, M. P.; Que Jr, L. Dioxygen Activation at Mononuclear Nonheme Iron Active Sites: Enzymes, Models, and Intermediates. *Chem. Rev*. **2004**, 104, 939–986.
70. Costas, M. Selective C–H Oxidation Catalyzed by Metalloporphyrins. *Coord. Chem. Rev.* **2011**, 255, 2912–2932.
71. Cramer, J. C. **2004**. Essentials of Computational Chemistry: Theories and Models. 2nd Ed. John Wiley and Sons, UK.
72. Crestoni, M. E. Fornarini, S. Probing the cytochrome P450-like reactivity of high-valent oxo iron intermediates in the gas phase. *Inorg. Chem*. **2005**, 44, 5379–5387.

73. Crestoni, M. E. Fornarini, S. Compound I of naked heme (iron protoporphyrin IX). *Inorg. Chem*. **2007**, 46, 9018–9020.
74. Crestoni, M. E. Fornarini, S. Lanucara, F. Oxygen-Atom Transfer by a Naked Manganese (V)–Oxo–Porphyrin Complex Reveals Axial Ligand Effect. *Chem. Eur. J.* **2009**, 15, 7863–7866
75. Crestoni, M. E. Fornarini, S. Lanucara, F. Warren, J. J. Mayer, M. Probing 'Spin-Forbidden'Oxygen-Atom Transfer: Gas-Phase Reactions of Chromium− Porphyrin Complexes. *J. Am. Chem. Soc*. **2010**, 132, 4336–4343.
76. Davidson, E. Feller, D. 1986. Basis Set Selection for Molecular Calculations. *Chem. Rev.* **1986,** 86, 681 -696.
77. Davydov, R.; Perera, R.; Jin, S.; Yang, T.-C.; Bryson, T. A.; Sono, M.; Dawson, J.H.; Hoffman, B. M. Substrate modulation of the properties and reactivity of the oxy-ferrous and hydroperoxo-ferric intermediates of cytochrome P450cam as shown by cryoreduction-EPR/ENDOR spectroscopy. *J. Am. Chem. Soc.* **2005**, 127, 1403–1414.
78. Dawson, J. H. Holm, R. H. Trudell, J. R. Barth, G. Linder, R. E. Bunnenberg, E. Djerassi, C. Magnetic circular dichroism studies. 43. Oxidized cytochrome P-450. Magnetic circular dichroism evidence for thiolate ligation in the substrate-bound form. Implications for the catalytic mechanism. *J. Am. Chem. Soc.* **1976**, 98, 3707–3709.
79. Dawson, J. H. Probing structure-function relations in heme-containing oxygenases and peroxidases. *Science.* **1988**, 240, 433–439.
80. de Visser, S.P. Ogliaro, F. Shaik, S. How Does Ethene Inactivate Cytochrome P450 En Route to Its Epoxidation? A Density Functional Study. *Angew. Chem. Int. Ed*. **2001**, 40, 2871–2874.
81. de Visser, S.P.; Ogliaro, F.; Harris, N.; Shaik, S. Multi-state epoxidation of ethene by cytochrome P450: a quantum chemical study. *J. Am. Chem. Soc.* **2001**, 123, 3037–3047.
82. de Visser, S.P.; Ogliaro, F.; Shaik, S. How does ethene inactivate cytochrome P450 en route to its epoxidation? A density functional study. *Angew. Chem. Int. Ed.* **2001**, 40, 2871–2874.
83. de Visser, S.P.; Ogliaro, F.; Sharma, P.K.; Shaik, S. Hydrogen bonding modulates the selectivity of enzymatic oxidation by P450: a chameleon oxidant behavior of Compound *I. Angew. Chem. Int. Ed.* **2002**, 41, 1947–1951.

84. de Visser, S.P.; Ogliaro, F.; Sharma, P.K.; Shaik, S. What factors affect the regioselectivity of oxidation by cytochrome P450? A DFT study of allylic hydroxylation and double bond epoxidation in a model reaction. *J. Am. Chem. Soc*. **2002**, 124, 11809–11826.
85. de Visser, S. P. Shaik, S. A proton-shuttle mechanism mediated by the porphyrin in benzene hydroxylation by cytochrome P450 enzymes. *J. Am. Chem. Soc*. **2003**, 125, 7413–7424.
86. de Visser, S.P.; Shaik, S.; Sharma, P.K.; Kumar, D.; Thiel, W. Active species of horseradish peroxidase (HRP) and cytochrome P450: two electronic chameleons. *J. Am. Chem. Soc.* **2003**, 125, 15779–15788.
87. de Visser, S.P. Kumar, D. Shaik, S. How do aldehyde side products occur during alkene epoxidation by cytochrome P450? Theory reveals a state-specific multi-state scenario where the high-spin component leads to all side products. *J. Inorg. Biochem.* **2004**, 98, 1183–1193.
88. de Visser, S.P.; Kumar, D.; Cohen, S.; Shacham, R.; Shaik, S. A predictive pattern of computed barriers for C–H hydroxylation by Compound I of cytochrome P450. *J. Am. Chem. Soc.* **2004**, 126, 8362–8363.
89. de Visser, S.P.; Kumar, D.; Neumann, R.; Shaik, S. Computer-generated high-valent iron-oxo and manganese-oxo species with polyoxometalate ligands: how do they compare with the iron-oxo active species of heme enzymes? *Angew. Chem. Int. Ed.* **2004**, 43, 5661–5665.
90. de Visser, S. P. What Factors Influence the Ratio of C-H Hydroxylation Versus C=C Epoxidation by a Nonheme Cytochrome P450 Biomimetic? *J. Am. Chem. Soc*. **2006**, 128, 15809–15818.
91. de Visser, S. P. Substitution of Hydrogen by Deuterium Changes the Regioselectivity of Ethylbenzene Hydroxylation by an Oxo-iron-porphyrin Catalyst. *Chem. Eur. J.* **2006**, 12, 8168–8177.
92. de Visser, S. P. Propene activation by the Oxo-iron active species of Taurine/α-Ketoglutarate Dioxygenase (TauD) enzyme. How does the catalysis compare to heme-enzymes? *J. Am. Chem. Soc.* **2006**, 128, 9813–9824.
93. de Visser, S.P. What external perturbations influence the electronic properties of catalase Compound I? *Inorg. Chem*. **2006**, 45, 9551–9557.

94. De Visser, S.P. Oh, K. Han, A. Nam, W. 2007. Combined Experimental and Theoretical Study on Aromatic Hydroxylation by Mononuclear Nonheme Iron(IV)-Oxo complexes.. *Inorganic Chemistry*, **2007,** 46, 4632-4641.
95. de Visser, S. P. Tan, L.S. Is the bound substrate in nitric oxide synthase protonated or neutral and what is the active oxidant that performs substrate hydroxylation? *J. Am. Chem. Soc.* **2008**, 130, 12961–12974.
96. de Visser, S.P.; Tahsini, L.; Nam, W. How does the axial ligand of cytochrome P450 biomimetics influence the regioselectivity of aliphatic versus aromatic hydroxylation? *Chem. Eur. J.* **2009**, 15, 5577–5587.
97. de Visser, S. P. Trends in substrate hydroxylation reactions by heme and nonheme iron (IV)-oxo oxidants give correlations between intrinsic properties of the oxidant with barrier. *J. Am. Chem. Soc.* **2010**, 132, 1087–1097.
98. de Visser, S.P.; Nam, W. High-valent iron-oxo porphyrins in oxygenation reactions. In Handbook of Porphyrin Science, Kadish, K.M., Smith, K.M., Guilard, R., Eds.; World Scientific Publishing Co.: New Jersey, **2010**, Chapter 44, pp. 85–140, ISBN-13 978-981-4307-23-9.
99. de Visser, S. P. Kumar, D. (Eds). Iron-containing enzymes: Versatile catalysts of hydroxylation reaction in nature, RSC Publishing, Cambridge (UK), **2011**.
100. de Visser, S. P.; Latifi, R.; Tahsini, L.; Nam, W. The Axial Ligand Effect on Aliphatic and Aromatic Hydroxylation by Non-heme Iron(IV)-oxo Biomimetic Complexes. *Chem. Asian J.* **2011**, 6, 493–504.
101. de Visser, S. P. Predictive studies of oxygen atom transfer reactions by Compound I of cytochrome P450: aliphatic and aromatic hydroxylation, epoxidation and sulfoxidation. *Adv. Inorg. Chem.* **2012**, 64, 1–31.
102. de Visser, S. P.; Rohde, J.-U.; Lee, Y.-M.; Cho, J.; Nam, W. Intrinsic Properties and Reactivities of Mononuclear Nonheme Iron–Oxygen Complexes Bearing the Tetramethylcyclam Ligand. *Coord. Chem. Rev*. **2013**, 257, 381–393.
103. de Visser, S. P.; Quesne, M. G.; Martin, B.; Comba, P.; Ryde, U. Computational Modelling of Oxygenation Processes in Enzymes and Biomimetic Model Complexes. *Chem. Commun*. **2014**, 50, 262–282.
104. De Vivo, M. Lodola, A. 2012. The Increasing role of QM/MM in Drug Discovery. *Advances in Protein Chemistry and Structural Biology.* **2012,** 87, 337 – 362.

105. De Vivo, M. Masetti, M. Bottegoni, G. Cavalli, A. 2016. Role of Molecular Dynamics and Related Methods in Drug Discovery. *J. Medicinal Chemistry*. **2016,** 59, 4035 – 4061.

106. Denisov, I.G. Makris, T.M. Sligar, S.G. Schlichting, I. Structure and chemistry of cytochrome P450. *Chem. Rev*. **2005**, 105, 2253–2277.

107. Depaz, I.M.B. Toselli, F. Wilce, P.A. Gillam, E.M.J. Differential Expression of Cythochrome P450 Enzymes from the CYP2C Subfamily in the Human Brain. *Drug Metabolism and Disposition.* **2015**, 43, 353 – 357.

108. Dill, K. Broomberg, S. 2002. Molecular Driving Forces: Statistical Thermodynamics in Chemistry and Biology. Garland. *Science,* USA **2002**.

109. Ditchfield, R.; Hehre, W. J.; Pople, J. A. Self-Consistent Molecular-Orbital Methods. IX. An Extended Gaussian-Type Basis for Molecular-Orbital Studies of Organic Molecules. *J. Chem. Phys*. **1971**, *54*, 724–728.

110. Dolinski, T. Czodrowski P, Li H, Nielsen JE, Jensen J.H, Klebe G, Baker N.A. PDB2PQR: Expanding and upgrading automated preparation of biomolecular structures for molecular simulations. *Nucleic Acids Res,* 35, W522-5, 2007.

111. Domyati, D. Hope, S. L. Latifi, R. Hearns, M. D. Tahsini, L. Cu(I) Complexes of Pincer Pyridine-Based N-Heterocyclic Carbenes with Small Wingtip Substituents: Synthesis and Structural and Spectroscopic Studies. *Inorg. Chem*. **2016**, 55, 11685–11693.

112. Evans, W. Relling, M. 1999. Pharmacogenomics: Translating Functional Genomics into Rational Therapeutics. *Science.* **1999,** 286**,** 487 – 491.

113. Eyring, H. 1935. The Activated Complex in Chemical Reactions. *Journal of Chemical Physics.* **1935,** 3, 107 - 115.

114. Falnes, P. Ø.; Johansen, R. F.; Seeberg, E. AlkB-mediated Oxidative Demethylation Reverses DNA Damage in Escherichia coli. *Nature*. 2002, 419, 178–182.

115. Faponle, A. Quesne, M. Sastri, C., Banse, F., de Visser, S. Differences and Comparisons of the Properties and Reactivities of Iron(III)-Hydroperoxo Complexes with Saturated Coordination Sphere. *Chem. Eur. J.* **2015,** 21, 1221-1236.

116. Faponle, A.S. Quesne, M. de Visser, S.P. Origin of the Regioselective Fatty Acid Hydroxilation versus Decarboxylation by a Cytochrome P450 Peroxygenase: What drives the Reaction to Biofuel Production? *Chem. Eur. J.* **2016**, 22, 16, 5478 – 5483.

117. Faponle, A. S.; Seebeck, F. P.; de Visser, S. P. Sulfoxide Synthase versus Cysteine Dioxygenase Reactivity in a Nonheme Iron Enzyme. *J. Am. Chem. Soc*. **2017**, *139*, 9259–9270.

118. FDA. (2015). The Drug Development Process. 2017, from FDA webpage: https://www.fda.gov/forpatients/approvals/drugs/

119. Fetzner, S. Steiner, R. A. Cofactor-independent oxidases and oxygenases. *Appl. Microbiol. Biotechnol*. **2010**, 86, 791–804.

120. Feyereisen, R. Weck-Reichhart, D. 2000. Cytochromes P450: A success story. *Genome Biology*. **2000,** 1, 3003.1-3003.9.

121. Fisser, A. Sali, A.. ModLoop: automated modelling of loops in protein structures. *Bioinformatics.* **2003**, 19 (18), 2500 – 2501.

122. Flanigan, D.M. Romanov-Michailidis, F. White, N.A. Rovis, T. Organocatalytic Reactions Enabled by N-Heterocyclic Carbenes. *Chem. Rev*. **2015**, 115, 9307–9387.

123. Ford, K. Ryslik, G. Sodhi, J. Halladay, J. Diaz, D. Dambach, D. Masuda, M. 2015. Computational Predictions of the Site of Metabolism of Cytochrome P450 2D6 substrates: Comparative Analysis, molecular docking, bioactivation and toxicological implications. *Drug Met. Review.* **2015,** 47, 291 - 319.

124. Franzus, B. Snyder, E.I. A Solvent-Sensitive Rearrangement of 7-Substituted Norbornadienes to Cycloheptatriene Using Complex Hydrides. *J.Am.Chem.Soc.* **1963**, 85, 3902–3903.

125. Friedrich, L. E. The two hydrogen-oxygen bond-dissociation energies of hydroquinone. *J. Org. Chem*. **1983**, *48*, 3851–3852.

126. Frisch, M. J.; Trucks, G. W.; Schlegel, H. B.; Scuseria, G. E.; Robb, M. A.; Cheeseman, J. R.; Scalmani, G.; Barone, V.; Mennucci, B.; Petersson, G. A.; Nakatsuji, H.; Caricato, M.; Li, X.; Hratchian, H. P.; Izmaylov, A. F.; Bloino, J.; Zheng, G.; Sonnenberg, J. L.; Hada, M.; Ehara, M.; Toyota, K.; Fukuda, R.; Hasegawa, J.; Ishida, M.; Nakajima, T.; Honda, Y.; Kitao, O.; Nakai, H.; Vreven, T.; Montgomery, J. A., Jr.; Peralta, J. E.; Ogliaro, F.;

Bearpark, M.; Heyd, J. J.; Brothers, E.; Kudin, K. N.; Staroverov, V. N.; Kobayashi, R.; Normand, J.; Raghavachari, K.; Rendell, A.; Burant, J. C.; Iyengar, S. S.; Tomasi, J.; Cossi, M.; Rega, N.; Millam, J. M.; Klene, M.; Knox, J. E.; Cross, J. B.; Bakken, V.; Adamo, C.; Jaramillo, J.; Gomperts, R.; Stratmann, R. E.; Yazyev, O.; Austin, A. J.; Cammi, R.; Pomelli, C.; Ochterski, J. W.; Martin, R. L.; Morokuma, K.; Zakrzewski, V. G.; Voth, G. A.; Salvador, P.; Dannenberg, J. J.; Dapprich, S.; Daniels, A. D.; Farkas, Ö.; Foresman, J. B.; Ortiz, J. V.; Cioslowski, J.; Fox, D. J. Gaussian, Inc., Wallingford CT, **2009**.

127. Fujikura, K.; Ingelman-Sundberg, M.; Lauschke V. Genetic variation in the human cytochrome P450 supergene family. *Pharmacogenetics Genomics,* **2015**, 12, 584–594.

128. Fukuzumi, S. Kotani, H. Lee, Y.M. Nam, W. Sequential Electron-Transfer and Proton-Transfer Pathways in Hydride-Transfer Reactions from Dihydronicotinamide Adenine Dinucleotide Analogues to Non-heme Oxoiron(IV) Complexes and p-Chloranil. Detection of Radical Cations of NADH Analogues in Acid-Promoted Hydride-Transfer Reactions. *J.Am.Chem.Soc.* **2008**, 130, 15134-15142.

129. Furci, L. Lopes, P. Eakanunkul, S. Zhong, S. MacKerell, A. Wilks, A. Inhibition of the Bacterial Heme Oxygenases from Pseudomonas aeruginosa and Neisseria meningitidis: Novel Antimicrobial Targets. *J. Med. Chem.* **2007,** 50, 3804 – 3813.

130. Geng, C. Y. Ye, S. F. Neese, F. Analysis of Reaction Channels for Alkane Hydroxylation by Nonheme Iron(IV)–Oxo Complexes. *Angew. Chem. Int. Ed*. **2010**, 49, 5717–5720.

131. Gholap, R. Kut, O. Bourne, J. Hydroformylation of Propylene using an unmodified cobalt carbonyl catalyst: a Kinetic study. *Ind. Eng. Chem. Res,* **1992**, 31 (7), 1597-1601.

132. Ghosh, A.; Taylor, P. R. High-Level Ab Initio Calculations on the Energetics of Low-Lying Spin States of Biologically Relevant Transition Metal Complexes: A First Progress Report. *Curr. Opin. Chem. Biol*. **2003**, 7, 113–124.

133. Goldberg, D. P. Corrolazines: New frontiers in high-valent metalloporphyrinoid stability and reactivity. *Acc. Chem. Res.* **2007**, 40, 626–634.

134. Goodin, D. B. McRee, D. E. The Asp-His-iron triad of cytochrome c peroxidase controls the reduction potential electronic structure, and coupling of the tryptophan free radical to the heme. *Biochemistry* **1993**, 32, 3313–3324.

135. Gosh, C. Hossain, M. Solanki, J. Dadas, A. Marchi, N. Janigro, D. Pathophysiological implications of neurovascular P450 in brain disorders. *Drug Discovery Today,* **2016,** 21 (10), 1609 – 1619.

136. Grant, J.L.; Hsieh, C.H.; Makris, T.M. Decarboxylation of fatty acids to terminal alkenes by cytochrome P450 compound I. *J. Am. Chem. Soc.* **2015**, 137, 4940–4943.

137. Green, M. T. Evidence for sulfur-based radicals in thiolate compound I intermediates. *J. Am. Chem. Soc*. **1999**, 121, 7939–7940

138. Grimme, S. Semiempirical Hybrid Density Functional with Perturbative Second-order Correlation. *J. Chem. Phys*. **2006**, 124, 034108.

139. Grimme, S. Anthony, J. Ehrlich, S. Krieg, H. 2010. A consistent and accurate ab initio parameterization of density functional dispersion correction (DFT-D) for the 94 elements H-Pu. *J. Chem. Phys*., **2010,** 132,154104.

140. Grimme, S. Density Functional theory with London Dispersion corrections. *Computational Molecular Science.* **2011**, 1, 211 – 228.

141. Grocholski, T. Koskiniemi, H. Lindqvist, Y. Mantsala, P. Niemi, J. Schneider, G. 2010. Crystal Structure of the Cofactor-Independent Monooxygenase SnoaB from Streptomyces nogalater: Implications for the Reaction Mechanism. *Biochemistry*. **2010,** 49, 934 - 944.

142. Grogan, G. Cytochromes P450: exploiting diversity and enabling application as biocatalysts. *Curr. Opin. Chem. Biol.* **2011**, 15, 241–248.

143. Grosdidier, A. Zoete, V. Michielin, O. 2011. SwissDock, a small-protein molecule docking web service based on EADock DSS. *Nucleic Acid Res.* 39, W272.

144. Groves, J.T. Key elements of the Chemistry of Cytochrome P-450: The Oxygen Rebound Mechanism. *J. of Chem. Educ.* **1985**, 62(11), 928 – 931.

145. Groves, J.T. The bioinorganic chemistry of iron in oxygenases and supramolecular assemblies. *Proc. Natl. Acad. Sci*. USA, **2003**, 100, 3569–3574.

146. Guengerich, F.P.; Kim D.H. Enzymic oxidation of ethyl carbamate to vinyl carbamate and its role as an intermediate in the formation of 1,N6-ethenoadenosine. *Chem. Res. Toxicol.* **1991**, 4, 413–421.

147. Guengerich, F.P. Common and Uncommon Cytochrome P450 Reactions Related to Metabolism and Chemical Toxicity. *Chem. Res. Toxicol,* **2001**, 14, 611 – 650.

148. Guengerich, F.P., Kelly, S.L., Waterman, M.R., Lamb, D.C. Cytochromes P450 and drug discovery. *Current Opinion in Biotechnology.* **2007**, 18, 504-512.

149. Gupta, S. 1987. QSAR Studies on Enzyme Inhibitors. *Chem. Rev.* **1987,** 87, 1183 - 1253.

150. Güell, M.; Luis, J. M.; Solà, M.; Swart, M. Importance of the Basis Set for the Spin-state Energetics of Iron Complexes. *J. Phys. Chem. A.* **2008**, 112, 6384–6391.

151. Haag, W. Yao, D. 1992. Rate constants for Reaction of Hydroxyl Radicals with Several Drinking Water Contaminants. *Environmental Science Technology*. **1992,** 26, 1005-1013.

152. Habershon, S. Automated Predicted of Catalytic Mechanism and Rate Law Using Graph-Based Reaction Path Sampling. *J. Chem. Theory Comput,* **2016,** 12, 1786 1798.

153. Harvey, J. 2009. *Ab Initio* Transition State Theory for polar reactions in Solution. *Faraday Discussions.* **2010,** 145, 487 - 505.

154. Hay, P. J.; Wadt, W. R. Ab initio Effective Core Potentials for Molecular Calculations. Potentials for the Transition Metal Atoms Sc to Hg. *J. Chem. Phys*. **1985**, 82, 270–283.

155. Hehre, W., Stewart, R., Pople, J. **1969**. Self-Consistent Molecular-Orbital Methods. I. Use of Gaussian Expansions of Slater Type Atomic Orbitals.

156. Hehre, W. J. Ditchfield, R. Pople, J. A. Self—Consistent Molecular Orbital Methods. XII. Further Extensions of Gaussian—Type Basis Sets for

Use in Molecular Orbital Studies of Organic Molecules. *J. Chem. Phys.* **1972**, 56, 2257–2261.

157. Hernández-Ortega, A.; Quesne, M. G.; Bui, S.; Heuts, D. P. H. M.; Steiner, R. A.; Heyes, D. J.; de Visser, S. P.; Scrutton, N. S. Origin of the proton-transfer step in the cofactor-free (1H)-3-hydroxy-4-oxoquinaldine 2,4-dioxygenase: effect of the basicity of an active site His residue. *J. Biol. Chem.* **2014**, 289, 8620–8632

158. Hernández-Ortega, A.; Quesne, M. G.; Bui, S.; Heyes, D. J.; Steiner, R. A.; Scrutton, N. S.; de Visser, S. P. Catalytic Mechanism of Cofactor-Free Dioxygenases and How They Circumvent Spin-Forbidden Oxygenation of Their Substrates. *J. Am. Chem. Soc.* **2015**, 137, 7474–7487.

159. Hersleth, H.P. Ryde, U. Rydberg, P. Görbitz, C.H. Andersson, K.K. Structures of the high-valent metal-ion haem-oxygen intermediates in peroxidases, oxygenases and catalases. *J. Inorg. Biochem.* **2006**, 100, 460–476.

160. Himo, F. Recent Trends in Quantum Chemical Modelling of Enzymatic Reactions. *J. Am. Chem. Soc.* **2017**, 139, 6780 – 6786.

161. Hirao, H. Kumar, D. Que Jr., L. Shaik, S. Two-State Reactivity in Alkane Hydroxylation by Non-Heme Iron−Oxo Complexes. *J. Am. Chem. Soc*. **2006**, 128, 8590–8606.

162. Hitzenberger, M.; Hofer, T. S. Probing the range of applicability of structure- and energy-adjusted QM/MM link bonds. *J. Comput. Chem*. **2015**, *36*, 1929–1939.

163. Hratchian, H. P.; Parandekar, P. V.; Raghavachari, K.; Frisch, M. J.; Vreven, T. QM:QM electronic embedding using Mulliken atomic charges: Energies and analytic gradients in an ONIOM framework. *J. Chem. Phys*. **2008**, *128*, 034107.

164. Hunter, S.G. NIST Chemistry Webbook, NIST Standard Reference Database, Number 69; Eds.: P. J. Linstrom, W. G. Mallard, National Institute of Standards and Technology: Gaithersburg MD, 20899, (retrieved June 7, **2017**), http://webbook.nist.gov.

165. Hollmann, F. Arends, I. W. C. E. Buehler, K. Schallmey, A. Bühler, B. Enzyme-mediated oxidations for the chemist. *Green Chemistry*. 2011, 13, 226–265.

166. Hopkinson, M. N. Richter, C. Schedler, M. Glorius, F. An Overview of N-heterocyclic carbenes. *Nature.* **2014**, 510, 485–496.

167. Huang, X.; Groves, J. T. Beyond ferryl-mediated hydroxylation: 40 years of the rebound mechanism and C–H activation. *J. Biol. Inorg. Chem*. **2017**, *22*, 185–207.

168. Ingelman-Sundberg, M. Rodriguez-Antona, C. Pharmacogenetics of drug-metabolizing enzymes: implications for a safer and more effective drug therapy. *Philos. Trans. R. Soc. Lond. Biol. Sci.* **2005**, 29(360), pp. 1563 – 1570.

169. İşci, Ü. Faponle, A. S. Afanasiev, P. Albrieux, F. Briois, V. Ahsen, V. Dumoulin, F. Sorokin, A. B. de Visser, S. P. Site-selective formation of an iron(IV)–oxo species at the more electron-rich iron atom of heteroleptic μ-nitrido diiron phthalocyanines. *Chem. Sci.* **2015**, 6, 5063–5075.

170. Jackson, T. A. Rohde, J.U. Seo, M. S.; Sastri, C. V.; DeHont, R. Stubna, A. Ohta, T. Kitagawa, T. Münck, E. Nam, W. Que Jr, L. Axial Ligand Effects on the Geometric and Electronic Structures of Nonheme Oxoiron(IV) Complexes. *J. Am. Chem. Soc*. **2008**, 130, 12394–12407.

171. Jacobi, D. Abraham,W. Pischel, U. Gubert, L. Stosser, R. Schnabel, J. Oxidation of aryl-substituted cycloheptatrienes by photoinduced electron transfer. *J.Chem.Soc.Perkin.Trans.* **1999**, 2, 1695-1702.

172. Jana, K. Bandyopadhyay, T. Ganguly, B. Setereoselective Metabolism of Omeprazole by Cythocrome P450 2C19 and 3A4: Mechanistic Insights from DFT Study. *J. Phys. Chem. B.* **2018**, 122, 5765 – 5775.

173. Jeong, Y.J. Kang, Y.Han, A.R. Lee, Y.M. Kotani, H.Fukuzumi,S. Nam, W. Hydrogen Atom Abstraction and Hydride Transfer Reactions by Iron(IV)–Oxo Porphyrins*. *Angew. Chem. Int. Ed.* 2008, 47, 7321-7324.

174. Ji, L. Faponle, A. S. Quesne, M. G. Sainna, M. A. Zhang, J. Franke, A. Kumar, D. Van Eldik, R. Liu, W. de Visser, S. P. Drug metabolism by cytochrome p450 enzymes: what distinguishes the pathways leading to substrate hydroxylation over desaturation? *Chem. Eur. J.* **2015**, 21, 9083–9092.

175. Ji, L. Franke, A. Brindell, M. Oszaica, M. Zahl, A. van Eldik, R. *Chem. Eur. J.* Combined Experimental and Theoretical Study on the Reactivity of Compounds I and II in Horseradish Peroxidase Biomimetics. **2014**, 20, 14437-14450.

176. Johnson, E. Stout, D. Structural Diversity of Eukaryiotic Membrane Cytochrome P450s. *The Journal of Biological Chemistry*. **2013**, 288, 17082-17090.

177. Joseph, C. A.: Maroney, M. J. Cysteine dioxygenase: Structure and mechanism. *Chem. Commun*. **2007**, 3338–3349.

178. Kadish, K.M. Smith K.M. Guilard, R. (Eds.) Handbook of Porphyrin Science. World Scientific: New Jersey, **2010**.

179. Kaizer, J.; Klinker, E. J.; Oh, N. Y.; Rohde, J.-U.; Song, W. J.; Stubna, A.; Kim, J.; Münck, E.; Nam, W.; Que, L., Jr. Nonheme FeIVO Complexes that Can Oxidize the C-H Bonds of Cyclohexane at Room Temperature. *J. Am. Chem. Soc*. **2004**, 126, 472-473.

*180.* Kamachi, T. Yoshizawa, K. A Theoretical Study on the Mechanism of Camphor Hydroxylation by Compound I of Cytochrome P450. *J. Am. Chem. Soc*. **2003**, 125, 4652*–4661*.

181. Kang, Y. Chen, H. Jeong, Y. J. Lai, W. Bae, E. H. Shaik, S. Nam, W. Enhanced Reactivities of Iron (IV)-Oxo Porphyrin π-Cation Radicals in Oxygenation Reactions by Electron-Donating Axial Ligands. *Chem. Eur. J.* **2009**, 15, 10039–10046.

182. Karamzadeh, B.; Kumar, D.; Sastry, G.N.; de Visser, S.P. Steric factors override thermodynamic driving force in regioselectivity of proline hydroxylation by prolyl-4-hydroxylase enzymes. *J. Phys. Chem.* A **2010**, 114, 13234–13243.

183. Karlsson, A. Parales, J. V. Parales, R. E. Gibson, D. T. Eklund, H. Ramaswamy, S. Crystal structure of naphthalene dioxygenase: side-on binding of dioxygen to iron. *Science* **2003**, 299, 1039–1042.

184. Kästner, J. Thiel, S. Senn, H. Sherwood, P. Thiel, W. Exploiting QM/MM Capabilities in Geometry Optimization: A Microiterative Approach Using Electrostatic Embedding. *J. Chem. Theory Comput*. **2007**, 3, 1064-1072

185. Katzung, B.G. Masters, S.B. Trevor, A.J. Basic & Clinical Pharmacology. Twelfth Edition. **2012**, USA, McGraw Hill Medical.

186. Kaur, P. Chamberlain, A. Poulos, T. Sevrioukova, I. Structure-Based Inhibitor Design for Evaluation of a CYP3A4 Pharmacophore Model. *J. Med. Chem.* **2016**, 59, 9, 4210 – 4220.

187. Kendrew, S. G.; Hopwood, D. A.; Marsh, E. N. G. Identification of a monooxygenase from Streptomyces coelicolor A3(2) involved in biosynthesis of actinorhodin: purification and characterization of the recombinant enzyme. *J. Bacteriol.* **1997**, 179, 4305–4310.

188. Kim, S.C. Yoon, H.J. Lee, J.W. Yu, J. Park, E.S.Chi, S.C. Investigation of the release behavior of DEHP from infusion sets by paclitaxel-loaded polymeric micelles. *Int. J. Pharm.* **2005**, 293, 303-3010.

189. Kirchmair, J. Williamson, M. Tzyack, J. Tan, L. Bond, P. Bender, A. Glen, R. 2012. Computational Prediction of Metabolism: Sites, Products, SAR, P450 Enzyme Dynamics, and Mechanisms. *J. Chem. Inf. Model.* **2012,** 52, 617 - 648.

190. Kleipis, J. Introduction to First-Principles Electronic Structure Methods: Application to Actinide Materials. *Journal of Materials Research.* **2006**. UCRL-JRNL-221153.

191. Klingenberg, M. Pigments of Rat Liver Microsomes. *Archieves of Biochemistry and Physics.* **1958**, 75, 376-386.

192. Koch, W. Holthausen, M. A Chemist's Guide to Density Functional Theory. Second edition. **2001**. Wiley-VCH Verlag GmbH.

193. Kovaleva, E. G.; Lipscomb, J. D. Versatility of Biological Non-heme Fe(II) Centers in Oxygen Activation Reactions. *Nat. Chem. Biol*. **2008**, 4, 186–193.

194. Kralj, M.; Uzelac, L.; Wang, Y.-H.; Wan, P.; Tireli, M.; Mlinarić-Majerski, K.; Piantanida, I.; Basarić, N. Enhancement of antiproliferative activity by phototautomerization of anthrylphenols. *Photochem. Photobiol. Sci*. **2015**, *14*, 1082–1092.

195. Krebs, C.; Fujimori, D. G.; Walsh, C. T.; Bollinger Jr, J. M. Non-Heme Fe(IV)–Oxo Intermediates. *Acc. Chem. Res*. **2007**, *40*, 484–492.

196. Krechkivska, O. Wilcox, C. O'Connor, G. D. Nauta, K. Kable, S. H. Schmidt, T. W. Ionization Energies of Three Resonance-Stabilized Radicals: Cyclohexadienyl (dn, n = 0, 1, 6, 7), 1-Phenylpropargyl, and Methylcyclohexadienyl. *J. Phys. Chem. A.* **2014**, 118, 10252−10258.

197. Kryatov, S. V.; Rybak-Akimova, E. V.; Schindler, S. Kinetics and Mechanisms of Formation and Reactivity of Non-heme Iron Oxygen Intermediates. *Chem. Rev*. **2005**, 105, 2175–2226.

198. Kuhnel, K. Ke, N. Cryle, M. J. Sligar, S. G. Schuler, M. A. Schlichting, I. Crystal structures of substrate-free and retinoic acid-bound cyanobacterial cytochrome P450 CYP120A1. *Biochemistry*. **2008**, 47, 6552–6559.

199. Kumar, D.; de Visser, S. P.; Sharma, P. K.; Cohen, S.; Shaik, S. Radical Clock Substrates, Their C–H Hydroxylation Mechanism by Cytochrome P450, and Other Reactivity Patterns: What Does Theory Reveal About the Clocks' Behavior? *J. Am. Chem. Soc.* **2004**, 126, 1907–1920.

200. Kumar, D.; de Visser, S.P.; Shaik, S. Oxygen economy of cytochrome P450: what is the origin of the mixed functionality as a dehydrogenase–oxidase enzyme compared with its normal function? *J. Am. Chem. Soc.* **2004**, 126, 5072–5073.

201. Kumar, D.; de Visser, S. P.; Sharma, P. K.; Hirao, H.; Shaik, S. Sulfoxidation Mechanisms Catalyzed by Cytochrome P450 and Horseradish Peroxidase Models: Spin Selection Induced by the Ligand. *Biochemistry* **2005**, 44, 8148–8158.

202. Kumar, D.; de Visser, S.P.; Shaik, S. Multistate reactivity in styrene epoxidation by Compound I of cytochrome P450: mechanisms of products and side products formation. *Chem. Eur. J.* **2005**, 11, 2825–2835.

203. Kumar, H. Hirao, L. Que Jr., S. Shaik, Theoretical Investigation of C− H Hydroxylation by (N4Py) FeIV O2+: An Oxidant More Powerful than P450? *J. Am. Chem. Soc.* **2005**, 127, 8026–8027.

204. Kumar, D.; Tahsini, L.; de Visser, S. P.; Kang, H. Y.; Kim, S. J.; Nam, W. Effect of Porphyrin Ligands on the Regioselective Dehydrogenation Versus Epoxidation of Olefins by Oxoiron(IV) Mimics of Cytochrome P450. *J. Phys. Chem*. A. **2009**, 113, 11713–11722.

205. Kumar, D. Karamzadeh, B. Sastry, G.N. de Visser, S.P. What factors influence the rate constant of substrate epoxidation by compound I of cytochrome P450 and analogous iron (IV)-oxo oxidants? *J. Am. Chem. Soc*. **2010**, 132, 7656–7667.

206. Kumar, D.; Sastry, G. N.; de Visser, S. P. Effect of the Axial Ligand on Substrate Sulfoxidation Mediated by Iron(IV)-oxo Porphyrin Cation Radical Oxidants. *Chem. Eur. J.* **2011**, 17, 6196–6205.

207. Kumar, D. Sastry, N. De Visser, SP. Axial Ligand effect on the Rate constant of Aromatic Hydroxylation by Iron(IV)-Oxo complexes Mimicking Cytochrome P450 Enzymes. *J. Phys. Chem,* **2012**, 116, 718 – 730.

208. Kumar, D. Latifi, R. Kumar, S. Rybak-Akimova, E. V. Sainna, M.A. de Visser, S.P. Rationalization of the Barrier Height for pZ-styrene Epoxidation by Iron (IV)-Oxo Porphyrin Cation Radicals with Variable Axial Ligands. *Inorg. Chem*. **2013**, 52, 7968–7979.

209. Kumar, S.; Faponle, A. S.; Barman, P.; Vardhaman, A. K.; Sastri, C. V.; Kumar, D.; de Visser, S. P. Long-Range Electron Transfer Triggers Mechanistic Differences Between Iron(IV)-Oxo and Iron(IV)-Imido Oxidants. *J. Am. Chem. Soc*. **2014**, 136, 17102–17115.

210. Kurahashi, T. Hada, M. Fujii, H. Critical role of external axial ligands in chirality amplification of trans-cyclohexane-1, 2-diamine in salen complexes. *J. Am. Chem. Soc*. **2009**, 131, 12394–12405.

211. Laberstrom, P. Persson, B.A. 1984. Determination of Omeprazole and Metabolites in Plasma and Urine By Liquid Chromatography. *Journal of Chromatography*. **1984**, 309, 347 - 356.

212. Lai, W. Chen, H. Matsui, T. Omori, K. Unno, M. Ikeda-Saito, M. Shaik, S. 2010. Enzymatic Ring-Openning Mechanism of Verdoheme by Heme Oxygenase: A combined X-ray Crystallography and QM/MM Study. *J.Am. Chem. Soc.* **2010**, 132, 12960 – 12970.

213. Lamb, D.C. Lei, L. Warrillow, A.G.S., Lepesheva, G. Mullins, J. Waterman, M.R. Kelly, S.L. The First Virally Encoded Cytochrome P450. *J. Virol.* **2009,** *83(16),* 8266 -8269.

214. Lanucara, F. Crestoni, M. E. Biomimetic Oxidation Reactions of a Naked Manganese (V)–Oxo Porphyrin Complex. *Chem. Eur. J.* **2011**, 17, 12092–12100.

215. Latifi, R.; Bagherzadeh, M.; de Visser, S. P. Origin of the Correlation of the Rate Constant of Substrate Hydroxylation by Nonheme Iron(IV)–oxo Complexes with the Bond-Dissociation Energy of the C-H Bond of the Substrate. *Chem. Eur. J.* **2009**, *15*, 6651–6662.

216. Latifi, R. Valentine, J.S. Nam, W. de Visser, S.P. Predictive studies of H-atom abstraction reactions by an iron(iv)-oxo corrole cation radical oxidant. *Chem. Co*mm. **2012**, 48, 3491-3493.

217. Latifi, R. Sainna, M.A. Rybak-Akimova, E.V. de Visser, S.P. Does Hydrogen-Bonding Donation to Manganese(IV)–Oxo and Iron(IV)–Oxo Oxidants Affect the Oxygen-Atom Transfer Ability? A Computational Study. *Chem. Eur. J.* **2013**, 19, 4058–4068.

218. Lauschke, V., Ingelman-Sundberg, M., Fujikura, K. Genetic Variation in the human Cytochrome P450 supergene family. *Pharmacogenetics and Genomics*, **2015**, 12, 584-94.

219. Lee, C.; Yang, W.; Parr, R. G. Development of the Colle-Salvetti Correlation-energy Formula into a Functional of the Electron Density. *Phys. Rev*. B **1988**, 37, 785–789.

220. Li, X. Energy-Represented Direct Inversion in the Iterative Subspace within Hybrid Geometry Optimization Method. *J. Chem. Theory. Comput.* **2006**, 2, 835 – 839.

221. Li, D. Wang, Y. Han, K. Recent density functional theory model calculations of drug metabolism by cytochrome P450. *Coord. Chem. Rev*. **2012**, 256, 1137–1150.

222. Li, X.-X.; Postils, V.; Sun, W.; Faponle, A.S.; Solà, M.; Wang, Y.; Nam, W.; de Visser, S.P. Reactivity patterns of (protonated) Compound II and Compound I of Cytochrome P450: Which is the better oxidant? *Chem. Eur. J.* **2017**, 23, 6406–6418.

223. Lide, D.R. CRC Handbook of Chemistry and Physics, 90th Ed., Internet Version **2010**.

224. Lin, H. Truhlar, D. 2006. QM/MM: What have we learned, where are we, and where do we go from here? *Theoretical Chemmical Acc.* **2007,** 117, 185 – 199.

225. Lohmann, W. Karst, U. 2008. Biomimmetic modelling of oxidative drug metabolism. *Anal Bioanal Chem.* **2008,** 391, 70-96.

226. Lonsdale, R.; Harvey, J. N.; Mulholland, A. J. Inclusion of Dispersion Effects Significantly Improves Accuracy of Calculated Reaction Barriers for Cytochrome P450 Catalyzed Reactions. J. Phys. *Chem. Lett.* **2010**, 1, 3232–3237.

227. Lonsdale, R. Mulholland, A.J. QM/MM modellingof drug-metabolizing enzymes. *Curr Top Med Chem.* **2014**, 14(11), 1339-1347.

228. Luben, M. Meetsma, A. Wilkinson, E. Feringa, B. Que, L. 1995. Nonheme Iron Centers in Oxygen Activation: Characterization of an Iron-(III) Hydroperoxyde Intermediate. *Angew. Chem. Int. Ed. Engl.* **1995,** 34, 13-14.

229. Lundemo, M.T., Woodley, J.M. 2015. Guidelines for Development and Implementation of Biocatalytic P450 Processes. *Appl Microbiol and Biotechnol.* **2015,** 99, 2465-2483.

230. Machovina, M. M.; Usselman, R. J.; DuBois, J. L. Monooxygenase Substrates Mimic Flavin to Catalyze Cofactorless Oxygenations. *J. Biol. Chem*. **2016**, *291*, 17816–17828.

231. Mandal, D. Shaik, S. Interplay of Tunneling, Two-State Reactivity, and Bell-Evans-Polanyi Effects in C-H Activation by Nonheme Fe(IV)O Oxidants.. *J. Am. Chem. Soc*. **2016**, 138, 2094–2097.

232. Mansuy, D. 2007. A brief history of the contribution of metalloporphyrin models to cytochrome P450 chemistry and oxidation catalysis. *Comptes Rendus Chemie*. **2007**, 10, 392-413.

233. Marenich, A. Cramer, C. Truhlar, D. 2009. Universal Solvation Model Based on Solute Electron Density and on a Continuum Model of The Solvent Defined by the Bulk Dielectric Constant and Atomic Surface Tensions. *J. Phys. Chem.* **2009,** 113, 6378 – 6396.

234. Martin, R.L., Hay, P.J., Pratt, L.R. **1998**. Hydrolysis of Ferric Ion in Water and Conformational Equilibrium.

235. Martinho, M. Banse, F. Bartoli, J.F. Mattioli, T.A. Battioni, P. Horner, O. Bourcier, S. Girerd, J. New Example of a Non-Heme Mononuclear Iron(IV) Oxo Complex. Spectroscopic Data and Oxidation Activity. *Inorg. Chem.* **2005**, 44, 9592–9596.

236. Mayer, J. M. Hydrogen Atom Abstraction by Metal− Oxo Complexes: Understanding the Analogy with Organic Radical Reactions. *Acc. Chem. Res.* **1998**, 31, 441–450.

237. Mayer, J. M. Proton-coupled electron transfer: a reaction chemist's view. *Annu. Rev. Phys. Chem*. **2004**, 55, 363–390.

238. McDonald, A. R.; Que Jr, L. High-valent Nonheme Iron-oxo Complexes: Synthesis, Structure, and Spectroscopy. *Coord. Chem. Rev*. **2013**, 257, 414–428.

239. McIntosh, J.A. Farwell, C.C. Arnold, F.H. 2014. Expanding P450 catalytic reaction space through evolution and engineering. *Current Opinion in Chemical Biology*. **2014,** 19, 126-134.

240. Mekmouche, Y. Ménage, S. Toia-Duboc, C. Fontecave, M. Galey, J. B. Lebrun, C. Pécaut, H2O2-Dependent Fe-Catalyzed Oxidations: Control of the Active Species. *Angew. Chem. Int. Ed*. **2001**, 40, 949–952.

241. M. Meot-Ner, In Gas Phase Ion Chemistry, Ed.: M. T. Bowers, Academic Press, New York, 1979; Vol. 1

242. Meunier, B.; de Visser, S. P.; Shaik, S. Mechanism of Oxidation Reactions Catalyzed by Cytochrome P450 Enzymes. *Chem. Rev*. **2004**, 104, 3947–3980.

243. Morris, G. M., Huey, R., Lindstrom, W., Sanner, M. F., Belew, R. K., Goodsell, D. S. and Olson, A. J. (2009) Autodock4 and AutoDockTools4: automated docking with selective receptor flexiblity. *J. Computational Chemistry*. **2009,** 16, 2785-2791.

244. Muller, K.; Wiegrebe, W.; Younes, M. Formation of Active Oxygen Species by Dithranol, III Dithranol, Active Oxygen Species and Lipid Peroxidation in vivo. *Arch. Pharm*. **1987**, *320*, 59–66.

245. Müller, K. Antipsoriatic and proinflammatory action of anthralin: Implications for the role of oxygen radicals *Biochem. Pharmacol.* **1997**, *53*, 1215–1221.

246. Munro, A. W. Girvan, H. M. McLean, K. J. Variations on a (t) heme—novel mechanisms, redox partners and catalytic functions in the cytochrome P450 superfamily. *Nat. Prod. Rep.* **2007**, 24, 585–609.

247. Murray, M. 2000. Mechanisms of Inhibitory and Regulatory Effects of Methylenedioxophenyl Compounds on Cytochrome P450 dependent Drux Oxidation. *Current Drug Metabolism.* **2000,** 1, 67 – 84.

248. Muster W. Breidenbach, A. Fischer, H. Kirchner, S. Muller, L. Pahler, A. Computational Toxicology in Drug Development. *Drug Discovery Today.* **2008**, 13, 303 -310.

249. Nam, W. High-Valent Iron(IV)–Oxo Complexes of Heme and Non-Heme Ligands in Oxygenation Reactions. *Acc. Chem. Res.* **2007**, 40, 522–531.

250. Nam, W.; Lee, Y.-M.; Fukuzumi, S. Tuning Reactivity and Mechanism in Oxidation Reactions by Mononuclear Nonheme Iron(IV)-Oxo Complexes, *Acc. Chem. Res.* **2014**, 47, 1146–1154.

251. Nambu, S. Matsui, T. Goulding, C. Takahashi, S. Ikeda-Saito, M. 2013. A new Way to Degrade Heme: The Mycobacterium Tuberculosis Enzyme MhuD Catalyzes Heme Degradation without Generating CO. *Journal of Biological Chemistry.* **2013,** 14, 10101 – 10109.

252. Neese, F. ORCA. 2.9 ed. Bonn, Germany, **2009**.

253. Neidig, M. L. Decker, A. Choroba, O.W. Huang, F. Kavana, M. Moran, G.R. Spencer, J.B. Solomon, E. I. Spectroscopic and electronic structure studies of aromatic electrophilic attack and hydrogen-atom abstraction by non-heme iron enzymes. *Proc. Natl. Acad. Sci.* USA. **2006**, 103, 12966–12973.

254. Nelson, D.R. The cytochrome p450 homepage. *Hum Genomics*. **2009**, 1, 59-65.

255. Neu, H. M. Baglia, R. A. Goldberg, D. P. A Balancing Act: Stability versus Reactivity of Mn(O) Complexes. *Acc. Chem. Res*. **2015**, 48, 2754–2764.

256. Nicholls, P. Fita I. Loewen, P.C. Enzymology and structure of catalases. *Adv. Inorg. Chem.* **2000**, 51, 51–106.

257. NIST[1] Chemistry WebBook, NIST Standard Reference Database, Number 69 (Eds.: P. J. Linstrom, W. G. Mallard) National Institute of Standards and Technology, Gaithersburg MD, 20899, http://webbook.nist.gov.

258. O'Brien, P. Catalytic Promiscuity and the Divergent Evolution of DNA Repair Enzymes. *J. Chem. Rev.* **2006**, 106, 720–752.

259. Ochterski, J.W. **1999**. Vibrational Analysis in Gaussian. 1 – 19.

260. Ochterski, J.W. **2000**. Thermochemistry in Gaussian. 1 – 17.

261. Ogliaro, F. Harris, N. Cohen, S. Filatov, M. de Visser, S. P. Shaik, S. A Model "Rebound" Mechanism of Hydroxylation by Cytochrome P450: Stepwise and Effectively Concerted Pathways, and Their Reactivity Patterns. *J. Am. Chem. Soc*. **2000**, 122, 8977–8989.

262. Ogliaro, F.; Cohen, S.; de Visser, S.P.; Shaik, S. Medium polarization and hydrogen bonding effects on Compound I of cytochrome P450: what kind of a radical is it really? *J. Am. Chem. Soc.* **2000**, 122, 12892–12893.

263. Ogliaro, F.; de Visser, S.P.; Cohen, S.; Kaneti, J.; Shaik, S. The experimentally elusive oxidant of cytochrome P450: A theoretical "trapping" defining more closely the "real" species. *ChemBioChem.* **2001**, 2, 848–851.

264. Ogliaro, F.; de Visser, S.P.; Groves, J.T.; Sason Shaik, S. Chameleon states: high-valent metal-oxo species of cytochrome P450 and its ruthenium analog. *Angew. Chem. Int. Ed.* **2001**, 40, 2874–2878.

265. Olah, J. Mulholland, A.J. Harvey, J. Understanding the determinants of selectivity in drug metabolism through modelling of dextromethorphan oxidation by cytochrome P450. *PNAS.* **2011**, 108, 15, pp. 6050 – 6055.

266. Olbe, L. Carlsson, E. Lindberg, P. 2003. A Proton-Pump Inhibitor Expedition: The Case Histories of Omeprazole and Esomeprazole. *Nature Reviews: Drug Discovery.* **2003,** 2, 132 – 139.

267. Olsen, L. Rydberg, P. Rod, T. Ryde, U. Prediction of Activation Energies for Hydrogen Abstraction by Cytochrome P450. *J. Med. Chem*, **2006**, 49 (22), 6489 – 6499.

268. Ortiz de Montellano, P. Cytochrome P450: Structure, Mechanism and Biochemistry. 3rd ed., Kluwer Academic/Plenum Publishers, New York, **2005**.

269. Ortiz de Montellano, P.R. Catalytic Sites of Hemoprotein Peroxidases. *Annu. Rev. Pharmacol. Toxicol*. **1992**, 32, 89–107.

270. Ortiz de Montellano, P.R. Hydrocarbon Hydroxylation by Cytochrome P450 Enzymes. *Chem. Rev*. **2010**, 110, 932–948.

271. Ortiz de Montellano P. Cytochrome P450: structure, mechanism, and biochemistry, Springer International Publishing Switzerland, **2015**.

272. Park, J. Lee, Y.M. Nam, W. Fukuzumi, S. Brønsted Acid-Promoted C–H Bond Cleavage via Electron Transfer from Toluene Derivatives to a Protonated Nonheme Iron(IV)-Oxo Complex with No Kinetic Isotope Effect. *J. Am. Chem. Soc*. **2013**, 135, 5052–5061.

273. Perdew, J. P. Density-functional Approximation for the Correlation Energy of the Inhomogeneous Electron Gas. *Phys. Rev*. B **1986**, 33, 8822–8824.

274. Perdew, J.P. Wang, Y. Accurate and simple analytic representation of the electron-gas correlation energy. *Phys. Rev. B.* **1992**, 45, 13244.

275. Pickl, M. Kurakin, S. Cantu-Reinhard, F.G. Schmid, P. Pocheim, A. Winkler, C.K. Kroutil, W. de Visser, S.P. Faber, K. Mechanistic studies of fatty acid activation by cytochrome P450 enzymes reveals unexpected desaturase activity. Manuscript in preparation.

276. Pittala, V. Salerno, L. Romeo, G. Modica,M. Siracusa, M. 2013. A Focus on Heme Oxygenase -1 (HO-1) inhibitors. *Curr. Med. Chem.* **2013,** 30, 3711 – 3732.

277. Porro, C.S., Sutcliffe, M.J., de Visser, S.P. 2009. Quantum Mechanics/Molecular Mechanics Studies on the Sulfoxidation of Dimethyl Sulfide by Compound I and Compound 0 of Cytochrome P450: Which is the Better Oxidant? *J. Phys. Chem. A.* **2009**, 113, 11635–11642

278. Postils, V.; Company, A.; Solà, M.; Costas, M.; Luis, J. M. Computational Insight into the Mechanism of Alkane Hydroxylation by Non-Heme Fe(PyTACN) Iron Complexes. Effects of the Substrate and Solvent. *Inorg. Chem*. **2015**, 54, 8223–8236.

279. Poulos, T.L. Thirty years of heme peroxidase structural biology. *Arch. Biochem. Biophys*. **2010**, 500, 3–12.

280. Poulos, T. L. Heme enzyme structure and function. *Chem. Rev*. **2014**, 114, 3919–3962.

281. Prokop, K.A. de Visser, S.P. Goldberg, D.P. Unprecedented rate enhancements of hydrogen-atom transfer to a manganese(V)-oxo corrolazine complex.. *Angew. Chem. Int. Ed*. **2010**, 49, 5091-5095.

282. Pratter, S. M.; Konstantinovics, C. DiGiuro, C. L. M. Leitner, E. Kumar, D. de Visser, S. P. Grogan, G. Straganz, G. D. Inversion of Enantioselectivity of a Mononuclear Non-Heme Iron (II)-dependent Hydroxylase by Tuning the Interplay of Metal-Center Geometry and Protein Structure. *Angew. Chem. Int. Ed.* **2013**, 52, 9677–9681.

283. Que Jr, L. One Motif--many Different Reactions. *Nat. Struct. Biol*. **2000**, 7, 182–184.

284. Que Jr, L. The Road to Non-Heme Oxoferryls and Beyond. *Acc. Chem. Res*. **2007**, 40, 493–500.

285. Quesne, M. G.; Latifi, R.; Gonzalez-Ovalle, L. E.; Kumar, D.; de Visser, S. P. Quantum Mechanics/Molecular Mechanics Study on the Oxygen

Binding and Substrate Hydroxylation Step in AlkB Repair Enzymes. *Chem. Eur. J.* **2014**, *20*, 435–446.

286. Quesne, M. Borowski, T. De Visser, S. 2016. Quantum Mechanics/Molecular Mechanics modelling of Enzymatic Processes: Caveats and Breakthroughs. *Chem. Eur. J.* **2016**, 22, 2562 – 2581.

287. Quesne, M.G. Senthilnathan, D. Singh, D. Kumar, D. Maldivi, P. Sorokin, A. B. de Visser, S.P. Origin of the Enhanced Reactivity of μ-Nitrido-Bridged Diiron (IV)-Oxo Porphyrinoid Complexes over Cytochrome P450 Compound I. *ACS Catal*. **2016**, 6, 2230–2243.

288. Rafanan, E. R.; Le, L.; Zhao, L. L.; Decker, H.; Shen, B. Cloning, Sequencing, and Heterologous Expression of the elmGHIJ Genes Involved in the Biosynthesis of the Polyketide Antibiotic Elloramycin from Streptomyces olivaceus Tü235. *J. Nat. Prod.* **2001**, 64, 444–449.

289. Rana, S. Dey, A. Maiti, D. 2015. Mechanistic elucidation of C-H oxidation by electron rich non-heme iron(iv)-oxo at room temperature. *Chem. Comm.* **2015,** 51, 14469-14472.

290. Raven, E.L. Understanding functional diversity and substrate specificity in haem peroxidases: what can we learn from ascorbate peroxidase? *Nat. Prod. Rep.* **2003**, 20, 367–381.

291. Renault, H., Bassard, J.E., Hamberger, B. Weck-Reichhart, D. 2014. Cytochrome P-450 Mediated metabolic Engineering: current Progress and Future Challenges. *Current Opinion in Plant Biology.* **2014,** 19, 27-34.

292. Rettie, A.E.; Rettenmeier, A.W.; Howald, W.N.; Baillie, T.A. Cytochrome P-450-catalyzed formation of delta4-VPA, a toxic metabolite of valproic acid. Science **1987**, 235, 890–893.

293. Reynald, R. Sansen, S. Stout, C. Johnson, E. 2012. Structural Characterization of Human Cytochrome P450 2C19: Active Site Differences Between P450s 2C8, 2C9 and 2C19. *J. Biol.Chem.* **2012,** 287, 44581 – 44591.

294. Ribeiro, A.K., Ramos, M.J., Fernandes, P.A. 2010. Benchmarking of DFT Functionals for the Hydrolysis of Phosphodiester Bonds. *J. Chem. Theory. Comp*. **2010,** 6, 2281 – 2292.

295. Rittle, J., Green, M.T. Cytochrome P450 Compound I: Capture, Characterization, and C-H Bond Activation Kinetics. *Science.* **2010**, 330, 933-937.

296. Roberts, J. E. Hoffman, B.M. Rutter, R. Hager, L.P. O Endor of Horseradish peroxidase Compound I. *J. Am. Chem. Soc*. **1981**, 103, 7654–7656.

297. Roelfes, G. Lubben, M. Leppard, S. Schudde, E. Hermant, R. Hage, R. Wilkinson, E. Que, L. Feringa, B. 1997. Functional Models for Iron-Bleomycin. *Journal of Molecular Catalysis A: Chemical.* **1997,** 117, 223 – 227.

298. Rohde, J.U. In, J.H. Lim, M. H. Brennessel, W.W. Bukowski, M.R. Stubna, A. Münck, E. Nam, W. Que Jr, L. Crystallographic and Spectroscopic Characterization of a Nonheme Fe(IV)=O Complex. *Science* **2003**, 299, 1037-1039.

299. Rohmann, K. Holscher, M. Leitner, W. 2016. Can contemporary Density Functional Predict Energy Spans in Molecular Catalysis Accurately Enough To Be Applicable for *In Silico* Catalyst Design? A Computational/Experimental Case Study for the Ruthenium-Catalyzed Hydrogenation of Olefins. *Journal of the American Chemical Society.* **2016,** 138, 433-443.

300. Rosa, A. Ricciardi, G. Reactivity of compound II: electronic structure analysis of methane hydroxylation by oxoiron (IV) porphyrin complexes. *Inorg. Chem*. **2012**, 51,s 9833–9845.

301. Rude, M.A., Baron, T.S., Brubaker, S., Alibhai, M., Del-Cardayre, S.B., Schirmer, A. 2011. Terminal Olefin (1-Alkene) Biosynthesis by a Novel P450 Fatty Acid Decarboxylase from Jeotgalicoccus Species. *Applied and Environmental Microbiology*. **2011,** 77, 1718-1727.

302. Rush, L.E. Pringle, P.G. Harvey, J. N. Computational Kinetics of Cobalt-Catalyzed Alkene Hydroformylation. *Angew. Chem. Int. Ed.* **2014**. 53, 8672-8676.

303. Rydberg, P. Gloriam, D. Zaretzki, J. Breneman, C. Olsen, L. 2010. SMARTCyp: A 2D Method for Prediction of Cyochrome P450-Mediated Drug Metabolism. *ACS Med. Chem. Lett.* **2010,** 1, 96 - 100.

304. Ryle, M. J.; Hausinger, R. P. Non-heme Iron Oxygenases. *Curr. Opin. Chem. Biol.* **2002**, 6, 193–201.

305. Sahu, S. Widger, L. R. Quesne, M. G. de Visser, S. P. Matsumura, H. Moënne-Loccoz, P. Siegler, M. A. Goldberg, D.P. Secondary Coordination

Sphere Influence on the Reactivity of Nonheme Iron(II) Complexes: An Experimental and DFT Approach. *J. Am. Chem. Soc.* **2013**, 135, 10590–10593.

306. Sainna, M. A.; Kumar, S.; Kumar, D.; Fornarini, S.; Crestoni, M. E.; de Visser, S. P. A Comprehensive Test Set of Epoxidation Rate Constants for Iron(IV)–oxo Porphyrin Cation Radical Complexes. *Chem. Sci*. **2015**, 6, 1516–1529.

307. Saltzman, H. Sharefkin, J. G. Organic Syntheses, Wiley, New York, **1973**, Collect. Vol. 5, p 658.

308. Sastri, C. Seo, M. Park, M. Kim, K. Nam, W. 2005. Formation, Stability, and Reactivity of a mononuclear nonheme oxoiron(IV) complex in aqueous solution. *Chem. Commun.* **2005**, 1405 – 1407.

309. Sastri, V. Plastics in Medical Devices: Properties, Requirements, and Applications. **2014**. Oxford, UK. Elsevier.

310. Sastri, C.V. Lee, J. Oh, K. Lee, Y. J. Lee, J. Jackson, T. A. Ray, K. Hirao, H. Shin, W. Halfen, J. A. Kim, J. Que Jr, L. Shaik, S. Nam, W. Axial ligand tuning of a nonheme iron(IV)–oxo unit for hydrogen atom abstraction. *Proc. Natl. Acad. Sci.* USA **2007**, 104, 19181–19186.

311. Schafer, A.; Horn, H.; Ahlrichs, R. Fully optimized contracted Gaussian basis sets for atoms Li to Kr. *J. Chem. Phys*. **1992**, *97*, 2571–2577.

312. Schlichting, I. Berendzen, J.. Chu, K. Stock, A. M Maves, S. A. Benson, D. E. Sweet, R. M. Ringe, D. Petsko, G. A. Sligar, S. G. The catalytic pathway of cytochrome P450cam at atomic resolution. *Science.* **2000**, 287, 1615–1622.

313. Schmider, H. L.; Becke, A. D. Optimized Density Functionals from the Extended G2 Test Set. *J. Chem. Phys*. 1998, 108, 9624–9631.

314. Schöneboom, J.C.; Lin, H.; Reuter, N.; Thiel, W.; Cohen, S.; Ogliaro, F.; Shaik, S. The elusive oxidant species of cytochrome P450 enzymes: characterization by combined quantum mechanical/molecular mechanical (QM/MM) calculations. *J. Am. Chem. Soc.* **2002**, 124, 8142–8151.

315. Schramm, V. 2005. Enzymatic transition states and transition state analogues. *Current Opinion in Structural Biology.* **2005,** 15, 604 -613.

316. Schwabe, T.; Grimme, S. Towards Chemical Accuracy for the Thermodynamics of Large Molecules: New Hybrid Density Functionals

Including Non-Local Correlation Effects. *Phys. Chem. Chem. Phys*. **2006**, 8, 4398–4412.

317. Schwab, M., Zanger, U.M. 2013. Cytochrome P450 Enzymes in drug metabolism: Regulation of Gene Expression, enzyme activities, and impact of Genetic Variation. *Pharmacology and Therapeutics*. **2013,** 138, 103 – 141.

318. Schwerdtfeger, P. 2011. The Pseudopotential Approximation in Electronic Structure Theory. *ChemPhysChem.* **2011,** 12, 3143 - 3155.

319. Sciara, G.; Kendrew, S. G.; Miele, A. E.; Marsh, N. G.; Federici, L.; Malatesta, F.; Schimperna, G.; Savino, C.; Vallone, B. The structure of ActVA-Orf6, a novel type of monooxygenase involved in actinorhodin biosynthesis. EMBO J. **2003**, 22, 205–215.

320. Senn, H. Thiel, W. 2007. QM/MM studies of enzymes. *Current Opinion in Chemical Biology.* 11, **2007**, 182 – 187.

321. Setzu, H. Goff, G. Feyereisen, R. Origins of P450 diversity. *Philos. Trans. R. Soc. Lond. B. Biol. Sci.* **2013,** 368, (1612):20120428.

322. Shaik, S. What happens to molecules as they react? A valence bond approach to reactivity. *J. Am. Chem. Soc*. **1981**, 103, 3692–3701.

323. Shaik, S. De Visser, S.P. Oglirao,F. Schwarz, H. Schroder, D. Two State Reactivity mechanisms of Hydroxilation and epoxidation by cytochrome P450 revealed by theory. *Curr. Opinion in Chem. Bio.* **2002**. 6, 556 – 567.

324. Shaik, S. Cohen, S. de Visser, S.P. Sharma, P.K. Kumar, D. Kozuch, S. Ogliaro, F. Danovich, D. The "Rebound Controversy": An Overview and Theoretical Modeling of the Rebound Step in C-H Hydroxylation by Cytochrome P450. *Eur. J. Inorg. Chem.* **2004**, *Microreview*, pp. 207 – 226.

325. Shaik, S. Kumar, D. de Visser, S. P. Altun, A. Thiel, W. Theoretical Perspective on the Structure and Mechanism of Cytochrome P450 Enzymes. *Chem. Rev*. **2005**, 105, 2279–2328.

326. Shaik, S. Kumar, D. De Visser, S. 2008. A valence Bond Modelling of Trends in Hydrogen Abstraction Barriers and Transition States of Hydroxylation Reactions catalysed by Cytochrome P450 Enzymes. *J. Am. Chem. Soc*. **2008,** 130, 10128 – 10140.

327. Shaik, S. Cohen, S. Want, Y. Chen, H. Kumar, D. Thiel, W. P450 Enzymes: Their Structure, Reactivity and Selectivity, Modeled by QM/MM calculations. *Chem Rev*. **2010[1]**, 110, 949 – 1017.

328. Shaik, S. Lai, W. Chen, H. Wang, Y. The Valence Bond Way: Reactivity Patterns of Cytochrome P450 Enzymes and Synthetic Analogues. *Accounts of Chem. Res*. **2010**[2], 43, 1154 – 1165.

329. Shaik, S. Valence bond all the way: From the degenerate H-exchange to cytochrome P450. *Phys. Chem. Chem. Phys.* **2010**, 12, 8706–8720.

330. Shaik, S. Milko, P. Schyman, P. Usharani, D. Chen, H. Trends in aromatic oxidation reactions catalyzed by Cytochrome P450 Enzymes: a valence bond modelling. *J. Chem. Theory Comput*. **2011**, 7, 327–339.

331. Sharma, P.K.; de Visser, S.P.; Ogliaro, F.; Shaik, S. Is the ruthenium analogue of Compound I of cytochrome P450 an efficient oxidant? A theoretical investigation of the methane hydroxylation reaction. *J. Am. Chem. Soc*. **2003**, 125, 2291–2300.

332. Sharma, P. de Visser, S. Shaik, S. 2003. Can a Single Oxidant with two Spin States Masquerade as Two Different Oxidants? A Study of the Sulfoxidation Mechanism by Cytochrome P450. *J. Am. Chem. Soc*. **2003**, 125, 8698 – 8699.

333. Sharma, P. Kevorkiants, R. de Visser, S. Shaik, S. 2004. Porphyrin Traps its Terminator! Concerted and Stepwise Porphyrin Degradation Mechanisms induced by Heme-Oxygenase and Cytochrome. *Angew. Chem. Int. Ed.* **2004,** 43, 1129 - 1129.

334. Sherwood, P.; de Vries, A. H.; Guest, M. F.; Schreckenbach, G.; Catlow, C. R. A.; French, S. A.; Sokol, A. A.; Bromley, S. T.; Thiel, W.; Turner, A. J.; Billeter, S.; Terstegen, F.; Thiel, S.; Kendrick, J.; Rogers, S. C.; Casci, J.; Watson, M.; King, F.; Karlsen, E.; Sjøvoll, M.; Fahmi, A.; Schäfer, A.; Lennartz, C. QUASI: A general purpose implementation of the QM/MM approach and its application to problems in catalysis. *J. Mol. Struct*. **2003**, *632*, 1–28.

335. Shono, T. Nozoe, T. Maekawa, H. Yamaguchi, Y. Kanetaka, S.Masuda, H. Okada, T. Kashimura, S. *Tetrahedron.* **1991**, 47, 4-5, 593-603.

336. Schyman, P. Usharani, D. Wang, Y. Shaik, S. 2010. Brain Chemistry: How does P450 Catalyze de O-Demethylation Reaction of 5-Methoxytryptramine to Yield Serotonin? *J. Phys. Chem.* **2010**, 114, 7078-7089.

337. Sieffert, N. Buhl, M. 2009. Noncovalent Interactions in a Transition-Metal Triphenylphosphine Complex: A density Functional Case Study. *Inorg. Chem*. **2009,** 48, 4622 - 4624.

338. Siegbahn, P.E.M. Himo, F. The Quantum chemical cluster approach for modelling enzyme reactions. *Comput. Mol. Sci*, **2011**, 1, 323 – 336.

339. Siitonen, V.; Blauenburg, B.; Kallio, P.; Mäntsälä, P.; Metsä-Ketelä, M. Discovery of a two-component monooxygenase SnoaW/SnoaL2 involved in nogalamycin biosynthesis. *Chem. Biol*. **2012**, *19*, 638–646.

340. Singh, D.; Kumar, D.; de Visser, S.P. Methane hydroxylation by axially ligated iron(IV)-oxo porphyrin cation radical models. *Int. J. Sc. Technol*. **2015**, 1, 26–40.

341. Sivaraja, M Goodin, D. B. Smith, M. Hoffman, B. M. Identification by Endor of TRP19 as the Free-Radical Site in Cytochrome c Peroxidase Compound ES. *Science* **1989**, 245, 738–740.

342. Slater, J.C. Atomic Shielding Constants. *Physical Review*. **1930**, 36, 57-64.

343. Smith, W.; Forester, T. R. DL_POLY_2.0: A general-purpose parallel molecular dynamics simulation package. Journal of Molecular Graphics. *J. Mol. Graphics* **1996**, *14*, 136–141.

344. Smith, G. Wolf, C.R. Deeni, Y.Y. Dawe, R. Evans, A.T. Comrie, M.M. Ferguson, J. Ibbotson, S.H. Cutaneous expression of cytochrome P450 CYP2S1: individuality in regulation by therapeutic agents for psoriasis and other skin diseases. *The Lancet*, **2003** 361, 1336 – 1343.

345. Solomon, E. I.; Brunold, T. C.; Davis, M. I.; Kemsley, J. N.; Lee, S.-K.; Lehnert, N.; Neese, F.; Skulan, A. J.; Yang, Y.-S.; Zhou, J. Geometric and Electronic Structure/Function Correlations in Non-Heme Iron Enzymes. *Chem. Rev*. **2000**, 100, 235–349.

346. Solomon, E. I.; Light, K. M.; Liu, L. V.; Srnec, M.; Wong, S. D. Geometric and Electronic Structure Contributions to Function in Non-heme Iron Enzymes. *Acc. Chem. Res.* **2013**, 46, 2725–2739.

347. Song, W.J. Sun, Y.J. Choi, S.K. Nam, W. Mechanistic Insights into the Reversible Formation of Iodosylarene–Iron Porphyrin Complexes in the Reactions of Oxoiron(IV) Porphyrin π-Cation Radicals and Iodoarenes:

Equilibrium, Epoxidizing Intermediate, and Oxygen Exchange. **2005**, 12, 1, 130-137.

348. Song, W. J. Ryu, Y. O. Song, R. Nam, W. Oxoiron (IV) porphyrin π-cation radical complexes with a chameleon behavior in cytochrome P450 model reactions, *J. Am. Chem. Soc*. **2005**, 10, 294–304.

349. Sono, M. Roach, M. P. Coulter, E. D. Dawson, J. H. Heme-containing oxygenases. *Chem. Rev*. **1996**, 96, 2841–2888.

350. Steiner, R. A.; Janssen, H. J.; Roversi, P.; Oakley, A. J.; Fetzner, S. Structural basis for cofactor-independent dioxygenation of N-heteroaromatic compounds at the alpha/beta-hydrolase fold. *Proc. Natl. Acad. Sci. USA* **2010**, *107*, 657–662.

351. Stephens, P.J. Devlin, F.J. Chabalowski, C.F. Frisch, M.J. Ab Initio Calculation of Vibrational Absorption and Circular Dichroism Spectra Using Density Functional Force Fields. *J. Phys. Chem.* **1994**, 98, 11623 – 11627.

352. Straganz, G. D.; Nidetzky, B. Variations of the 2-His-1-Carboxylate Theme in Mononuclear Non-Heme FeII Oxygenases. *ChemBioChem* **2006**, 7, 1536–1548.

353. Stipanuk, M. H. Sulfur Amino Acid Metabolism: Pathways for Production and Removal of Homocysteine and Cysteine. *Annu. Rev. Nutr*. **2004**, 24, 539–577.

354. Su, T. Chesnavich, W. J. Parametrization of the ion–polar molecule collision rate constant by trajectory calculations. *J. Chem. Phys*. **1982**, 76, 5183–5185.

355. Taguchi, T.; Yabe, M.; Odaki, H.; Shinozaki, M.; Metsa-Ketela, M.; Arai, T.; Okamoto, S.; Ichinose, K. Biosynthetic Conclusions from the Functional Dissection of Oxygenases for Biosynthesis of Actinorhodin and Related Streptomyces Antibiotics. *Chem. Biol.* **2013**, 20, 510–520.

356. Tahsini, L. Bagherzedah, M. Nam, W. de Visser, S.P. Fundamental Differences of Substrate Hydroxylation by High-Valent Iron(IV)-Oxo Models of Cytochrome P450. *Inorg. Chem*. **2009**, 48 (14), 6661–6669.

357. Tang, X. Li, J. Moore, B. Minimization of the Thiolatomycin Biosynthetic Pathway Reveals That the Cytochrome P450 Enzyme TImF is Required for Five-Membered Thiolactone Ring Formation. *ChemBioChem*. **2017**, 18, 1072 – 1076.

358. Tang, M.-C.; Zou, Y.; Watanabe, K.; Walsh, C.T.; Tang, Y. Oxidative cyclization in natural product biosynthesis. *Chem. Rev*. **2017**, 107, 5226−5333.

359. Taxak, N. Patel, B. Baratham, P. Carbene Generation by Cytochromes and Electronic Structure of Heme-Iron-Porphyrin-Carbene Complex: A Quantum Chemical Study. *Inorganic Chemistry.* **2013,** 52, 5097 – 5109.

360. Tchesnokov, E.P. Faponle, A.S. Davies, C.G. Quesne, M.G. Turner, R. Fellner, M. Souness, R.J. Wilbanks, S.M. de Visser, S.P. Jameson, G.N.L. An iron–oxygen intermediate formed during the catalytic cycle of cysteine dioxygenase. *Chem. Commun*. **2016**, 52, 8814–8817.

361. Thareja, S. 2015. Steroidal 5a-Reducatase Inhibitors: A Comparative 3D-QSAR Study Review. *Americal Chemical Society.* **2015,** 115, 2883 - 2894.

362. Thierbach, S.; Bui, N.; Zapp, J.; Chhabra, S. R.; Kappl, R.; Fetzner, S. Substrate-assisted O2 activation in a cofactor-independent dioxygenase. *Chem. Biol*. **2014**, 20, 1–9.

363. Thomas, K. E. Alemayehu, A. B. Conradie, J. Beavers, C. M. Ghosh, A. The Structural Chemistry of Metallocorroles: Combined X-ray Crystallography and Quantum Chemistry Studies Afford Unique Insights. *Acc. Chem. Res*. **2012**, 45, 1203–1214.

364. Tian, S. Wang, J. Li, Y., Li, D. Xu, L. Hou, T. 2015. The Application of *in silico* drug-likeness predictions in pharmaceutical research. *Advanced Drug Delivery Reviews.* **2015,** 86, 2 - 10.

365. Timmins, A.; Saint-André, M.; de Visser, S. P. Understanding How Prolyl-4-hydroxylase Structure Steers a Ferryl Oxidant toward Scission of a Strong C-H Bond. *J. Am. Chem. Soc*. **2017**, *139*, 9855–9866.

366. Timmins, A.; de Visser, S. P. How Are Substrate Binding and Catalysis Affected by Mutating Glu127 and Arg161 in Prolyl-4-hydroxylase? A QM/MM and MD Study. *Frontiers Chem*. **2017**, *5*, article 94.

367. Todorov, I. T.; Smith, W.; Trachenko, K.; Dove, M. T. DL_POLY_3: new dimensions in molecular dynamics simulations via massive parallelism. *J. Mater. Chem.* **2006**, *16*, 1911–1918.

368. Tomasi, J. Persico, M. 1994. Molecular Interactions in Solution: An Overview of Methods based on Continuos Distributions of the Solvent. *Chem Rev.* **1994,** 94, 2027 – 2094.

369. Tomasi, J.; Mennucci, B.; Cammi, R. Quantum Mechanical Continuum Solvation Models. Chem. Rev. **2005**, 105, 2999–3093.

370. Trewick, S. C.; Henshaw, T. F.; Hausinger, R. P.; Lin-dahl, T.; Sedgwick, B. Oxidative Demethylation by Escherichia coli AlkB Directly Reverts DNA Base Damage. *Nature* **2002**, 419, 174–178.

371. Truhlar, D. Cramer, C. Implicit Solvation Models: Equilibria, Structure, Spectra and Dynamics. *Chem. Rev.* **1999,** 99, 2161 - 2200.

372. Tse, C.-W.; Chow, T. W.-S.; Guo, Z.; Lee, H. K.; Huang, J.-S.; Che, C.-C. Nonheme Iron Mediated Oxidation of Light Alkanes With Oxone: Characterization of Reactive Oxoiron(IV) Ligand Cation Radical Intermediates by Spectroscopic Studies and DFT Calculations. *Angew. Chem. Int. Ed*. **2014**, 53, 798–803.

373. UCSF Chimera--a visualization system for exploratory research and analysis. Pettersen EF, Goddard TD, Huang CC, Couch GS, Greenblatt DM, Meng EC, Ferrin TE. *J Comput Chem.* **2004,** 25(13):1605-12.

374. Urlacher, V.B. Girhard, M. Cytochrome P450 monooxygenases: an update on perspectives for synthetic application. *Trends in Biotechnology*, **2012**, 30(1), 26-36

375. Uttamsingh, V. Gallegos, R. Liu, J. Habeson, S. Bridson, G. Cheng, C. Wells, D. Graham, P. Zelle, R. Tung, R. Altering Metabolic Profiles of Drugs by Precision Deuteration: Reducing Mechanism Based Inhibition of CYP2D6 by Paroxetine. *The Journal of Pharmacology and Experimental Therapeutics.* **2015,** 354, 43-54.

376. Vardhaman, A.K.; Sastri, C.V.; Kumar, D.; de Visser, S.P. Nonheme ferric hydroperoxo intermediates are efficient oxidants of bromide oxidation. *Chem. Commun*. **2011**, 47, 11044–11046.

377. Vardhaman, A.K. Barman, P. Kumar, S. Sastri, C. V. Kumar, D. de Visser, S.P. Comparison of the Reactivity of Nonheme Iron (IV)–Oxo versus Iron (IV)–Imido Complexes: Which is the Better Oxidant? *Angew. Chem. Int. Ed.* **2013**, 52, 12288–12292

378. Veitch, N.G. Smith, A. T. Horseradish Peroxidase. *Adv. Inorg. Chem*. **2000**, 51, 107–162.

379. Vincent, M.A. Hillier, I.H. Ge, J. How is N–N bond formation facilitated by P450 NO reductase? A DFT study. *Chemical Physics Letters.* **2005**, 407, 4-6, 333-336.

380. Voltz, T.J., Rock, D.A., Jones, J.P. 2002. Evidence for Two Different Active Oxygen Species in Cytochrome P450 BM3 Mediated Sulfoxidation and N-Dealkylation Reactions. *J. Am. Chem. Soc.* **2002,** 124, 9724 – 9725.

381. Vosko, S. Wilk, L. Nusair, M. Accurate spin-dependent electron liquid correlation energies for local spin density calculations: a critical analysis. *Canadian Journal of Physics*, **1980**, 58(8): 1200-1211

382. Wang, D. Ray, K. Collins, M. J. Farquhar, E. R. Frisch, J. R. Gómez, L. Jackson, T. A. Kerscher, M. Waleska, A. Comba, P. Costas, M. Que Jr, L. Nonheme oxoiron (IV) complexes of pentadentate N5 ligands: spectroscopy, electrochemistry, and oxidative reactivity. *Chem. Sci.* **2013**, 4, 282–291.

383. Wang, Y. Kumar, D. Yang, C.L. Han, S. Shaik, S. *J. Phys. Chem. B.* **2007**, 111, 7700-7710.

384. Watanabe, Y.; Nakajima, H.; Ueno, T. Reactivities of oxo and peroxo intermediates studied by hemoprotein mutants. *Acc. Chem. Res*. **2007**, 40, 554–562.

385. Wertz, D.H. 1980. Relationship between the Gas-Phase Entropies of Molecules and Their Entropies of Solvation in Water and 1-Octanol. *J. American Chemical Society.* **1980,** 102, 5316 – 5332.

386. Wickramasinghe, R. Villee, C. Early role during chemical evolution for cytochrome P450 in oxygen detoxification. *Nature* **1975,** 256, 509 – 511.

387. Wong, S.D. Bell C. B. Liu, L.V. Kwak, Y. England, J. Alp, E. E. Zhao, J. Que Jr, L. Solomon, E. I. Nuclear Resonance Vibrational Spectroscopy on the FeIV=O S=2 Non-Heme Site in TMG3tren: Experimentally Calibrated Insights into Reactivity. *Angew. Chem. Int. Ed.* **2011**, 50, 3215–3218.

388. Wright, M. 2004. An Introduction to Chemical Kinetics. John Wiley and Sons Ltd. **2004**. USA.

389. Xu, C. Johnson, C.R. Chemoenzymatic studies: From cycloheptatriene to the core of zaragozic acids. *Tetrahedron Letters*. **1997**, 38, 1117-1120.

390. Xu, J. Wang, X., Guo, W. 2015. The cytochrome P450 superfamily: Key players in plant development and defence. *Journal of Integrative Agriculture*. **2015,** 14, 1673 - 1686.

391. Yang, T. Quesne, M.G. Neu, H. M. Cantú Reinhard, F. G. Goldberg, D. P. de Visser, S. P. Singlet versus Triplet Reactivity in an Mn (V)–Oxo Species: Testing Theoretical Predictions Against Experimental Evidence. *J. Am. Chem. Soc.* **2016**, 138, 12375–12386.

392. Yano, J.K.; Wester, M.R.; Schoch, G.A.; Griffin, K.J.; Stout, C.D.; Johnson, E.F. The structure of human microsomal cytochrome P450 3A4 determined by X-ray crystallography to 2.05Å resolution. *J. Biol. Chem.* **2004**, 279, 38091–38094.

393. Ye, J. S.; Dickens, M. L.; Plater, R.; Li, Y.; Lawrence, J.; Strohl, W. R. Isolation and sequence analysis of polyketide synthase genes from the daunomycin-producing Streptomyces sp. strain C5. *J. Bacteriol.* **1994**, 176, 6270–6280.

394. Ye, S. F. Neese, F. Nonheme oxo-iron(IV) intermediates form an oxyl radical upon approaching the C-H bond activation transition state. *Proc. Natl. Acad. Sci.* USA **2011**, 108, 1228–1233

395. Ye, S.; Geng, C.-Y.; Shaik, S.; Neese, F. Electronic Structure Analysis of Multistate Reactivity in Transition Metal Catalyzed Reactions: The Case of C-H Bond Activation by Non-Heme Iron(IV)-Oxo Cores. *Phys. Chem. Chem. Phys*. **2013**, 15, 8017–8030.

396. Ye, S. Kupper, C. Meyer, S. Andris, E. Navrátil, R. Krahe, O. Mondal, B. Atanasov, M. Bill, E. Roithová, J. Meyer, F. Neese, F. Magnetic Circular Dichroism Evidence for an Unusual Electronic Structure of a Tetracarbene–Oxoiron(IV) Complex. *J. Am. Chem. Soc.* **2016**, 138, 14312–14325.

397. Yi, C.; Yang, C. G.; He, C. A Non-heme Iron-mediated Chemical Demethylation in DNA and RNA. *Acc. Chem. Res*. **2009**, 42, 519–529.

398. Yoon, J. Wilson, S. A. Jang, Y. K. Seo, M. S. Nehru, K. Hedman, B. Hodgson, K. O. Bill, E. Solomon, E. I. Nam, W. Reactive intermediates in oxygenation reactions with mononuclear nonheme iron catalysts. *Angew. Chem. Int*. Ed. **2009**, 48, 1257–1260.

399. Zhang, Y. Biggs, J.D. Mukamel, S. Characterizing the Intermediates Compound I and II in the Cytochrome P450 Catalytic Cycle with Nonlinear X-ray Spectroscopy: A Simulation Study. Chemphyschem, **2015**, 16 (9) 2006-2014.

400. Zhao, Y. Truhlar, D. 2008. The M06 suite of density functionals for main group thermochemistry, thermochemical kinetics, noncovalent interactions, excited states, and transition elements: two new functionals and systematic testing of four M06-class functionals and 12 other functionals. *Theor. Chem. Acc*. **2008**, 120, 215-41.

401. Zoete, V. Cuendet, M. Grosdidier, A. Michielin, O. SwissParam, a Fast Force Field Generation Tool For Small Organic Molecules. *J. Comput. Chem.* **2011**, 32(11), 2359-68.